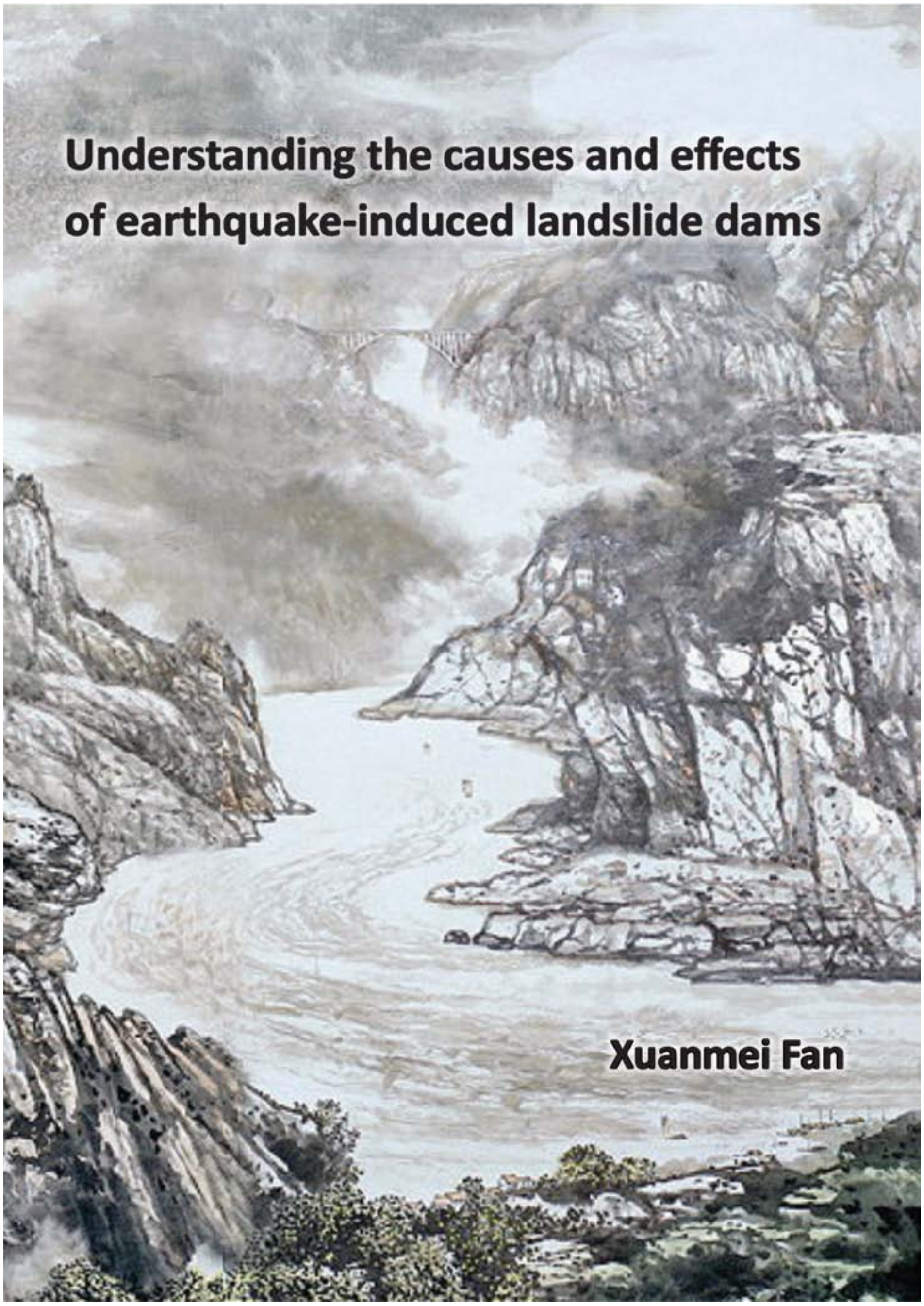

Understanding the causes and effects of earthquake-induced landslide dams

Xuanmei Fan

UNDERSTANDING THE CAUSES AND EFFECTS OF EARTHQUAKE-INDUCED LANDSLIDE DAMS

Xuanmei Fan

Examining committee:

Prof.dr. F.D. van der Meer	University of Twente
Prof.dr. A.S. Skidmore	University of Twente
Prof.dr. O. Korup	Universität Potsdam
Prof. H.-B. Havenith	Université de Liège
Prof. Q. Xu	Chengdu University of Technology

ITC dissertation number 233
ITC, P.O. Box 6, 7500 AA Enschede, The Netherlands

ISBN 978-90-6164-978-90-6164-361-6
Cover designed by Job Duim & Simeng Dong
Printed by ITC Printing Department

ITC UNIVERSITY OF TWENTE.
FACULTY OF GEO-INFORMATION SCIENCE AND EARTH OBSERVATION

UNDERSTANDING THE CAUSES AND EFFECTS OF EARTHQUAKE-INDUCED LANDSLIDE DAMS

DISSERTATION

to obtain
the degree of doctor at the University of Twente,
on the authority of the rector magnificus,
prof.dr. H. Brinksma,
on account of the decision of the graduation committee,
to be publicly defended
on Thursday September 12, 2013 at 12.45 hrs

by

Xuanmei Fan

born on July 9, 1981

in Gansu, China

This thesis is approved by

Prof. dr. Victor G. Jetten, promoter
Dr. Cees van Westen (assistant promoter)

To my beloved family

Acknowledgements

After drinking a glass of wine in the midnight, I know this is the right moment for looking back over the past four years. This story started actually from 2008, right after the devastating Wenchuan earthquake I was sent by my home university to ITC for attending a short course. I met my supervisor, Cees van Westen at that time and he encouraged me to purse a sandwich PhD in ITC and take the research topic on the landslide dams induced by the Wenchuan earthquake, as it was one of the most serious issues facing our Chinese government at that time. I thereby came back to ITC again in Sep, 2009, and started my PhD journey. This PhD thesis is the result of this challenging but joyful journey, upon which many wonderful people have contributed and given their great support. Without them, I would have never been able to accomplish this thesis.

First and foremost I wish to give special thanks to my supervisor Dr. Cees van Westen. It was indeed a great pleasure and very good fortune to work with Cees. I appreciate all his contributions of time and brilliant ideas to make my PhD research productive and stimulating. He always commented in details on my manuscripts, even can point out the spelling mistake of the name of Chinese city (correcting *“Mainyang”* to *“Mianyang”*). I admire him not only because of his immense knowledge, but also because of his great personality. He is such an open-minded and caring person with seemingly unlimited patience. All I have learned from him is a priceless treasure for the rest of my life. I wish to continue collaborating with him in the future.

I would like to express my gratitude to my promotor Prof. Victor Jetten for being my promotor, and his support and stimulating discussions in the final stage of my PhD. He can always look at problems from different angles, which broadened my view. His thoughtful comments were very helpful to shape this thesis in its present form.

To my supervisor in China, Prof. Qiang Xu, who was also my MSc supervisor. I am especially grateful to him for bringing me into the world of “Landslides” and his trust in me always, which has helped me to build up my confidence. I still remember that he tried hard to convince me that I can be a very good scientist and should definitely continue pursuing PhD. I have learned a lot from his amazing field experience and the power of solving problems in the real world.

This research was carried out under the collaboration between ITC and my home institute, the State Key Laboratory of Geo-hazard Prevention (SKLGP), Chengdu University of Technology. Special thanks to Prof. Niek Rengers, who initiated this collaboration in 2006 and has devoted great efforts to this collaboration over these years. Niek is the most easy-going and the warmest professor I have ever known. He has given me unconditional support whenever and wherever I needed. Many thanks to his families as well, I had great time with Maria, Ellen, Nicolien and other family members. They made me feel like home in the Netherlands.

I am truly grateful to Prof. Theo van Ash, who has given inspiring comments to my papers and has been my referee at any time I needed. He has a very strong sense of humor. The joy and enthusiasm he has for research was contagious and motivational for me. It was a great pleasure to discuss both scientific and non-scientific topics with him.

I would like to thank Dr. David Rossiter, who has contributed a lot to my professional and personal time at ITC. He has given great help to the statistics part of my work. He is a good teacher, an efficient co-author and a good friend. There are always new things that I can learn from him.

I could not have done this research without the great support from my home institute, SKLGP and many amazing individuals there. Especially, I appreciate Prof. Runqiu Huang for selecting and sending me to ITC for pursuing this degree. It has been a great honor for me to be the first joint PhD candidate between ITC and SKLGP. He is one of the most intelligent scientists I have ever worked with. His enthusiasm and very positive attitude to research and all kinds of collaborations have motivated me a lot. Many thanks to Prof. Chuan Tang and Prof. Jing Zhu, the most charming and kindest couple, for their constant encouragement and great support both academically and personally. Thanks to Qin Zhao, Haiyan Wang, Wenkai Feng, Haihua Li and Feng Du for their supportive service. I am grateful to all the people who have participated in data collection and fieldwork for this research, especially to Weile Li, Yi Zhang, Xiujun Dong, Shuai Zhang, Jianwei Zhou and Ruihua Xiao. I thank Simeng Dong for her help on the cover design and friendship.

I have been very fortunate to collaborate with many marvelous experts, who have broadened my horizons. Most of them were also my co-authors. I appreciate Prof. Oliver Korup for his tremendous help to my first paper. He suggested that the focus of the paper should be the impact of landslide dams on the post-earthquake sediment flux. He has helped me to strengthen my argument and taught me a great deal about writing skills. Special thanks to Prof. Hans-Balder Havenith for all interesting discussions, his trust in me and great help on applying post-doc fellowship. I want to thank Prof. Grasso for nice discussions and hosting me in Grenoble, France. Many thanks to Dr. Gonghui Wang, Prof. Fuchu Dai, Prof. Janusz Wasowski, Prof. Chyi-Tyi Lee, Prof. Jia-Jyun Dong, prof. Alexander Strom, Dr. Chong Xu and Dr. Wenjie Xu for inspiring discussions, sharing data and kind encouragements.

I would like to thank all the colleagues in the ESA department for their support and interesting discussions during our "lunch talk" and other department activities. Many thanks to my PhD fellows, in particular the "landslide mafia group" (Tolga, Byron, Andre, Khamarrul, Pankaj, Saibal, Tapas), with whom I had interesting discussions and exchanged many ideas. Especially to Tolga, we worked in the same study area and had many brainstorms. His enthusiasm to research strongly inspired me. And thanks to Sumbal, Effie, Thea, Pablo, Shruthi, Van, Haydar, Shafique and Nasrullah.

Many thanks also to all staff members at ITC for their helps and supportive service. Special thanks to Loes for always being supportive; to Marga for library service; to Job for the nice cover designing. Thanks to Theresa, Anke, Tina, Christie, Petra and Roelof for their help on various occasions.

For this thesis I would like to thank my reading committee members, Prof. Freek van der Meer, Prof. Andrew Skidmore, Prof. Oliver Korup, Prof. Hans-Balder Havenith and Prof. Qiang Xu for their time.

I grateful acknowledge the funding sources that made my PhD work possible. I was funded by the Chinese Scholarship Council for two years and by my home institute SKLGP for one and half years.

I have been fortunate to come across many funny and good friends, without whom life would be bleak. Heartfelt thanks to all my friends, who has companied me in this PhD journey, in particular to Sanaz, our "Queen" for her immense practical and emotional support, most importantly for becoming a lifelong friend. We shared all our happiness, sadness, excitement…which I will never forget. A special acknowledgement goes to my office mate: Sharon, she is an amazing person in many ways, being our "live dictionary", always giving useful suggestions...; and I am also grateful to my other great office mates, Anandita, Fekerte (for your friendships and kind encouragement); Khamarrul, Byron and Abel (for always being supportive). Special thanks to Divyani and Matthew for sharing great stories and yummy food. And thanks also to Tanmoy, Mustafa, Sonia, Wiebke, Carolina, Maitreyi, and Sejal, Mitava, Enrico and Chandra for interesting chats about culture and life.

I am grateful to my close Chinese friends, particularly to Fangyuan, with whom I have shared not only laughter but also tears in my ups and downs. She has given me great company and lifelong friendship. Special thanks to Chenxiao, who is like my brother, has taken very good care of me (being my personal chef) and given me tremendous support in the last year of my PhD. Again I want to tell him as always "We are family!"; to Yijian, who taught me a lot and shared so many memories…to Fangfang, Xia Li, Pu Hao and Tina for their valuable friendship and company. I really miss the time

we cooked and hanged out together. Many thanks to Xiang Zhang, Xi Zhao, Teng Fei, Meng Bian, Xiaogang, Liang Zhou, Dongpo, Sudan, Biao Xiong for their helps. Thanks also go to Bob Su, Lichun Wang, Tiejun Wang, Linlin, Donghai, Xiaojin, Xuelong, Shaoning, La Zhuo, Hongyan, Ying Zhang. There are too many to mention, but I do wish to express my gratitude to the Chinese student community for their support.

I feel most deeply indebted to my parents and parents in law for their unconditional love and endless support in all my pursuits. I am grateful to my parents for raising me with good education to be able to pursue science. To my husband, Ran Tang, I want to express my deepest gratitude for his unfailing love and support, which are essential for this PhD. They have given me the freedom to explore the world outside. My family is the source of my life energy and love. This thesis is dedicated to them. All I want to say is “我爱你们！”

Table of Contents

List of Figures

List of Tables

1 Introduction

Life is like riding a bicycle.
To keep your balance, you must keep moving (Albert Einstein).
That is why I started my PhD journey three years ago.

1.1 Background

As one of the most destructive geo-hazards, landslides pose serious threats to people and property, destroying houses and other structures, blocking roads, severing pipelines and other utility lifelines, and damming rivers. One kind of natural hazard may induce other hazards, the so-called "domino or chain effect". For example, strong earthquakes are among the prime triggering factors of landslides (Keefer, 1984), which may block rivers, forming landslide dams. Some of these dams may pose serious threats to people and property due to upstream inundation and downstream dam-breach flooding.

The 2008 Wenchuan earthquake (M_w 7.9, China) highlighted the importance of assessing and mitigating the hazards from coseismic landslide dams. It induced an unprecedented amount of landslides (Huang and Li, 2009; Dai et al., 2011; Gorum et al., 2011) and landslide dams (Cui et al., 2009; Fan et al., 2012a), out of which 32 were breached artificially in order to reduce the potential for further catastrophic dam-breach floods (Xu Q et al. 2009). This catastrophic event provides a unique opportunity to study the coseismic landslide dams in order to obtain a better understanding of their causal factors, spatial distribution, dynamic decay and impacts.

Landslide dams are common worldwide, especially in tectonically active mountain regions (Costa and Schuster, 1988; Korup, 2004; Evans et al., 2011). Many outburst floods and debris flows caused by the catastrophic release of water masses from landslide-impounded lakes have been documented (Mason, 1929; Cenderelli, 2000; Dai et al., 2005). The 27 largest floods of the Quaternary Period with discharges greater than 100,000 m^3/s were listed by O'Connor and Costa (2004), most of which were caused by breaches of glacier or landslide dams. Therefore, landslide dams receive more attention and awareness due to their potential dangers with expanding population and increasing land use pressure. Since the publication of the benchmark paper of Costa and Shuster (1988), numerous researches on landslide dams have been done in the past decades. Recent attempts have included the establishment of global and nationwide databases of landslide dams, progress in predictive, quantitative and GIS-based modeling (Korup, 2002). In the following sections I review and summarize the previous works on landslide dams worldwide according to some relevant aspects.

1.1.1 Existing landslide dam databases

Landslide dam inventories are essential for analyzing and understanding the characteristics, causes, failure mechanisms and effects of landslide dams. Table 1 listed several existing landslide dam databases in the world. The first comprehensive one might be considered the bibliography of 463 landslide dams collected by Costa and Schuster (1991).

Table 1.1 List of the existing landslide dam database

Region	Number	Description	Reference
Worldwide	463	Including some well-documented cases mainly from the European Alps, North America, China and Japan	Costa and Schuster (1991)
Canadian Cordillera	38	Including 16 existing and 22 historical landslide dams	Clague and Evans (1994)
Northern Apennines	68	Including the characteristics of 68 landslide dams in the northern Apennines	Casagli and Ermini (1999)
New Zealand	38	Including 24 earthquake-induced landslide dams, while the triggering factor of the other 14 is uncertain	Adams (1981)
New Zealand	232	Including detailed dam geomorphometric variables	Korup (2004)
Japan	79	43 of 79 cases have complete records of 16 geomorphic variables	Swanson et al. (1986); Tabata et al. (2002)
China	147	Including the information of the location, formation time, longevity, triggering factor of landslide dams	Chai et al. (1995)
China	257	Landslide dams induced by the 2008 Wenchuan earthquake (only the location information)	Cui et al. (2009)
China	32	Including the volume, geomorphometric features and failure mode of 32 large landslide dams induced by the Wenchuan earthquake	Xu et al. (2009)

There are also a large number of catastrophic landslide dam events widely distributed in the world. For example, Mason (1929) and O'Connor and Costa (2004) described the failure of the earthquake-induced Raikhot landslide dam on the Indus river within the western Himalaya, Pakistan in 1841, which caused probably the largest flood in recorded history, with an estimated peak discharge of about 540,000 m^3/s (Shroder, 1998). The largest landslide dam on Earth is the 550 m high Usoi landslide dam in Tajikistan induced by a large earthquake in 1911, which created Lake Sarez (Gesiev, 1984 and O'Connor and Costa, 2004). The largest landslide dam in China was formed by the Yigong landslide (~3×10^8 m^3) on April 9, 2000 in Tibet, which breached two months later and caused a flash flood with a peak discharge of ~120,000 m^3/s, resulting in 30 fatalities and >100 people missing (Shang et al., 2003; Xu et al, 2012). Harp and Crone (2006) and Schneider (2009) studied the largest landslide, Hattian slide, triggered by the Kashmir earthquake (M 7.6) in Pakistan, which formed a natural dam impounding two lakes in the Karli river.

Most of the existing landslide dam databases are descriptive, compiling local case studies and historical events, without mentioning trigger mechanisms, complete and standardized geomorphic features, failure modes and lifespan of the landslide dams.

1.1.2 Landslide dam formation and classification

A landslide dam can form in a wide range of geological and geomorphological settings, from high alpine debris avalanches to quick-clay failures in wide valley floors. According to the analysis of 390 landslide dams worldwide (Schuster, 1993), earth slumps and rock slides are the most common mass movements triggering blockage of fluvial systems (50%), followed by debris, mud and earth flows (25%), rock and debris avalanches (19%), sensitive clay failures as well as rock and earth falls (6%). Most of the landslide dams (>80%) were induced by rainstorms/snowmelts and earthquakes (Schuster, 1993; Peng and Zhang, 2012), although other less common causes, such as volcanic (Umbal and Rodolfo, 1996) and anthropogenic activity (Asanza et al., 1992) have been documented. The triggers and damming-landslide types vary in different regions. For example, Korup (2004) studied 232 landslide dams in New Zealand, and found that the triggering mechanism of 59% landslide dams remain unexplained, 39% were triggered by earthquakes, and only 3% were formed during high-intensity rainstorms. In addition, rock avalanches are the most common type and account for 27% of the data in New Zealand, while Ermini and Casagli (2003) found that sliding processes involving rotational and translational movements are the most frequent landslide type causing blockage (more than 40% of the 353 cases), followed by rock avalanches (17%) and debris flows (14%).

Regarding landslide dam classification, a geomorphic classification scheme proposed by Swanson et al. (1986) might be the earliest one. This classification was further modified by Costa and Schuster (1988), who classified landslide dams with respect to their geomorphic interactions with the valley floors into six types. It has been recently modified by Hermanns et al. (2004 and 2011) with several additional morphological types. These classifications present the geomorphic features of landslide dams in a certain degree, but without involving any geotechnical parameters or indexes, they are not indicative of landslide stability. There is no standardized classification based on the magnitude and impact of landslide dams or lakes due to the large variation between the small and extremely large events.

1.1.3 Longevity, stability and failure mechanism of landslide dams

The longevity of landslide dams varies largely from minutes to several thousand years, depending on many factors, including volume, size, shape and sorting of blockage material; rates of seepage through the blockage; and rates of sediment and water flow into the newly formed lake (Costa and Schuster, 1988). Based on 73 cases, Costa and Schuster (1988) found that 85% of cases lasted less than 1 year, 56% less than 1 month and 27% less than 1 day. These figures obtained from 204 cases by Peng and Zhang (2012a) are 87%, 71% and 34%, respectively. Ermini and Casagli (2003) also constructed the landslide dam longevity curve based on 205 cases, showing that 40% of dams collapsed only one day after their formation.

Therefore, given the relatively short longevity of landslide dams, evaluating their stability and potential hazard is significant for the mitigation measures. Korup and Tweed (2007) concluded that the stability of landslide dams is a function of their geometry; internal structure; material properties and grain size distribution; volume and rate of water and sediment inflow; and seepage process. Unfortunately, the internal structure and particle size distribution become evident only after dam failure such that reliably predicting landslide-dam stability remains a key challenge. Few studies have focused on qualitatively assessing the stability of landslide dams using a geotechnical approach, i.e. analyzing the geotechnical, sedimentological and particle size distribution of dam materials by field investigation and laboratory tests (Weidinger et al., 2002; Casagli et al., 2003; Dunning and Armitage, 2011; Weidinger, 2011). There are also a number of studies on predicting landslide dam stability using geomorphometric factors, such as landslide dam volume and dimensional features (height, width and length), impounded-lake volume, upper catchment area, peak flow of the dammed stream etc. Casagli and Ermini (1999) proposed a blockage index (*BI*) to predict landslide dam stability from the cases collected in the Northern Apennines, using dam volume and upper catchment area factors. Later Ermini and Casagli (2003) defined a new geomorphic dimensionless index (*DBI*) by combining dam height, volume and upper catchment area. Korup (2004) has tested these indexes to estimate the stability of landslide dams in New Zealand. Recently, Dong et al (2009 and 2011) developed discriminant and logistic regression models using such geomorphometric features. Both the geotechnical and geomorphic methods are applied in local case studies, using site-specific geo-environment characteristics and relationships, which cannot be applied directly in other areas.

With regard to the failure mode of landslide dams, Costa and Schuster (1988) presented a classification into three types: overtopping, piping and slope failure. Overtopping seems to be the most common failure mode, whereas piping or slope failure of dams is relatively rare (Schuster, 1993). Overtopping is normally caused by water spilling over the dam crest subsequently eroding a channel along the downstream face of the dam (Manville, 2001). Piping is defined as internal erosion initiated by percolation which removes solid particles and produces tubular underground conduits that appear initially as springs or seepage on the downstream face (Singh, 1996; Waltham, 2002). With the volume of voids increasing, the pipe grows progressively and results in the development of an open breach or even collapse. Slope failure is initiated when the hydraulic pressure exerted by the impounded water overcomes the dam materials' frictional resistance to shear. It is commonly associated with both piping and overtopping when vertical erosion over-steepens the breach sidewalls leading to gravitational collapse (Manville, 2001). The three types mentioned above are quite well known, however, little is known about the actual processes involved with dam failure. Walder and O'Connor (1997) stated that mechanisms of dam breach formation are still poorly understood, since there were only few direct observations of actual dam failures. In addition, most of the dangerous dams were breached artificially to avoid uncontrolled outburst flooding (Canuti et al., 1999; Xu et al., 2009). Wishart (2007) and Awal (2008) studied the overtopping process by experimental tests.

1.1.4 Impacts of landslide dams

Korup (2005) subdivided the impact of landslide dams on fluvial systems into on-site and off-site (i.e. upstream inundation and downstream outburst flooding) components. On-site hazards are the formation of displacement waves caused by secondary landsliding into the natural reservoir. Current research on this issue mainly focuses on (a) predicting the dam-break flood or debris flow, and (b) evaluating the long-term effects of landslide dams on landscape evolution, sediment flux and channel morphology.

Regarding (a), peak discharge is a key variable to represent the dam-breach flood magnitude. It can be estimated using empirical and numerical simulation methods. The empirical methods rely on regression relations between the peak discharge and other parameters, such as the impounded lake volume, depth, and area (Evans, 1986; Costa and Schuster, 1988; Walder and O'Connor, 1997; Cenderelli, 2000; Clague and Evans, 2000). Peng and Zhang (2012a) built the statistical regression models not only for the peak discharge but also for breach size (depth, top and bottom width) and breach duration, based on 52 cases. Most these empirical methods provide less accurate results with a large scatter in predictions, and only take into account water flows rather than hyperconcentrated debris-flow phases (Korup and Tweed, 2007). The numerical flood modelling methods include physically based models (i.e., Fread, 1991; Walder and O'Connor, 1997; Cencetti et al., 2006) and GIS-based hydraulic models (i.e., Dhondia and Stelling, 2002; Li et al., 2011; Butt et al., 2012). Compared to empirical models, the numerical models can predict more factors (flood routing, depth, velocity, duration and the affected area), but require detailed input variables and are also often time-consuming. Research has also been done on assessing the human risks (loss of life) caused by dam-breach floods (i.e., Brown and Graham, 1988; DeKay and McClelland, 1993; Jonkman et al., 2005, Peng and Zhang, 2012b, see Jonkman et al., 2008 for an overview).

Concerning (b), the topographic evolution of mountain landscapes is a coupled process of tectonic uplift, landslide erosion and valley incision (Larsen and Montgomery, 2012). Mass wasting due to landslides is a major source of sediment in tectonically active mountain belts (Hovius et al., 1997; Korup et al., 2004; Wenske et al., 2012). The impact of landslide dams on the sediment flux in mountain rivers occurs in two opposite ways: on the one hand, damming can inhibit sediment transport and incision through trapping incoming sediment; on the other hand, during and immediately after dam failure, large amounts of sediment are released together with floods or debris flows (Korup and Tweed, 2007). Hewitt (1998 and 2006) investigated the large landslide dams in the upper Indus River, Karakoram Himalayas, and depicted that the landslide dam deposits are rarely removed completely by fluvial incision, forming complex deposition and terracing features both upstream and downstream. Wenske et al. (2012) assessed the mechanisms of hillslope erosion and hillslope-channel coupling on individual slopes after the initial landslide failure, and found that they are controlled by the relative frequency of erosive flooding events and the magnitude of rainfall-driven hillslope processes. Ouimet et al. (2007) created a quantitative numerical framework for evaluating the influence of large landslides and landslide dams in the context of bedrock river incision and landscape evolution in the eastern margin of the Tibetan Plateau in China.

There are a number of recent studies that focus on the post-earthquake sediment flux, as great earthquakes normally trigger a large number of landslides, enhancing fluvial suspended sediment loads in a certain period after an earthquake (Koi et al, 2008; Chuang et al., 2009; Hovius et al., 2011). Chen et al. (2011) analyzed the impact of topography, lithology, rainfall and earthquakes on landsliding and sediment transport during heavy typhoons and earthquakes from 1996 to 2007 in Taiwan, using the landslide ratio and sediment discharge of two catchments. Lin et al. (2012) studied the 2006 Taitung earthquake and the subsequent typhoon events in Taiwan and found they had a positive impact on the sediment flux. Korup (2012) gives a comprehensive review on sediment yields in rivers impacted by volcanic eruptions, earthquake- and storm- triggered landslide episodes, and catastrophic dam breaks.

1.2 Problem Statement

Despite a large body of literature on the above mentioned aspects of landslides dams, relatively limited work has been carried out on a number of issues, such as:

(1) So far few studies have focused specifically on landslide dams that have been triggered by the same earthquake due to the scarcity of direct observational evidence (Adams, 1981; Pearce and Watson, 1986; Hancox et al., 1997). As mentioned in Table 1.1, most of the existing inventories are compilations of historical landslide dams that were triggered by different events in different regions. Most of them are quite descriptive and also include some uncertainties. There is almost no comprehensive earthquake-triggered event-based landslide dam inventory. The Wenchuan earthquake provided the opportunity to generate such an inventory.

(2) Because of the above shortcoming, no study has systematically analyzed the controlling factors of event-based coseismic landslide dam inventories, and their comparison with general coseismic landslide inventories.

(3) There is limited research carried out on the threshold values of the factors involved that cause a temporal and spatial landslide blockage of a river course (Korup, 2002). There is a complex relationship between the genetic mechanism, runout and volume of landslides as well as the

geomorphic and hydraulic parameters of rivers, which eventually determine the occurrence of a landslide dam at a given location.

(4) The significance of landslide dams lies in their temporary or permanent existence at the interface between hillslopes and the valley-floor system as well as their impacts on sediments flux and landscape evolution. However, little work has been done to investigate the longevity and geomorphic decay of coseismic landslide dams, as well as their impacts on modulating the immediate post-earthquake flux of water and sediment at the regional scale.

(5) Predicting the stability, failure time and dynamic failure process of landslide dams as well as the hydraulic-dynamic parameters of dam-break flood are crucial for emergency mitigation. However, there are few studies on the hazard assessment of landslide dams and their potential impacts on downstream communities (Liu et al., 2009; Cui et al., 2010; Li et al., 2011). Korup (2002) states that developing and refining methods of predicting flood impact would rank highest among priorities for future research.

(6) Coseismic landslide dam hazard is a typical example of a multi-hazard situation, involving several cascading phenomena. A multi-hazard chain may initiate from an earthquake to coseismic landslides and landslide dams, and end with dam-break flooding. How to analyze the probability of each event through this chain over a large area affected by an earthquake is poorly documented in the literature (Lee et al., 2000; Lacasse et al., 2008).

1.3 Research Objectives

The general objective of the research presented in this thesis is to better understand the causes and effects of earthquake-induced landslide dams, using the exceptional situation caused by the Wenchuan earthquake. This is carried out by developing a model to predict landslide dam formation at a regional scale as well as assessing the geomorphic decay of these dams and evaluating their impacts in order to reduce the potential landslide dam hazards in future. To achieve this main objective, the following specific objectives were defined, which also correspond to the issues addressed in sub-section 1.2:

- to create a virtually complete event-based inventory of landslide dams induced by a single triggering event (the Wenchuan earthquake) (chapter 3)

- to determine the factors that control the spatial distribution of landslides and landslide dams induced by the Wenchuan earthquake (chapter 4)

- to develop a model to predict coseismic landslide dam formation at a regional scale (chapter 5)

- to quantitatively analyze the dam and lake survival time in the study area (chapter 6)

- to model dam-break floods and to discuss the appropriate and effective procedure for emergency mitigation of landslide dams (chapter 7)

- to develop a conceptual model for the quantitative assessment of earthquake-induced landslide dam break floods (chapter 8)

1.4 Thesis Outline

This thesis consists of eight chapters, including the introduction, the description of the study area, the synthesis and five core chapters which have been submitted or published as peer-reviewed journal papers. The contents of the papers have been reorganized according to the chapter arrangement. The main contents of chapters are summarized as follows:

Chapter 1 introduces the research background by reviewing previous studies, defines the research objectives and presents the structure of the thesis.

Chapter 2 introduces the 2008 Wenchuan earthquake as well as the geomorphic and geological setting of the study area. The main features related to the representative coseismic and post-earthquake landslides and landslide dams are also summarized.

Chapter 3 presents the event-based inventory of landslide dams induced by the Wenchuan earthquake. The source data and the interpretation method are introduced, and a comparison is given of the spatial distribution of landslides and landslide dams, and several relations of geometric parameters of landslide dams and barrier lakes are presented.

Chapter 4 analyzes the factors controlling the spatial distribution of non-damming landslides and damming landslides using bi-variate statistical methods. The results of this chapter pave the way for the follow-up work on landslide (dam) susceptibility assessment.

Chapter 5 develops an empirical method to predict coseismic landslide dam formation at a regional scale using landscape parameters obtained from DEMs, considering river features and the corresponding landslide runout and volume required to block it. The performance of this method is evaluated in predicting dam formations in a selected catchment with abundant damming and non-damming landslides.

Chapter 6 quantifies the geomorphic decay of landslide dams after the Wenchuan earthquake by estimating the residence time of the landslide dams based on multi-temporal remote sensing images. The transient water and sediment storage of landslide dams as well as their impacts on post-earthquake sediment flux are also evaluated in this chapter.

Chapter 7 presents the results of simulating dam-breach flood scenarios of the most dangerous landslide dam (Tangjiashan landslide) using an integrated approach that combines the physically-based BREACH model and the 1D-2D SOBEK hydrodynamic model. This chapter also presents a general procedure for the emergency mitigation of landslide dams.

Chapter 8 summarizes the results of the previous chapters 2 to 7, presents a conceptual model for probabilistic hazard assessment of earthquake-induced landslide dams, and provides general conclusions and recommendations for future work.

2 Study Area

This chapter is based on:

Xuanmei Fan, Cees J. van Westen, Qiang Xu, Victor Jetten, Runqiu Huang, Chuan Tang, Tolga Gorum. Five years on: what have we learned from the landslides associated with the Wenchuan earthquake. In: Engineering Geology (invited paper for a special issue, in preparation).

Runqiu Huang, Xiangjun Pei, **Xuanmei Fan***, Weifeng Zhang, Shigui Li, Biliang Li (2012). The characteristics and failure mechanism of the largest landslide triggered by the Wenchuan earthquake, May 12, 2008, China. In: Landslides 9, 131-142. (* corresponding author).

Xuanmei Fan, Qiang Xu (2010). Xiejiadianzi landslide, Pengzhou. In: Xu, Q., Pei, X., Huang, R. (eds), Large-scale landslides induced by the Wenchuan earthquake. Beijing: Science Press, pp. 407-422. (book chapter in Chinese)

Abstract

The devastating 2008 Wenchuan earthquake with a magnitude of M_w 7.9 was the largest seismic event in China in more than 50 years. It triggered numerous landslides over a broad area, some of which dammed rivers, posing severe threats to downstream settlements. This chapter presents the general tectonic, geomorphic, geological and meteorological background information of the study area as well as stream features, which will be used in the following chapters. The coseismic landslides are classified into rock/debris avalanches, debris flows, rock/debris slides and rock falls. A number of representative examples of each type and the corresponding landslide dam features were studied. According to dam composition material and sedimentological features, landslide dams were categorized into three types: dams mainly composed of large boulders and blocks; dams composed of unconsolidated fine debris; and dams with partly intact rock strata at the base topped by large boulders and blocks or soil with rock fragments, showing two-layered or three-layered depositional structure. This classification is linked to the typology of damming landslides and considered to be a preliminary indicator of dam stability. In addition, dam stability also largely depends on valley morphometry as well as landslide runout distance and mechanism. The post-earthquake debris flow damming events induced by subsequent rainfalls are also introduced. It was found that there is still a large amount of loose sediment remaining on the slope, which may continue promoting heavy debris flows in the coming years or decades.

2.1 Introduction

The devastating May 12, 2008 (M_w 7.9) Wenchuan earthquake was the largest seismic event in China in more than 50 years. It occurred on the NE-trending Longmenshan thrust fault zone (LTFZ) at a focal depth of 14-19 km. The LTFZ separates the Sichuan basin from the steep and heavily dissected eastern margin of the Tibetan Plateau in China. The LTFZ consists of three major sub-parallel faults: the Wenchuan-Maowen (WMF), Yingxiu-Beichuan (YBF) and Pengguan faults (PF) (Fig. 2.1). The coseismic rupture initiated near Yingxiu town (31.061^{o}N, 103.333^{o}E) and propagated unilaterally towards the northeast, generating a 240-km long surface rupture along the Yingxiu Beichuan fault, and a 72-km long rupture along the Pengguan fault (Xu X et al., 2009; Lin et al., 2009; Shen et al., 2009). Prior to the occurrence of the Wenchuan earthquake, Li et al. (2008) reported 66 earthquakes with $M_s>4.7$ mainly concentrated on the Minjiang fault and the southern part of the Longmenshan fault zone since 638 AD. For instance, there were two large earthquakes, the M 7.2 1976 Songpan earthquake and the 1933 M 7.5 Diexi earthquake, which were induced by the tectonic activity along the Minjiang fault zone, Fig. 2.1(Chai et al., 1995).

Shortly after the Wenchuan earthquake, numerous investigations were carried on revealing the fault surface rupture, fault plane geometry, rupture mechanism and coseismic deformation using various methods. Field geological surveys tracing the fault surface ruptures and measuring the vertical and horizontal offsets along the rupture zone provided the most reliable information of the fault surface rupture and displacement (Lin et al., 2009; Ran et al., 2009; Xu X et al., 2009; Zeng et al., 2009). Their measurements are generally similar, showing a maximum vertical displacement of 6.5 m and a horizontal offset of about 5 m. GPS and InSAR data were also used to quantify the variability of fault geometry and slip rate distribution (Yarai et al., 2008; Hao et al., 2009; Shen et al., 2009), indicating that in the southwest (from Yingxiu to Beichuan) the fault plane dips moderately to the northwest, becoming nearly vertical in the northeast (from Beichuan to Qingchuan region), associated with a change from predominantly thrusting to strike-slip motion. Nakamura et al. (2009), who investigated the rupture process of the Wenchuan earthquake using teleseismic waveform data, also found that the earthquake is composed of at least two main fault segments: one with a low dip angle and the other with a high dip angle, which are dominated by thrust and strike–slip motions, respectively. This prominent feature of the Wenchuan earthquake played an important role in the spatial distribution of landslides, resulting in a much higher landslide density along the thrusting segment of the fault than that of the strike-slip segment (Gorüm et al., 2011).

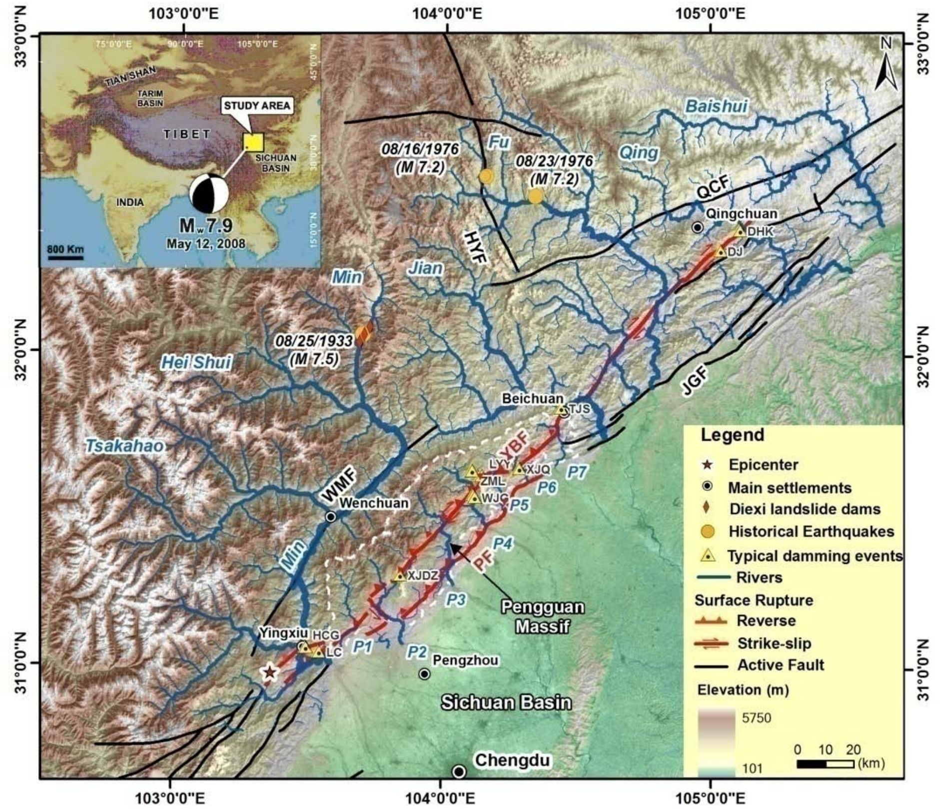

Figure 2.1 Topography of the study area (inset shows location). Major rivers are shown in blue. The major catchments are: Min river, Jian river, Fu river, Qing River, and 7 smaller rivers (P1-P7) in the Pengguan Massif bounded by the white dashed line. WMF: Wenchuan-Maowen fault; YBF: Yingxiu-Beichuan fault; PF: Pengguan fault; JGF: Jiangyou-Guanxian fault; QCF: Qingchuan fault; HYF: Huya fault; MJF: Minjiang fault (after Xu X et al., 2009). The epicenter location is from USGS (2008). Yellow triangles represent the typical coseismic and post-earthquake damming landslides. DGB: Daguangbao landslide, LYY: Laoyingyan landslide, DHK: Donghekou landslide, XJDZ: Xiejiadianzi landslide, XJQ: Xiaojiaqiao landslide, DJ: Dongjia landslide, WJG: Wenjia gully debris flow, ZML: Zoumaling debris flow, HCG: Hongchun gully debris flow, LC: Longchi debris flow.

Several studies examined the effects of coseismic landslides related to the Wenchuan earthquake, which can be grouped into following aspects:

(1) Coseismic landslide mapping and investigation of large landslides. Preliminary and rapid image interpretation was done by Huang and Li

(2009) and Sato and Harp (2009). Chigira et al. (2010) and Ren and Lin (2010) analyzed the landslide distribution between Beichuan and Pingtong based on PRISM and AVNIR-2 satellite images. Yin et al. (2009) and Qi et al. (2010) presented investigations of some large landslides. The most comprehensive landslide inventories for the entire earthquake hit-region were made by Dai et al. (2011), who mapped 56,000 landslide polygons, and by Gorum et al. (2011), who mapped 60,000 landslides as points. The inventory from Dai et al., (2011) has been updated by Xu et al. (2013), who mapped 197,481 landslides. This number largely exceeds other inventories, because of the larger extent of the mapping area and also the larger mapping scale.

(2) Coseismic landslide susceptibility assessment. Tang et al. (2011) and Song et al. (2012) assessed the susceptibility of landslides in Beichuan region using the analytical hierarchy process (AHP) and bayesian network methods. Xu et al. (2012) applied six different models in a catchment and found that the logistic regression model provides the highest success rate for the coseismic landside prediction. For triggering earthquake events that have relatively large return periods, this creates the difficulty that it is very unlikely that such an event occurred in recent times, making a susceptibility model unlikely to be validated by another event in the same region.

(3) Research on coseismic landslide dams. Cui et al. (2009) identified 257 landslide dams triggered by the Wenchuan earthquake and made a preliminary risk evaluation of some key landslide-dammed lakes. In order to avoid the potential hazard of dam-break floods, the Chinese army created artificial spillways in 32 of the dams using explosives and heavy machinery. Xu et al. (2009) qualified the hazard of these 32 dams by considering dam height, dam composition materials and maximum capacity of the landslide-dammed lakes. Wang et al. (2008) and Liu et al. (2009) numerically modelled the Tangjiashan landslide, and Liou et al. (2010) as well as Xu et al. (2010) detected the changes of its barrier lake based on satellite image classification.

2.2 Geomorphology, Geology and Climate

The Longmenshan mountain range, located in the eastern margin of the Tibetan Plateau, is bounded by the Longmenshan thrust fault zone (LTFZ) which runs through a mountain range with elevations ranging from 500 m in the Sichuan Basin to >5,000 m over a distance of ~50 km, with tributaries of the Yangtze River flowing oblique or perpendicular from the north or northwest to the south or southeast. Deeply incised bedrock rivers are flanked by hillslopes commonly >30° steep within the LTFZ, and underlain by deformed Paleozoic sediments and metamorphic rocks, Mesozoic sediments, and Precambrian crystalline and metamorphic rocks (Burchfiel et al., 1995; Kirby et al., 2003). Fig. 2.2 shows the spatial variation of lithology, which was compiled from ten 1:200,000 scale standard geological map. It varies from Pre-Sinian rocks to Quaternary sediment. Fig.2.2 also depicts the boundary of the study area which is restricted to the areas with the highest landslide density and topography, with an extensive area of 35,000 km^2. The Pengguan Massif is a Precambrian folded structure that consists mainly of the granitic rocks. Dai et al. (2011) found that Pre-Sinian schist, Cambrian sandstone and siltstone intercalated with slate as well as granitic rocks are more favourable for coseismic landside occurrence.

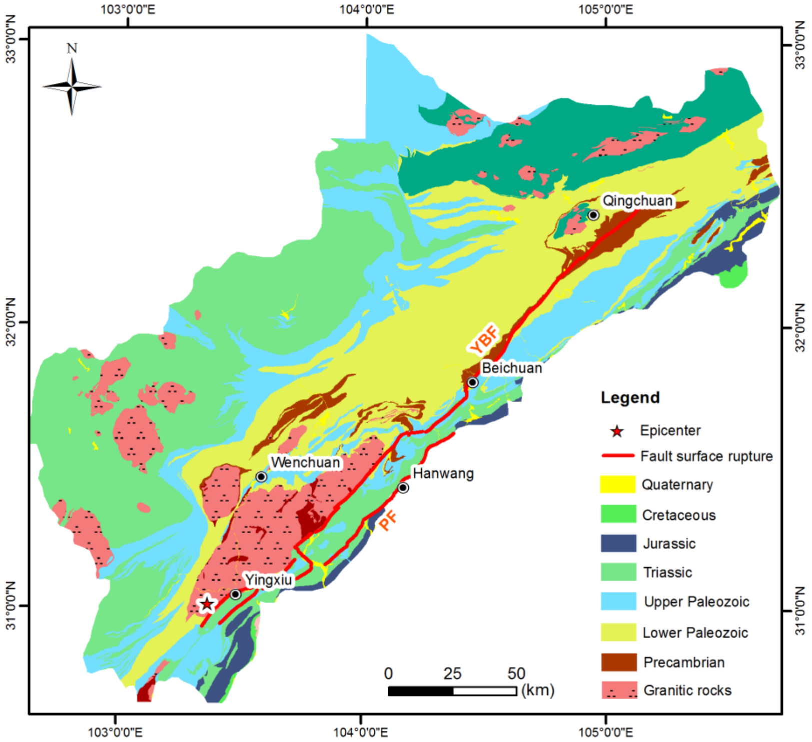

Figure 2.2 Generalized geological map showing major faults and fault surface ruptures. See the caption of Fig. 2.1 for the fault names.

The study area has a humid subtropical climate. Due to the great difference in the terrain, the climate is highly variable. According to the data from 1961 to 2007, Beichuan region receives the highest mean annual rainfall of about 1300 mm, followed by Mianzhu region (1050 mm), while Wenchuan region has the lowest mean annual rainfall of about 520 mm. Fig.2.3 shows the variation of mean monthly rainfall measured in the rain gauges in Beichuan, Mianzhu and Wenchuan. It indicates that the monsoon starts from June and ends in Sep with the peaks in July and August (He et al., 2008). The mean monthly rainfall in July and August in Beichuan is around 343 mm and 337 mm. The Wenchuan earthquake occurred before the monsoon started, and therefore there was not so much antecedent rainfall.

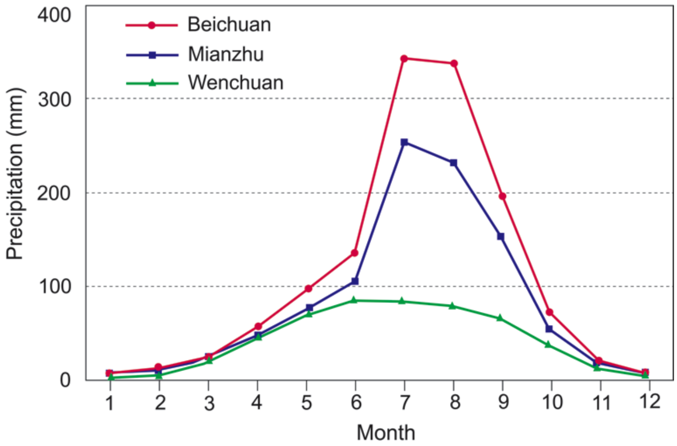

Figure 2.3 Variation of mean monthly rainfall from 1961 to 2007

2.3 Stream Network

2.3.1 Stream network and profiles

Major river basins draining the study area include the Min river and its tributaries, the Hei Shui and Tsakahao rivers in the west, as well as the Jian, Fu and Baishui rivers in the east. Besides, a series of relatively small streams (named P1-P7 for the sake of simplification) drain the Pengguan Massif in front of the Longmenshan zone adjacent to the Sichuan Basin (Fig. 2.1). The lower part of the Min river turns southwest and flows along the Wenchuan-Maowen fault, and then crosses the Pengguan Massif to drain into the Sichuan Basin. The Hei Shui and Tsakahao rivers join the Min river west of the Pengguan Massif. All the rivers eventually drain across the Sichuan Basin into the Yangzi river. Kirby et al. (2003) have analyzed river longitudinal profiles using a channel steepness index and found that these profiles reflect active differential rock uplift along the eastern margin of the Tibetan Plateau. Kirby and Ouimet (2011) updated their previous analysis by several new sets of observations, revealing a strong correlation between channel gradients and width that suggest a dynamic adjustment to regional tectonic forces, as well as a clear relationship between the variations in channel steepness indices and the variations in erosion rate.

The stream channel profiles were extracted from a pre-earthquake 25-m DEM generated from 1:50,000 scale digital topographical maps, following the method of Kirby et al. (2003). The spikes along the channel were removed and the data were smoothed using a 1 km moving window. The channel gradients were calculated over a constant vertical interval of 15 m from the smoothed elevation data. As shown in Fig. 2.4, the Min river exhibits a generally convex upward profile, while the Jian, Qing and Fu rivers have a concave shape with high gradients in the upper ~30 km. Smaller rivers in the Pengguan Massif (P1-P7) have relatively higher channel gradients in the upstream than in downstream, where the rivers flow into Sichuan basin (Fig. 2.4).

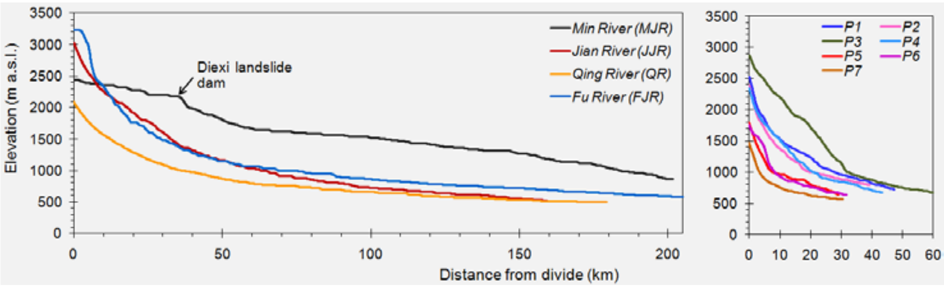

Figure 2.4 Longitudinal profiles of major rivers in the Longmenshan mountain range extracted from a 25-m DEM, see Fig. 2.1 for the river locations.

2.3.2 Theoretical background of stream features

In this section, the stream features (i.e. the stream gradient, width, drainage area and stream steepness index) were calculated based on the DEM, using the method developed by Kirby et al. (2003) and Kirby and Ouimet (2011). The results will be used in chapter 3, 4 and 6.

Channel dimensions are difficult to directly measure from DEMs and require time-consuming field measurements. Therefore, power-law functions are commonly used to estimate the channel width (W). The traditional hydraulic scaling of river width ($W \sim A^{0.5}$, A is the drainage area, as a proxy for discharge) was found to commonly underestimate stream-power variability in channels incising bedrock (i.e. Finnegan et al., 2005; Whittaker et al., 2007). Finnegan et al. (2005) modified this traditional relationship as:

$$W=A^{3/8}\,S^{-3/16} \tag{2.1}$$

where S is the channel bed slope or channel gradient, and A is the drainage area (km^2). Equation (2.1) was tested to perform better than the traditional relationship and reveals a strong correlation between channel gradients and width that describes river width trends in terrain with spatially nonuniform rock uplift rates, suggesting a dynamic adjustment to regional forcing (Kirby and Ouimet, 2011). The variation of river width is shown in Fig. 2.5 and 2.6.

The rate of river incision into bedrock is commonly modelled as a power-law relationship between river-bed slope S and upstream drainage area A_c (Flint, 1974),

$$S = k_s\,A_c^{-\theta}, \tag{2.2}$$

where k_s is the channel steepness index, and θ is the concavity index (e.g. Whipple, 2004). Assuming that k_s carries vital information about fluvial erosion potential (e.g. Kirby et al, 2003), the normalized steepness for the major rivers in the study area was computed (i.e. Fig.2.6A-C), using a fixed $\theta = 0.45$, a value common to rivers in active mountain belts (Whipple, 2004).

Unit stream power Ω is typically used as a proxy for variations in channel incision rate in tectonically active areas as expressed in Equation (2.3) (Finnegan et al., 2005):

$$\Omega=\rho gQS/W \tag{2.3}$$

where Ω is the unit stream power (Watts/m^2), ρ is the water density (kg/m^3), g is gravitational acceleration (m/s^2), Q is the discharge (m^3/s), S and W are the same as those in Equation (2.1). If the river width (W) in Equation (2.3) is determined from Equation (2.1), the Equation (2.3) will be converted into Equation (2.4), a stream power index (Ω'), assuming $Q{\sim}A$ (Finnegan et al., 2005)

$$\Omega'=\rho gAS/W=\rho gAS/(A^{3/8}\,S^{-3/16}){\sim}A^{5/8}\,S^{19/16} \tag{2.4}$$

The stream features mentioned above were calculated based on the Equations (2.1) to (2.4) and the 25-m pre-earthquake DEM, using the Matlab code created by Whipple et al. (2007). As examples, the stream width and stream power index at 2 km intervals along all major channels (drainage areas>10 km^2) are shown in Fig. 2.5.

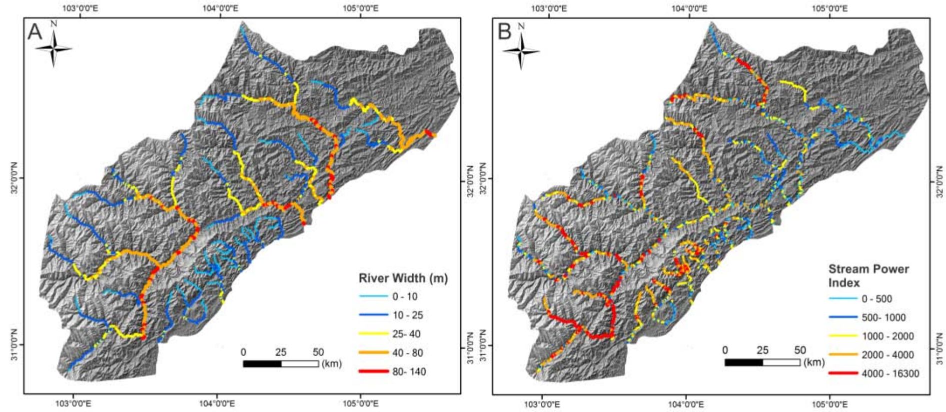

Figure 2.5 Maps of stream features: (A) Stream width and (B) Stream power indicator

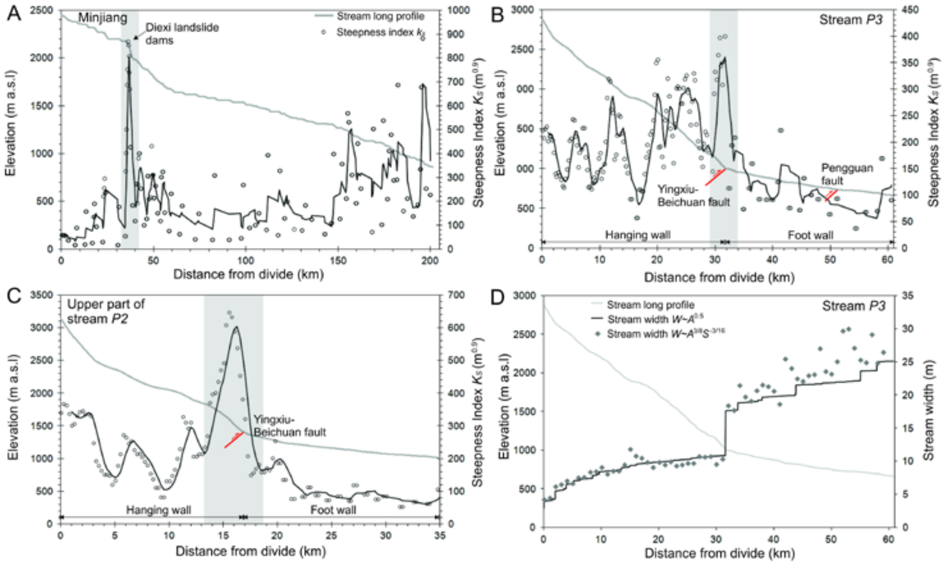

Figure 2.6 Influence of historical landslide dams and tectonic forcing on steepness index k_s, and its five-point moving average (black line) of selected

mountain river long profiles (grey lines) for an arbitrarily fixed θ=0.45 (see Equation (2.2)). A: Min river and historical Diexie landslide dams; B: Stream P3 in the Pengguan Massif; C: Upper to middle part of Stream P2 in the Pengguan Massif; and D: Stream width calculated by the traditional hydraulic scaling ($W \sim A^{0.5}$) and Equation (2.1). See Fig. 2.1 for the river locations. The five-point moving average filter was used to smooth data by calculating the average value of five points around the output sample.

2.3.3 Historical large-scale landslide dams and channel profile analysis

Some historical large-scale landslide dams and catastrophic dam break floods have been reported in the study area. On June 1, 1786, a strong earthquake (*M 7.7*), occurred in the Kangding-Luding area, resulted in a large landslide dam that blocked the Dadu river. Ten days later, the sudden breaching of the dam caused catastrophic downstream flooding and 100,000 fatalities (Dai et al., 2005). Furthermore, the Diexi earthquake (*Ms 7.5*) of August 25, 1933 produced nine large landslide dams. Three of these dams (Dahaizi, Xiaohaizi, and Deixi, see Fig. 2.1) had a maximum height of 160 m above the Min River. After seven weeks the three lakes merged, and emptied in a dam-break flood that rushed downstream for a distance of 250 km, killing more than 2,500 people (Chai et al., 2000).

The interpretation of longitudinal river profiles using the steepness index is regarded as a useful approach not only to quantify tectonic and climatic forcing (i.e. Whipple, 2004; Ouimet et al., 2007; Whittaker et al., 2007), but also to identify and quantify the geomorphic feedback between mountain rivers and large-scale landslides (i.e. Korup, 2006; Ouimet et al.,2007; Korup et al., 2010). The river profiles in the study area reflect both the geomorphic imprint of large-scale landslide dams and fault slip. Fig. 2.6A demonstrates an abrupt knickpoint with a ~200 m drop in a breach channel through the Diexi landslide dams, which spatially coincides with high values of steepness index. Korup (2006) found similar knick points and abrupt peaks of the steepness index which are related to large-scale rock-slope failures in the Swiss Alps and the New Zealand Alps. Concerning the effect of tectonic forcing on river long profiles, Fig. 2.6B and C show that the long-term slip on the Beichuan-Yingxiu fault locally steepens the streams, therefore, increasing the stream steepness index and the incision rate. This finding supports the previous results from Whittaker et al. (2007) and Kirby and Ouimet (2011). Fig. 2.6D gives an example of the variation of stream width along the long profile.

2.4 Typology of Coseismic Damming Landslides

The landslide dam stability largely depends on the dam comprising materials that in turn are strongly related to the types of damming landslides and valley morphometry. The river-blocking landslides triggered by the Wenchuan earthquake can be classified into rock/debris avalanches, debris flows, rock/debris slides (including deep-seated landslides) and rock falls, following the terminology of Cruden and Varnes (1996). This classification is made mainly based on landslide failure mechanism and type of movement. In order to avoid a complex classification, types of landslide material were simplified, also because rock and debris are always mixed. Field investigation found that most of landslides triggered by the Wenchuan earthquake are bedrock slides. In this section, a number of representative cases for each type and the related sedimentological features of the resulting landslide dams are described.

2.4.1 Rock/debris avalanches

Rock avalanche (also called sturzstrom) was defined by Hsü (1975) as a large bulk of mostly dry rock debris deriving from the collapse of a slope or cliff and moving at a high velocity and for a long distance. Its speed can be in the order of tens of meters per second, the volume in the order of 10^6 m^3. The run-out distance of a rock avalanche often exceeds several kilometers and the mobility becomes visible by the run up on opposite valley slopes. According to these features, we classified the Daguangbao landslide and Laoyingyan landslide as rock avalanches.

(1) Daguangbao landslide

The most notable example of a coseismic rock avalanche is the Daguangbao landslide, the largest landslide triggered by the Wenchuan earthquake, located in Anxian county, only 6.5 km from the thrusting part of the Yingxiu-Beichuan fault (Fig. 2.1 and Fig. 2.7). The source area of the Daguangbao landslide is about 2.4 km long and 1.2 km wide, while the deposition area is approximately 3.2 km long and 2.2 km wide (Fig. 2.7). It covers an area of 7.8 km^2 and an estimated volume of 1.17×10^9 m^3 (Huang and Fan, 2013) to 8.4×10^8 m^3 (Chigira et al, 2010). The sliding mass travelled about 4.5 km and blocked the Huangdongzi valley, forming a landslide dam nearly 600 m high. This dam probably is the third highest natural dam in the world, exceeded by the Rondu-Mendi'A' landslide dam with a height of 950 m along the Indus River in Baltistan, Pakistan (Hewitt, 1998) and the Usoi dam with a height of around 700 m in Tajikistan (Gasiev, 1984; Weidinger, 1998; Alford et al., 2000; Korup, 2002).

The head scarp is serrated and near vertical (70°-90°), with a maximum vertical height of 700 m. The sliding mass crossed the Huangdongzi valley and ran up the opposite slope with a height of more than 500 m, forming many thrust and anti-slope (uphill facing) scarps (Fig. 2.7 and 2.8). The strata in the landslide area are mainly composed of carbonates, including the siltstone and mudstone of the Triassic system (T); limestone of the Permian system (P); sandy mudstone of the Carboniferous system (C); dolomite of the Devonian system (D); limestone interbedded mudstone and dolomitic rocks of the Sinian system (Z) as shown in Fig. 2.8 (the lower cases represent for different groups in a geological system, Huang et al, 2012). The strata are densely jointed, dipping at 35°-38° towards the valley.

The damming deposits are very heterogeneous with a large range of particle sizes. The top layer of the main deposition zone is mainly composed of fine rock fragments and debris mixed with large blocks and boulders with grain sizes varying from 2 m to 10 m. The middle and bottom layers did not strongly disaggregate, and consist of some almost intact rock masses (Fig. 2.8). The Daguangbao dam is considered very stable because of its very large size and the rather low discharge of the dammed valley.

The occurrence of the Daguangbao landslide and its huge size are controlled by the combined effect of seismic, terrain and geological factors. The landslide is on the hanging wall and very close to the Yingxiu-Beichuan fault. Therefore, it is assumed to have experienced large ground shaking during the earthquake. In addition, the originally steep terrain, the high local relief (~1600 m), the active tectonics and the densely jointed strata all favour the landslide occurrence. See Huang et al (2012) for a more detailed explanation of its failure mechanism.

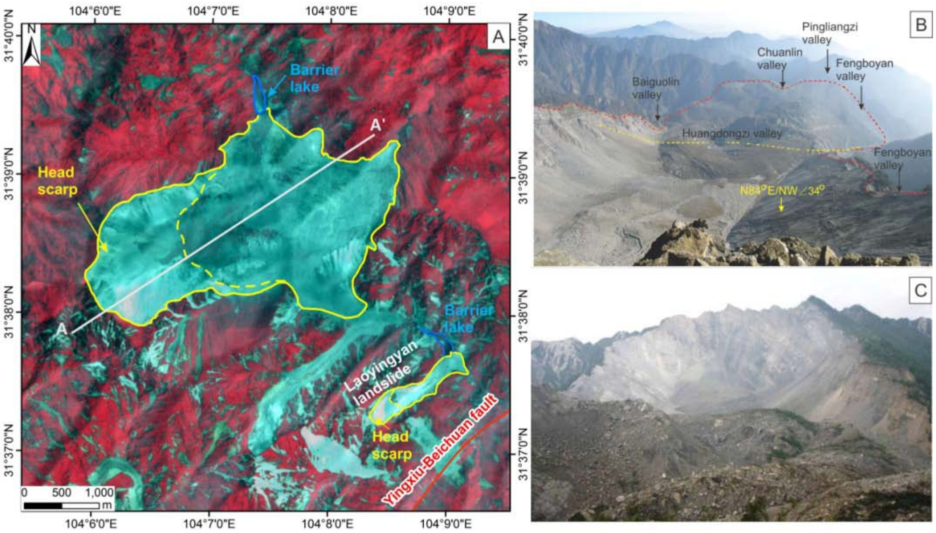

Figure 2.7 Daguangbao landslide. A: ALOS AVNIR image of the Daguangbao and the Laoyingyan landslide; B: View from head scarp to the accumulation zone of the Daguangbao landslide; C: Head scarp of the Daguangbao landslide

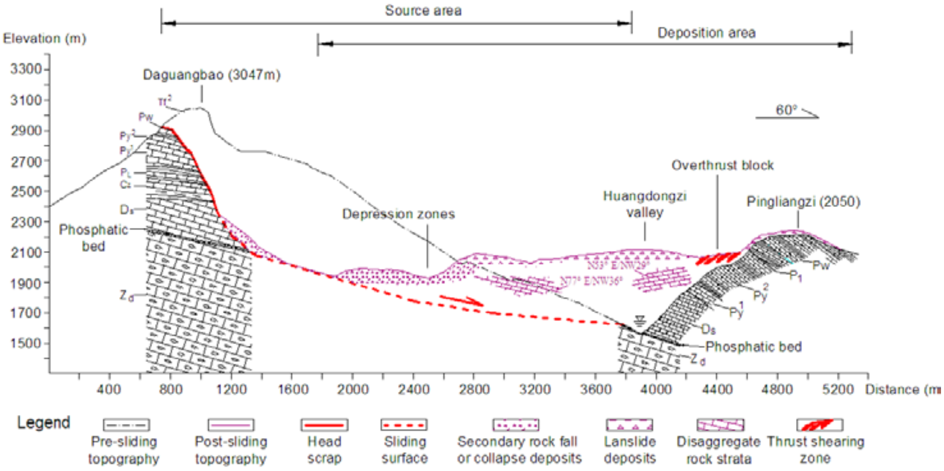

Figure 2.8 Post-earthquake A-A’ geological profile of the Daguangbao landslide, see Fig. 2.6 for the profile location

(2) Laoyingyan landslide

The Laoyingyan landslide is located 2.5 km downstream of the Daguangbao landslide as shown in Fig. 2.7. About 1.5×10^7 m^3 rock mass travelled 1 km and dammed the Huangdongzi valley, forming a 105 m high dam that impounded a barrier lake with an estimated capacity of 2.2×10^6 m^3 (Fig. 2.9 and 2.10). The lake submerged an upstream hydropower station, resulting in more than 20 fatalities. The dam was stabilized by constructing an artificially spillway shortly after the earthquake.

The landslide formed a steep (~ 60^o) head scarp, with a vertical height of about 280 m (Fig. 2.9 and 2.10). The source rock is mainly dolomitic limestone with a dip angle of 55^o-60^o. The landslide dam body is mainly composed of large blocks and boulders with an average particle size of 2 m (accounting for 60%-70%). The height of one of the large boulders found in the field is about 7 m (Fig. 2.9E). The volume of the dam body was estimated to be 8.5×10^6 m^3. The causal factors and failure mechanism of the Laoyingyan landslide are similar to those of the Daguangbao landslide.

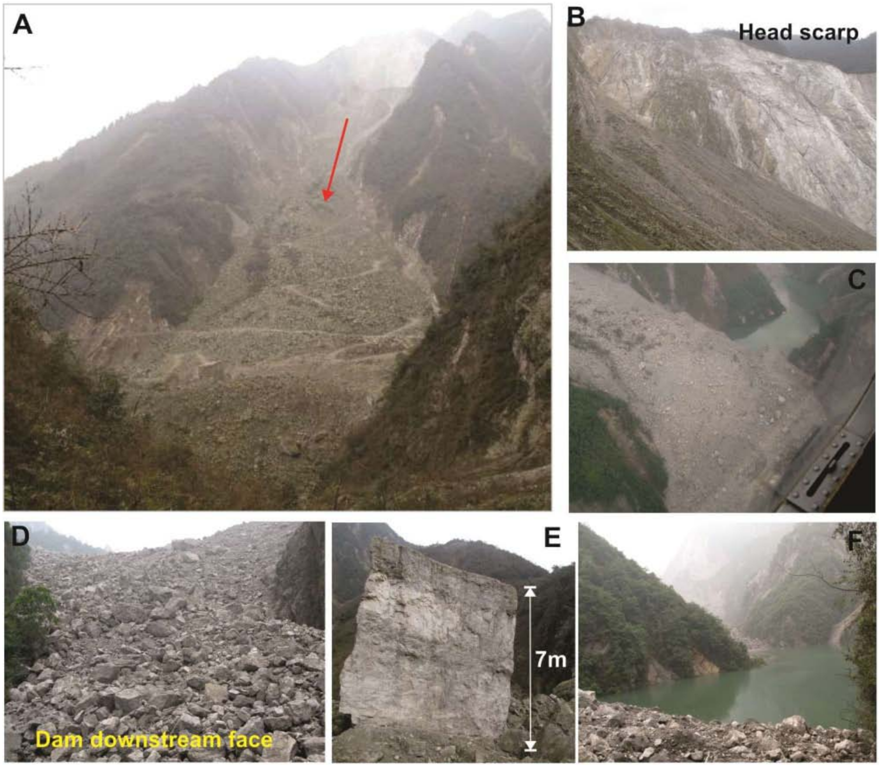

Figure 2.9 Laoyingyan landslide. A: Overview of the Laoyingyan landslide; B: Head scarp; C: Helicopter view of the dam body; D: Dam downstream face; E: The largest boulder in the deposition zone; and F: Barrier lake.

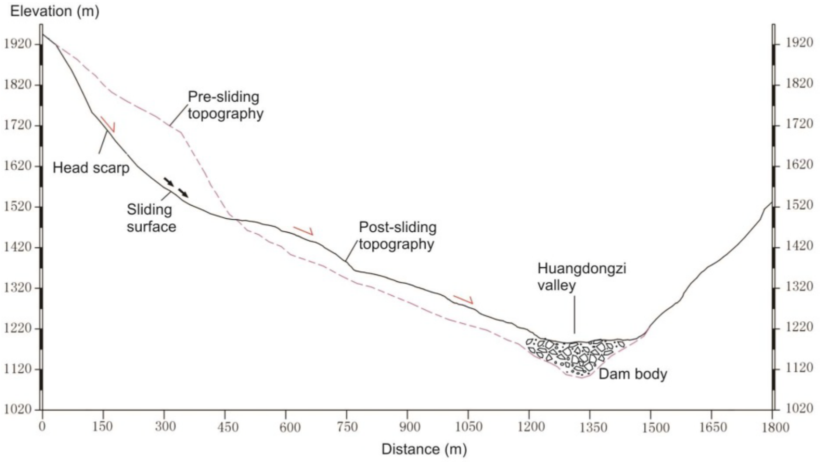

Figure 2.10 Typical profile of the Laoyingyan landslide

2.4.2 Debris flows

According to the definition of Dikau et al. (1996) and Iverson and Denlinger (2001), debris flows consist of a mixture of fine material (sand, silt and clay), coarse material (gravel and boulders), with a variable quantity of water, which flow rapidly with one or more surges, commonly following pre-existing drainage ways. Three distinctive elements are distinguishable in a debris flow: the source area, the main track (transportation area) and the depositional fan. Debris flows are of primary concern due to their long runout and the resulting destructive impacts. The Donghekou landslide and Xiejiadianzi landslide are two representative coseismic debris flows.

(1) Donghekou debris flow

The Donghekou landslide located in Qingchuan County, near the northeastern end of the Yingxiu-Beichuan fault, killed 780 people and blocked the convergence of the Qingzhujiang river and the Hongshi river, forming the Donghekou landslide dam and two barrier lakes (Fig. 2.11A-D). The dam body is about 20 m high, 350 m wide and 750 m long, with an estimated volume of 1.2×10^7 m^3 (Fig. 2.11E). The Hongshihe and the Qingzhujiang barrier lakes have a capacity of 2×10^6 m^3 and 3×10^6 m^3, respectively. There is a relatively small debris slide upstream of the Donghekou landslide, the Hongshihe slide, which also dammed the river temporally, running up to the other side of the valley for 30 m. The dam was naturally overtopped and eroded shortly after the earthquake due to its weak and loose composition of debris.

The Donghekou landslide was initiated as a rock slide and travelled a vertical distance of 700 m from 1300 m to 600m, over a horizontal distance of 2400 m into the river (Fig. 2.12). The angle of reach, defined as the angle of the line connecting the initiation of the landslide source to the distal margin of the landslide deposits, can be estimated as being 16°. Initial failure formed a steep head scarp with a height of 80 m and a dip angle of 50-70° (Fig. 2.11D). The source rock is composed of the dolomitic limestone (Yuanji formation of the upper Sinian system), as well as carbonaceous and siliceous slate (Qiujiahe formation, lower Cambrian system). The bedrock is mainly Lower Cambrian sandstone and phyllite. Folds and small sub-faults are well developed in the landslide area.

The displaced mass moved down along a mountain gully (Fig. 2.11B), entraining a large amount of unconsolidated substrate materials and water in the gully, and transforming into a distal debris flow. The grain size of the deposits decreases from the rear to the front of the landslide. Large limestone blocks and boulders are mainly found in the rear of the accumulation area, while the content of fine grained materials increases markedly in the front of the landslide. The dam body was mainly composed of loose soil and fragmented rocks with grain sizes of 30-50 cm. It was artificially broken by constructing a spillway (Fig. 2.11F). The landslide failure mechanism analysis and runout dynamic modelling have been done by Sun et al. (2011) and Huang et al. (2012).

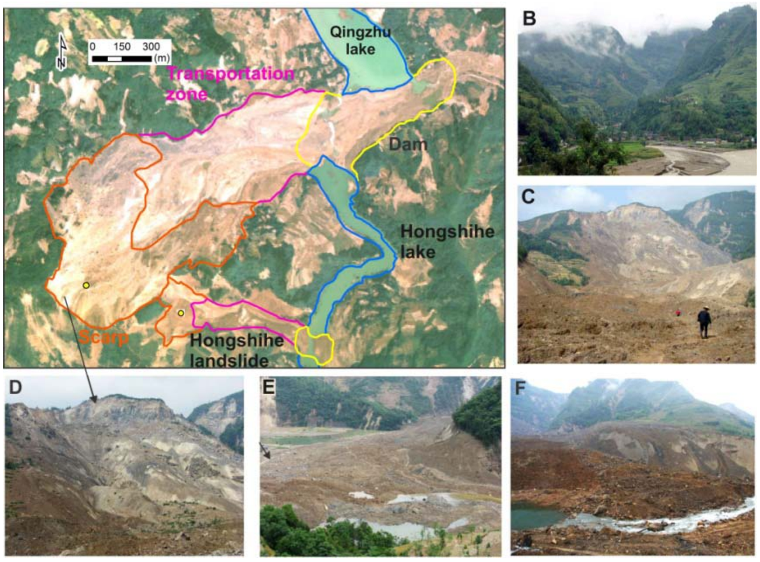

Figure 2.11 Donghekou landslide. A: Aerial photo of the Donghekou landslide; B and C: Overview photo before and after the earthquake; D: Head scarp; E: The dam body and two barrier lakes; and F: Artificial spillway

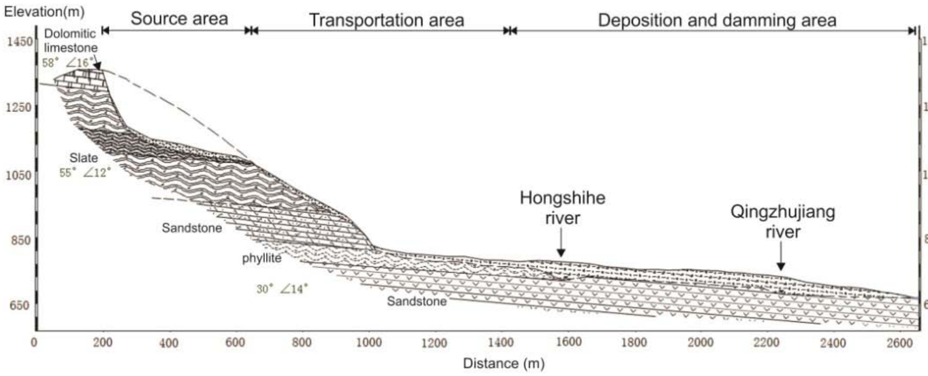

Figure 2.12 Geological profile of the Donghekou landslide

(2) Xiejiadianzi debris flow

The Xiejiadianzi landslide is a typical debris flow that can be represented by three zones (e.g. source area, transportation zone and deposition zone, Fig. 2.13). Similar to the Donghekou landslide, it was also initiated as a rock slide and then developed into a debris flow, moving down along a small valley below the source area and causing about 100 deaths. The debris travelled a vertical distance of 660 m over a horizontal distance of 1230 m into the river, yielding an angle of reach of 21°. The debris depositional fan blocked the Baishui river, forming a 10 m high dam that impounded a barrier lake with a maximum capacity of 1.0×10^6 m^3.

The initial failure developed in a rock slope composed mainly of Proterozoic granite, creating a steep main head scarp with a height of 80 m and several smaller secondary scarps. The bedrock in the landslide transportation and deposition zone is mainly feldspathic sandstone of the upper Jurassic system. They are separated by the Yingxiu-Beichuan fault, passing through the toe of the head scarp (Fig. 2.13), where a 50 m wide platform was formed. The volume of the landslide source material and deposits in the fan was estimated as being 0.4×10^6 m^3 and 0.9×10^6 m^3, respectively (Dai et al., 2011). The dam body consists mainly of soil and fragmented rocks with a few large blocks and boulders covering the crest.

Evidences of liquefaction were found in the field, such as reverse grading exposed by valley incision on the fan and the presence of a mudline on the large rock boulders (Fig. 2.13). Wang et al (2013) found clayey soils in the basal deposit exposed during road construction 10 month after the earthquake, which were still very soft when exposed, suggesting that the displaced landslide material were transported as a liquefied flow. Chigira et al. (2010) and Dai et al. (2011) observed reverse grading on the fan, indicating that valley fill sediments were mobilized by pore pressure build up or liquefaction.

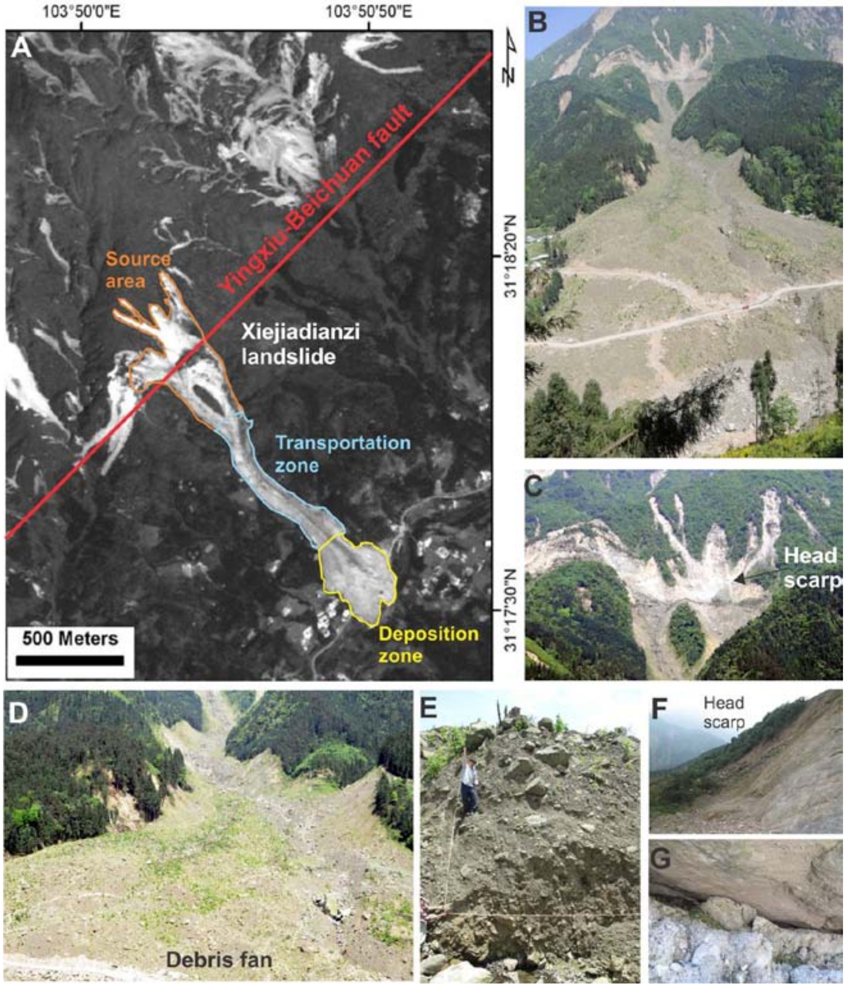

Figure 2.13 Xiejiadianzi landslide. A: ALOS PRISM Pan image of the Xiejiadianzi landslide; B: Overview photo; C: Source area; D: Depositional zone; E: Exposure of the deposits in the debris fan revealed by the valley incision; F: Head scarp, and G: Fine sediments under and mudline on a large block, indicating possible liquefaction phenomenon.

There are two theories to explain the dynamic mechanism of coseismic debris flows that initiate as a rock slide or fall from a cliff above a gully and then transform into a debris flow:

(1) Rapid undrained loading by the rock slide from above that cause the liquefaction or partial liquefaction of the valley fill (Sassa, 1985). It is widely reported that mobility of debris flows is increased by such kinde of sudden loading, which also results in the enlargement of debris deposits by entrainment of the liquefied material (i.e. Crosta et al., 2003; Hungr and Evans, 2004; Fan and Xu, 2009; Iverson et al., 2011).

(2) Long duration of seismic shaking causes liquefaction of valley material. Wang et al. (2013) argued that the main part of the Xiejiadianzi landslide is from the seismogenic liquefaction of the valley colluviums, by performing undrained cyclic shear tests of samples took from the valley. This might played an more important role than the rapid undrained loading.

2.4.3 Rock/debris slides

Rock/debris slides normally occur along a recognisable slip surface, which can be translational (along a near-planar failure surface) or rational (along a circular failure surface). Field observations indicate that shallow and deep-seated rock/debris slides account for a large proportion of the slope failures in the study area. The Xiaojiaqiao landslide in Anxian county is a representative deep-seated rock slide, having a vertical and horizontal travel distance of 200 m and 600 m, respectively (Fig. 2.14A and B). It formed a 65 m high dam with an estimated volume of 2.4×10^6 m^3, impounding the second largest barrier lake with a maximum capacity of 2.2×10^7 m^3.

The head scarp of the landslide is about 160 high and 60^o steep (Fig. 2.11C). The source rock is composed of Upper Devonian dolomitic limestone, dipping at $40\text{-}50^o$ toward to the valley. The movement of the landslide was constrained by the opposite valley slope, causing that the stratified rock mass did not disintegrate completely. The dam body consists of two layers: the top layer with mainly rock fragments (~40%) as well as large boulders and blocks (~50%); and the bottom layer with almost intact rock mass (Fig. 2.14D and E). As the dam has threatened tens of thousands people downstream, it was artificially breached by constructing a spillway to avoid the catastrophic dam-breach flood.

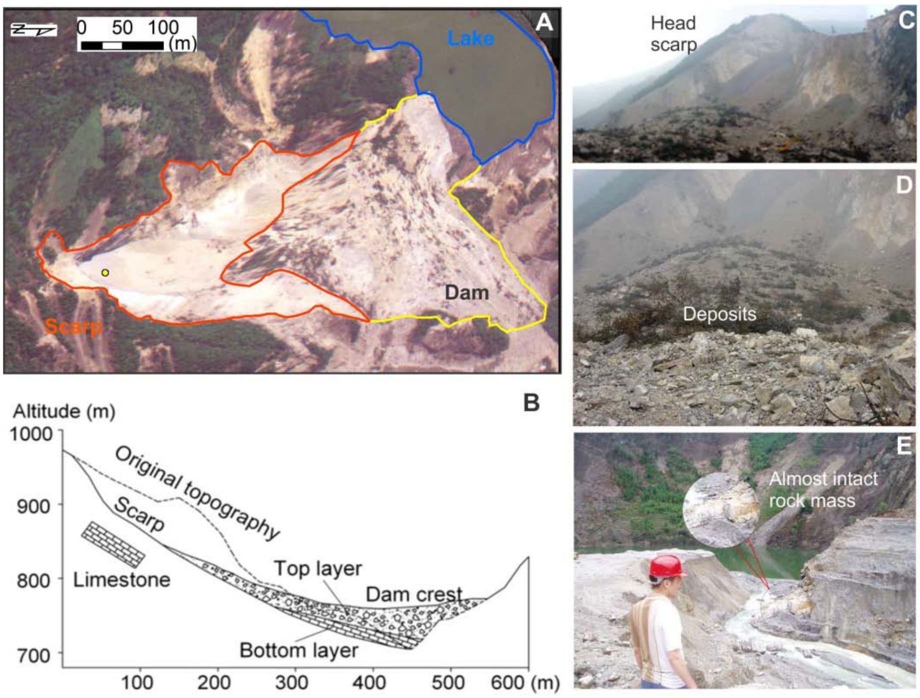

Figure 2.14 Xiaojiaqiao landslide. A: Aerial photo of the Xiaojiaqiao landslide; B: Typical profile of the landslide; C: Head scarp; D: Depositional zone; and E: Exposure of the dam body by an artificial spillway, showing the almost intact rock mass at the bottom.

2.4.4 Rock falls

Rock falls are also a major type of coseismic mass movements that mostly occurred in the upper part of slopes due to the topographic amplification effect on seismic waves (Bouchon et al., 1996), as shown in Fig. 2.15A. However, only a small proportion of them partially or completely blocked tributaries of main rivers due to their relatively small magnitude and limited runout (Fig. 2.15B and C). For example, the Dongjia rock fall located in Qingchuan county, dammed a valley and buried 13 people (Fig. 2.15D and E). The failure rock slope consists mainly of sandy slate that was cut into blocks by a set of near vertical joints (Fig. 2.15F). A steep head scarp with a height of 76 m was controlled by these joints. The volume of damming deposits was estimated around 8.8×10^5 m^3, assuming an average thickness of 21 m. The dam body was composed of large boulders (40%) as well as soil and rock fragments with a grain size of 5-20 cm (60%).

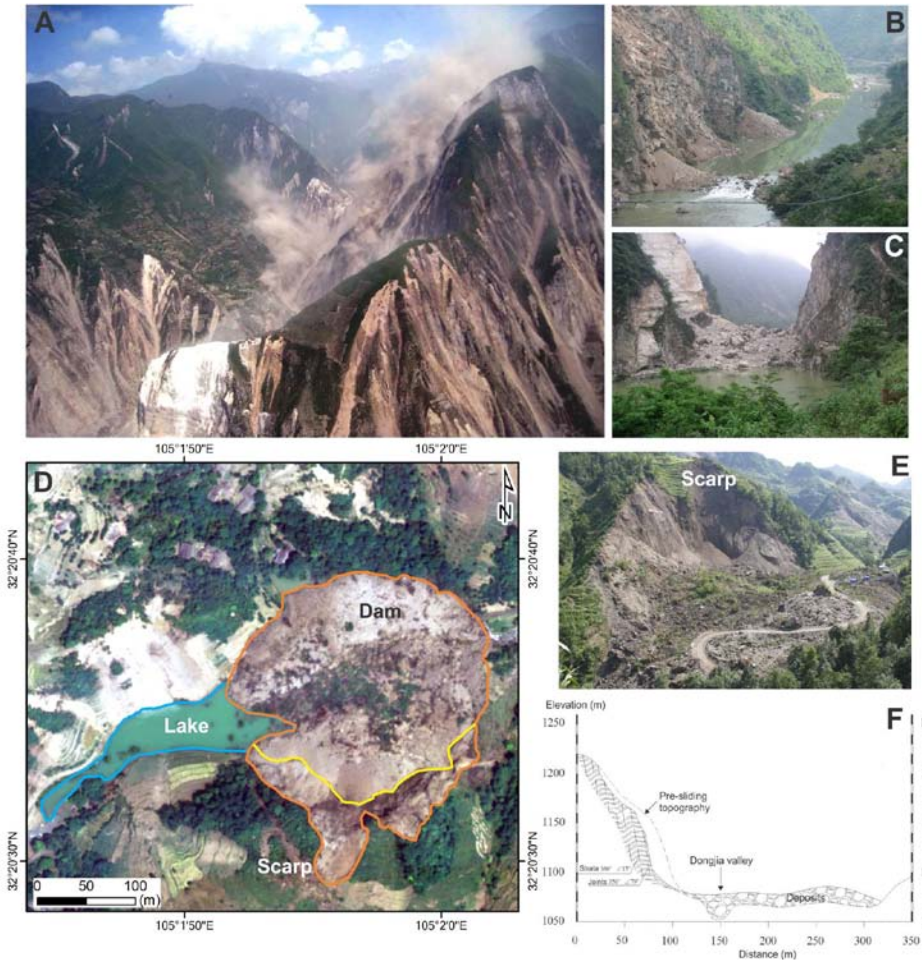

Figure 2.15 Rock falls. A: Shallow rock falls initiating from the upper part of slopes; B: Rock falls interrupted tributaries; C: A damming rock fall; D: Aerial photo of the Dongjia rock fall; E: Overview photo of the Dongjia rock fall and F: Typical profile of the Dongjia rock fall

2.5 Post Earthquake Damming Events Induced by Rainstorms

Strong earthquakes may produce a large amount of loose sediment from coseismic landslides, which lead to heavy debris flows during post-earthquake rainstorms. Lin et al. (2003) and Chang et al. (2009) evaluated the impact of the Chi-Chi earthquake on the occurrence of post-earthquake debris flows, and concluded that the frequency of debris flows was greatly increased. A number of intense post-earthquake landslides and debris flows in the Wenchuan earthquake-hit region were reported. Tang et al. (2011) investigated the landslides and debris flows induced by the first heavy rainfall four months after the earthquake in the Beichuan region. Xu et al. (2012) studied the debris flows triggered by another heavy rainstorm that occurred during 12-14 August 2010, including the Wenjia gully and Zoumaling gully debris flows in the Qingping catchment, the Hongchun gully debris flow near the town of Yingxiu and the Longchi debris flow near Dujiangyan city, as shown in Fig. 2.1. According to the record from the Qingping station, the maximum hourly rainfall was about 70 mm, when the debris flow occurred (Xu et al., 2012). The source supply of the Wenjia gully debris flow was from the loose deposits of the second largest coseismic landslide, the Wenjia landslide with an estimated volume of 2.75×10^{7} m^{3} and runout distance of about 4 km (Fig. 2.16A). Massive debris of 450×10^{6} m^{3} covered Qingping town and blocked the Mianyuan river (Fig. 2.16B). Tang et al. (2011) identified 21 debris flows along the Min river, among which, the Hongchun gully debris flow interrupted the river course and resulted in the flooding of the newly reconstructed Yingxiu town (Fig. 2.16C and D).

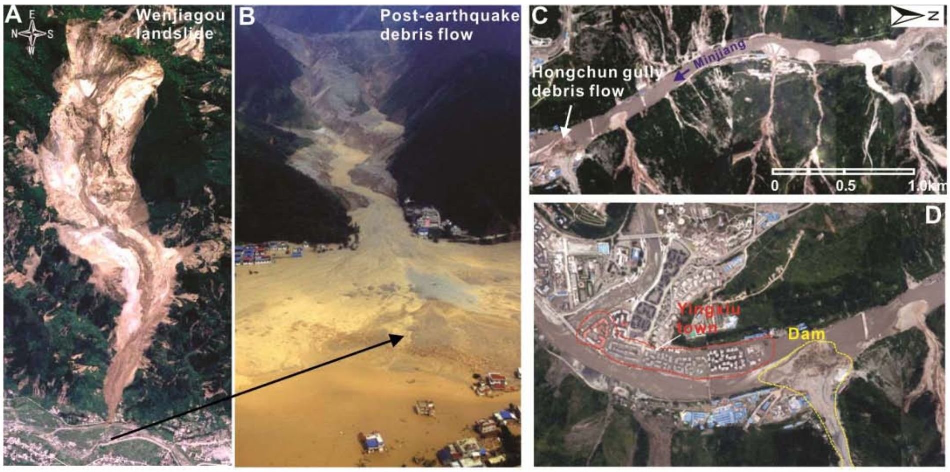

Figure 2.16 Post-earthquake debris flow damming events. A: Aerial photo of the coseismic Qingping landslide taken on May 18, 2008; B: Reactivated Qingping debris flow by heavy rainfall on 12 to 14 August 2010, dammed the Mianyuan river; C: Aerial photo of the debris flows along the Minjiang river taken on August 15, 2010; D: Hongchun gully debris flow partially dammed the Minjiang river, causing the flooding of the newly constructed Yingxiu town.

2.6 Typology of landslide dams

As introduced in Section 1.1.2, there are several existing classifications of landslide dams (Swanson et al., 1986; Costa and Schuster, 1988; Hermanns et al., 2011), but they are mainly based on dam geometry with respect to the valley floor, though ignoring dam materials, structure and geotechnical properties, which are widely accepted to play an important role in controlling the landslide dam stability (Casagli and Ermini, 2003 and Dunning et al., 2005). Therefore, in order to use the landslide dam typology as a preliminary indicator of dam stability, a two-step classification is proposed, based on:

(1) The plan view distribution of landslide deposit within the valley, which is referred to the most widely used classification from Costa and Schuster (1988), including six types as shown in Fig. 2.17;

Type I: dams which do not span the valley from one valley side to the other;

Type II: dams which span the entire valley floor and may run up the opposite slope;

Type III: dams which span the valley and, in addition, move considerable distances up and down the valley from the failure, and typically involve the largest volume of landslide material;

Type IV: dams which are formed by contemporaneous failures from both valley sides, followed by frontal or slide contact between the two masses;

Type V: dams form when the same landslide has multiple lobes of debris that extend across a valley floor and form two or more landslide dams in the same reach of river;

Type VI: dams involve one or more failure surfaces that extend under the stream or river valley and emerge on the opposite valley side from the landslide.

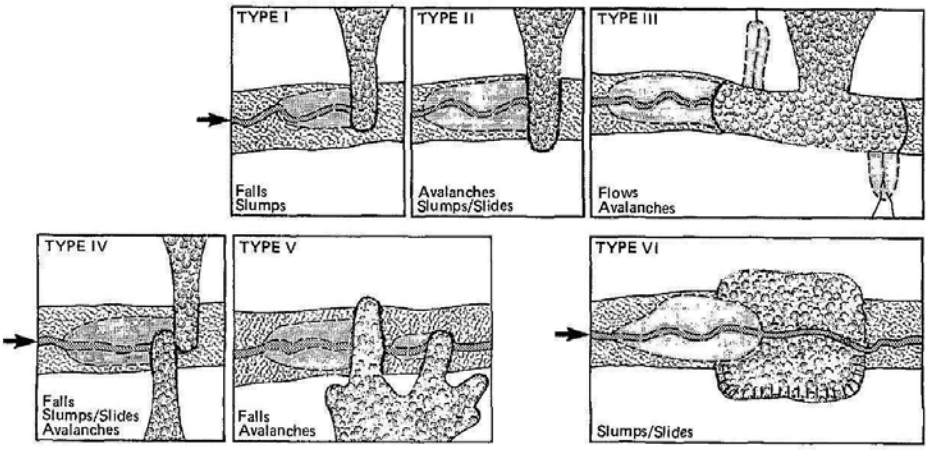

Figure 2.17 Six main types of landslide dams based on the geomorphic features of landslide deposits (from Costa and Schuster, 1988)

(2) The dam composition material and sedimentological features. According to the field investigations of more than 30 large landslide dams including above-introduced cases, the coseismic landslide dams can be grouped into three sub-types (Fig. 2.18).

Sub-type I: landslide dams mainly composed of large boulders and blocks. Dams of this type are most probably formed by rock avalanches or rock falls initiating from densely jointed rock slopes, such as the aforementioned Laoyingyan rock avalanche and the Dongjia rock fall.

Sub-type II: landslide dams mainly composed of unconsolidated fine debris, which are usually formed by debris flows, avalanches and slides with long runout and substantial entrainment along their travelling path. The Donghekou and the Xiejiadianzi landslides are good examples of this type. Dams formed by the post-earthquake debris flows mainly belong to this type, showing a low stability and a high susceptibility to erosion.

Sub-type III: landslide dams with partly intact rock strata at the base topped by large boulders and blocks or soil with rock fragments, showing a two-layered (e.g. the Xiaojiaqiao dam) or three layered (the Tangjiashan dam in Chapter 7) internal structure. Such dams are mainly formed by deep-seated rock slides or avalanches that fail as a largely intact mass and run into relatively narrow valleys. Due to the topographic constraints on the landslide movement, the sliding rock mass cannot be disintegrated completely, part of which still keeps the original geological structure.

With respect to dam stability, dams of Sub-*type III* tend to be more consolidated than Sub-*type I* and *II*, which therefore are less likely to be breached or completely collapse. The almost intact rock mass in the dam body can be impermeable, though the fine sediment on the top or middle layer may be eroded due to overtopping. It is believed that dams of Sub-type I composed of boulders and blocks are less likely to fail than those of Sub-type II containing unconsolidated or highly permeable debris (Costa and Schuster, 1988; Korup and Tweed, 2007). In addition, dam stability is related to landslide runout distance as well. Landslides with long runout distance are more likely to be disintegrated and fragmented during the travelling process, producing heavily crushed debris topped by a thin boulder carapace (Davies and McSaveney, 2002). The behaviour of landslide dams is also strongly linked to their geometry that is determined mainly by the landslide volume and valley geomorphometry. In general, the broader a valley, the shallower a dam and more likely for the dam to be overtopped and breached.

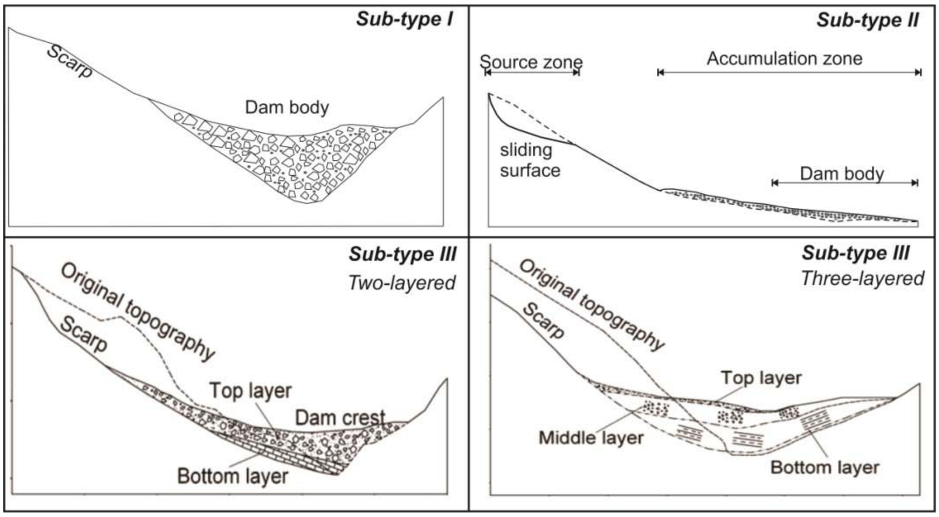

Figure 2.18 Three sub-types based on dam composition material and sedimentological features

2.7 Discussion and conclusions

Different from the common gravitational landslides, ground shaking plays a significant role in the coseismic slope failure. Newmark (1965) created a method to evaluate the coseismic landslide stability by considering a critical acceleration, which represents the threshold base acceleration required to overcome shear resistance and initiate sliding. This method was applied by Jibson et al. (2000) for the hazard assessment of coseismic landslides triggered by the 1994 Northridge earthquake.

Fundamentally, earthquakes affect the stability of slopes in two ways: (1) the ground shaking may reduce the frictional strength of the substrate by shattering of rock mass or liquefaction; and (2) the seismic acceleration may result in short-lived and episodic changes of the tensile and shear stresses in the hillshopes during earthquakes. Meunier et al. (2008) mentioned that these changes may be sufficient to cause failure. Based on the field investigation and above case studies, the failure mechanism of the landslides triggered by the Wenchuan earthquake can also be explained by these two aspects.

First, the widespread shattering has been found in many coseismic landslides in the study area, and appears to be especially severe in slopes on the hanging wall (Huang and Li, 2009 and Chigira et al., 2010). It has also been reported from the epicentral area of many earthquakes (Brune, 2001). Numerous cracks were found in many coseismic landslides, reflecting the intensive shattering and cracking. The long duration seismic shaking can largely reduce the shear strength of the substrate and even cause liquefaction of saturated material in some cases (e.g. the Xiejiadianzi landslide introduced in Section 2.4.2). Liquefaction phenomena have also been observed in other earthquake regions, for example, in the San Francisco Bay area during the 1989 Loma Prieta earthquake (Kayen et al., 1998) and in Niigata, Japan during the 2004 Mid-Niigata Prefecture earthquake (Sassa et al., 2005).

Second, tensile stress caused by the strong ground shaking mainly appeared in the crown of landslides, where the peak ground acceleration (PGA) is supposed to be the largest due to the topographic amplification (Bouchon et al., 1996). The rock mass is subjected to fail by tensile force due to their low tensile resistance strength. As a result, coseismic landslides always have high and steep head scarps. Meanwhile the seismic shaking also contributes to the shear stress (sliding force) along the sliding zone. Eventually, when the sliding force exceeds the resistance force, a landslide will happen.

In addition, the tectonic and geological structure of landslides was also found to be a dominating factor of coseismic landslide occurrence. Most of the investigated landslides were initiated from densely-jointed rock slopes. Dai et al. (2011) studied several rock avalanches triggered by the Wenchuan earthquake with the seismogenic fault traversing their source areas, and found that the shearing and brecciation associated with fault movement in history, rendering the rock slopes prone to failure.

The classification of landslide dams in this study can only be used as a preliminary indicator of dam stability. More reliable assessment requires a geotechnical approach taking into account a variety of dynamic loading scenarios, and also relies on knowledge about the accurate dam and barrier-lake geometry (Risley et al., 2006; Korup and Tweed, 2007).

There is still a large amount of loose sediment remaining on the slopes, which may be reactivated and remobilized during the heavy post-earthquake rainstorms. Therefore, predicting the post-earthquake debris flows and evaluating their potential for damming rivers are still of great concern and remain as a main challenge.

3 Event-based Landslide Dam Inventory

This chapter is based on:

Xuanmei Fan, Cees J. van Westen, Qiang Xu, Tolga Gorum, Fuchu Dai, 2012. Analysis of landslide dams induced by the 2008 Wenchuan earthquake. In: Journal of Asian Earth Sciences 57, 25-37.

Abstract

Landslide dams caused by earthquakes are extremely hazardous disruptions of the flow of water and sediment in mountain rivers, capable of delivering large outburst floods that may devastate downstream areas. We analyzed a unique inventory of 828 landslide dams triggered by the M_w 7.9 2008 Wenchuan earthquake, China, constituting ~1.4% of more than 60,000 coseismic slope failures mapped and attributed to this event. While 501 landslides blocked the rivers completely, the remainder caused only partial damming or channel diversion. The spatial distribution of landslide dams follows the same trend of that of the total landslide distribution, with landslide dams being most abundant in the steep watersheds of the hanging wall of the Yingxiu-Beichuan Thrust Fault, and in the northeastern part of the strike-slip fault near Qingchuan. Besides the co-seismic landslide density and the river width also played a key role in determining the landslide dam formation. Narrow rivers are more prone to be dammed than wide rivers. The correlation between river width and landslide dam volume follows a linear relation, which can be used to roughly estimate the possibility of dam formation. However, the applicability of this correlation needs to be validated in other regions. The morphometric parameters were analyzed, revealing power-law relations between landslide area and dam width, landslide source area and dam area, as well as lake area and lake volume. The inventory presented in this study will enrich the worldwide earthquake-induced landslide dam database.

3.1 Introduction

A number of landslide-dam inventories (Costa and Schuster, 1988, 1991; Chai et al., 1995; Casagli and Ermini, 1999; Korup 2004, Hewitt, 2006 and 2011; Hermanns et al., 2011; Weidinger, 2011) have been created by compiling and reconstructing historic large events. However, there is hardly any work specifically on earthquake-induced landslide dams (Adams, 1981; Hancox et al., 1997; Evans et al., 2011), due to the scarcity of well-documented inventories. Much previous work is scattered in local case studies (e.g. Dunning et al., 2006; Harp and Crone, 2006; Nash et al., 2008; Duman, 2009; Schneider, 2009) and mainly focused on historic occurrences, instead of a systematic compilation of a comprehensive dataset on size and stability. Little work exists on systematic analysis of the regional distribution patterns and the related controlling factors, the post-event failure rate and the longevity of coseismic landslide dams. This chapter aims to contribute to the systematic analysis of earthquake-induced landslide dams. We present one of the first and largest complete event-based landslide-dam inventories, with detailed geomorphometric parameters of landslide dams and quake lakes. Using detailed remote sensing interpretation and fieldwork, a unique database of 828 landslide dams triggered by the Wenchuan earthquake was created. In order to reduce the potential for dam-break floods, the Chinese army created artificial spillways in 32 of the dams using explosives and heavy machinery. Xu et al. (2009) qualified the hazard of these 32 dams by considering dam height, dam composition and maximum capacity of the landslide-dammed lakes.

This event-based inventory is unprecedented in size, and provides a unique opportunity to study the immediate post-earthquake dynamics of landslide dams, their geomorphometric features and the spatial distribution pattern at the regional scale. We assess methods to quantify the mean failure time of landslide dams and failure rate. A detailed understanding of the post-earthquake behaviour of landslide dams will contribute to a better understanding of landslide dam formation and longevity.

3.2 Landslide Dam Inventory

Event-based landslide inventories at a catchment- or regional scale aim at mapping all slope failures following a single landslide triggering episodes, such as an earthquake, intense rainstorms or significant snowmelt, and is essential for generating landslide susceptibility and hazard maps (e.g.

Kamp et al., 2008; Lee, et al., 2008, van Westen et al., 2008 and Cui et al. 2009). Landslide susceptibility and hazard assessments are often based on the assumption that the past is the key to the future, and therefore inventories of past landslides and their causal relationships can be used to predict future ones. For triggering earthquake events that have relatively large return periods, this creates the difficulty that it is very unlikely that such an event occurred in recent times, and that the landslides can be mapped. This is one of the reasons that earthquake induced landslide susceptibility assessment still is done using fairly simple methods (Jibson et al., 2000).

3.2.1 Source data for landslide and landslide dam mapping

Gorum et al. (2011) described the method for mapping landslides in the earthquake-affected Wenchuan region using 52 pre- and post- earthquake satellite images. The same data was used in this study, complemented by EO-1 (10-m spatial resolution) of July 2008 and ASTER images (15 m) of July, 2010 for mapping the landslide dams and impounded lakes. Fig. 3.1 indicates the spatial coverage of the satellite images. The pre-earthquake images consisted of multispectral data such as ASTER (15-m spatial resolution) and ALOS AVNIR-2 (10 m) as well as panchromatic data from ALOS PRISM (2.5 m) and the Indian Cartosat-1 (2.5 m). Post earthquake images included SPOT-5 (2.5 m), IKONOS (2.5 m), ASTER, ALOS AVNIR-2 and PRISM data as well as a limited number of aerial photos (0.3 m) which covered some large landslides (see the Appendix 1). To precisely identify the position of the landslide dams, the aerial photographs and satellite images were geometrically corrected using ground-control points (GCPs) measured in the field by DGPS and points selected from the 1: 50,000-scale digital topographical maps. A pre-earthquake DEM with 25 m × 25 m grid spacing was produced from 1:50,000 scale digital topographical maps, by interpolating the contour lines with contour intervals ranging between 10 m for low relief mountain areas and 20 m for high relief areas. According to the Chinese national standard, the horizontal and vertical accuracy of the 25 meter DEM at a 90% level of confidence is better than 20 m and 10 m, respectively.

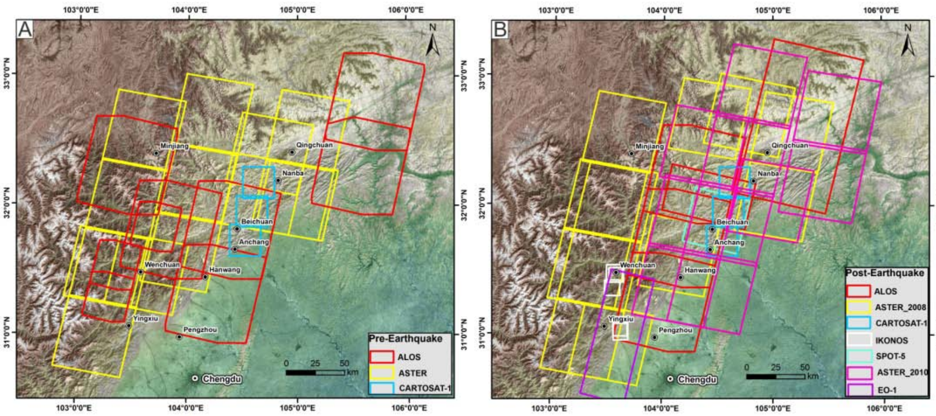

Figure 3.1 Pre- and post-earthquake image coverage map

3.2.2 Mapping and image interpretation

Landslide dams were mapped through visual interpretation by comparing pre- and post-earthquake false colour composites or panchromatic images, assisted by field checks in accessible areas containing about 60% of dams. The coseismic landslides are clearly recognizable from change detection of monoscopic images, using image characteristics such as tone, texture, pattern and shape. Although stereoscopic image interpretation would have been better for optimal landslide interpretation, it was not practically feasible to generate stereo images for such an extensive area of about 35,000 km^2. Therefore, the stereo-based interpretation was carried out for selected areas around large landslide dams. These were identified by diagnostic features such as a higher reflectance compared to the surrounding areas with vegetation cover; and geomorphic features such as scarps; bare rock-fall talus; and asymmetric hummocky deposits featuring flow lobes, and transverse or longitudinal ridges. The resolution of the available images did not allow to map landslides and lakes that were less than 200 m^2. Landslide dams were classified into two classes: (1) full blockage, where landslide debris completely obstructed rivers, forming a lake; and (2) partial blockage, where debris obstructed the river without forming an impoundment.

We mapped scar and deposit areas for landslides completely or partly blocking the rivers, as well as any associated quake lakes. The area of quake lakes changes with time because of incoming water and sediment discharge. Therefore, we compared the multi-temporal images and assumed the largest area derived from images to represent the full lake area, and mapped the lakes before any artificial breaching was carried out.

Some medium-resolution images precluded the distinction between landslide scar and deposit areas (Fig. 3.2a and b). While the high-resolution images allow us to map in detail the initiation, transportation and accumulation area for 64% of the landslide dams. Cross checking of pre- and post- earthquake images revealed that some pre-existing landslides were enlarged or reactivated during the earthquake, while several dams failed shortly after they were formed (Fig. 3.2c-f). We used pan sharpening of high-resolution panchromatic images (PRISM) to increase the resolution of multispectral images (ALOS AVNIR-2) to allow for more details, such as coarse grained rock slide deposits and the linear bedding structure (Fig. 3.2g and h).

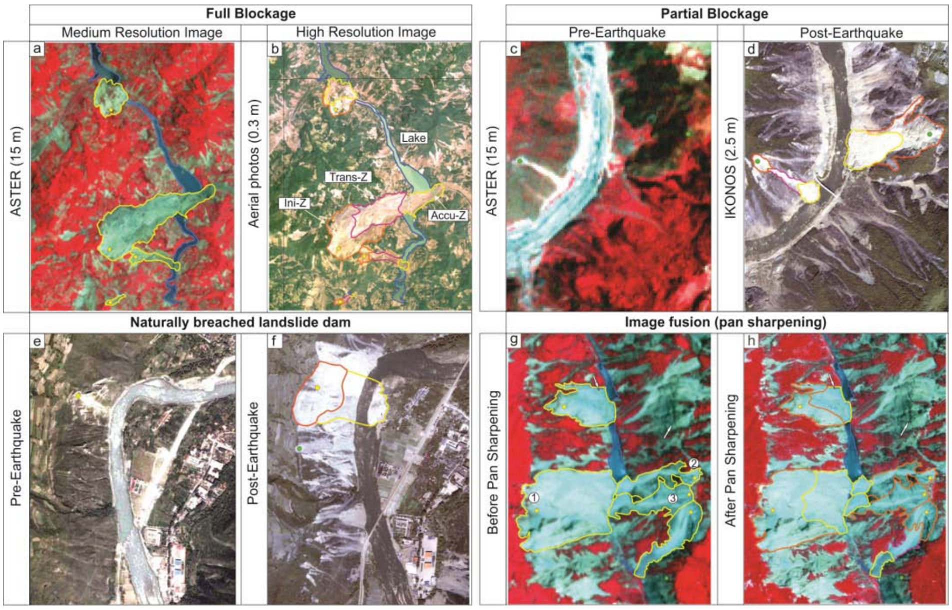

Figure 3.2 Examples of medium (a and c) and high resolution images (b and d) showing landslide dam polygon mapping. Detailed mapping allowed delineating the initiation (Ini-Z), transportation (Trans-Z) and accumulation (Accu-Z) parts of damming landslides, whereas the landslides can only be mapped as single polygons using medium resolution images. Complete and partial blockages as well as the reactivated landslides can be observed by comparing pre- and post-earthquake images. Some landslide dams were dissected by rivers already several hours after they were formed (e and f). A landslide dam can be formed by several landslides (e.g.①, ② and ③) jointly as shown in g.

Fig. 3.3 shows the distribution of the landslide dams in relation to the overall landslide distribution mapped by Gorum et al. (2011). Fig. 3.4 shows an example of the detailed inventory of landslide dams in a small part of the area indicated in Fig. 3.3. The types of river-blocking landslides, following the terminology of Cruden and Varnes (1996) are indicated in the inset of Fig. 3.3. Rock slides are the most common type and account for 35% of the data, because the fractured rock slopes were found very susceptible to seismic shaking (Chigira et al, 2010). The largest coseismic landslide caused by the Wenchuan earthquake (indicated in Fig. 3.3) was the Daguangbao landslide, with an area of 7.8 km^2 and an estimated volume of 1.17×10^9 m^3 (Huang and Fan, 2013). The Tangjiashan landslide dam had impounded the largest lake with an estimated maximum volume of 3×10^8 m^3. The dam is located ~85 km upstream of Mianyang city, i.e. the second largest in Sichuan with a population of ~1.2 million. The Chinese authorities decided to evacuate parts of Mianyang city (Liu et al., 2009), until the Tangjiashan landslide dam was artificially breached, and the lake was drained.

Our inventory contains 828 river-blocking landslides; 501 (61%) caused complete damming of rivers, while 327 (39%) only partially dammed the rivers. Partially damming landslides ranged in area from 768 m^2 to 1.3×10^6 m^2, which are slightly smaller than the completely damming landslides with areas ranging from 1,249 m^2 to 7.1×10^6 m^2. Quake lake areas varied from 217 m^2 to 6.5×10^6 m^2. The landslides triggered by the Wenchuan earthquake cover an estimated total area of ~811 km^2 (Dai et al., 2011), and the damming landslides covered an area of ~54 km^2, which is ~7% of the total landslide area.

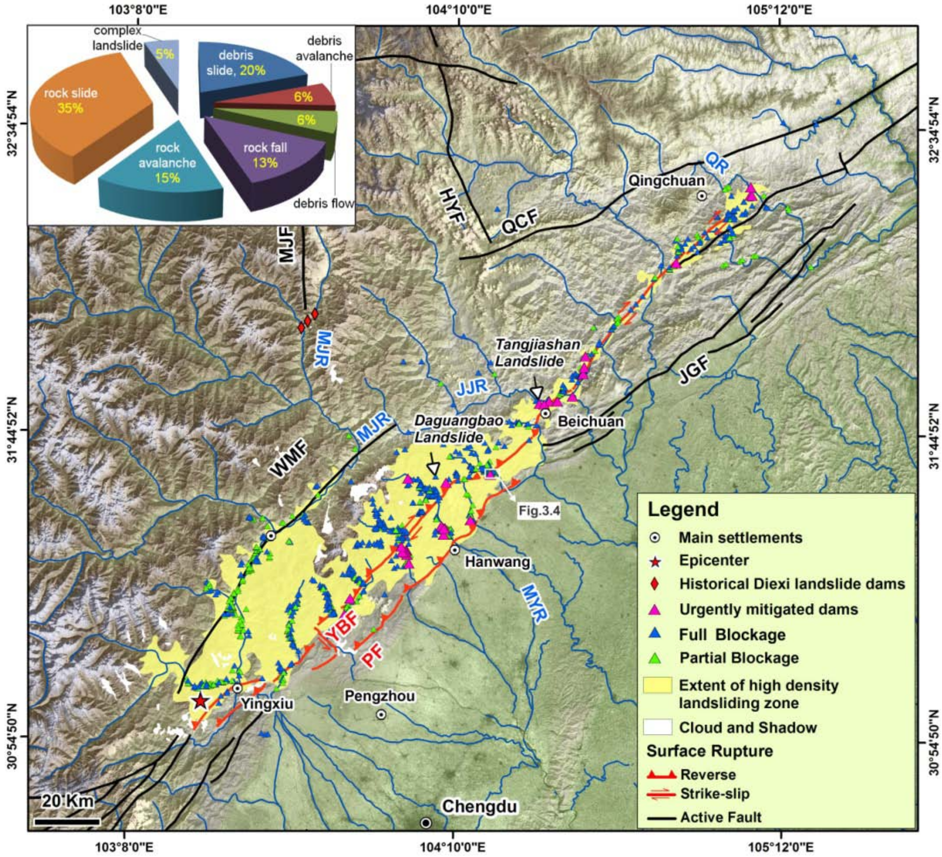

Figure 3.3 Distribution of landslide dams triggered by the Wenchuan earthquake, China. The high landslide density zone is defined by a landslide area density >0.1 km^{-2}; also shown are epicenters of historical earthquakes (USGS, 2008) and historical Diexi landslide dams. White polygons are unmapped due to the presence of clouds and shadows in post-earthquake imagery. The major fault and river names are indicated in Fig. 2.1.

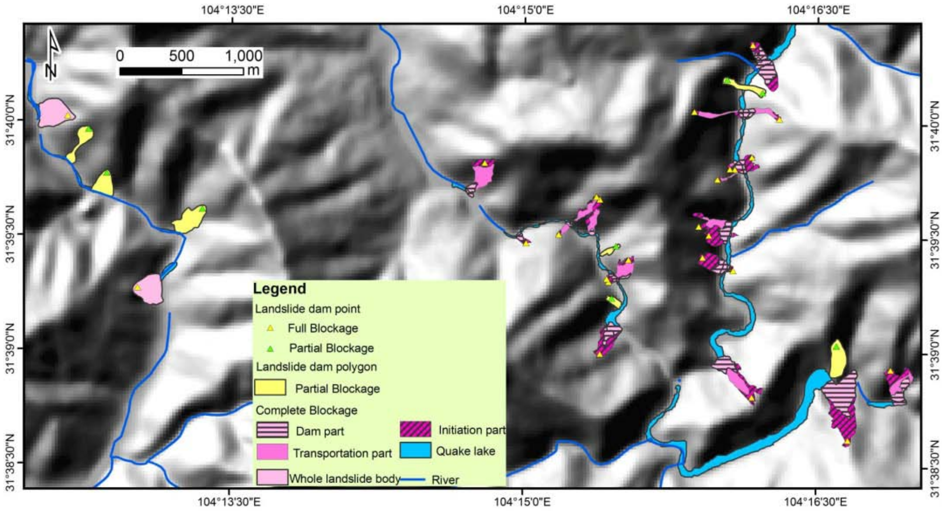

Figure 3.4 An example showing landslide dam polygon mapping in an area indicated in Fig.3.3.

3.3 Spatial Distribution Analysis of Landslide Dams

We estimated the spatial density of all coseismic landslides (Gorum et al., 2011) and landslide dams within a circular moving window of 1 km^2 radius, obtaining maximum values of 54.1 landslides/km^2 and 4.5 landslide dams/km^2 respectively (Fig. 3.5A and B). A swath profile along the fault in a 240 km long and 25 km wide rectangular zone (Fig. 3.5C) as well as four perpendicular 25 km by 20 km long swaths (Fig. 3.5C1-C4) illustrate the mean normalized point density of landslides and landslide dams. A swath profile width of 25 km was selected, because it represents the extent of the surface projection of the hanging wall of the Yingxiu-Beichuan fault. Fig. 3.5 C shows the variation of mean normalized point densities for landslides and landslide dams along the fault from SW to NE. Both follow the same trend, with peaks in the SW section from Yingxiu to Beichuan and near the fault tip near Qingchuan. The landslide-dam density peaks at several river junctions, spatially mimicking the pattern of coseismic landslide abundance. Landslide dams are most abundant in steep watersheds (P1-P7) of the Pengguan Massif, along the thrust segment of the Yingxiu-Beichuan fault (YBF, Fig. 3.5 B). Their density decreases dramatically to the NE extending from Beichuan town to the fault tip. Four swath cross sections (Fig. 3.5C-1 to C-4) show that peaks in landslide density near the drainage network coincide with a high density of landslide dams. Both landslide and landslide-dam densities are higher on the hanging wall of the Yingxi-Beichuan fault (YBF) than on the footwall. However, this difference is not so apparent for the cross-section 2, where the footwall of YBF is also the hanging wall of the Penguan fault (PF).

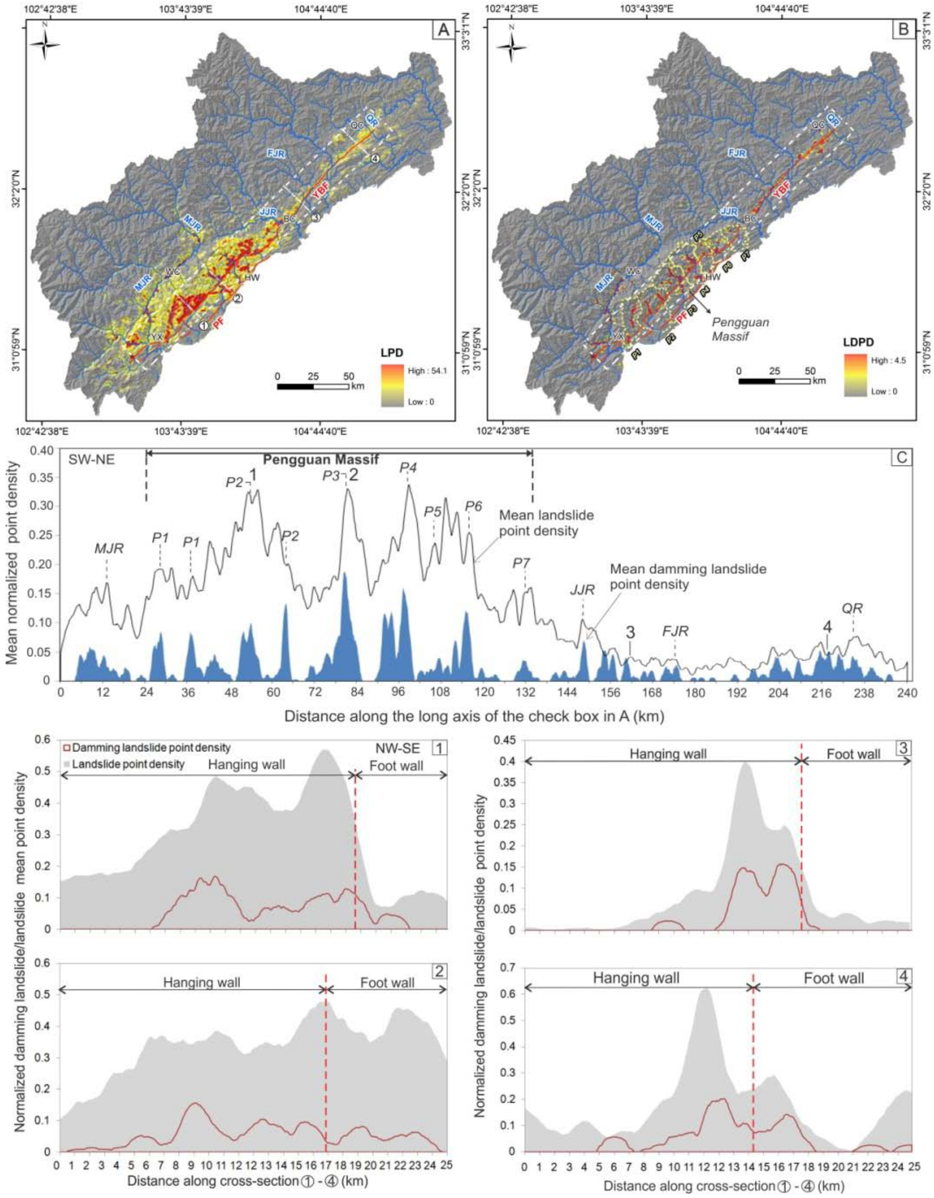

Figure 3.5 Comparison of densities of blocking and non-blocking landslides. A. and B. show the landslide and landslide dam point density, respectively. White

dashed lines are 240-km by 25-km swath profiles and cross sections (1-4). LPD and LDPD represent the landslide and landslide dam point density, respectively. C. Mean normalized landslide and landslide dam densities along the SW-NE profile and four NW-SE cross sections, respectively. Red lines in are Yingxiu-Beichuan fault (YBF) and Pengguan fault (PF). Yellow dash lines are the boundary of the P1-P7 watersheds in the Pengguan Massif. YX, WC, BC, and QC are the cities of Yingxiu, Wenchuan, Beichuan and Qingchuan, respectively. MJR, JJR, FJR, and QR represent Min, Jian, Fu and Qing rivers, respectively.

Landslide dams are most abundant in P1-P7 steep watersheds in the Pengguan Massif and the Min river (*MJR*) (Fig. 3.5B). Different from the dams in the Pengguan Massif, most of dams (>90%) along the deeply incised Min River have mainly caused the partial blockage, since the Min river has large discharge and width. In general, landslide density directly affects landslide-dam density, although landslide volume and river width were also found to play key roles. The river width was estimated by Equation (2.1) following the method introduced in Chapter 2. The landslide volume was estimated by applying volume-area (*V-A*) scaling parameters using the equation presented by Larsen et al. (2010), because it was obtained from about 4000 landslides and also took landslide material (soil or bedrock) into account.

$$V=0.146A^{1.332} \tag{3.1}$$

The variation of landslide dam volume in the main catchments was analyzed, and the results are presented in Fig. 3.6, in which also the channel width of rivers is indicated by the red line. Landslide dams that blocked the wider rivers (e.g. Jian and Fu rivers) usually have larger volumes. An exception is for the Min river, where partial blocking landslides were more abundant (Fig. 3.6 and Fig. 3.7). Narrow rivers with a small catchment area are more prone to be dammed, thus landslide dam density is higher along the P1-P7 rivers (with a width of <15 m and catchment area of 132-463 km^2) than along the Jian and Fu rivers with a width of >30 m and catchment area of 4100 km^2 and 2400 km^2, respectively (Fig. 3.6). The correlation between river width and landslide dam volume follows a linear relation (Fig. 3.7)

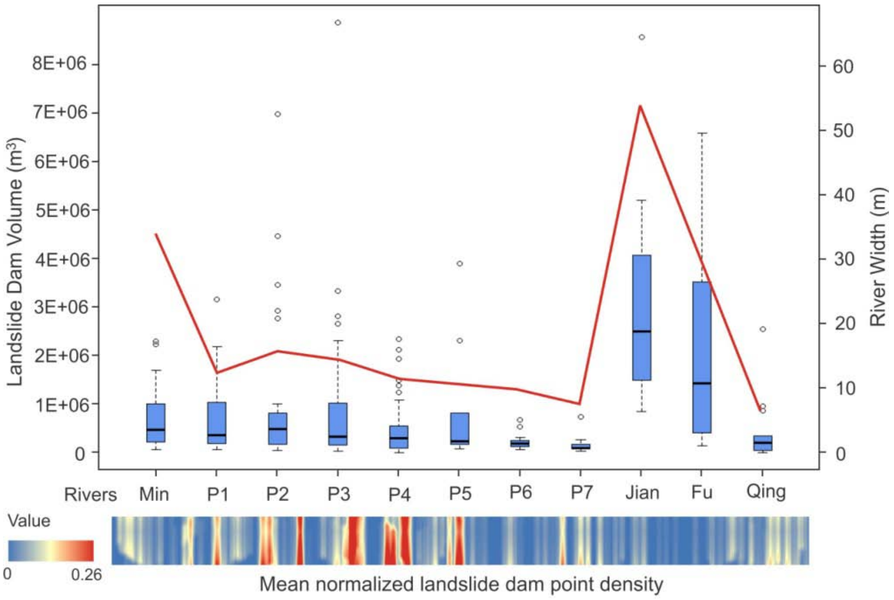

Figure 3.6 Box and whisker plot of landslide dam volume in major catchments with comparison of river width. The spectrum shows the variation of mean landslide dam point density along the SW-NE swath profile in Fig.6.

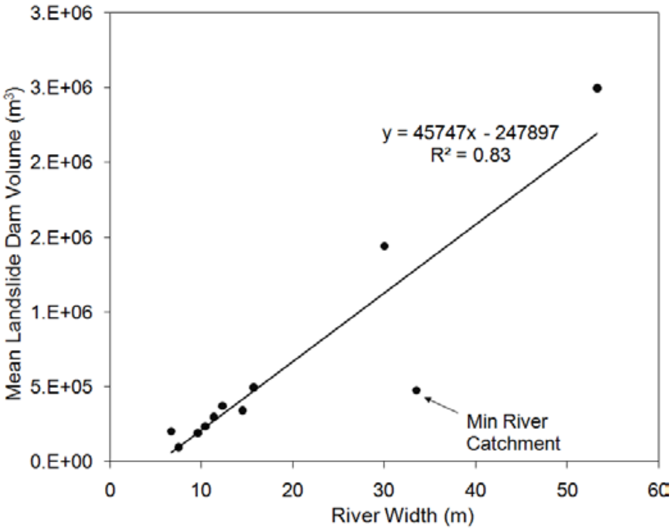

Figure 3.7 Correlation between the mean landslide dam volume in different catchments (in Fig.3.6) and the river width. Because most dams in the Min river are partial blocking with comparatively small volume regarding to the river width, the Min river catchment appears to be an outlier.

3.4 Analysis of Geomorphometric Parameters

A number of geomorphometric parameters of the landslide dams and associated quake lakes have been considered important for a first empirical assessment of dam stability and potential hazard of dam-break floods (Fig. 3.8). We derived these attributes following the terminologies defined in previous work (Costa and Schuster, 1988; Dong et al., 2009).

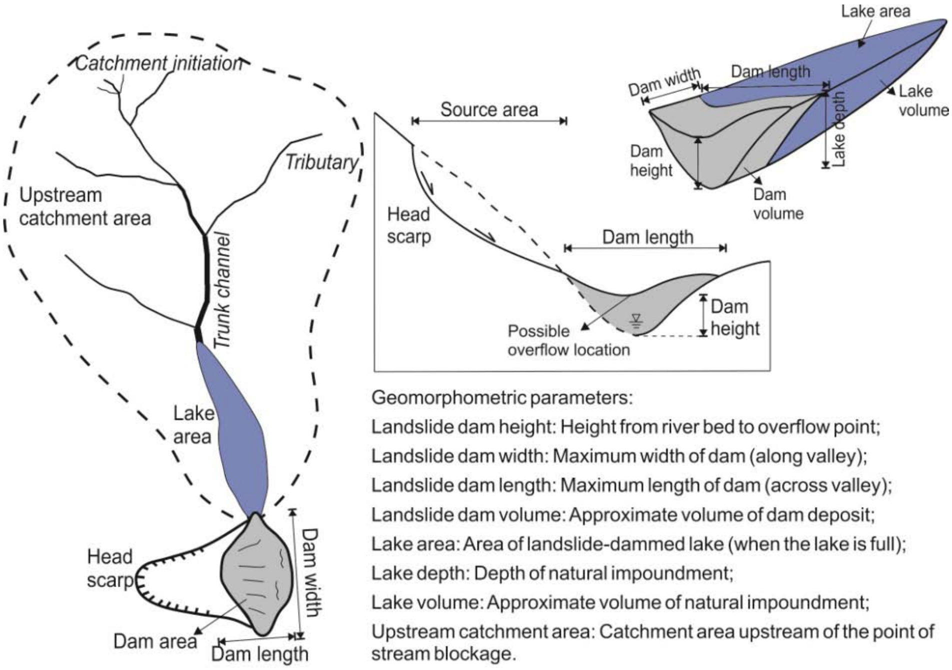

Figure 3.8 Sketch of geomorphometric properties of landslide dam and impounded lakes.

Most of the parameters such as the landslide dam length, width, area and quake lake area, can be directly extracted from landslide dam and lake polygons, while others (e.g. landslide dam height and volume as well as the quake lake depth and volume) require further calculations. The height difference between the highest and the lowest point under the related lake polygon was assumed as the lake depth, which was calculated based on the pre-earthquake DEM with the vertical accuracy of 10 m. The dam height was considered to be equal to the lake depth if the lake is full. The lake volume was calculated using GIS-based volumetric algorithms (the "TIN

Polygon Volume" function). To reduce possible errors that might be caused by the DEM accuracy, only the volume for 319 lakes with a depth more than 10 m and an area exceeding 1000 m² was calculated. The results were validated using field measurement data of 24 lakes that were surveyed by a Chinese expert team and the Chinese army directly after the earthquake (Xu et al., 2009; Fig. 3.9). The lake volume was estimated by field measured lake area and average lake depth by using the handheld GPS, Laser distance finder, and boat with sonar (or rope and weight) (Zhang, 2010).

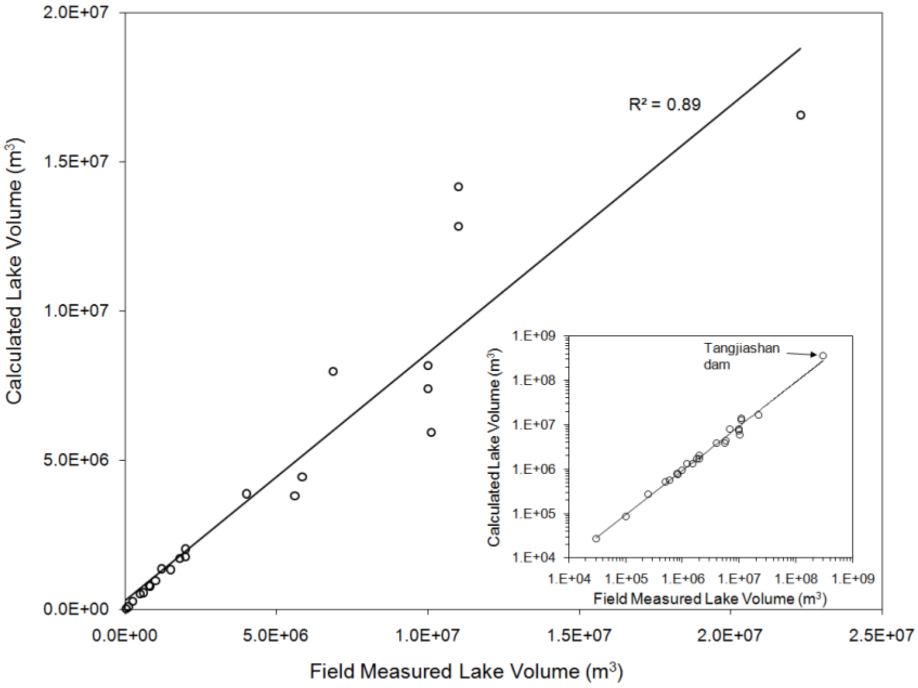

Figure 3.9 Validation of the quake-lake volume estimates using field measurement data. Inset has logarithmic axes for better displaying the extreme dimensions of the Tangjiashan dam.

The calculated and field measured lake volumes with logarithmic axes are shown in the inset of Fig. 3.9, which show a good fit. To better underpin the contribution of smaller lakes, we excluded the Tangjiashan lake from Fig. 3.9. The results demonstrate that the lake volume calculations show a good match with the field measurement data ($R^2 = 0.89$). For the Tangjiashan dam, the calculated dam height and lake volume is 115 m and $\sim 3.5 \times 10^8$ m³, respectively, which are close to the field measurements with the dam height ranging from 82 to 124 m and the lake volume of 3.0×10^8

m^3. The calculated volumes of large lakes are more variable than those of smaller lakes, since slight changes in lake depth will lead to large volumetric changes.

Based on our inventory, we extracted the geomorphometric parameters from the full blockages indicated in Fig. 3.8 and analyzed some empirical relationships between these parameters as shown in Fig. 3.10. The results show a power-law relationship ($R^2=0.72$) between the landslide area and the resulting landslide dam width along the valley, implying that the landslide area is a good indicator for predicting dam width (Fig. 3.10A). A total length of ~76 km of river reaches was directly covered by damming landslide debris. Fig. 3.10B shows that the landslide source (initiation) area can be used to estimate the landslide dam area. The relation between the quake lake volume and the dam height is less clear ($R^2=0.53$), and can be related to several additional factors such as the local valley morphometry, upper catchment area and terrain (Fig. 3.10C). The empirical scaling relationship between lake area and volume that we constrained by field measurements is clear, showing a positive power-law relation ($R^2=0.8$), with the V_L varying over 6 magnitude orders from 10^3 m^3 to 10^9 m^3 (Fig. 3.10D). The lake volume is an essential parameter for dam failure hazard and risk assessment, which has been used in various empirical equations to predict dam-break flood peak discharge (Evans,1986; Costa and Schuster,1988; Walder and O'Connor,1997). Therefore, the relation in Fig. 3.10D can also be applied in similar regions for a rapid estimation of lake volume, and the related hazard evaluation and mitigation.

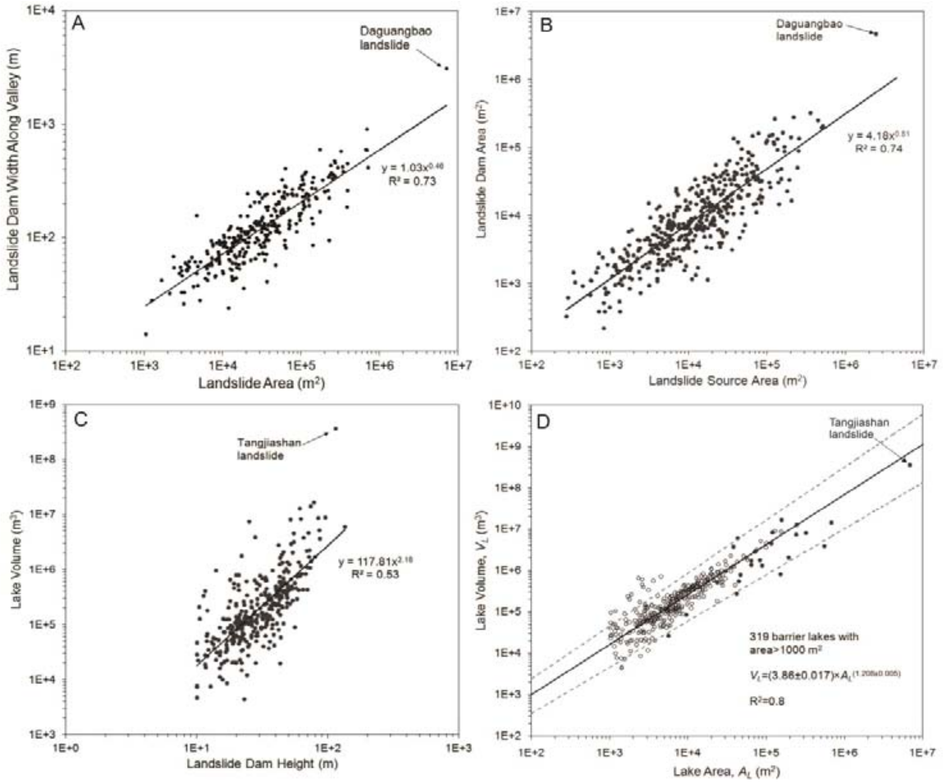

Figure 3.10 A) Plot of landslide dam width along valley (W_D) versus landslide dam area (A_D); B) Plot of landslide source area (A_s) versus landslide dam area (A_D); C) Plot of quake lake volume (V_L) versus landslide dam height (H_D); D) Plot of quake lake volume (V_L) versus lake area (A_L). Filled circles in D. represent lakes with flied measured volume as shown in Fig.3.9. Thick black lines are best fit obtained by the Reduced Major Axis Regression (RMA). Dashed grey lines show 95% confidence intervals.

3.5 Discussion and Conclusions

The temporary or permanent blockage of streams by landslides is a characteristic secondary hazard in mountainous areas affected by strong earthquakes or major rainfall events. It is also possible to happen without recognized triggers, i.e. the Mayunmarca landslide dam occurred in 1974, Peru (Hutchinson and Kojan, 1975). Such impoundments may pose a large risk to downstream areas given the potential for catastrophic lake outbreak flooding. Our inventory of landslide dams caused by the Wenchuan earthquake records abundant river blockage following a single regional landslide triggering event. It presents the spatial distribution pattern of landslide dams with comparison to all co-seismic landslides. They are most abundant in the Pengguan massif, along the thrusting part of the Yingxiu-Beichuan fault (YBF), due to following reasons:

(1) Steep and rough terrain with hillslope inclinations $>30^{o}$ is prone to generate landslides. Fig. 3.11 depicts the elevation variation along the Yingxiu-Beichuan fault, showing that the mean elevation in the Pengguan Massif is about 400 m higher than that in the northeast from Beichuan to the end of the fault. This difference contributes to the higher landslide and landslide dam densities in the Pengguan massif.

(2) The Pengguan Massif is composed of fragmented Precambrian crystalline gneisses and granitoids separated from a series of Triassic mudstones by the Yingxiu-Beichuan fault (Chigira et al., 2010). Field investigation revealed that the fragmented rocks favour landslide (dam) occurrences. Most of large rock avalanches occurred there in intensely jointed granite rock masses.

(3) The changes of fault geometry and slip rate from the southwest to the northeast were quantified by GPS and InSAR data (Yarai et al., 2008; Hao et al., 2009), showing that in the Pengguan Massif the fault plane dips moderately to the northwest, becoming nearly vertical in the northeast (from Beichuan to Qingchuan region), associated with a change from predominantly thrusting to strike-slip motion. High fault-slip rate (large seismic energy) concentrated in the thrusting part of the fault in the Penguan Massif (Gorum et al., 2011).

(4) Deeply incised narrow valleys (*P1-P7* in Fig. 3.11) with small catchment areas varying from 132 to 463 km^2 were readily blocked.

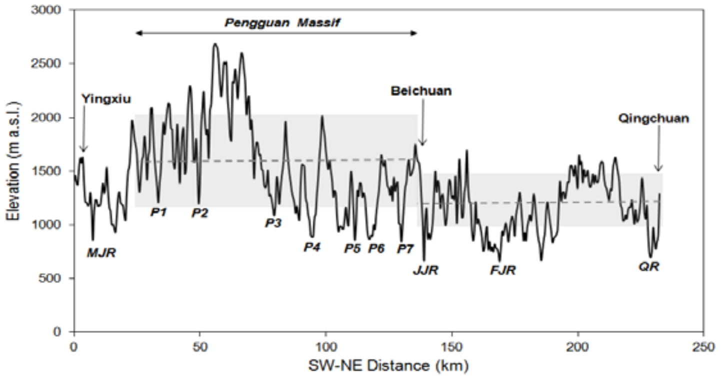

Figure 3.11 Elevation profile along the Yingxiu-Beichuan fault. The dashed lines represent the mean elevation in the Pengguan Massif and the northeast part of the fault. Grey boxes delimit the + 1 standard deviation (S.D.) from the mean.

The correlation between landslide dam volume and river width relies on the empirical scaling relationships we used, although the changes of the scaling relationship will not significantly change the relative comparison of landslide dam volume and river width in different catchments. The landslide volume-area scaling relationship we used from Larsen et al. (2010) takes the landslide type and material into account, thus was considered appropriate. The one for estimating the river width (Equation(2.1) in Chapter 2) is also considered to be most suitable for the rivers in the tectonically active mountainous regions compared to the conventional scaling relationship ($W \sim A^{0.5}$) (Finnegan et al., 2005). The correlation between river width and landslide dam volume we extracted from this study follows a linear relation, demonstrating that damming of wide rivers generally requires landslides with large volume. However, the applicability of this correlation is still unknown before being validated in other regions.

The Wenchuan earthquake provided a unique opportunity to generate an event-based landslide dam inventory of 828 individual landslide dams, of which 501 completely blocked rivers. We focused on comparing the spatial distribution pattern of coseismic landslides and landslide dams, as well as analyzing geomorphometric parameters of landslide dams. Further research is directed towards analyzing the seismic, geological, topographic and hydrological factors that determine the occurrence of landslide dams, with the ultimate aim to come to a conceptual model for landslide dam susceptibility and hazard assessment. The long-term effect of landslide dams on valley morphology and sediment budgets is another aspect that deserves further research attention. The deposition of lacustrine, alluvial, or deltaic sediments in reservoirs can result in changes of stream gradient, surface morphology, and superficial geology upstream from the dam, whereas dam-break floods or debris flow may rework downstream reaches.

4 Controls on the Distribution of Landslides and Landslide Dams

This chapter is based on:

Xuanmei Fan, Cees J. van Westen, Qiang Xu, Tolga Gorum, Gonghui Wang, Runqiu Huang, 2011. Spatial distribution of landslide dams triggered by the 2008 Wenchuan earthquake. In: Proceedings of the Second World Landslide Forum, 3-7 October, Roma, Italy.

Xuanmei Fan, Cees J. van Westen, Chenxiao Tang, Victor Jetten, Qiang Xu, Runqiu Huang, 2013. Controls on the distribution of landslides and landslide dams induced by the 2008 Wenchuan earthquake. Natural Hazards and Earth System Sciences. (in preparation)

Tolga Gorum, **Xuanmei Fan**, Cees J. van Westen, Runqiu Huang, Qiang Xu, Chuan Tang, Gonghui Wang, 2011. Distribution pattern of earthquake-induced landslides triggered by the 12 May 2008 Wenchuan earthquake. In: Geomorphology 133, 152-167.

Abstract

The 2008 Wenchuan earthquake induced more than 60,000 coseismic landslides, among which about 800 dammed rivers. This chapter analyzes the relationships between landslides that lead to damming and a number of predisposing factors, and compares these relations with those of all earthquake-induced landslides. Benefiting from this large database, we first analyzed the spatial variation of area density for both the non-damming and damming landslides in order to better understand their distribution pattern and controlling factors. We then quantified the weight of the possible factors by the weight of evidence (WOE) method. Thirteen triggering and geo-environmental factor maps were prepared and implemented on a GIS platform. A statistical script was applied to standardize the factor maps and calculate their weights automatically. The results show that distance to fault surface rupture, peak ground acceleration (PGA) and lithology play dominating roles in landslide occurrence. The fault type and hanging/foot wall effect were overlooked in previous studies, but were found important for coseismic landslides. For the damming landslides, distance-to-river factor ranks second in terms of the weight. The topographic factors (slope, internal relief and terrain roughness) are more significant than the hydrological factors for the non-damming landslides. The results are instructive for selection and weighting of predictors of landslide susceptibility models, and will be used in later chapters for analyzing landslide dam susceptibility.

4.1 Introduction

Over the past decades, a growing number of studies have attempted to assess landslide susceptibility or hazard by combining different causative factors using various methods. The landslide susceptibility, also called the spatial probability is defined as the likelihood of the occurrence of landslides in a given location or terrain unit (i.e. Dai et al., 2002; Guzzetti et al., 2005). If temporal probability of landsliding and size probability are also considered, the landslide susceptibility can be converted into landslide hazard, which can be assessed by the multi-temporal landslide inventories or the recurrence of landslide triggering events (i.e. earthquakes or rainfalls).

Methods for assessing landslide susceptibility or hazard have been reviewed by (van Westen et al., 1997; Guzzetti et al., 1999; Corominas and Moya, 2008), and can be generally grouped into three categories: heuristic, physically-based and statistical approaches. A heuristic approach is a direct or qualitative approach, based on experts' prior knowledge of all causative factors of landsliding. The experts assign weights to the classes of factor maps and overlay them to create a susceptibility map (Blake et al., 2002; van Westen et al., 2003). Physically-based model approaches are based on slope stability models, which can provide quantitative results (Wu and Sidle. 1995). However, they require a large amount of detailed input data, and can therefore be applied only when the ground conditions are fairly homogenous and the landslide types are known. Statistical approaches are indirect, based on the analysis of spatial associations of known landslide occurrences with casual factors (Castellanos Abella and van Westen, 2008; Ghosh et al., 2011), including bi-variate and multi-variate analysis (i.e. discriminant analysis, logistic regression and neural networks etc). Analyzing the relations between causal factors and the past landslide events is the first and fundamental step for above approaches, according to the assumption that future landslides are more likely to occur under conditions similar to those contributing to the past landslides.

The 2008 Wenchuan earthquake triggered a vast number of landslides (about 56,000 mapped as polygons by Dai et al., 2011 and around 60, 000 mapped as points by Gorum et al., 2011). Among them, more than 800 blocked rivers, forming landslide dams as introduced in Chapter 3 (Fan et al., 2012a). In terms of the amount of coseismic landslides and landslide dams, the Wenchuan earthquake ranks first among other earthquakes, such as the 1994 Northridge earthquake (Parise and Jibson, 2000), the 1999 Chi-Chi earthquake (M_W 7.6; Khazai and Sitar, 2004), the 2005 Kashmir earthquake in Pakistan (M_W 7.6; Sato et al., 2007) and the 2010 Haiti earthquake (M_w 7.0; Gorum et al., 2012). Thus, it provides us a valuable opportunity to study and compare the factors that control the spatial distribution of coseismic landslides and landslide dams. Given this objective, the well-established weight of evidence (WOE) method was preferred over the other bivariate and multivariate method to quantify the relative importance of each factor. It is worth mentioning that this study did not attempt to create a coseismic landslide susceptibility model due to the normally large return periods of strong earthquakes, making a susceptibility model unlikely to be validated by another event in the same region. Therefore, generation of a susceptibility map for the Wenchuan earthquake does not seem to be very meaningful as such a large event has a very large return period, and a future earthquake is likely to occur with a different magnitude, fault rupture and epicentre location. Additionally, the geo-environment can be significantly changed by strong earthquakes, together with climate change and land-use change, which might make the susceptibility model lose the prediction power.

4.2 Method and Data

4.2.1 Theory of weights of evidence (WOE)

The weights of evidence method (from now on referred to as WOE) was developed for the identification and exploration of mineral deposits (Bonham-Carter et al., 1989), and is based on the Bayesian probability theory which uses the prior and posterior (conditional) probability. Since two decades, this method has also been applied in landslide susceptibility assessment (e.g. van Westen et al., 2003; Neuhäuser and Terhorst, 2007; Regmi et al., 2010). The first step of WOE is to select the relevant causal factors based on the expert field knowledge related to the occurrence of the landslide features, which are then prepared as input factor maps in a GIS environment. The factor maps should be in raster format for the convenience of the WOE calculation. By overlaying the landslide inventory map with each factor map, the statistical relationship can be measured, and assessed whether these are significant for the analyzed factors in relation to the occurrence of landslides (Bonham-Carter, 1994; Neuhäuser and Terhorst, 2007). In this method, positive and negative weights (W_i^+ and W_i^-) are assigned to each of the different classes into which a factor map is classified, as presented in Equation (4.1 and 4.2) from van Westen et al. (2003).

$$W_i^+ = log_e \frac{P\{B_i|S\}}{P\{B_i|\bar{S}\}} \qquad (4.1)$$

$$W_i^- = log_e \frac{P\{\bar{B}_i|S\}}{P\{\bar{B}_i|\bar{S}\}} \quad (4.2)$$

where B_i and $\bar{B}_i$ represent the presence and absence of a landslide casual factor i, S and $\bar{S}$ are the presence and absence of landslides. W_i^+ indicates the importance of the presence of a factor for landslide occurrence, while W_i^- reflects the importance of the absence of a factor for landslide occurrence. A factor is evaluated to be positively correlated with landside occurrence when $W_i^+>0$ and $W_i^-<0$, and negatively correlated when $W_i^+<0$ and $W_i^->0$. The weight contrast ($C=W_i^+-W_i^-$) reflects the overall spatial association between the casual factor and landslide occurrence. If C is positive, the factor is favourable for landslide occurrence, and vice versa. If C is close to zero, this indicates that the factor is uncorrelated to the landslides. For the ease of the automatic calculation, we use ILWIS (2009, ITC) script files created by van Westen (2002) to carry out the same set of operations for all the factor maps.

4.2.2 Data preparation

(1) Damming and Non-damming landslide inventory maps

Landslide and landslide dam inventories are the direct data for the WOE approach, which can be either point or polygon-based. In this study, we used the polygon-based landslide inventory created by Dai et al. (2011), including around 56,000 landslides which are referred to as the "non-damming landslides", and the landslide dam inventory as presented in Chapter 3 (Fan et al., 2012a), including around 800 polygons, referred to as the "damming landslides". Notably, the landslide deposit areas should not be considered in the analysis, as only source areas are of interest in landslide occurrence. Taking the slope factor as an example, if the deposit areas are involved, landslides might be found occurring on very gentle slopes. Whereas the damming landslide dataset differentiated between scarp and deposit areas, the non-damming landslide dataset did not, and mapped the landslides as single polygons. To avoid such kind of biased results, we took the upper 30% with the highest elevation within the undifferentiated landslide polygons and assumed that these were representing the landslide initiation areas. Mapping the initiation areas manually for 56,000 landslides was not possible. The damming and non-damming landslide initiation polygons were converted into pixel-based raster map with a grid size of 25 m for further analysis.

(2) Seismic factors

For earthquake-induced landslides, the commonly used triggering factors are: distance to fault surface rupture, peak ground acceleration (PGA) and seismic intensity. The distance-to-fault map was made by the distance calculation function in ArcGIS, and was classified in 5-km wide intervals (Fig.4.1A). The PGA map was obtained from the US Geological Survey (2008), and is based on an unknown number of records of accelerometers, with interpolation of estimated amplitudes where data are lacking (Fig.4.1B). This map is rough and also contains some flaws (i.e. the strange islands with low PGA values) that are probably caused by a wrong interpolation. It also does not include site amplification effect. However, there is no better map available. The PGA factor is highly correlated to the distance-to-fault factor. Therefore, we will focus mainly on distance-to-fault.

(3) Geo-environment factors

The geo-environment factors used in this study are: lithology, topographic factors (slope, internal relief, terrain roughness, aspect and curvature) and hydrological factors (distance to rivers, drainage density and mean basin stream power index). Among them, lithology and aspect are categorical factors, and the rests are continuous factors that were classified into classes before overlaying with landslide data.

The lithology is obtained from a digital geological map that was compiled from ten 1:200,000 scale standard geological map sheets (Fig. 2.2). Based on the lithological similarities, we grouped the lithology into 21 rock types (Appendix 2). The data was converted to raster with a 25 m resolution. Unfortunately, the geological structure information is limited to only a few large landslides and not sufficient to be spatialized over such a large area. Thus it was not considered in this analysis.

We prepared raster maps of topographic factors from the 25-m DEM using inbuilt algorithms in ArcGIS and SAGA (Fig.4.1C-F). The continuous data were converted into different categories based on the frequency distribution of different topographic values in landslide covering area and for the entire area. The internal relief is defined as the elevation difference between any point on slopes and the nearest stream. Terrain roughness was defined as the standard deviation of elevations within a certain distance (Wilson and Gallant, 2000; Lee et al., 2008), which was calculated in this case using a radius of 3 pixels. The reader is referred to Ayalew and Yamagishi (2005) and García-Rodríguez et al. (2008) for detailed description of above factors. Terrain roughness is correlated to the slope factor.

Hydrological factors also play important roles in controlling landslide and especially landslide dam occurrence (Fig.4.1G-I). The stream network was generated from the 25-m DEM with the upslope contributing area of 10 km^2 as a threshold (which was also used by Korup (2004)). We divided the study area into different sub-catchments using ArcHydro toolbox. We then calculate drainage density and stream power index for each sub-catchment. See Chapter 2 (Section 2.3) for the calculation method.

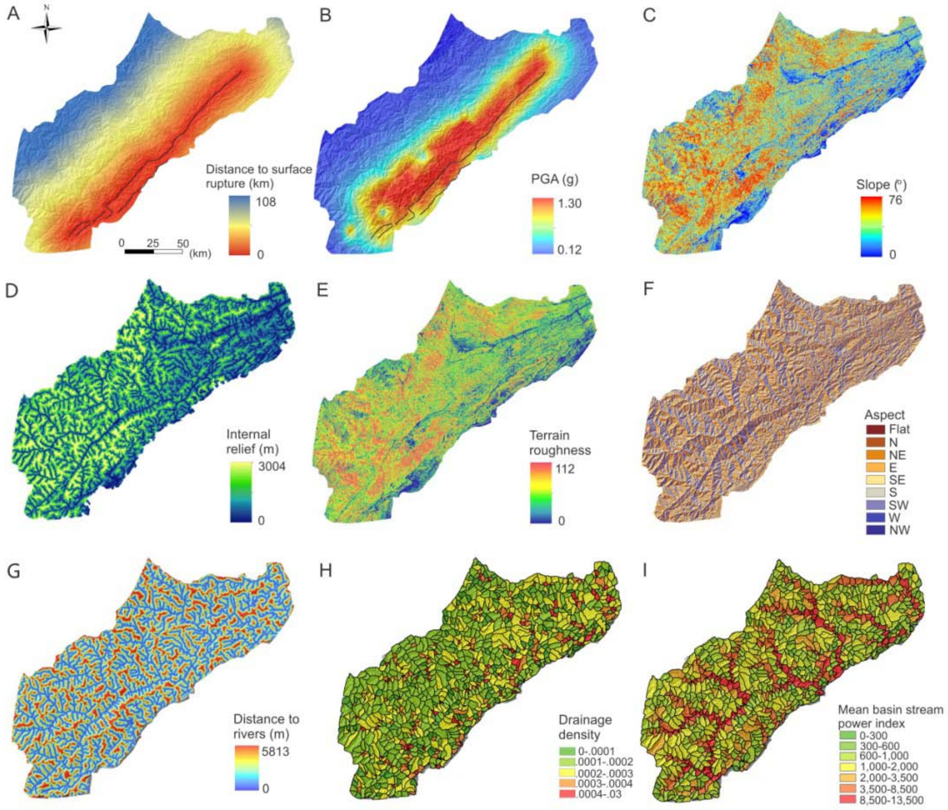

Figure 4.1 Factor maps used in the WOE analysis. A and B are seismic factors (the black lines represent for the fault surface ruptures); C-F are topographic factors (terrain roughness and stream power index are dimensionless); G-I are hydrological factors.

4.3 Results and Discussion

4.3.1 Analysis of the distribution of landslides and landslide dams

The distribution of damming and non-damming landsides is investigated by analyzing their area-density variation with above seismic and geo-environmental factors. The area density is defined as the percentage of landslide area within each class of different factors (Keefer, 2000 and Dai et al., 2011).

(1) Seismic factors

The speciality of the seismogenic fault of the Wenchuan earthquake is that it has both a thrust and a dextral strike-slip component. This characteristic and the hanging/foot wall effect of the fault are assumed to play an important role in controlling landslide occurrence as discussed in Chapter 3, which is also shown in previous studies, Huang and Li (2009) and Gorum et al. (2011). In order to see the effect of fault type and hanging/foot-wall difference, we combined them with the distance-to-fault factor.

Fig. 4.2A and B show the variation of non-damming landslide-area density (NLAD) and damming landslide-area density (DLAD) with the distance to both the thrust-dominated and strike-slip-dominated fault segment. It can be seen that both NLAD and DLAD along the thrust-dominated fault segment are higher than those along the strike-slip segment. In the thrust section, the non-damming and damming landslides were distributed in a much wider region, compared to the strike-slip section; while along the strike-slip segment, the NLAD and DLAD values decrease rapidly within a 0-20 km and 0-10 km narrow band, respectively. A clear anomaly of the non-damming and damming curves is found at a distance of 25-30 km, corresponding to the Wenchuan-Maowen fault located along the Min river. This is an active fault, but it was not ruptured during the Wenchuan earthquake. However, landslides and landslide dams (mainly the partially damming ones) are densely distributed along this fault, due to the long-term tectonic activity and strong river incision. Fig. 4.2C and D show the hanging-wall and footwall effect on the landslide occurrence. Both the NLAD and DLAD are much higher in the hanging-wall of the fault than in the footwall. No damming landslides occurred where the distance exceeds 45 km in the hanging wall and 15 km in the footwall. The results presented in Fig. 4.2 demonstrate that the fault type and hanging-wall/footwall are critical in controlling landslide occurrence. Some studies (i.e. Dai et al., 2011 and Gorum et al., 2011) considered the distance to epicenter as a factor and found it has little influence on the landslide concentration. The correlations of NLAD and DLAD values with PGA are presented in Fig. 4.3A, showing the relative high values when the PGA is above 0.8 g.

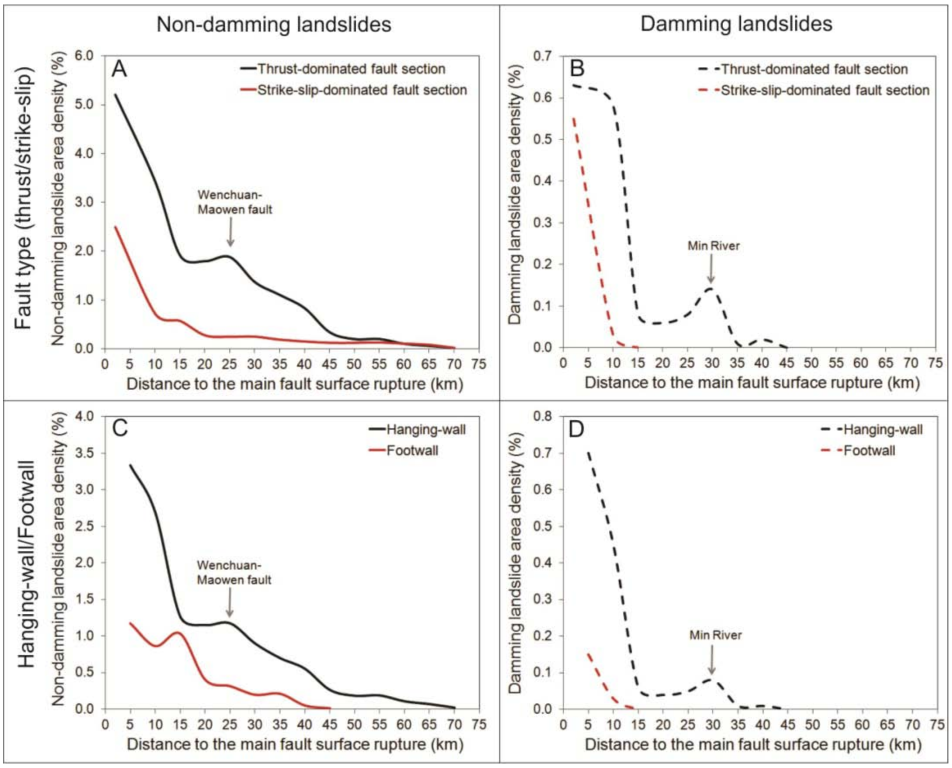

Figure 4.2 Variation of non-damming and damming landslide area density with distance to fault surface rupture: (A) along the thrust-dominated fault segment; (B) along strike-slip-dominated fault segment; (C) on the hanging-wall; and (D) on the footwall

(2) Geo-environment factors

Fig.4.3 and Fig. 4.4 present some examples of the spatial association of topographic factors with the non-damming and damming landslide concentration. Both NLAD and DLAD values increase significantly when the slope angle exceeds 40^{o} (Fig. 4.3B), most likely due to the topographic amplification of seismic waves (Ashford et al., 1997). Regarding the internal relief, the concentration of non-damming and damming landslides has different trends (Fig. 4.3C). Most of the damming landslides are present on slopes relatively close to the rivers and therefore have a relatively lower internal relief than the non-damming landslides. Almost no damming landslides occurred at slopes with an internal relief above 2000 m, while non-damming landslides were most abundant in zones with internal relief between 1500 m to 2800 m. Considering the distance to rivers, it is not surprising that the damming landslides are more frequent in the vicinity of rivers, showing much lower DLAD than the NLAD values when the distance to rivers exceeds 1000 m (Fig. 4.3D). Both the DLAD and NLAD present very low values on the areas directly adjacent to the rivers. This is partly due to the fact that these might be floodplain areas, but also to the fact that landslides need to have a certain dimension in order to be able to block the river, and therefore start to have the highest density at some distance from the stream lines. With respect to the aspect, Fig.4.4 demonstrates that the east- and southeast-facing slopes have higher NLAD values than other directions. The DLAD values also reach peak on the east-facing slopes. This might be explained by the stronger amplification of seismic waves on the slopes facing away from the wave propagating direction (Gelebi et al., 1988).

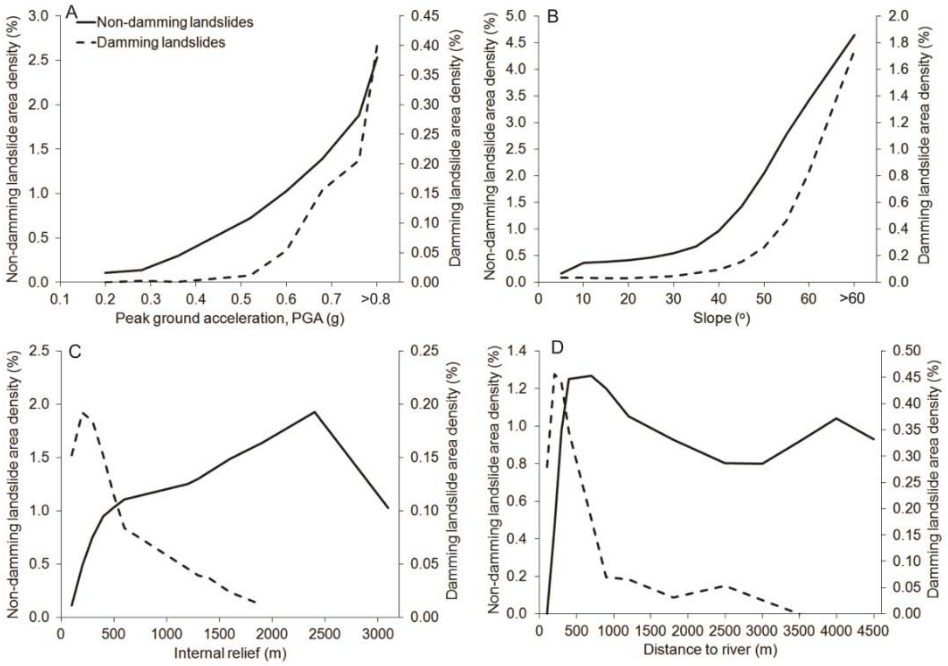

Figure 4.3 Variation of non-damming and damming landslide area density with (A) PGA (g); (B) slope (^{o}); (C) internal relief (m); and (D) distance to rivers (m)

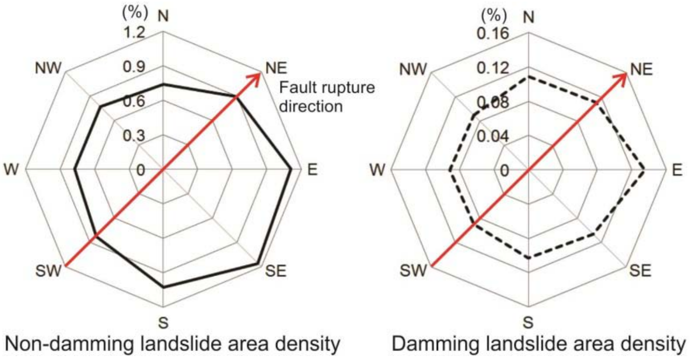

Figure 4.4 Variation of non-damming and damming landslide area density with aspect. The red arrow represents the Yingxiu-Beichuan fault rupture direction.

Lithology is widely recognized as a controlling factor to landslide occurrence. The non-damming and damming landslides occurred in various rock types varying from Pre-Sinian rocks to Quaternary unconsolidated deposits. The slopes composed by Pre-Sinian schists and andesites have the highest NLAD and DLAD, followed by Cambrian sandstones and siltstones intercalated with slate, granitic rocks and Permian limestone and shale (Fig. 4.5). Field investigation also revealed that the Pre-Sinian schists are very weak and fractured, producing a large amount of landslides. The sandstone and siltstone intercalated with shale of the Cambrian age largely affects the integrity and strength of the slopes, resulting in a high density of landslides and landslide dams. The densely jointed Granitic rocks are distributed mainly in the Pengguan massif in the hanging-wall of the Yingxiu-Beichuan fault, which produced many rock avalanche. Limestone and limestone intercalated with shale are generally well stratified and densely jointed, generating both deep-seated rockslides on cataclinal slopes and shallow rockslides or rock falls on anaclinal slopes. Large rock avalanches were mostly observed in the intensely cracked granitic rock masses as well as sandstones and siltstones.

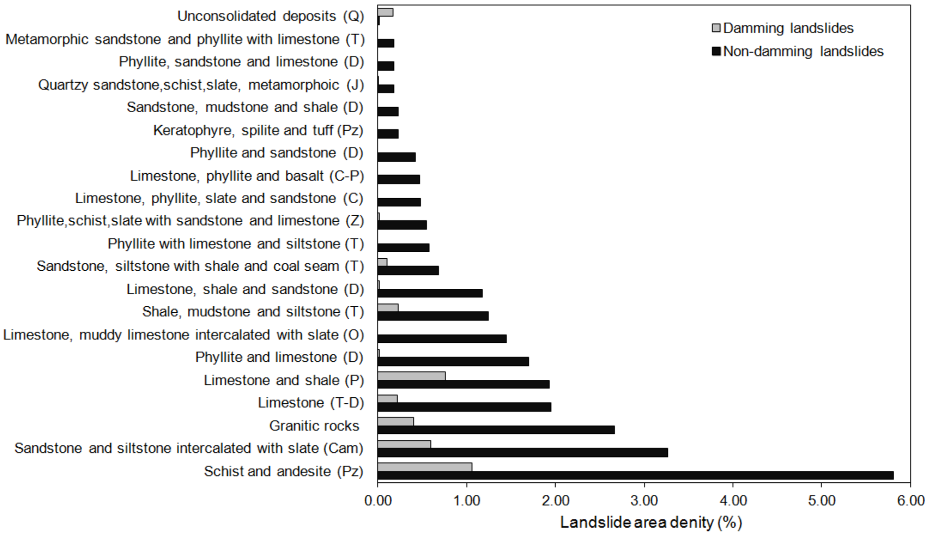

Figure 4.5 Variation of non-damming and damming landslide area density with lithology. Age: Q – Quaternary; J – Jurassic; T – Triassic; P – Permian; C-P – Carboniferous through Permian; C – Carboniferous; D – Devonian; O – Ordovician; Cam – Cambrian; Z – Sinian; Pz – Pre-Sinian

4.3.2 Weighting of factors

Following the method presented in the subsection 4.2.1, we calculated the weights of each class of different factors for both the non-damming and damming landslides, as shown in Appendix 2 and Fig. 4.6. The resulting weight contrast (C) directly indicates the relevance of each class to landslide occurrence, and therefore helps to choose the most relevant factor classes for landslide susceptibility assessment.

(1) Weighting of individual factors

For the seismic factors, distance to fault surface rupture has pronounced weights for both the non-damming and damming landslides, showing positive values within 10 km to the rupture and high negative values with the increase of distance (Fig. 4.6A). PGA is also found to strongly associate to landslide occurrence, indicating that low PGA values have negative effect on landslide occurrence. The fault type and hanging/footwall effect are proved to be important predictors. Thrusting fault and hanging-wall side favour landslide occurrence (Appendix 2).

Concerning the topographic factors, slope, internal relief and terrain roughness have higher positive and negative weight contrast values than aspect and curvature (Fig. 4.6 and Appendix 2). The reason is that aspect and curvature are indirect factors, which may become more effective by being combined with other factors, i.e. aspect with geological structure and curvature with PGA (considering the topographic amplification effect). Steep slopes (>40°) with higher terrain roughness are positively related to both the non-damming and damming landslide occurrence (Fig. 4.6B). The internal relief affects the non-damming and damming landslide occurrence in an opposite way. High internal relief is favourable for the non-damming landslide occurrence, but unfavourable for the damming ones (Fig. 4.6C). For the non-damming landslides, the east, southeast and south facing directions have positive effects, while the east-facing direction is most effective for the damming landslides. The negative and positive curvature values represent concave and convex, respectively. Convex slopes favour the non-damming landslide occurrence. Curvature is not a good indicator for damming landslides, as its weight contrast values are close to zero (Appendix 2).

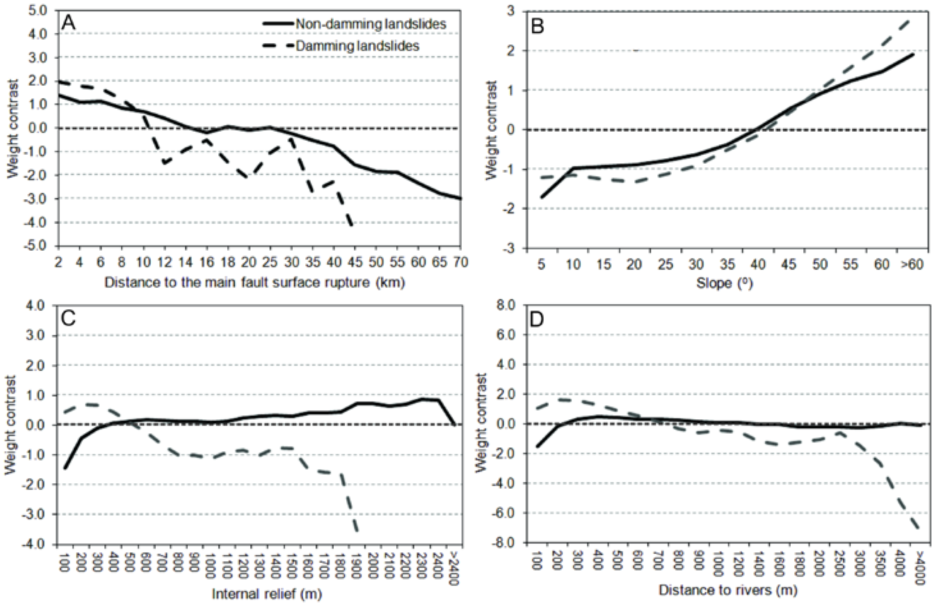

Figure. 4.6 Weight contrast of non-damming and damming landslides for: (A) distance to the main fault surface rupture; (B) Slope; (C) Internal relief; and (D) Distance to rivers

For the hydrological factors, distance to rivers obviously plays a significant role in landslide dam formation (Fig. 4.6D). The weight contrast is positive within 700 m to rivers, while it is negative within 200 m to rivers for the non-damming landslides. The mean basin stream power index and drainage density are less effective than distance-to-river factor (Appendix 2). The mean basin stream power index indicates the stream erosion or incision, and therefore is more related to dam stability rather than dam formation.

(2) Weighting of refined factors

Some factors may become more meaningful when they are combined with other relevant factors, for example, distance-to-fault with fault type, hanging-wall/footwall and lithology. Such kind of combination can also remove the overruling of the distance-to-fault factor on other factors, as it is only relevant to compare the different classes of these factors for the same distance band from the fault. Fig. 4.7 shows that the thrust-dominated fault section generally has larger weight contrast than the strike-slip-dominated part for both the damming and non-damming landslides. Hanging-wall also has higher weight contrast than footwall. That is why we observed much higher landslide and landslide dam density on the hanging wall of the thrusting component of the Yingxiu-Beichuan fault as introduced in Chapter 3. The weight contrast of damming landslides shows maximum negative value where the distance to fault exceeds 15 km in the footwall.

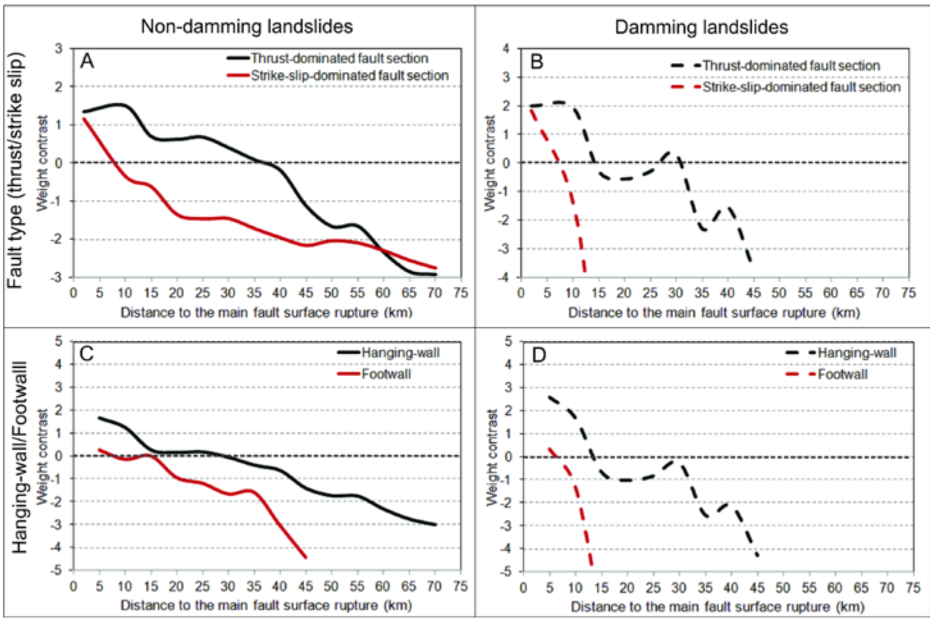

Figure 4.7 Weight contrast of non-damming and damming landslides: (A) and (B) for thrust-dominated fault section strike-slip dominated fault section; (C) and (D) for hanging-wall and footwall.

We compared the weight contrast of different lithologies in the same distance-to-fault zone in Appendix 2. From 0-45 km band, the most effective lithologies that favour non-damming landslide occurrence are the Pre-Sinian schists and andesites, Cambrian sandstones and siltstones intercalated with slate and granitic rocks. For the damming landslides in 0-10 km band, the most effective lithologies are schists and andesites, the Permian limestones and shales and granitic rocks. The most unfavourable lithologies for non-damming landslide occurrence are the unconsolidated deposits (alluvial gravel and clay) and the Devonian phyllites and limestones, while those for damming landslides are the Devonian sandstones, mudstones and shales as well as phyllites and limestones. These results are consistent with the density analysis in Fig. 4.5.

4.3.3 Ranking for factors

The WOE method provides weights for each class of different factors. However, it does not directly show the relative importance of every factor. Therefore, we derived a factor rate to rank the factors, following the method from Ghosh et al. (2011):

$$R = |C_{max} - C_{min}| / |C_{max} - C_{min}|_{\min} \tag{4.3}$$

where C is the weight contrast of classes of a factor. For each factor, the absolute difference between the maximum and minimum C values is calculated, which is then divided by the lowest absolute difference of all factors (0.47 for the non-damming landslides and 0.22 for the damming landslides in Table 4.1).

As the rate of factors is a relative value, it only reflects the relative contribution of different individual factors within each type (non-damming and damming). The result in Table 4.1 indicates that the distance to fault surface rupture, PGA and lithology are the most significant predictors for both the non-damming and damming landslides. Different from the non-damming landslides, the hydrological factors play more important roles than the topographic factors for the damming landslides.

Table 4.1 Rating of factors for the non-damming and damming landslides

Factor	Non-damming landslides				Damming landslides			
	Weight contrast (*C*)			Rate	Weight contrast (*C*)			Rate
	Max	Min	Max-Min	(*R*)	Max	Min	Max-Min	(*R*)
Distance to fault surface rupture	-2.76	1.38	4.14	9	-7.91	1.95	9.86	44
Peak ground acceleration (PGA)	-2.42	1.49	3.91	8	-8.92	1.9	10.82	49
Lithology	-1.86	2.01	3.87	8	-7.77	2.39	10.16	46
Terrain roughness	-1.45	1.67	3.12	7	-1.8	2.49	4.29	19
Slope	-0.97	1.9	2.87	6	-1.31	2.86	4.17	19
Fault type (thrusting/strike-slip)	-1.1	1.1	2.2	5	-1.13	1.13	2.26	10
Internal relief	-1.44	0.87	2.31	5	-3.54	0.71	4.26	19
Distance to rivers	-1.49	0.47	1.96	4	-7.27	1.62	8.89	40
Mean basin stream power index	-0.74	1.1	1.84	4	-3.28	1.61	4.89	22
Curvature	-0.74	0.66	1.4	3	-0.1	0.19	0.29	1
Hanging/foot wall effect	-0.53	0.53	1.06	2	-1.23	1.23	2.46	11
Drainage density	-0.38	0.48	0.86	2	-2.13	1.46	3.59	16
Aspect	-0.21	0.26	**0.47**	1	-0.17	0.05	**0.22**	1

4.4 Discussion and Conclusions

Some previous studies indicated that selecting and weighting of possible factors before assessing landslide susceptibility or hazard are useful for improving the assessment results (i.e. Ayalew and Yamagishi, 2005; Blahut et al., 2010; Ghosh et al., 2011). There are several ways to weight factors qualitatively or quantitatively: (1) heuristic evaluation based on expert knowledge, which is too subjective to be reliable in some cases; (2) calculating landslide frequency or density for each possible factor, which is simple but can still provide first-hand information; (3) quantifying the weight of factors by the weights of evidence method (WOE); (4) quantifying the spatial association between landslides and factors using the Yule's coefficient (Yule, 1921 and Fleiss, 1991) and the distance distribution analysis (Berman, 1977 and 1986), which is not commonly used in landslide research (Ghosh et al., 2011); and the multi-variate analysis.

In this study, we first analyzed and compared the variation of non-damming and damming landslide-area density with commonly used factors. This contributes to a better understanding of their spatial distribution pattern and related controlling factors. We then quantified the weight of factors by the WOE method, which is a bi-variate statistical technique and often used as a selection procedure for multivariate statistical analysis. It is worth mentioning that the independence of the factors should be tested before using them in susceptibility models. A problem of the WOE method as mentioned by Regmi et al. (2010) is that the weight of a class might be very low when only few landslide pixels are present in this class. In this case, it is better to assign a zero weighted value to this class or combine it with other classes. The method might also provide biased weights due to the lack of a standard classification criterion of the factor classes. Nevertheless, the weight can still represent relative importance of the separate factors in general.

The results of this study demonstrate that distance to fault surface rupture, PGA and lithology play dominating roles in non-damming and damming landslide occurrence. Not surprisingly, the hydrological factors have stronger influence on damming landslides than the non-damming ones. The fault type and hanging/foot wall effect were ignored in previous studies, but were found important for coseismic landslides. The WOE method is a useful and fundamental step for selection and weighting of predictors of multivariate landslide susceptibility models.

5

Empirical Prediction of Coseismic Landslide Dam Formation at Regional Scale

This chapter is based on:

Xuanmei Fan, David G. Rossiter, Cees J. van Westen, Qiang Xu, Tolga Gorum. 2013. Empirical prediction of coseismic landslide dam formation. In: Earth Surface Processes and Landforms (moderate revision under review in *Earth Surface Processes and Landforms*).

Abstract

In this study we develop an empirical method to estimate the volume threshold for predicting coseismic landslide dam formation using landscape parameters obtained from DEMs. We hypothesize that the potential runout and volume of landslides, together with river features, determine the likelihood of the formation of a landslide dam. To develop this method, a data base was created by randomly selecting 140 damming and 200 non-damming landslides from 501 landslide dams and >60 000 landslides induced by the Mw 7.9 2008 Wenchuan earthquake in China. We used this data base to parameterise empirical runout models by stepwise multivariate regression. We find that factors controlling landslide runout are landslide initiation volume, landslide type, internal relief (H) and the H/L ratio (between H and landslide horizontal distance to river, L). In order to obtain a first volume threshold for a landslide to reach a river, the runout regression equations were converted into inverse volume equations by taking the runout to be the distance to river. A second volume threshold above which a landslide is predicted to block a river was determined by the correlation between river width and landslide volume of the known damming landslides. The larger of these two thresholds is taken as the final damming threshold. This method was applied to several landslide types over a fine geographic grid of assumed initiation points in a selected catchment. The overall prediction accuracy was 97.2% and 86.0% for non-damming and damming landslides, respectively. The model was further tested by predicting the damming landslides over the whole region, with promising results. We conclude that our method is robust and reliable for the Wenchuan event. In combination with pre-event landslide susceptibility and frequency-size assessments, it can be used to predict likely damming locations of future coseismic landslides, thereby helping to plan emergency response.

5.1 Introduction

Landslide dams are common worldwide, especially in tectonically-active mountain regions, which are defined as the permanent or ephemeral interruption of a river course by landslide deposits (Costa and Schuster, 1988; Hermanns et al., 2011). They pose serious threats to people and property due to upstream inundation and downstream dam-breach flooding (Korup, 2002; Evans et al., 2011). Many catastrophic dam-breach outburst floods have been documented (Mason, 1929; Cenderelli, 2000; O'Connor and Costa, 2004; Dai et al., 2005). Strong earthquakes are among the prime triggering factors of landslide dams (Adams, 1981; Pearce and Watson, 1986). Even a single triggering event can cause the formation of hundreds of landslide-dammed lakes (e.g. 1783, Calabria, Italy; Cotecchia and Melidoro, 1974). The 2008 Wenchuan earthquake (China) highlighted the importance of assessing and mitigating the hazards from coseismic and post-seismic landslide dams. It induced a large number of landslide dams that fully blocked rivers (>500, Fan et al., 2012a), of which 32 were breached artificially in order to reduce the hazard of catastrophic dam-breach floods (Xu et al. 2009). The largest landslide-dammed lake (estimated volume 3×10^8 m^3) was formed by the Tangjiashan landslide dam. Before being breached it posed a serious threat to 2.5 million people downstream, especially in the city of Mianyang, located 85 km downstream (Liu et al., 2009, Fan et al., 2012b). In the context of the Wenchuan earthquake induced landslides (this study), we restrict our attention to landslide dams which completely blocked a river and lead to the formation of dammed lakes.

The longevity of landslide dams is defined as the time that landslide-dammed lake remains. It varies widely, from minutes to several thousand years, but most (>60%) of them fail within one month of formation (Ermini and Casagli, 2003). Longevity is a function of dam geometry, internal structure, material properties, lake volume, inflow rate, and seepage. About one-quarter of the dams induced by the Wenchuan earthquake failed within one week and 60% within one month after the earthquake (Fan et al., 2012c), leading to a large additional post-earthquake hazard. This time frame is too short for a comprehensive regional inventory, especially during the immediate post-earthquake disaster response phase. Therefore it would be desirable to make a pre-earthquake prediction of coseismic landslide dam formation at regional scale, for different earthquake scenarios. Such predictions could contribute to coseismic landslide hazard prevention, mitigation and emergency response, including contingency planning for dam breaching. Three sources of information are needed for these predictions: (1) landslide susceptibility assessment; (2) size-frequency relations; and (3) volume thresholds for a landslide to reach and block a river. In this paper we concentrate on the latter.

To predict coseismic landslide dam formation the following steps are required: (1) assessing the spatial probability of coseismic landslide occurrence; (2) estimating landslide runout distance; and (3) predicting whether a landslide which reaches a river channel will have sufficient volume to dam it, considering the river characteristics. Several methods, both qualitative and quantitative, have been developed for landslide susceptibility assessment (Jibson et al., 2000; Guzzetti et al., 2005, Corominas and Moya, 2008; Lee et al., 2008; Owen et al., 2008; van Westen et al., 2008); by contrast few previous studies have computed volume thresholds above which a landslide is expected to dam a river course (Swanson et al, 1986; Korup, 2005) and none have related landslide volume to river features. Therefore in this study we focus on (2) and (3).

The estimation of potential landslide size is essential to predict the possibility of river blockage. The most commonly-used approach at regional scale is analyzing landslide size-frequency statistics by fitting the area or volume of past landslide events from historical inventories to various distributions, e.g. inverse power-law (Guzzetti et al., 2002, Brunetti, et al., 2009), double Pareto (Stark and Hovius, 2001), or inverse gamma (Malamud et al., 2004); see van den Eeckhaut et al. (2007) for a review. This empirical-statistical approach provides the expected probability of landslide size, based on the assumption that the past is the key to the future, under which the statistics of landslide size will not change in the future under the same circumstances. This assumption is, however, controversial because both the triggering and slope conditions that favor slope failures in the past may no longer exist or may have changed due to, e.g., climate or land-use change (Corominas and Moya, 2008). Despite this, size-frequency analysis is a widely-applied method as currently there is no better solution. Furthermore, an earthquake may trigger landslides with varying size-frequency distributions, depending on magnitude, fault type, and other seismic, geological and topographic factors (Gorum et al., 2011; Huang and Fan, 2013).

Landslide runout is also a key factor determining the likelihood of landslide dam formation. Runout prediction methods can be classified into: (a) empirical models using observational data correlations (Heim, 1932; Scheidegger, 1973; Hsü, 1975; Corominas, 1996; Rickenmann, 1999; Tang et al., 2012a), see Legros (2002) for a review; (b) analytical and numerical models (Hutchinson, 1986; Savage and Hutter, 1989; Hungr, 1995; Iverson, 1997; McDougall and Hungr, 2004; Van Asch et al., 2004; Quan Luna et al., 2011); and (c) GIS-based empirical models, e.g. the CONEFALL and Flow-R methods for rock fall and debris flow runout simulation, respectively (Jaboyedoff and Labiouse, 2003 and 2011; Horton and Jaboyedoff, 2008). The analytical and numerical models can provide accurate runout predictions as well as additional information, such as velocity and affected area. However, they require input parameters that are difficult to obtain, extensive calibration, and are computationally intensive.

In this study we developed an empirical-statistical method to estimate the volume threshold for landslide dam formation at regional scale using landscape parameters and river features that can be obtained from digital elevation models. We developed and tested the approach using an extensive dataset from an exceptional event, the 2008 Wenchuan earthquake. We evaluated the robustness and reliability of the model by its performance in predicting dam formations in a selected catchment with abundant damming and non-damming landslides triggered by the Wenchuan event. To further test the applicability of the model, it was applied to predict the landslide dams in the whole earthquake-hit region.

5.2 Data and Methods

5.2.1 Dataset

To develop the empirical runout and volume regression models, a combined dataset of 140 completely damming and 200 non-damming landslides were randomly selected from the Wenchuan earthquake-induced landslide dam inventory (Fan et al., 2012a) and landslide inventory (Dai et al., 2011; Görüm et al., 2011) respectively; see Figure 5.1 for their spatial distribution. The sample size was determined by considering the degree of detail of the landslide and landslide dam mapping (i.e., whether the initiation, deposition and transportation zones were distinguished). In addition, the samples were widely distributed over the study area. A pre-earthquake DEM with 25-m grid spacing and a digitized geological map (1:250 000) were also available for the study area. The DEM was produced from 1:50 000 scale digital topographic maps by interpolating contour lines at intervals of 10 m and 20 m for low- and high-relief terrain, respectively. Table 5.1 lists the variables in the datasets and methods used for deriving them. The univariate distributions of the continuous variables were all strongly right-skewed, as expected, so they were log-transformed for subsequent analysis.

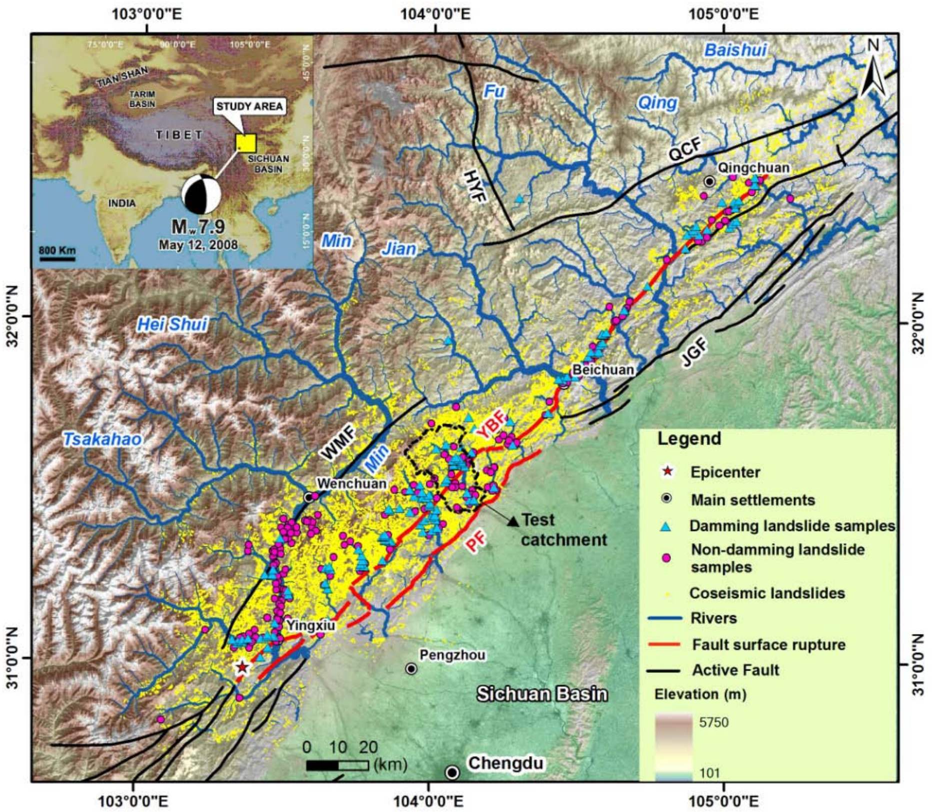

Figure 5.1 Study area (inset shows location). WMF: Wenchuan-Maowen fault; YBF: Yingxiu-Beichuan fault; PF: Pengguan fault; JGF: Jiangyou-Guanxian fault; QCF: Qingchuan fault; HYF: Huya fault; MJF: Minjiang fault (after Xu X. et al., 2009).

The most reliable way to calculate landslide volume is to determine the elevation difference between pre- and post- earthquake DEMs over 2D projection of the landslide and integrate over this area, but unfortunately a post-earthquake DEM was not available. Therefore we estimated landslide volume from empirical scaling relationships between landslide area and volume (Guzzetti et al., 2009; Larsen et al., 2010; Korup et al., 2012).

We selected the best-fit volume-area (V-A) relationship for a global dataset from Larsen et al. (2010), because it was obtained from more than 4 000 landslides and also took landslide material (soil or bedrock) into account. There is no such relationship specifically for the coseismic landslides. The chosen relation is.

$$V = \alpha A^{\gamma}, \tag{5.1}$$

where α is a dimensional coefficient (0.146), γ is a scaling exponent (1.332), V is the landslide volume (m^3) and A is the landslide area (m^2). In a previous study (Fan et al., 2012c), we varied the α and γ values in order to quantify the uncertainties using a Monte Carlo approach. However, our aim here is to use volume as one of the predictors in the statistical models, therefore, single values of α and γ are used.

Table 5.1 List of variables in the datasets

Attributes	Definition	Deriving methods
Landslide area, A (m^2)	Planform area of landslide initiation (scar) and deposit	Landslide (dam) polygons mapped from post-earthquake satellite images (Fan et al., 2012a)
Landslide volume, V (m^3)	Estimated landslide initiation volume	Empirical scaling relationship between landslide area and volume (Larsen et al., 2010)
Landslide runout, R (m)	Runout distance of landslide	Measured on satellite images and aerial photos
Internal Relief, H (m)	Elevation difference between landslide initiation point and the main river	Derived from landslide profiles obtained from the 25-m DEM in GIS environment
Distance to river, L (m)	Horizontal distance from landslide initiation to the main river	Calculated by distance from point to polyline (river network) function in GIS environment
H/L ratio	Ratio of H versus L	Calculated from H and L
Distance to fault, Ds (m)	Distance from landslide initiation to fault surface rupture	Calculated by distance from point to polyline (fault line) function in GIS environment
Landslide type	Modified classifications of Cruden and Varnes (1996)	Interpretation based on satellite images and aerial photos, assisted by field checks in accessible areas (Fan et al., 2012a)
Lithology	Rock type and features	Digitized geological map (1:250,000)

Landslides were grouped into four classes based on the classification of Cruden and Varnes (1996): rock/debris avalanche, debris flow, rock fall and rock/debris slide. Figure. 5.2 shows the landslide initiation volume, runout and H/L ratio variations by landslide types for both the damming and non-damming landslides. These characteristics of damming landslides are all larger than those of the non-damming ones. Debris/rock avalanches have a slightly larger volume than other types in both damming and non-damming cases. Runout and H/L ratio are more variable than landslide volume. Debris/rock avalanches and debris flows generally have longer runouts but smaller H/L ratios than rock falls and rock/debris slides.

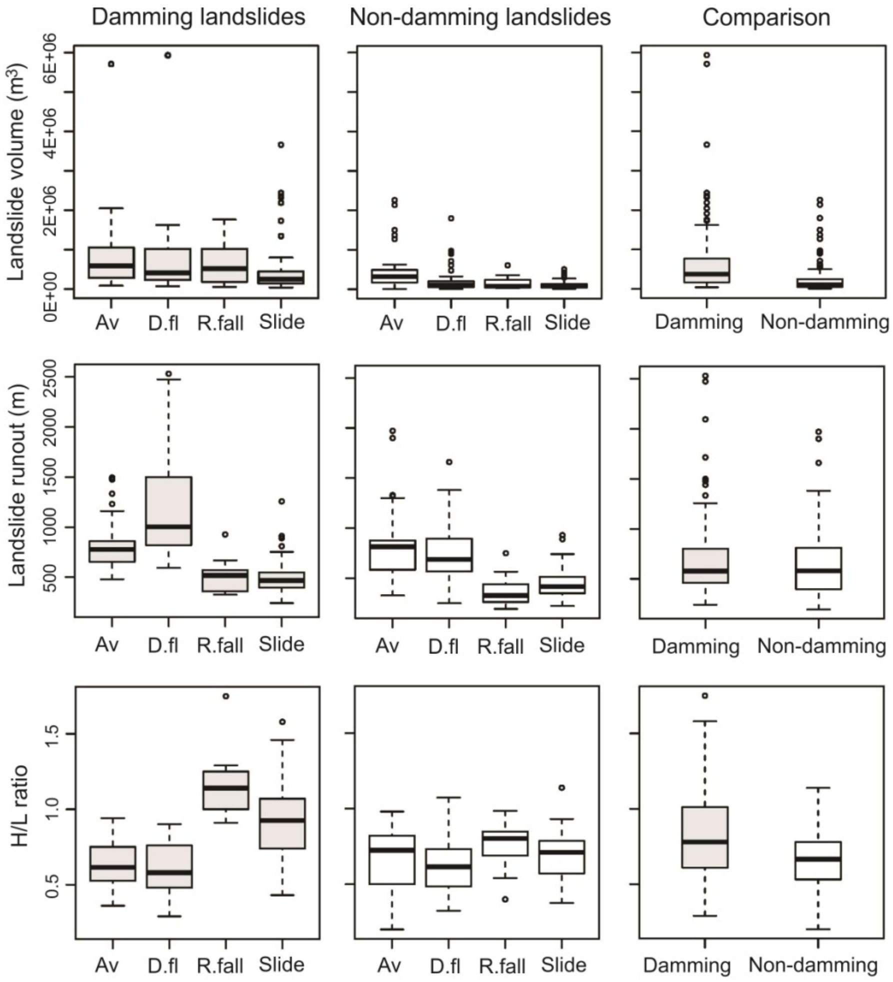

Figure 5.2 Boxplot showing landslide volume, runout and internal relief (H) to horizontal distance between landslide initiation and river (L) ratio variations with different landslide types: A-C: damming landslides; D-F: non-damming landslides; G-I: comparison between damming and non-damming landslides. Av: debris/rock avalanche; D.fl: debris flow; R.fall: rock fall; Slide: debris/rock slide. The horizontal line defines the median, and the box defines the upper and lower quartiles (75% and 25% respectively). The whiskers delineate 5th and 95th percentiles and the circles are the outliners.

5.2.2 Methods

Instead of analytical and numerical modeling, we chose an empirical-statistical method as it has the following advantages: (a) it fits well with the regional scale, at which site-specific information is limited for such a large area; (b) it benefits from the large dataset for model calibration and evaluation; (c) it is relatively easy to develop and apply; (d) the coefficients are interpretable in terms of presumed processes. A disadvantage of this method is that empirical relations should not be used for extrapolation outside the range of the original calibration dataset; thus although the method could be used elsewhere, the regression models must be recalibrated. To predict landslide runout, many previous studies use the empirical relation between landslide volume and the tangent of the reach angle (defined as the ratio between the vertical drop and the horizontal travel distance, similar to our H/L ratio) (Heim, 1932; Scheidegger, 1973; Hsü, 1975). However, Corominas (1996) concluded that reach angle is dependent not only on landslide volume, but also on other factors, such as landslide type and topographic constraints along the runout path. Therefore we fitted a stepwise multivariate regression model using all the possible predictors listed in Table 5.1 to obtain the best-fit landslide runout empirical prediction model and at the same time to explore which factors are statistically significant, as shown in the flowchart (Fig. 5.3A). For further analysis we assumed that volume is one of the controlling factors to determine landslide runout, and aimed to determine the required volume for a landslide to reach a river. To this end, we converted the runout model to an inverse volume model by taking the runout (R) to be the distance to river (L). The resultant uncertainty was analyzed by comparing the predicted volume with the observations, quantifying by the 90% confidence interval.

A stepwise linear multivariate regression was designed to find the most parsimonious linear combination of predictors which successfully match the observed values of the predictand, as expressed in Equation. (5.2).

$$y = b_0 + b_1x_1 + b_2x_2 + b_3x_3 + \ldots + b_nx_n \tag{5.2}$$

where y is the predictand ('dependent variable'), e.g. landslide runout, x_i (i=1,2,…n) are the predictors ('independent variables'), b_0 is the intercept, and b_i (i=1,2,…n) are the regression coefficient of x_i. Predictors were added to the regression equation one at a time until there was no improvement in parsimonious fit as determined by the adjusted R^2.

As shown in Fig. 5.3, the best-fit runout and corresponding inverse volume regression models were then implemented in a geographical information system (GIS) to predict landslide dam formation in a selected catchment as shown in Fig. 5.1 and Fig. 5.4. We first prepared the grid-based predictor maps, and then used them as input maps of the inverse volume model to compute the required volume for a landslide initiated in each grid cell to reach the closest main river. We named this the first volume threshold, V_{1i} (Fig. 5.3B), which is calculated using the raster-calculation function in ArcGIS (see Section 5.4). The river network and hydrological features (drainage area, channel gradient and river width) were extracted from the DEM following the method of Kirby et al. (2003) and Kirby and Ouimet (2011). We obtained a relationship between river width and landslide volume from the inventory of landslide dams induced by the Wenchuan earthquake in our previous work (Fan et al., 2012a). According to this relationship and the width of the river which could be potentially dammed by a landslide from the assumed initiation point, a second threshold (V_{2i}) for a landslide to have sufficient volume to dam that river was determined (see Section 5.4). The larger of the two thresholds was taken as the final required volume (V_{fi}) for a landslide initiated at a given grid cell to be able to both reach and dam the relevant river (Fig. 5.3B).

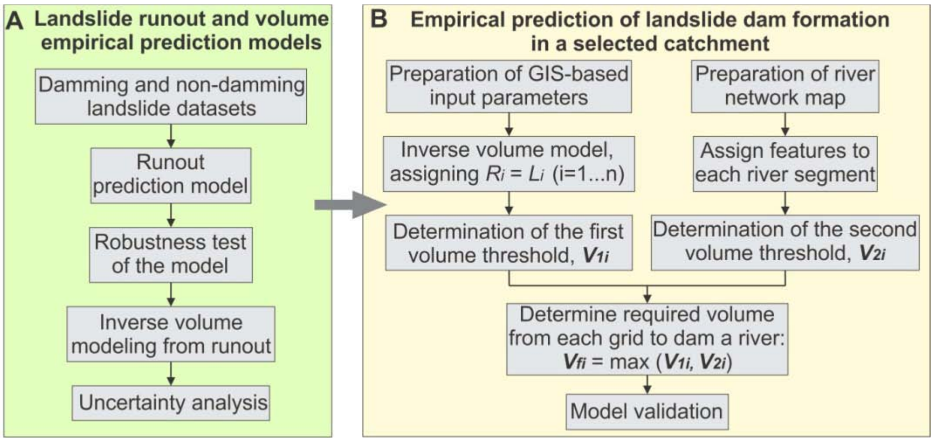

Figure 5.3 Flowchart for estimating the potential dam-formation landslides. L_i is the distance of the grid cell *i* to the closest main river.

A representative catchment with an area of about 400 km^2 was selected to evaluate the inverse volume models. This catchment is near the main fault (Yingxiu-Beichuan) and also contains abundant damming and non-damming landslides, including the second largest coseismic landslide (Qingping, Fig. 5.1), which impounded the second largest barrier lake

(Xiaojiaqiao) in the study area (Fig. 5.4). The binary prediction results (damming/non-damming) were compared with the actual damming and non-damming events in this catchment in order to evaluate the proposed method. We re-interpreted the non-damming landslides based on aerial photos in the catchment, as the previous inventory from (Dai et al., 2011) did not separate different zones of landslides (i.e. initiation, deposition and transportation), nor did it differentiate landslide type. In total, 2 743 non-damming landslides and 57 damming landslides were mapped as shown in Fig. 5.4. The landslide type pie charts show that debris/rock avalanches were most prone to dam rivers, as ten out of 48 of this type of slides formed dams.

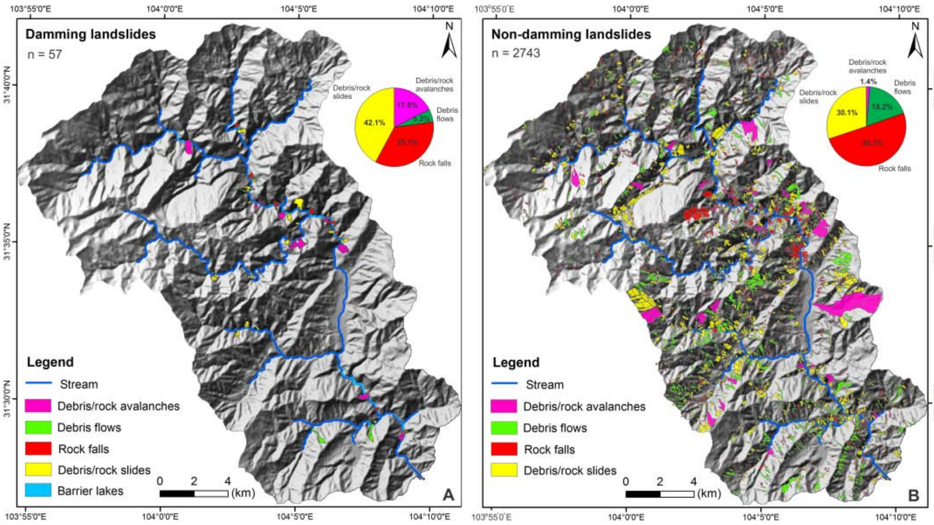

Figure 5.4 Mapping of (A) damming landslides and (B) non-damming landslides in a selected catchment in the study area as indicated in Fig.5.1

5.3 Results from the Statistical Analysis

5.3.1 Multivariate regression models of landslide runout

We first checked the correlation of possible predictors listed in Table 5.1, resulting in the correlation coefficients matrix shown in Table 5.2. Predictors with low correlation to others (absolute value of the correlation coefficient < 0.6, the same criteria used by Dong et al., 2009) were then used as variables in the stepwise multivariate regression analysis for both damming and non-damming landslides. Correlation between internal relief (H) and distance to river (L) is high, so only H is used in the regression model.

Table 5.2 Correlation coefficients of natural log-transformed continuous variables listed in Table 5.1

	Damming landslide dataset					Non-damming landslide dataset				
	ln(V)	*ln(H)*	*ln(L)*	*ln(H/L)*	*Ln(Ds)*	*ln(V)*	*ln(H)*	*ln(L)*	*ln(H/L)*	*Ln(Ds)*
Ln(V)	1.000	*0.593*	0.620	*-0.116*	*-0.058*	1.000	*0.581*	*0.576*	*-0.054*	*-0.027*
ln(H)	-	1.000	0.667	*0.290*	*0.306*	-	1.000	0.836	*0.185*	*0.081*
ln(L)	-	-	1.000	*-0.520*	*-0.067*	-	-	1.000	*-0.385*	*-0.105*
ln(H/L)	-	-	-	1.000	*0.438*	-	-	-	1.000	*0.323*
Ln(Ds)	-	-	-	-	1.000	-	-	-	-	1.000

Values in Italic show correlation coefficient < 0.6.

The best-fit runout regression equations for different types of damming and non-damming landslides are summarized in Table 5.3. Landslide initiation volume, internal relief (H), H/L ratio and landslide type proved to be significant statistical predictors of landslide runout. This result supports our hypothesis that landslide volume is a key factor controlling runout. The equations show that debris flows and debris/rock avalanches tend to have longer runout than the debris/rock slides and rock falls, given the same values of the predictors. The runout of most damming landslides is constrained by rivers, so that runout of damming slides is very close to L (distance to river), resulting in quite high R^2.

Fig. 5.5 shows the runout of different types of damming landslides predicted by the best-fit regression models developed for non-damming landslides. This cross-prediction is quite good, although it slightly underestimates a few long-runout debris flows. Since (1) the cross-prediction is good, (2) non-damming runout models are not limited by topographic constraints (i.e., the far slope of the river channel and adjacent hillside), and (3) the dataset of non-damming landslides is much larger, we chose these to predict landslide dam formation in the selected catchment (see Section 5.4). The R^2 of damming landslide runout models is quite high, since with a runout that is restricted by the river we might expect that the H/L ratio would be a poor predictor as L is very close to R in this case.

Table 5.3 Best-fitted regression models for the runout of different types of damming and non-damming landslides

Regression models for damming landslides					
Slide type	Intercept	Coeff. of ln(V)	Coeff. of ln(H)	Coeff. of ln(H/L)	Adjusted R^2
Debris/rock avalanche	0.454± 0.239	0.020 ± 0.017	0.903 ± 0.050	-0.944 ± 0.071	0.946
Debris flow	0.493 ± 0.206	0.042 ± 0.017	0.847 ± 0.050	-0.984 ± 0.045	0.990
Rock fall	0.049 ± 0.158	-0.003 ± 0.008	1.001 ± 0.032	-1.001 ± 0.042	0.992
Debris/rock slide	0.388 ± 0.208	0.018 ± 0.016	0.912 ± 0.051	-0.960 ± 0.056	0.929
All	0.318 ± 0.097	0.016 ± 0.008	0.925 ± 0.021	-1.018 ± 0.019	0.976
Regression models for non-damming landslides					
Slide type	Intercept	Coeff. of ln(V)	Coeff. of ln(H)	Coeff. of ln(H/L)	Adjusted R^2
Debris/rock avalanche	0.826 ± 0.489	0.171 ± 0.033	0.538 ± 0.105	-0.488 ± 0.094	0.866
Debris flow	2.141 ± 0.346	0.216 ± 0.025	0.291 ± 0.072	-0.182 ± 0.101	0.800
Rock fall	1.437 ± 0.528	0.196 ± 0.045	0.333 ± 0.107	-0.437 ± 0.158	0.795
Debris/rock slide	1.716 ± 0.326	0.148 ± 0.027	0.433 ± 0.070	-0.168 ± 0.095	0.737
All	0.575 ± 0.215	0.126 ± 0.016	0.654 ± 0.042	-0.575 ± 0.058	0.791

Note: "Coef." stands for the abbreviation of the "coefficient"; values in the table are mean ± standard error

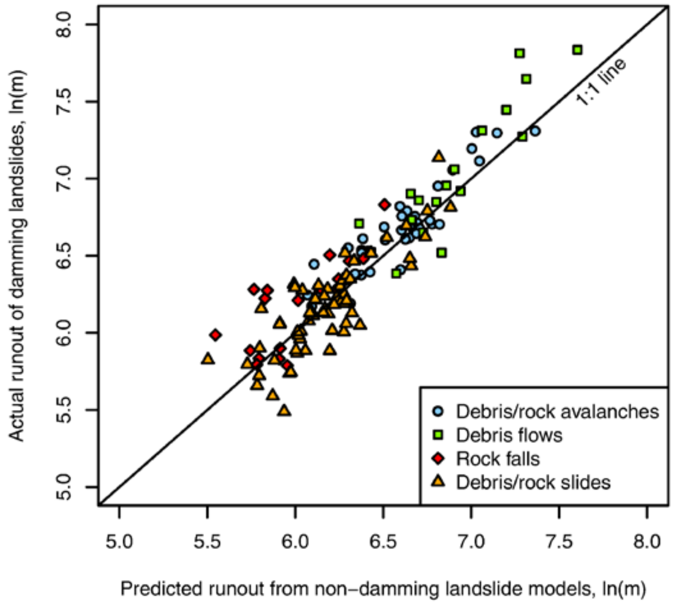

Figure 5.5 Predicting runout of different types of damming landslides by the best-fit regression models from the non-damming landslides

5.3.2 Cross validation of the runout regression model

The goal of empirical-statistical modeling is to predict effects of future events. Therefore we tested the predictive accuracy and robustness of the models by both leave-one-out cross-validation (LOOCV, Stone, 1974; Evgeniou and Pontil, 2004) and bootstrapping (Efron, 1979). The LOOCV method is intuitively named. Given a dataset with *n* observations, one observation is removed in turn and the remaining *n-1* observations are used to fit a model with the chosen predictors, and then to use this model predict at the omitted observation. By repeating and refitting the model *n* times, each observation in the dataset is used for testing. It is the limiting case of k-fold cross-validation (with k=1) and, although computationally-intensive, gives the maximum information on the performance of the overall model. Fig. 5.6 shows the results of LOOCV applied per landslide type, along with the 90% confidence interval band around the 1:1 line. The average RMSEP (root mean squared error of prediction) of different types of landslides is 0.05 ln(m), indicating that the runout models have good predictive accuracy.

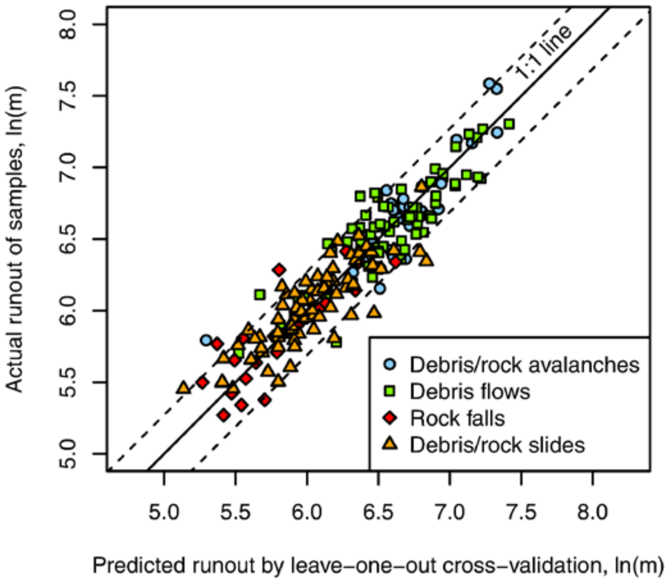

Figure 5.6 Cross-validation of runout regression models regarding different types of landslides: observed runout vs. leave-one-out cross-validation (LOOCV) predicted runout. Dashed lines show 90% confidence intervals.

Bootstrapping is a resampling approach based on building a sampling distribution for a statistic by resampling (with replacement) from the single available dataset a large number times, allowing to draw repeated samples which simulate repeated sets of observations. The model is fit for each bootstrap sample and the model coefficients are collected; the distribution of these can then be summarized. If they do not vary too much, we assert that the best-fit model (using the actual dataset) is robust. Table 5.4 shows the median values of the coefficient and goodness of the fit for all the non-damming landslides from n=1 000 bootstrapping simulations. The mean value and the standard error (S.E.) of the regression models show very slight differences from those obtained from the bootstrapping simulations, confirming the robustness of the runout models.

Table 5.4 Comparison of the regression coefficients and adjusted R^2 from bootstrapping simulations with the original regression statistics in Table 5.3

Coefficients	Regression result		Bootstrapping simulations		Difference of Mean	Difference of S.E.
	Mean	S.E.	Mean	S.E.		
Intercept	0.575	0.215	0.574	0.184	0.001	0.031
Coeff. of ln(V)	0.126	0.016	0.125	0.017	0.001	-0.001
Coeff. of ln(H)	0.654	0.042	0.657	0.043	-0.003	-0.001
Coeff. of ln(H/L)	-0.575	0.058	-0.574	0.057	-0.001	0.001

Note: S.E. is the standard error

5.3.3 Inverse volume modelling from landslide runout regression equations

As a side investigation, we also developed a volume regression model using the same method and dataset as the runout model, although we know that it is difficult to predict landslide volume from the available variables. The result presented in Appendix 3 shows that *H*, *H/L* ratio and landslide type are the most significant variables predicting landslide volume. However, as expected, the regression models have quite low adjusted R^2 (< 0.5), due to the complex triggering mechanisms, geological and geomorphologic settings which are not accounted for in our model. Thus, when predicting landslide dams from our set of variables, landslide volume estimation must rely on landslide-size frequency analysis or other volumetric calculation approaches (Chen et al., 2006; Tsutsui et al., 2007).

The main purpose of this study is to estimate the likelihood of dam formation based on the required volume allowing a landslide to reach and block a river. Therefore, we inverted the runout regression equations for different types of landslides (Equation (5.3)) to regression equations to predict volume from runout (Equation (5.4)). Since the runout model is uncertain, so is the inverse volume model. This uncertainty must be quantified and implemented in the GIS calculation (Section 5.5). To this end we compared the predicted volume from (Equation (5.4)) with the actual volume of non-damming landslides, and computed the root mean squared error of prediction, RMSEP (Fig. 5.7).

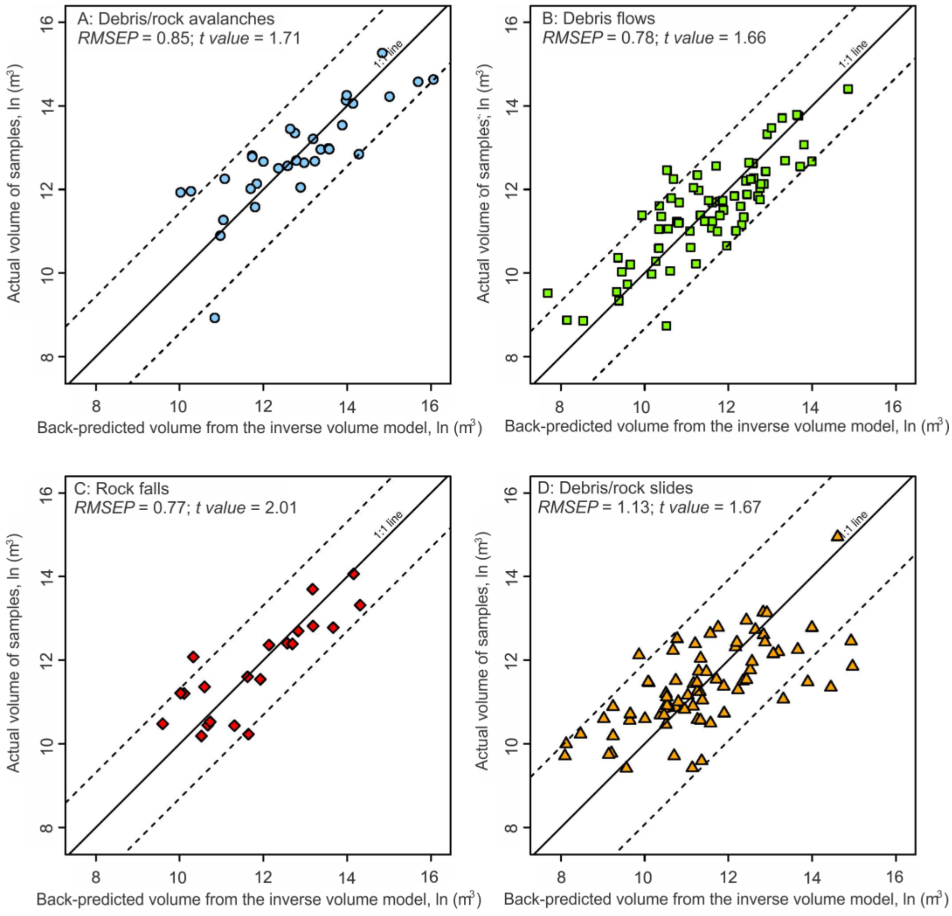

Figure 5.7 Computed landslide volume vs. actual volume of (A): debris/rock avalanches; (B): debris flows; (C) rock falls and (D) debris/rock slides

$$ln(R) = b_0 + b_V ln(V) + b_H ln(H) + b_{H/L} ln(H/L) \qquad (5.3)$$

$$ln(V) = [ln(R) - b_0 - b_H ln(H) - b_{H/L} ln(H/L)]/b_V \qquad (5.4)$$

where b_0 is the intercept, b_V, b_H and $b_{H/L}$ are the mean coefficients of $ln(V)$, $ln(H)$ and $ln(H/L)$, respectively, see Table 5.3 and 5.4 for the values. We calculated the 90% confidence interval for different types of landslides by multiplying their RMSEP with the t values, as shown in Fig. 5.7.

5.4 Empirical Prediction of Landslide Dam Formation in a Selected Catchment

To validate the runout and corresponding inverse volume models for different types of landslides, we implemented them in GIS to predict landslide dam locations in a selected catchment (Fig. 5.1 and Fig. 5.4). To this end, we first prepared the input grids for internal relief (H), the distance to river (*L*) and *H/L* ratio (Fig. 5.8), and then used them to analyze the final threshold volume for a landslide of a certain type to be able to dam its corresponding river (Fig. 5.3B).

5.4.1 Determining the first volume threshold (V_{1i})

We ran the inverse volume models for all four types of landslides in ArcGIS (Table 5.3 and Equation (5.4)), based on three scenarios: mean, lower and upper 90% confidence intervals. The outputs are twelve raster maps showing the first volume thresholds for different types of landslides for these three scenarios, as shown in Fig. 5.9A and C. If the volume of a landslide exceeds this threshold, it is regarded to have sufficient runout to reach a river.

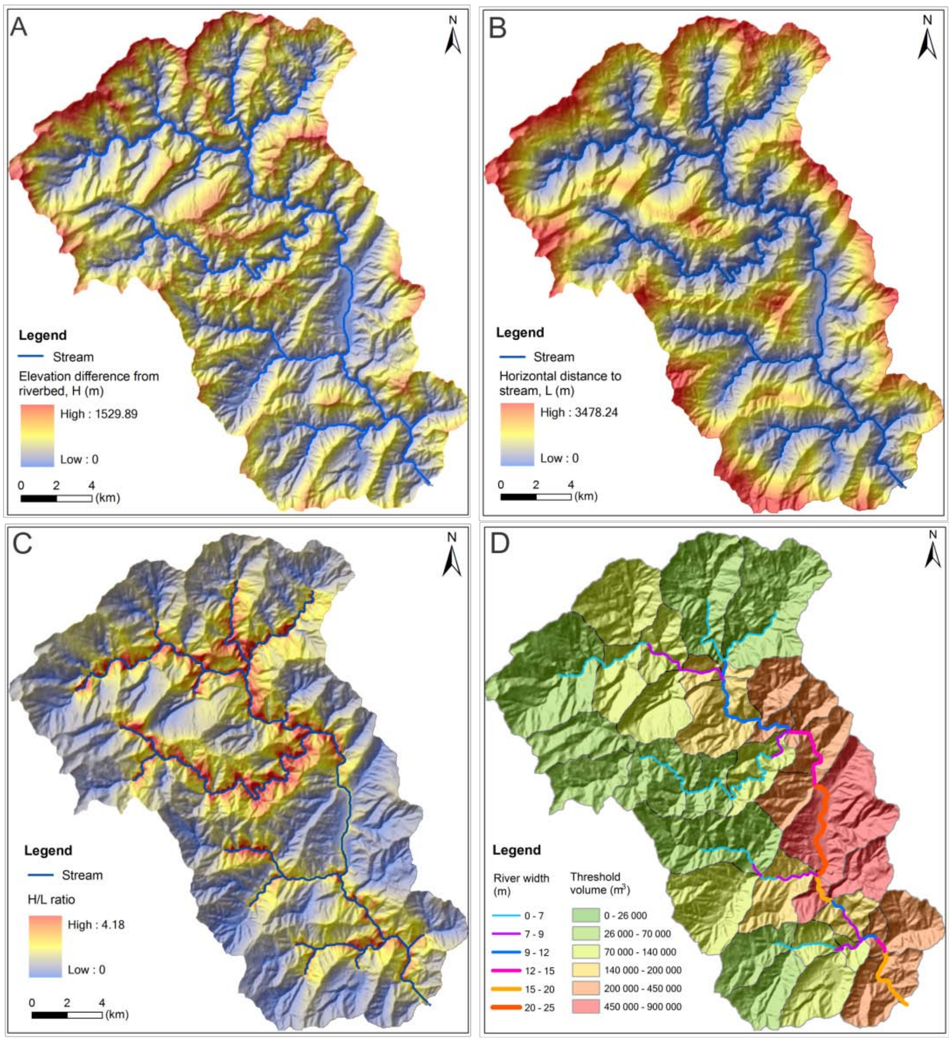

Figure 5.8 Input parameters for estimating volume threshold for a landslide to reach a river. A: Internal relief, *H* (elevation difference from riverbed); B: Distance to stream, *L*; C: *H/L* ratio; D: River width and the corresponding threshold volume of dam formation

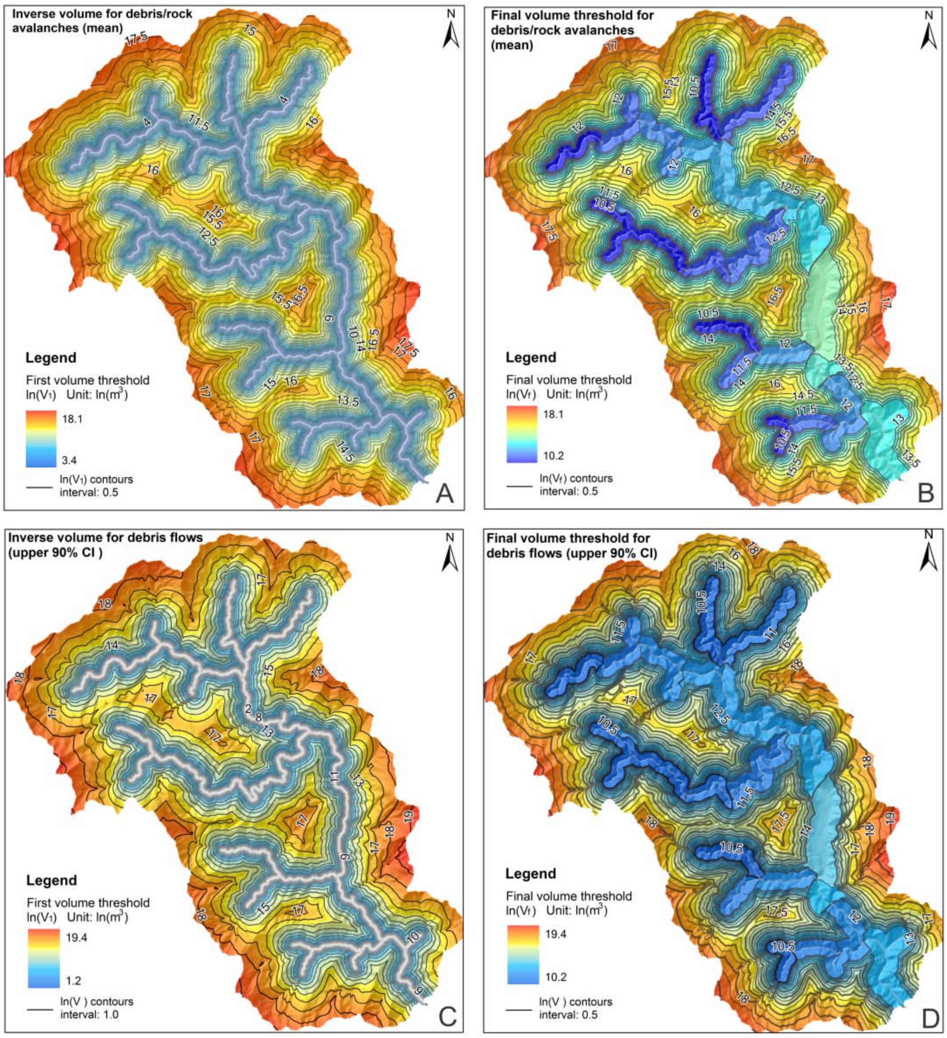

Figure 5.9 A and B: First and final threshold volume of debris/rock avalanches based on the mean scenario; C and D: First and final threshold volume of debris flows based on the upper 90% confidence interval (CI) scenario

5.4.2 Determining the second volume threshold (V_{2i})

We extracted the river network map from the pre-earthquake 25-m DEM using the ArcHyro tools of ArcGIS. Dam formation is controlled by the river features, such as the channel gradient, drainage area, channel steepness index and channel width. Our previous study (Fan et al., 2012a) found that the river width is linearly related to damming landslide volume, as shown in Equation (5.5).

$$V=45747W-247897 \qquad (R^2=0.83) \qquad (5.5)$$

where V is landslide volume (m^3) and W is channel width (m), estimated by the scaling relation $W=A^{3/8}S^{-3/16}$, where A is drainage area (km^2) and S is channel gradient (Finnegan et al., 2005 and Whittaker et al., 2007). The estimated river widths were checked and modified according to measurements on aerial photos. The second volume threshold was then determined by Equation (5.5). We assumed that landslides initiated within a given subcatchment would all reach that subcatchment's river segment, which was further assumed to have a single width. The subcatchments were first delineated automatically from DEM using ArcHydro, and then were merged or divided so that each corresponded to a similar river width (Fig. 5.8D).

5.4.3 Determining the final volume threshold (V_{fi}) and model evaluation

The final threshold volume of each grid (V_{fi}) was determined by selecting the larger of the first and second threshold volumes (Fig. 5.9B and D). This was used to predict the damming likelihood using the landslide type, location and volume information from the detailed landslide inventory presented in Fig. 5.4. The final threshold volume of a landslide was attributed to the grid cell where the landslide initiation point is located. If a landslide with a certain type has an actual volume exceeding the final threshold volume, it was classified as a potential damming landslide grid cell.

The performance of the proposed approach was assessed by the prediction accuracy, defined as the percentage of the samples of interest that are successfully predicted for the actual event. This evaluation was carried out separately for non-damming and damming landslides. Table 5.5 shows that this approach has good prediction accuracies for all types in the mean scenario for both the damming (80-100%) and non-damming landslides (86.8-99.1%). The uncertainty was quantified by the lower and upper 90% confidence interval (CI); these values are shown in the brackets in Table 5.5. Taking the rock fall type as an example, 1 368 out of 1 380 non-damming and 16 out of 20 damming rock falls were accurately predicted based on the mean scenario, resulting in an accuracy of 99.1%

and 80%, respectively. Compared to the mean scenario, the final threshold volume decreases in the lower CI scenario and increases in the upper CI scenario, resulting in a decline in the accuracy of non-damming landslide prediction and a corresponding rise in the accuracy of damming landslide prediction. In other words, the lower CI leads to an underestimation of the non-damming landslides and overestimation of the damming landslides, causing more false alarms, while the upper CI has the opposite effect. The mean scenario provides the optimal prediction accuracy. Note that the prediction accuracy of damming debris flows might be misleading, as there are only three observations. In total 2 666 out of 2 743 (97.2%) non-damming landslides are successfully predicted, and 49 out of 57 (86.0%) damming landslides.

Table 5.5 Performance evaluation of statistical models for different types of landslides

Observed	Predicted (*for debris/rock avalanches*)			
	Non-damming	Damming	Total	Accuracy (%)
Non-damming	33 *(26, 38)*	5 *(12, 0)*	38	86.8 *(68.4, 100)*
Damming	1 *(1, 4)*	9 *(9, 6)*	10	90.0 *(90.0, 60.0)*
Observed	Predicted (*for debris flows*)			
	Non-damming	Damming	Total	Accuracy (%)
Non-damming	475 *(451, 487)*	24 *(48, 12)*	499	95.2 *(90.4, 97.6)*
Damming	0 *(0, 2)*	3 *(3, 1)*	3	100.0 *(100.0, 33.3)*
Observed	Predicted (*for rock falls*)			
	Non-damming	Damming	Total	Accuracy (%)
Non-damming	1372 *(1364, 1375)*	8 *(16, 5)*	1380	99.4 *(98.8, 99.6)*
Damming	4 *(4, 10)*	16 *(16, 10)*	20	80.0 *(80.0, 50.0)*
Observed	Predicted (*for debris/rock slides*)			
	Non-damming	Damming	Total	Accuracy (%)
Non-damming	786 *(772, 800)*	40 *(54, 26)*	826	95.2 *(93.5, 96.8)*
Damming	3 *(2, 8)*	21 *(22, 16)*	24	87.5 *(91.7, 66.7)*

Note: the prediction results are presented in the format: mean (lower 90% CI, upper 90% CI). For example, “473 (451, 487)” means that 473 landslides are predicted as non-damming landslides in the mean scenario, this figure decreasing to 451 and increasing to 487 in the lower and upper confidence interval scenarios respectively.

5.5 Discussion

5.5.1 Discussion of the runout empirical regression model

In previous studies, the runout of small and large landslides has been related to the volume and angle of reach (also called “fahrböschung”) (Heim, 1932; Scheidegger, 1973; Corominas, 1996; Rickenmann, 1999; Legros, 2002). This relation is also supported by the present study. Notably, we found the landslide initiation relief (H) and the landslide type also exert control on the runout. As opposed to the tangent of the reach angle used in previous studies (tan(a)=H_d/R shown in Fig. 5.10), the *H/L ratio* used in this study is defined as the ratio between the height from the landslide initiation to riverbed (H) and its horizontal distance to river (L) (Fig. 5.10). Comparing to H_d and R that can only be obtained after a landslide occurs, H and L can be extracted from a DEM beforehand, therefore, our method is more useful for prediction.

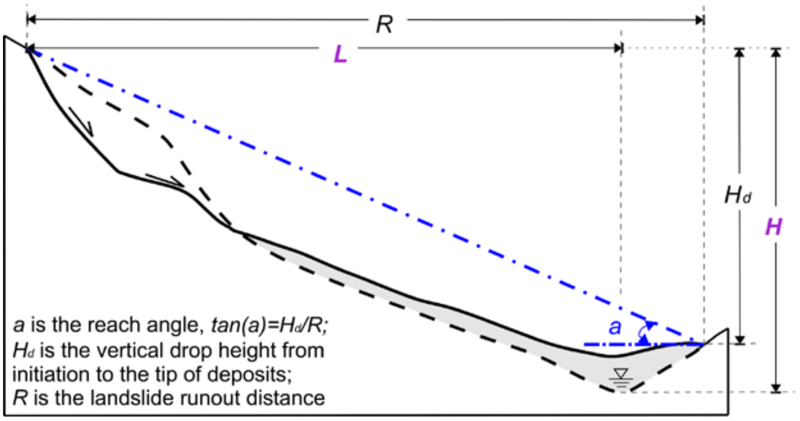

Figure 5.10 Schematic map of a damming landslide profile, illustrating the definition of the angle of reach (a), the runout (R), H_d, H and L

The lithology and the distance to fault of the landslide initiation point seem to have no correlation with the landslide runout, and so would seem to be related only to landslide initiation, not runout. The effects of the site-specific seismic factors on the landslide runout, such as the peak ground acceleration, topographic amplification of seismic waves, and fault slip rate, were not analyzed in this study, because these data are always not available prior to an earthquake.

5.5.2 Confidence in prediction

Most previous studies of empirical runout relations only focused on development of statistical relations. In contrast, this study not only employs two methods (leave-one-out cross-validation and bootstrapping) to evaluate and test the robustness of the regression models, but it also implements and tests them in a selected catchment in a GIS environment. The average false alarm rate was about 3%, as 77 non-damming landslides out of the total 2 800 landslides were mistakenly predicted as damming ones (Table 5.5). Our method does not calculate the spreading of the runout along a 3-D topography, therefore, the correlation between the landslide movement direction and river flow direction was not considered. We checked the sliding directions of these 77 false alarms and found 20 of them were parallel to the river. Accounting for this can further reduce the false alarms.

5.5.3 Sources of uncertainty

A systematic uncertainty analysis provides insight into the degree of confidence in model outputs, and can aid in evaluating model performance. There are several sources of uncertainty in the model inputs, all of which we have tried to minimize.

(1) It is preferable to use the landslide initiation area to estimate landslide volume rather than using the total coverage area of a landslide, since the latter leads to the overestimation of the volume. Therefore, in this study we delineate the initiation, transportation and deposition zones of most of landslides (area > 500 m^2) separately, and only the initiation area is used. Yet there are still subjective mapping errors caused by the difficulty of clearly distinguishing different zones. This kind of error should have a slight effect on the analysis, because volume is analyzed on a logarithmic scale.

(2) The area-volume scaling relations for the volume estimation vary in different studies, and also might change according to the landslide type and material (i.e. Guzzetti et al., 2009; Larsen et al., 2010). We simplified the volume estimation by Equation (5.1), while the bootstrapping result in Table 5.4 proves indirectly that this simplification does not significantly change the regression equations.

(3) The landslide type is important for determining the landslide runout and the volume threshold. We distinguished the landslide type mainly based on image interpretation, with assistance of some field checks in the accessible regions. Debris flows and avalanches are easily

identifiable on images, while rock falls and debris/rock slides are more difficult to distinguish, especially for small ones. However, this only slightly affects the results, as their model coefficients are quite similar.

Most of the above uncertainties are related to the bias and errors of landslide interpretation, which commonly appear in landslide inventories. Guzzetti et al. (2012) reviewed various factors affecting the reliability, completeness and resolution of an inventory map, and also gave recommendations to reduce uncertainty.

5.5.4 Model applicability and limitations

To further test the applicability of the method and the calibrated empirical-statistical regression models, we applied them in the whole earthquake-hit region to evaluate the prediction accuracy of different types of damming landslides. Fig. 5.11 shows the distribution of the 115 test samples, including 48 rock avalanches, 14 debris flows and 53 debris/rock slides. Here we followed the same steps and method as we applied in the selected catchment. First, the internal relief (H), horizontal distance to stream (L), H/L ratio raster maps were prepared as the input factors (i.e. in Fig. 5.12). They were then used for calculating the inverse volume for different types of landslides, the first threshold volume. The second threshold volume was determined according to the river width presented in Fig. 5.11. If a test sample has a volume larger than the final threshold volume, it is expected to dam a river. The prediction accuracy of debris/rock avalanches, debris flows and debris/rock slides in the mean scenario is 87.2% (41 out of 48), 78.6% (11 out of 14) and 77.4% (41 out of 53), respectively.

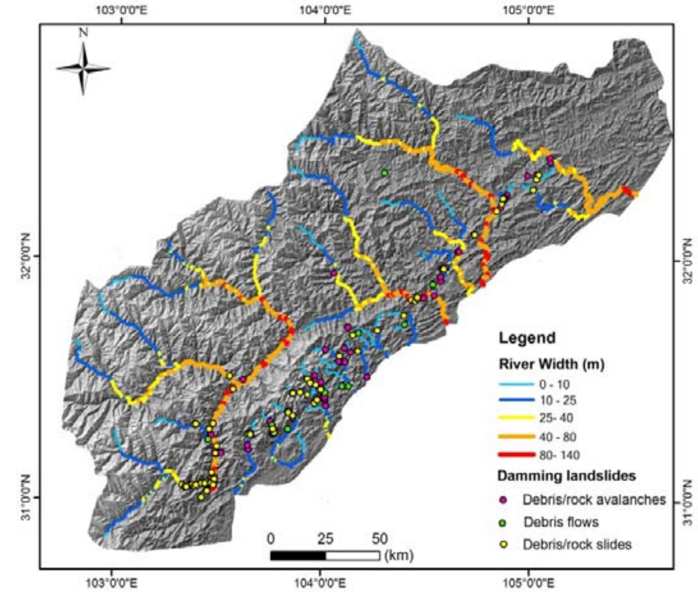

Figure 5.11 Tested samples in the whole study area

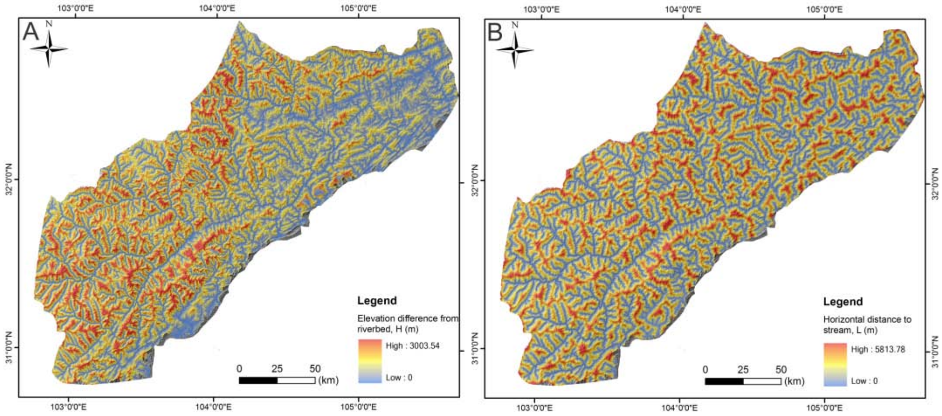

Figure 5.12 A: Internal relief (H) and B: horizontal distance to stream (L)

Our model was developed by presuming that the possible landslide initiation location and size are known. In order to use our results in susceptibility assessment, it should be integrated with landslide susceptibility and frequency-size assessments in order to estimate the damming probability of a landslide, $P_i(Dm)$ as expressed in Equation (5.6).

$$P_i(Dm) = P_i(L) \cdot P_i(S) \qquad (i = 1,2,\ldots.n) \qquad (5.6)$$

where $P_i(L)$ represents the spatial probability of landslide occurrence for each grid cell (also called a grid-based landslide susceptibility map), and $P_i(S)$ is the exceedance probability of a given landslide having a volume larger than the final threshold damming volume (V_{fi}, the output of our model). Eq. (6) can also be written as $P_i(S) = P_i(V_i > V_{fi})$. To estimate $P_i(S)$, we have to know the potential frequency-size distribution based on the particular earthquake scenario. We are currently investigating this.

Landslide susceptibility assessment and size-frequency information are in general available before a triggering event. Therefore, together with our model, the possible damming locations can be estimated beforehand. Because remote sensing images might often not be available immediately directly after the earthquake, and the identification of a large number of landslides over a large area from such imagery is also time consuming, our model may help to orient emergency response. In addition, the model can also be used to assess the damming probability of potential unstable slopes that may fail during the subsequent aftershocks.

The second volume threshold was determined based on a linear correlation between river width and landslide volume extracted from our dataset. However, the applicability of this correlation in other tectonically active mountain regions has not been tested.

When comparing our method to the CONEFALL or Flow-R software (Jaboyedoff and Labiouse, 2003; Horton and Jaboyedoff, 2008), the advantage of our model is that it accounts for landslide volume, while the disadvantage is that it cannot consider the 3D terrain, and thus ignores the landslide direction and the topographic complexity along the landslide runout path.

5.6 Conclusions

The 2008 Wenchuan earthquake induced a large number of landslides (> 60 000, Görüm et al., 2011) and landslide dams (501, Fan et al., 2012a), providing a unique opportunity to systematically assess coseismic landslide dam susceptibility. This study presents the first model to predict potential coseismic landslide dams at regional scale, using landscape characteristics obtained from DEMs. The dam-formation volume threshold we determined is based on the river features and terrain characteristics in the Wenchuan area, therefore, its applicability should be tested in other regions. However, the general method, as well as the runout and inverse volume regression equations, were evaluated as robust and therefore are recommended to be applied and further tested in regional-scale studies.

The method can be applied to predict the susceptible regions for landslide dam formation before an earthquake, with the aid of a coseismic landside susceptibility assessment and a frequency-size distribution analysis. It can also be applied shortly after an earthquake to predict the most likely damming locations in case that the earthquake information and high density landslide zones are known. These predictions can be used to orient the prevention, emergency response and mitigation of coseismic landside dam hazard. In addition, the volume of dammed lakes is also crucial to evaluate the potential danger arising from landslide dams. Therefore, our future research is directed towards ranking the dam hazard according to their possible locations, size and geometric features and the maximum volume of the impounded lakes, with the ultimate aim to create a framework to evaluate landslide dam risk.

6

Geomorphic Decay of Landslide Dams: Transient Water and Sediment Storage

This chapter is based on:

Xuanmei Fan, Cees J. van Westen, Oliver Korup, Tolga Görüm, Qiang Xu, Fuchu Dai, Runqiu Huang, Gonghui Wang, 2012. Transient water and sediment storage of the decaying landslide dams induced by the 2008 Wenchuan earthquake, China. In: Geomorphology 171-172, 58-68.

Xuanmei Fan, Cees J. van Westen, Qiang Xu, Tolga Görüm, Fuchu Dai, 2012. Analysis of landslide dams induced by the 2008 Wenchuan earthquake. In: Journal of Asian Earth Sciences 57, 25-37.

Abstract

Earthquake-triggered landslide dams are potentially adverse disrupters of water and sediment flux in mountain rivers, and capable of delivering catastrophic outburst flows to downstream areas. We analyze an inventory of 828 landslide dams in the Longmen Shan mountains, China, triggered by the M_w 7.9 2008 Wenchuan earthquake. This database is unique in that it is the largest of its kind attributable to a single regional-scale triggering event: 501 of the spatially clustered landslides fully blocked rivers, while the remainder only partially obstructed or diverted channels in steep watersheds of the hanging wall of the Yingxiu-Beichuan Fault Zone. The size distributions of the earthquake-triggered landslides, landslide dams, and associated lakes (a) can be modeled by an inverse gamma distribution; (b) show that moderate-size slope failures caused the majority of blockages; and (c) allow an assessment of seismically induced river-blockage effects on regional water and sediment storage. Monte Carlo simulations based on volumetric scaling relationships for soil (and bedrock) failures indicate that 14% (18%) of the estimated total coseismic landslide volume of 6.4 (14.6) × 10^9 m^3 was contained in landslide dams representing only 1.4% of the >60,000 slope failures attributed to the earthquake. These dams have created storage capacity of ~0.6 × 10^9 m^3 for incoming water and sediment. About 25% of the dams containing 2% of the total river-blocking debris volume failed one week after the earthquake; these figures had risen to 60% (~20%), and >90% (>90%) within one month, and one year, respectively, thus also emptying ~92% of the total potential water and sediment storage behind these dams within 12 months following the earthquake. Currently only ~0.08 × 10^9 m^3 remain available as natural reservoirs for storing water and sediment, while ~0.19 × 10^9 m^3, i.e. about a third of the total river-blocking debris volume, has been eroded by rivers. Dam volume and upstream catchment area control to first order the intactness of the barriers, and bivariate domain plots are consistent with the observation that most earthquake-triggered landslide dams were ephemeral. Nevertheless we conclude that landslide dams disproportionately modulate the short-term post-seismic sediment flux in the Longmen Shan on annual to decadal timescales.

6.1 Introduction

Natural damming of rivers by landslides is common in the mountainous regions all over the world (Costa and Schuster, 1988). The catastrophic release of water masses from landslide-impounded lakes has produced outburst floods and debris flows, causing loss of lives, housing and infrastructure (Korup, 2002; Dai et al., 2005). Numerous studies have focused on (a) documenting individual catastrophic events and case studies (Hewitt, 1998; Harp and Crone, 2006; Nash et al., 2008; Duman, 2009); (b) evaluating the geomorphic impacts of landslide dams on the fluvial drainage network (Pearce and Watson, 1986; Korup, 2005); (c) qualitatively assessing the stability of landslide dams with geomorphometric and statistical approaches (Ermini and Casagli, 2003; Korup, 2004; Dong et al., 2009); and (d) predicting probable dam-failure modes and the peak discharge of outburst floods (Walder and O'Connor,1997).

These and other studies emphasized historic case studies, prompting numerous, though often incomplete, compilations of mainly geometric, hydrological, and topographic characteristics (e.g. Casagli and Ermini, 2003; Korup 2004). Implications of landslide dams triggered during single events such as earthquakes have been rarely studied because of the scarcity of direct observational evidence (Adams, 1981; Pearce and Watson, 1986; Hancox et al., 1997). Here we present one of the first systematic regional studies on the longevity and geomorphic decay of coseismic landslide dams. Derived from detailed remote sensing interpretation and fieldwork, we analyze a unique database of landslide dams triggered by the M_w 7.9 Wenchuan earthquake that struck China's Sichuan Province on 12 May 2008. The earthquake triggered >60,000 landslides (Görüm et al., 2011), out of which >800 formed landslide dams. This database is the largest complete event-based landslide-dam inventory, and provides valuable opportunities for studying how natural river blockage modulates the immediate post-earthquake flux of water and sediment at the regional scale (e.g. Hovius et al., 2011).

The landslide dam inventory presented in Chapter 3 provides the source data for the analysis in this chapter. This chapter aims to quantitatively constrain the sediment budget and residence time of landslide dams, and discuss the implications of their gradual geomorphic decay, which is essential for assessing and mitigating potentially adverse consequences of coseismic river blockage, and its control on post-earthquake sediment flux in the Longmen Shan.

6.2 Frequency-size Distribution of Landslide Dams

Frequency-area or -volume relationships of landslide inventories are one way of gauging the past abundance, and presumed future probability of landslide occurrence as a function of their size (Stark and Hovius, 2001; Malamud et al., 2004; van den Eeckhaut et al., 2007). Several models have been proposed for describing empirical landslide size-frequency distribution, we find that the three-parameter inverse gamma probability density function used by Malamud et al. (2004), describes sufficiently well the empirical area distributions of all coseismic landslides; landslide dams; and lakes:

$$p(A_L;\rho,a,s)=\frac{1}{a\Gamma(\rho)}\left[\frac{a}{A_L-s}\right]^{\rho+1}\exp\left[-\frac{a}{A_L-s}\right], \tag{6.1}$$

where ρ controls the power-law decay for medium and large landslides; a is a location parameter of the maximum probability distribution (m^2); s controls the exponential decay for small landslide areas (m^2); and $\Gamma(\rho)$ is the gamma function of ρ (Malamud et al., 2004). This distribution has a power-law tail with exponent $-(\rho+1)$ for medium and large areas and an exponential rollover for small areas (Fig. 6.1A, Table 6.1). Landslide dams have a rollover that is higher by nearly an order of magnitude than that than for the entire coseismic landslide sample (14,000 m^2 vs. 1,500 m^2, respectively; Fig. 6.1A). Using the fraction of river-blocking landslides in a given bin to be a proxy of the susceptibility of landslides to form dams underlines the higher propensity of larger slope failures seem to interfere with the drainage network (Fig. 6.1B). Except for the largest event, the Daguangbao landslide, deposit volumes of 7-12 × 10^6 m^3 were most prone to impound lakes. Partial dams had areas A_d of 800 m^2 to 1.3 km^2, i.e. spanning more than three orders of magnitude. On average, they were slightly smaller than the fully river-blocking landslides with 1,300 m^2 $< A_\mathrm{d} <$ 7.2 km^2. Overall, >76 km of river reaches were directly covered by damming landslide debris, exclusive of the reaches affected by backwater inundation by lakes with areas from ~200 m^2 to 6.5 × 10^6 m^2.

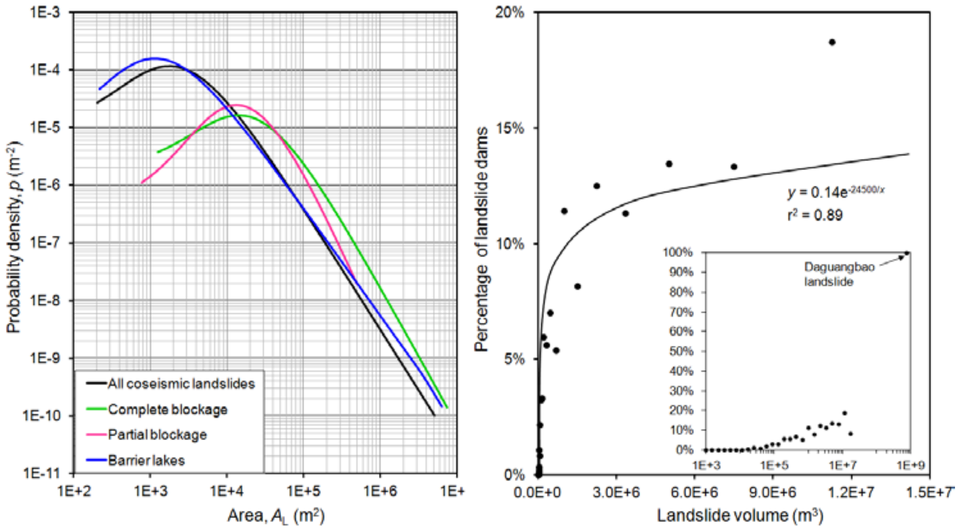

Figure. 6.1 (A) Probability density estimates of all landslides (Dai et al., 2011; Görüm et al., 2011), and those that partially and fully blocked rivers, and the associated barrier lakes (this study); attributed the 2008 Wenchuan earthquake. All data can be modeled with an inverse gamma probability density function (Equation 6.1) that we fitted using a maximum-likelihood estimator; (B) landslide volume versus percentage of landslide dams. Note how the peak density of river-blocking landslides is one order of magnitude higher compared to the peak density of all coseismic landslides.

Table 6.1 Best fit parameters of the inverse-gamma distributions for the landslide and landslide dam inventories of the Wenchuan earthquake

Data sets	ρ	a (m^2)	s(m^2)	r^2	Sample number
All landslides	1.11	5.26×10^3	-7.28×10^2	0.85	48006
Partially blocking landslides	2.03	5.56×10^4	-5.00×10^3	0.78	327
Completely blocking landslides	1.40	5.13×10^4	-7.14×10^3	0.89	501
Barrier lakes	0.87	-2.8×10^3	-3.55×10^2	0.86	501

6.3 Analysis of the Failure Rate of Landslide Dams

Comparison of pre- and post- earthquake images revealed that several hundreds of landslides were reactivated or enlarged during the earthquake, while most landslide dams, particularly those that caused only partial obstruction, were dissected by rivers already several hours after they were formed. We define the failure rate of full-blockage dams as the percentage of the dams that have failed over the time intervals bracketed by multi-temporal remote sensing data (Table 6.2; Fig. 6.2). The percentage can be expressed based on the number of landslides. An analysis of landslide dams that had remained intact as revealed from ASTER images dated July 2010 and covering nearly the full study area, indicates that 23 of the 501 (4.6%) completely river-blocking landslide dams were still in place 26 months after the earthquake. The 23 remained intact landslide dams accounted for around 45% of the total landslide dam volume, and were mainly formed by complex deep-seated slope failures. Since these survival dams are either located in remote regions or impounded very small lakes along tributaries, no attempts have been done to breach these dams artificially.

Table 6.2 Summary of multi-temporal remote sensing data used for assessing the landslide dam decay (failure) rate.

Data covered region	Date	Sensor	Resolution (m)	Barrier lake and landslide dam decay rate		
				Percent of dam number (%)	Percent of lake volume (%)	Percent of dissected dam volume (%)
Around Beichuan area, including 65 landslide dams	May 18, 2008	ALOS PRISM/ Aerial photos	2.5/0.3	24.6	1.0	2.0
	Oct 13, 2008	SPOT-5	2.5	93.8	91.0	95.8
	Jan 24, 2009	CARTOSAT-1	2.5	95.4	92.0	96.0
	July 19, 2010	ASTER	15	95.4	92.0	96.0
Pengzhou area, including 77 landslide dams	June 4, 2008	ALOS AVNIR-2	10	57.1	13.7	15.6
	July 8, 2008	EO-1	10	76.6	77.1	22.3

Computation of the failure rate in the intermediate periods was limited to imagery covering the Beichuan and Pengzhou regions (Table 6.2). Some 60% of dams failed within one month after the earthquake, showing a sharp decrease from 501 to 215 intact dams (Table 6.2; Fig. 6.2). This decrease levelled off two months after the earthquake. Heavy rainstorms could have been a major cause of the failure of ~90% dams within one year after the earthquake. Three heavy rainstorms hit the earthquake region in the first three years after the earthquake. One event occurred four months after the earthquake, on Sep 24, 2008, triggering 72 debris flows in the epicenter region (Tang et al., 2009). In the Beichuan area, 56 debris flows and reactivated landslides were detected through cross-checking remote sensing images. Three of them blocked rivers, while the others delivered a large amount of sediments to the rivers. Many of the coseismic landslide dams failed during or after this rainfall event. Another rainfall event occurred in 2009, but its effects are poorly documented. A rainstorm on 12-14 August, 2010 triggered 11 debris flows in Qingping, Mianzhu and about 50 debris flows in Dujiangyan, forming new dams. One of the dams in Dujiangyan caused the inundation of the relocation site for the new town of Yingxiu. Based on this information, three triangle symbols were plotted in Fig. 6.2 to show the three post-earthquake rainfall events.

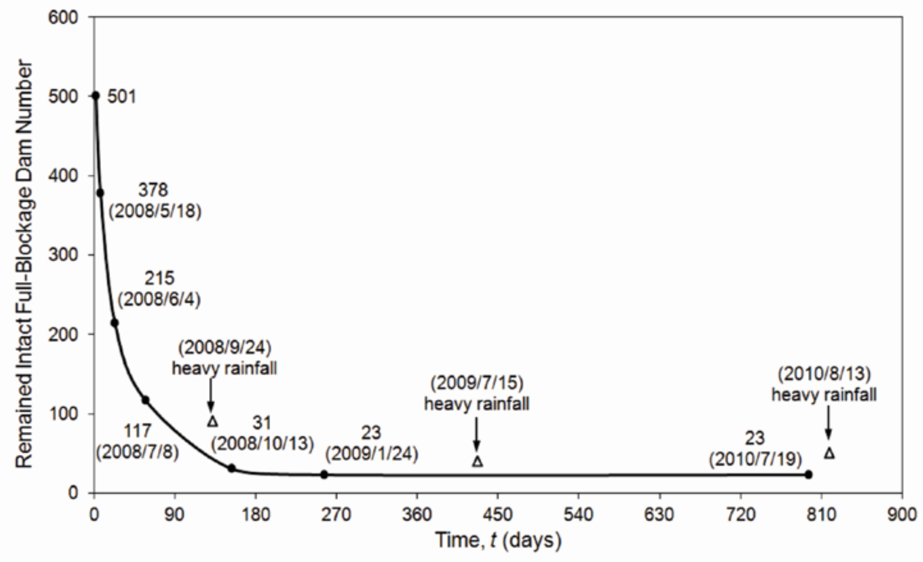

Figure 6.2 Decay of the number of remaining intact full-blockage landslide dams with time.

To put our analysis of dam longevity and decay into a broader context, we compiled three databases as shown in Fig. 6.3. The data from Costa and Schuster (1988), and Ermini and Casagli (2003) comprise 73 and 205 worldwide historical cases, respectively. Fig. 6.3 shows that the Wenchuan earthquake database fits to the function:

$$P_f = 0.973\, e^{-10.88/t} \ (R^2 = 0.97) \qquad (6.2)$$

It demonstrates the relationship between cumulative percent of failed landslide dams (P_f) with time in days (t). Fig. 6.3 indicates that about 30%

of dams that reportedly failed did so within one week after their formation, while >90% failed within a year. This figure also suggests that the survival time of landslide dams induced by the Wenchuan earthquake is generally shorter than that of the other two databases, most probably because the Wenchuan database contains a larger amount of small landslide dams than the other two. The earthquake occurred during the rainfall season, therefore most of the small landslide dams would have filled up quickly and failed by overtopping. In addition, the landslide dam survival time is controlled by, among others, the geomorphometric parameters, dam composition materials, the lake capacity and the discharge of the inflowing stream (Weidinger, 2011).

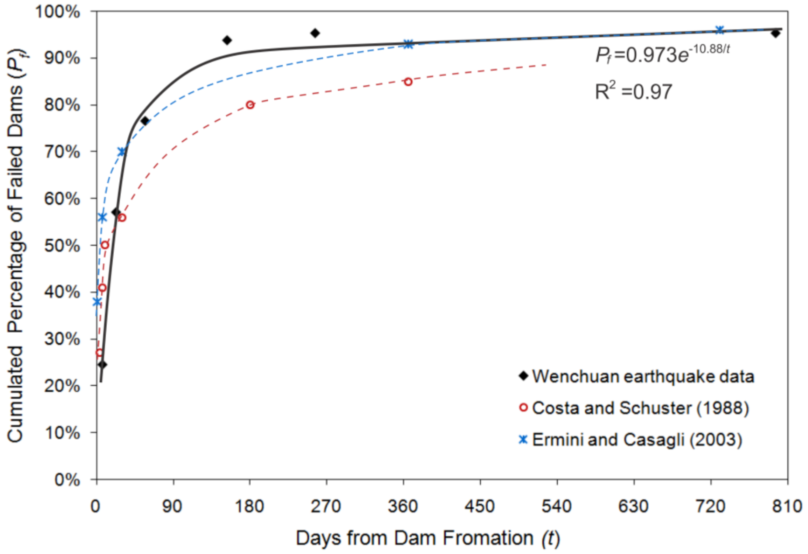

Figure 6.3 Longevity of full-blockage dams with comparison of two worldwide datasets.

6.4 Geomorphic Decay and Effects on Regional Post-seismic Sediment Flux

The effect of coseismic landslide dams on the overall sediment budget of the earthquake includes the dissected landslide dam materials by fluvial erosion and the backwater storage of sediment transferred from upstream. However, the amount of sediment additionally delivered from backwater sediments is unknown. Therefore, our analysis constrains on analysis of the sediment released from landslide dams through fluvial dissection and their decay. In order to quantify the contribution of coseismic landslide dams to the overall sediment budget of the Wenchuan earthquake, we expanded the method of Larsen et al. (2010) to constrain the total volume of coseismic landslide debris via a Monte Carlo simulation. Using the mapped landslide (dam) areas (Fig. 6.1), we estimated each individual landslide volume, V_L:

$$V_L = \alpha A_L^{\Upsilon}, \tag{6.3}$$

where α is a dimensional coefficient with unit [$m^{3-2\Upsilon}$] randomly drawn from an interval [0.015; 0.035], and Υ is a scaling exponent randomly drawn from an interval [1.1; 1.6] for soil and bedrock landslides, and [1.4; 1.6] for bedrock landslides. We reiterated this estimate for n = 10,000 times for each landslide, and summed up all landslide volumes per sample to obtain probability density estimates of the total volumes (Fig. 6.4). The parameter intervals are based on published reviews (van den Eeckhaut et al., 2007; Larsen et al., 2010), and designed to allow for maximum variance in terms of environmental boundary conditions for landsliding, and any error sources due to mapping methodology, remote sensing data quality, or statistical derivation of scaling statistics. We used the same method to estimate the potential maximum water and sediment storage in each landslide-dammed lake by using an empirical scaling relationship between lake area and volume that we constrained by field measurements (Fig. 3.9 and Fig. 3.10D in the Chapter 3). We approximated the minimum volume of sediment released from landslide dams through fluvial dissection, V_r, by a simplified geometric relationship

$$V_r = W_d H_d^2 / \tan \Psi, \tag{6.4}$$

where W_d is the along-valley width of the landslide dam, H_d is the average dam height, and Ψ is the mean bank angle of the breach channel cut through the dam. This approximation assumes a straight, symmetrically v-shaped breach channel of negligible gradient in uniform material with 32° $< \Psi <$ 37°, but nevertheless reproduces the central tendency of a global data set of dissected landslide dams (Fig. 6.5).

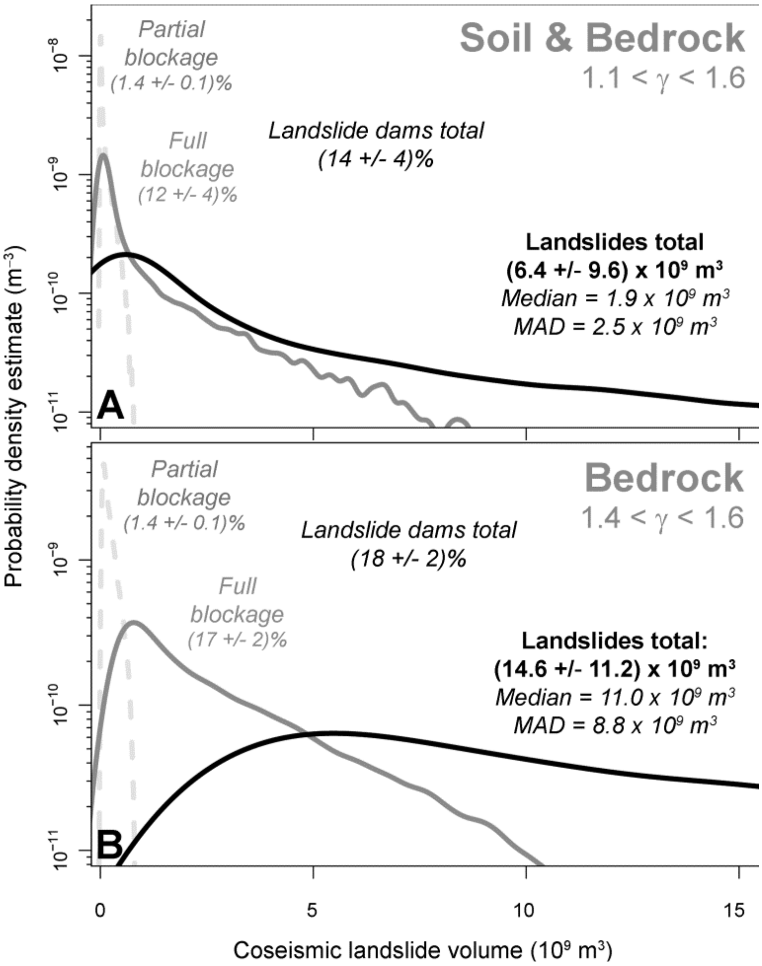

Figure 6.4 Probability density estimates of total volumes of coseismic landslides (black lines), including those having caused full, and partial river blockage (light and dark gray lines, respectively) triggered by the 2008 Wenchuan earthquake. Percentages are fraction of total volumetric estimate. Volumes for each landslide were derived by n = 10,000 random draws of scaling parameters in Equation (6.3) from fixed intervals, before being summed up for total volumes, for (A) both soil and bedrock landslides; and (B) mainly bedrock landslides. MAD = median absolute deviation.

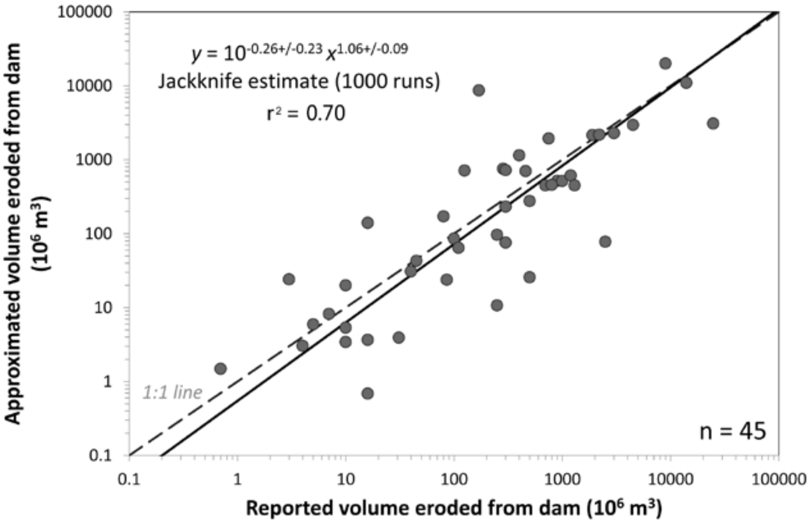

Figure 6.5 Approximation of the volume of dissected landslide dams from a global date set

Our Monte Carlo based estimates of the mean total coseismic landslide debris are (6.4 +/- 9.6) or (14.6 +/- 11.2) × 10^9 m^3, depending on whether we use volumetric scaling parameters for soil or mixed soil and bedrock landslides, respectively (Fig. 6.4; Larsen et al., 2010). While the river-blocking landslides make up only 1.4% of the total coseismic landslide number, their volumetric fraction is 14% and 18%, respectively.

The volumetric fraction of landslide dams and resultant lakes that decayed (failed) after the earthquake is shown in Table 6.2 and Fig. 6.6. Altogether, some 60% of dams, constituting 20% of the total landslide-dam volume, failed within one month after the earthquake (Table 6.2; Fig. 6.6). The total volumes of both dams and lakes estimated from Equation (6.3) show a similar nonlinear decay with time. Altogether, a reservoir volume of $>0.57 \times 10^9$ m^3 formed behind 319 of the 828 landslide dams. About two third of this temporary storage capacity for incoming water and sediment had been associated with the Tangjiashan landslide dam, and its artificial breaching on June 10, 2008 stands out as a conspicuous bump in the volumetric decay curve. From Equation (6.4) we estimate that the volume of sediment liberated by dissecting landslide dams is $(0.19 \pm 0.01) \times 10^9$ m^3, i.e. <5% of the total volume mobilized by coseismic landslides (Fig.6.6 B).

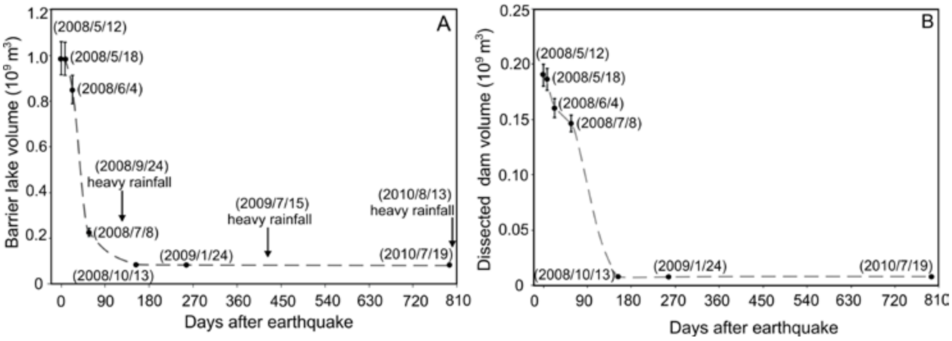

Figure 6.6 Time series of loss of volume of (A) estimated water and storage in landslide-dammed lakes, and (B) dissected landslide dams through breaching and subsequent fluvial erosion. Note that this is an overestimate given that parts of the dams may remain in place. Error bars show ±1 s.d. error.

6.5 Morphometric Controls on Landslide-dam Stability

The stability of landslide dams is a function of their geometry, internal structure, material properties, lake volume, inflow rate, and seepage processes (Costa and Schuster, 1988; Korup and Tweed, 2007). Unfortunately, the internal structure and particle size distribution become evident only after dam failure such that reliably predicting landslide-dam stability remains a key challenge. Casagli and Ermini (2003) showed that geomorphometric parameters help assess to first order the state of intactness, rather than the geotechnical stability, of landslide dams. They proposed a blockage index

$$I_b = \log\left(\frac{V_D}{A_C}\right) \tag{6.5}$$

where V_D is the volume of the landslide dam (m^3), and A_C is the catchment area upstream of the dam (km^2). We plotted I_b for the 23 existing lakes behind currently intact landslide dams, those that had been breached in different catchments, and those that were mitigated by authorities (Fig. 6.7B). We observe that no full blockages or lakes formed where $I_b < 2$, whereas dams had breached where $I_b < 4$, including some 75% of the artificially breached dams. Most of landslide dams in the gray shaded domain in Fig. 6.7B failed within one month after the earthquake. Barrier lakes where $I_b > 5$ have remained intact revealed by the July 2010 ASTER images.

In addition, we assume that the fluvial erosion potential might play an important role in the spatial distribution and stability of landslide dams. As introduced in Chapter 2, the fluvial erosion potential is commonly referred from a power-law relationship between river-bed gradient and upstream drainage area, the steepness index, k_s (Equation 2.2). We find that the Min River catchment (MJR), and catchments in the Pengguan Massif (P1-P7) have by far the highest k_s values (Fig. 6.7A), reflecting high-relief bedrock gorges flanked by steep hillslopes promoting landslide (dam) occurrence: More than 75% of landslide dams concentrated there, and >90% of the landslides along MJR formed partial dams (Fig. 3.5). We also find that the state of intactness varies with k_s. Only ~4% of the complete dams remained intact in the P1-P7 catchments, and none in the MJR, while ~15% of dams in JJR, FR and QR catchments, where k_s is lower, remained intact (Fig. 6.7B).

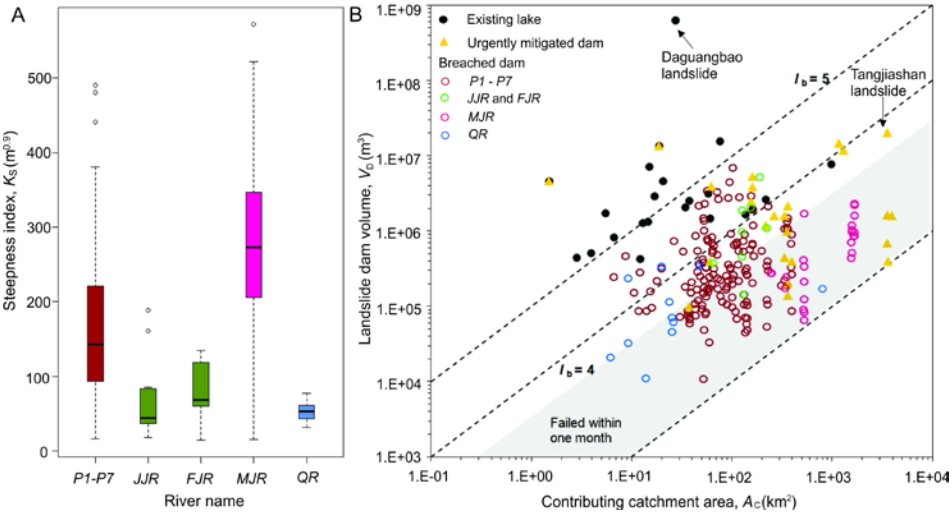

Figure 6.7 (A) Boxplot of steepness index of fully dammed river segments in different catchments; (B) contributing catchment area versus landslide dam volume for 287 coseismic landslide dams with empirical envelope curves for the blockage index I_b. Most of landslide dams in the grey shaded domain failed within one month after the earthquake. P1-P7, MJR, JJR, FJR and QR are the rivers in the study area as shown in Fig. 2.1

6.6 Discussion

Our inventory of landslide dams caused by the Wenchuan earthquake is unique in that it records abundant river blockage following a single regional landslide triggering event. We used this inventory to focus on immediate, i.e. annual-scale post-earthquake dynamics of landslide dams at the regional scale, assessing the decay of dam intactness and its influence on the post-seismic sediment flux. Our volumetric estimates were designed to quantify regional-scale sediment generation through landsliding and sediment delivery from the fluvial dissection of landslide dams. These estimates rely on a number of assumptions and simplifications, including (1) empirical volume-area scaling for both landslides and landslide-dammed lakes; (2) a maximum effective landslide (dam) mapping resolution in space and time dictated by the remote sensing data quality; and (3) geometric simplifications adhering to the estimates of how much sediment was eventually removed from breached or dissected landslide dams.

With regard to (1), our volumetric estimates corroborate those by Parker et al. (2011), who suggested that earthquake-triggered landslides involved 5-15 × 10^9 m^3. While our estimates overlap with this range (Fig. 6.1), the obvious deviations highlight the importance of using statistically robust methods for approximating mass balances related to regional slope-failure episodes. Our Monte Carlo approach to estimating the total coseismic volume has the advantage that it (a) does not rely on a single volumetric scaling relationship; (b) helps include constraints set by landslide type and material (Larsen et al., 2010); and (c) allows quantifying the inherent error margins as well as their propagation based on a large number ($n = 10{,}000$) of permutations in the scaling parameters. The percentage of river-blocking landslides in terms of volume remains at 14-18%, and demonstrates that a significant fraction of landslides has the potential to interfere with the flow of water and sediment in the drainage network.

Concerning (2), other error sources such as cloud cover or shadow effects are inherent to the remote sensing based mapping approach. Together with the time lag between earthquake and image capture, these preclude the compilation of landslide-dam complete inventories. Optical data are of limited use especially where multiple indistinguishable landslides have stripped hillslopes bare of any vegetation cover. Such pervasive stripping of vegetation cover at the scale of individual hillslopes may bias landslide mapping towards a higher abundance of larger landslides at the expense of smaller slope failures with contiguous or ill-defined scars, thus potentially favoring higher landslide volumetric estimates.

Regarding (3), the approach of evaluating the amount of sediment removed from the landslide dams is simple, but seems to capture to first order the overall trend of the sediment flux following dam failures, given that field observations confirm that in most cases only minor fractions of the river-blocking material has been sluiced downstream. However, while the geomorphic decay of landslide dams supports earlier reported trends of the rather short-lived nature of most of these blockages, their removal by fluvial erosion is slower. On valley floors, the formation of >800 landslide dams had created a temporary sediment storage consisting of dams and backwater, i.e. lacustrine and fluvial, deposits with a volume corresponding to 20-25% of that mobilized during the earthquake on hillslopes altogether. Yet most of this potential storage was obliterated and removed within several years following the earthquake.

Despite these caveats our results underline that river-blocking landslides involve disproportionate fractions of the total coseismic mass balance. While the spatial distribution of landslide dams mimics that of the coseismic landslides, particularly steep and high-relief bedrock gorges promote not only spatially clustered but also short-lived (<1 yr) natural river blockage. The rapid geomorphic decay of the mapped landslide dams supports earlier observations on selected worldwide data (Costa and Schuster, 1988). Our results also indicate that the normalized channel steepness index may be a useful measure for predicting the longevity of landslide dams, though further research is needed to test this notion. While fluvial dissection and artificial draining of a number of dams has contributed to emptying >90% of the potential backwater storage volumes, significant amounts of formerly river-blocking debris remains on valley floors and awaits entrainment during sufficiently competent floods. Hence, while the immediate hazard of catastrophic lake outbursts has been largely mitigated, we anticipate that significant sediment pollution may continue to be a major problem for rivers in the earthquake-affected region and their downstream reaches.

Our results also contribute to improving our understanding of how large earthquakes serve to build mountains through uplift, while also reducing local topography through widespread coseismic landsliding. Parker et al. (2011) estimated that the total volume of coseismic landslides triggered by the Wenchuan earthquake exceeded the volume of material added to the orogen through rock uplift, concluding that the Wenchuan earthquake caused a net loss in topography. Critical to this assessment is the fraction of landslide debris that is exported from the earthquake-affected region by fluvial erosion before the next similar disturbance takes place (Yanites et al., 2010, Hovius et al., 2011). Our analysis of volume decay of dissected landslide dams captures the short-term dynamics of sediment transport (Fig. 6.6B), and shows that 0.19×10^9 m^3, i.e. only < 5% of the total coseismic landslide volume, has been carried away within two years after the earthquake, leaving 82-86% still suspended on hillslopes, and 9-13% stored close to the drainage network as intact or formerly river-blocking deposits. Thus, the volume of landslide materials being removed by rivers so far is about 5-13% of the inferred volume gained from tectonic uplift, i.e. 2.6 ± 1.2 km^3 (Parker et al., 2011). Debris-flow episodes triggered by the three large post-earthquake rainstorms (Tang et al., 2009) remobilized and delivered only a very small fraction ($\sim 0.01 \times 10^9$ m^3) of the loose earthquake-derived debris from hillslopes to channels. Part of this low sediment delivery ratio to rivers may be due to the observation that most of earthquake-induce landslides initiate from the upper part of slopes or mountain ranges, and terminate on mid-slope portions (Meunier et al., 2008). The lack of pre- and post- earthquake sediment discharge data together with extensive disaster intervention and reconstruction efforts in many of the Longmen Shan's valleys precludes more accurate assessments of the post-earthquake sediment flux. The experience from 1999 Chi-Chi earthquake, Taiwan, (Lin et al., 2008, Hovius et al., 2011) showed that earthquake effects of enhancing fluvial suspended sediment loads dissipated some six years after the earthquake. Given that the less steep and less typhoon-drenched rivers of the Longmen Shan were affected by a much higher amount of river-blocking landslides, higher landslide numbers, and overall sediment input, we anticipate that the post-seismic sedimentary effects of Wenchuan earthquake wear off more slowly than in the Taiwan case. Based on the distribution of I_b values of the landslide-dam data, we speculate that the 23 survival landslide dams containing 45% of the coseismic landslide dams (volume), or 6% of the total coseismic landslide debris volume, may remain intact for an unspecified period of time, thus trapping further water and sediment. Eventually, however, the competition between uplift and erosion on timescales integrating multiples of the recurrence intervals of such large earthquakes will determine whether events such as the Wenchuan earthquake cause net build-up or net decay of mountain topography (Ouimet, 2010). The recurrence interval of this earthquake magnitude is estimated at 2000-4000 yr (Shen et al., 2009; Ran et al., 2010), and crucial for estimating the size-frequency distribution of landslides and landslide dams triggered by the next event.

6.7 Conclusions

The 2008 Wenchuan earthquake provided a unique opportunity to study an event-based landslide dam inventory of 828 coseismic landslide dams, and 501 associated lakes. This rare occasion provides insights on the spatio-temporal clustering and geomorphic decay of coseismic landslide dams. In summary, the formation and failure of landslide dams has involved significant fractions (14-18%) of the overall volumetric sediment generation of the 2008 Wenchuan earthquake, though recruiting only 1.4%, and mostly the larger, of all slope failures as temporary sediment storage on the valley-floor. Backwater impoundments constituted an estimated 20-25% of the total volume of material moved, but were gradually reduced during natural and artificial dam breaches. The volume of sediment released to trunk rivers is estimated at 0.19×10^9 m^3, i.e. <5% of the total coseismic landslide volume, and mainly occurred within a couple of years after the earthquake and future impacts are anticipated to occur on annual timescales. In essence, about only a third of the sediment volumes contained in landslide dams has been flushed downstream. However, the remaining landslide-dam debris together with that of the bulk volume (>85%) of smaller landslides awaits flushing during major sediment pulses in years and decades to come. On annual to decadal time scales, these findings have important implications for future flood and sediment management of the river systems in the earthquake-affected areas, given that many settlements have been re-established near active floodplains of major trunk rivers. On longer timescales, seismic and post-seismic sediment budgets will help quantitatively resolve the topographic net effect of large earthquakes that culminate in the competition between mountain-belt formation through uplift, and topographic decay through coseismic landsliding.

7

Simulating Dam-breach Flood Scenarios and Emergency Mitigation Measures

This chapter is based on:

Xuanmei Fan, Chenxiao Tang, Cees J. van Westen, Dinand Alkema, 2012. Simulating dam-breach flood scenarios of the Tangjiashan landslide dam induced by the Wenchuan earthquake. In: Natural Hazards and Earth System Sciences 12, 3031- 3044.

Abstract

Floods from failures of landslide dams can pose a hazard to people and property downstream, which have to be rapidly assessed and mitigated in order to reduce the potential risk. The Tangjiashan landslide dam induced by the M_w 7.9 2008 Wenchuan earthquake had impounded the largest lake in the earthquake affected area with an estimated volume of 3×10^8 m^3, and the potential catastrophic dam breach posed a serious threat to more than 2.5 million people in the downstream towns and Mianyang city, located 85 km downstream. Chinese authorities had to evacuate parts of the city until the Tangjiashan landslide dam was artificially breached by a spillway, and the lake was drained. We propose an integrated approach to simulate the dam-breach floods for a number of possible scenarios, to evaluate the severity of the threat to Mianyang city. Firstly, the physically-based BREACH model was applied to predict the flood hydrographs at the dam location, which were calibrated with observational data of the flood resulting from the artificial breaching. The output hydrographs from this model were inputted into the 1D-2D SOBEK hydrodynamic model to simulate the spatial variations in flood parameters. The simulated flood hydrograph, peak discharge and peak arrival time at the downstream towns fit the observations. Thus this approach is capable of providing reliable predictions for the decision makers to determine the mitigation plans. The sensitivity analysis of the BREACH model input parameters reveals that the average grain size, the unit weight and porosity of the dam materials are the most sensitive parameters. The variability of the dam material properties causes a large uncertainty in the estimation of the peak flood discharge and peak arrival time, but has little influence on the flood inundation area and flood depth downstream. The effect of cascading breaches of smaller dams downstream of the Tangjiashan dam was insignificant, due to their rather small volumes, which were only 2% of the volume of the Tangjiashan lake. The construction of the spillway was proven to have played a crucial role in reducing the dam-breach flood, because all the other natural breach scenarios would have caused the flooding of the downstream towns and parts of Mianyang city. However, in retrospect improvements on the spillway design and the evacuation planning would have been possible. The dam-break flood risk will be better controlled by reducing the spillway channel gradient and the porosity of the coating of the channel bottom. The experience and lessons we learned from the Tangjiashan case will contribute to improving the hazard mitigation and risk management planning of similar events in future.

7.1 Introduction

Natural damming of rivers by mass movements are very common and potentially dangerous phenomena (Costa and Schuster, 1988 and Evans et al., 2011), which have been documented all over the world, e.g. in Japan (Swanson et al., 1986), Canada (Clague and Evans, 1994), China (Chai et al., 1995), the northern Apennines in Italy (Casagli and Ermini, 1999) and New Zealand (Korup, 2005). Hazards and risks resulting from landslide dams have been reported in many historic accounts of catastrophic floods from natural dam failures. The 27 largest floods of the Quaternary Period with discharges greater than 100,000 m^3/s were listed by O'Connor and Costa (2004), most of which were caused by breaches of glacier or landslide dams. The largest flood in recorded history was caused by the failure of the earthquake-induced Raikhot landslide dam in 1841 on the Indus River in Pakistan, which has an estimated peak discharge of ~540, 000 m^3/s (Mason, 1929 and Shroder Jr, 1998). Harp and Crone (2006) and Schneider (2009) described the largest landslide triggered by the Kashmir earthquake (M_W 7.6, 2005) in Pakistan, which formed a natural dam impounding two lakes in the Karli river. Some other representative cases were studied by Alexander (1988), Reneau and Dethier (1996), Hewitt (1998), Cruden and Miller (2002), Hancox et al. (2005), Dunning et al. (2006), Gupta and Sah (2008) and Duman (2009). On overview of research work on landslide dams was made by Korup (2002) and Evans et al. (2011).

Many records of large landslide dams and catastrophic outburst floods are known in China. On 1st June 1786, a M 7.8 earthquake in the Kangding-Luding area triggered a large ($>10^6$ m^3) landslide dam that blocked the Dadu River. Ten days later, the dam breached resulting in catastrophic downstream flooding and 100,000 fatalities (Dai et al., 2005). Another examples is the sudden breach of three dams (Dahaizi, Xiaohaizi, and Deixi) induced by the Diexi earthquake causing a tragic flood that affected settlements along a downstream distance of 250 km, killing more than 2,500 people (Chai et al., 2000). Of all the recorded cases, the largest dam was formed by the Yigong landslide ($\sim 3\times10^8$ m^3) on April 9, 2000 in Tibet, which breached two months later and caused a flash flood with a peak discharge of ~120,000 m^3/s, resulting in 30 fatalities and over 100 people missing (Shang et al., 2003 and Xu et al., 2012).

The Tangjiashan landslide dam induced by the devastating 2008 Wenchuan earthquake (M_w 7.9) in China, highlighted the importance of the dam-breach flooding problem. This dam was the most dangerous one out of the >800 coseismic landslide dams mapped by Fan et al., (2012a, c), which had impounded the largest barrier lake with an estimated volume of 3×10^8 m^3, threatening more than 2.5 million people downstream. Chinese authorities decided to evacuate parts of the city until the Tangjiashan landslide dam was artificially breached by a spillway, and the lake was drained (Liu et al., 2009).

For emergency mitigation planning related to potential dam-break floods, the key issues are: (1) assessing the dam stability; (2) evaluating the potential dam breach process and mechanism; and (3) predicting the dam-break flood parameters, including the probable peak discharge, depth, velocity, duration and the affected area.

The stability assessment of landslide dams has been an important research theme for a long time. Recently, a geomorphic approach is widely used to correlate the dam and the impounded lake geomorphic features with the landslide dam's stability (Ermini and Casagli, 2003; Dong et al., 2009). Using this approach Cui et al. (2010) concluded that the Tangjiashan dam was unstable. The limitation of this method is that it ignores the dam structure and geotechnical properties of the dam materials (Dunning et al., 2005).

Concerning the dam breach process, Walder and O'Connor (1997) concluded that it was still poorly understood, since it involves a variety of processes, including sediment entrainment from the breach floor, the gravitational collapse of breach sides and the downstream dam face. In the Tangjiashan case, the availability of detailed field data and laboratory-tested geotechnical parameters allow us to use a physically-based model to simulate the dam breach process, predicting the dam-breach flood hydrograph, the failure time and the ultimate breach geometry.

Regarding the dam-break flood modelling, the peak discharge can be predicted by both empirical and numerical simulation methods. The empirical method relies on regression relations between the peak discharge and other parameters, such as the impounded lake volume, depth, and area (Evans, 1986; Costa and Schuster, 1988; see Peng and Zhang, 2012 for an overview). The numerical method includes both a physically based model, e.g. the US National Weather Service BREACH Model (Fread, 1991) and Chang and Zhang (2010), as well as a GIS-based hydraulic model (Li et al., 2011), which can also predict other flood characteristics (flood routing, depth, velocity, duration and the affected area). The empirical model is simple to apply, compared to the numerical model which requires detailed parameters, but it provides less accurate results.

The previous studies on the Tangjiashan landslide dam are mainly concentrated on describing the emergency mitigation works and on the estimation of the dam-break flood using empirical methods (Liu et al., 2009; Kuang et al., 2009; Xu et al., 2009; Cui et al., 2010), as well as on the prediction of the outburst flood hydrograph using physical models (Wang et al., 2008, Dai et al., 2010). However, there is little work on 2D hydraulic modelling of the dam-breach flood with consideration of different scenarios, neither on the calibration of the model and on the cascading breach of several smaller downstream dams. To fill these gaps, the physically-based BREACH model and the GIS-based hydraulic SOBEK 1D-2D model are integrated in this study to facilitate the dam-break flood modelling of the Tangjiashan dam. This study aims to model the dam-break floods of possible scenarios up to Mianyang city, based on our best understanding of the dam breach process.

7.2 Characteristics of the Tangjiashan Landslide Dam

7.2.1 Hydrologic and geological setting

The Tangjiashan landslide dam is located at 31.84° N, 104.43° E, ~5 km upstream of the town of Beichuan, which was completely devastated by the Wenchuan earthquake and the large co-seismic landslides, and has not been reconstructed. The landslide blocked the Tongkou river (also called Jianjiang) with an upstream catchment area of 3, 550 km^2 (Fig. 7.1). The river is 100-130 m wide and 0.5-4 m deep, having an asymmetrical V-shaped cross-section with right and left valley-side slope gradient of ~ 45° and 25°, respectively. The Tongkou river is mainly supplied by rainfall, with mean annual precipitation rate of 1287.5 mm. The recorded maximum daily precipitation is 323.4 mm. According to the record from the Beichuan hydraulic station, the average annual discharge of the Tongkou river is 81 m^3/s, and increases to 167 m^3/s during the monsoon season which lasts from May to October. The discharge before the dam breached was recorded as 90 m^3/s (Liu et al., 2009). Historical flood records indicate that most of floods occurred in June to September due to extreme rainstorms, with the highest frequency in July and August. In the past 100 years, the largest floods happened in 1902 and 1934 with peak discharges of 6720 m^3/s and 5750 m^3/s, respectively. Table 7.1 shows the peak discharges of floods with different return periods.

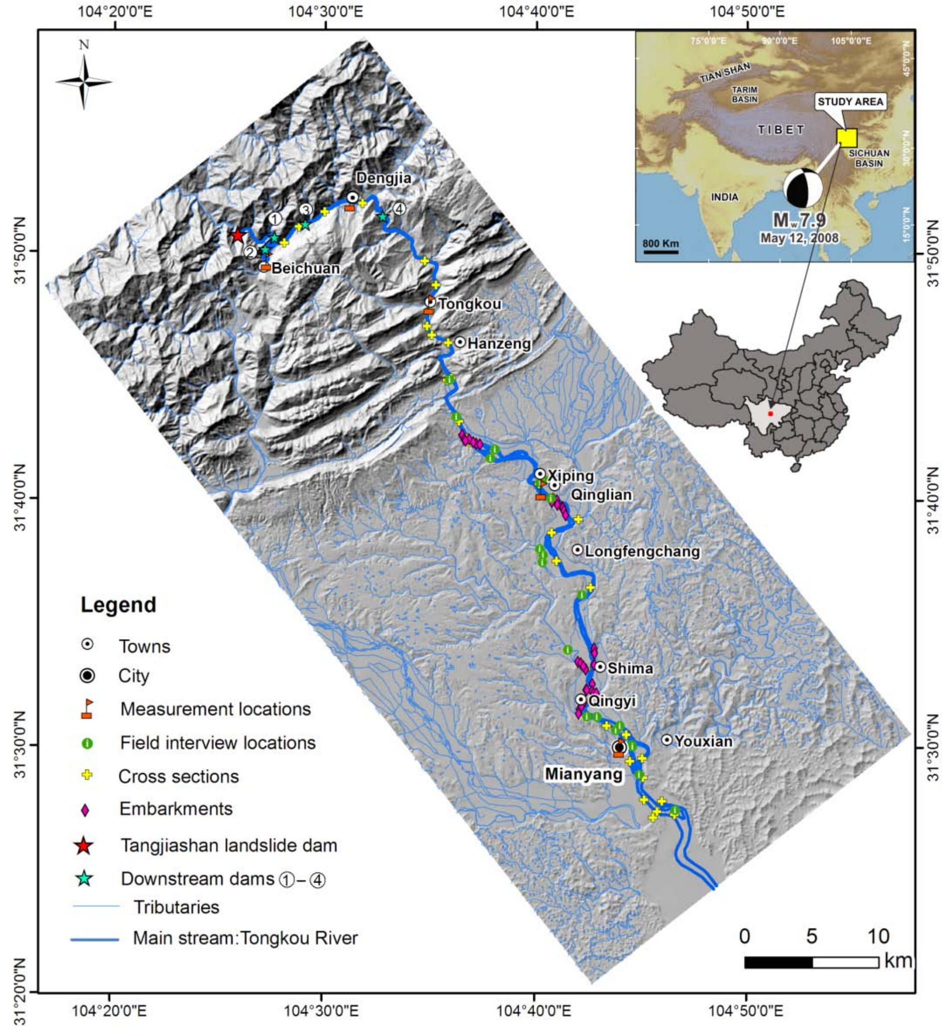

Figure 7.1 Location of the Tangjiashan landslide dam and the layout of the field measurements. The measurement location in Beichuan is the same as the Beichuan hydraulic station.

Table 7.1 Peak Discharge of floods with different return periods calculated from measurements at the Beichuan Hydraulic Station

Return period (years)	2	5	10	20	50	100	200
Peak discharge (m^3/s)	1180	2190	3040	3920	5120	6040	6970

The Tangjiashan landslide dam was formed by a rock slide in fragmented bedrock composed of siltstone, siliceous rocks and mudstone of the Qingping Group, from the lower Cambrian (Fig. 7.2 and 7.3, modified based on Xu et al., 2009). The bedrock was covered by colluvium (mixed soil and fine rock fragments) with dense vegetation. The landslide is located on the hanging wall of the main fault (Yingxiu-Beichuan fault), only 2 km away from the surface fault rupture. Due to the strong seismic energy, the steep terrain and the fragile geological structure, the landslide slid down into the river along the steep sliding surface (60°) and even ran up to the opposite slope, forming a 550 m high scarp (Fig. 7.2). The dam volume was estimated to be 2.04×10^{7} m^{3} with a height varying from 82 m to 124 m through preliminary field measures (Liu et al., 2009). The dam crest extended approximately 600 m across the valley and 800 m along the valley. It had impounded a lake with 2.47×10^{8} m^{3} of water till 7 June 2008, and with an estimated maximum capacity of 3×10^{8} m^{3} (Liu et al., 2009). We generated the post-earthquake DEM with 5-m spatial resolution from the field-measured 2-m interval contours covering the area from the dam site to the Beichuan town (Fig. 7.4). The dam volume was calculated to be 1.7×10^{7} m^{3} by comparing the pre- and post- earthquake DEMs. There are also several smaller landslide dams located at the downstream of the Tangjiashan dam (Fig. 7.4).

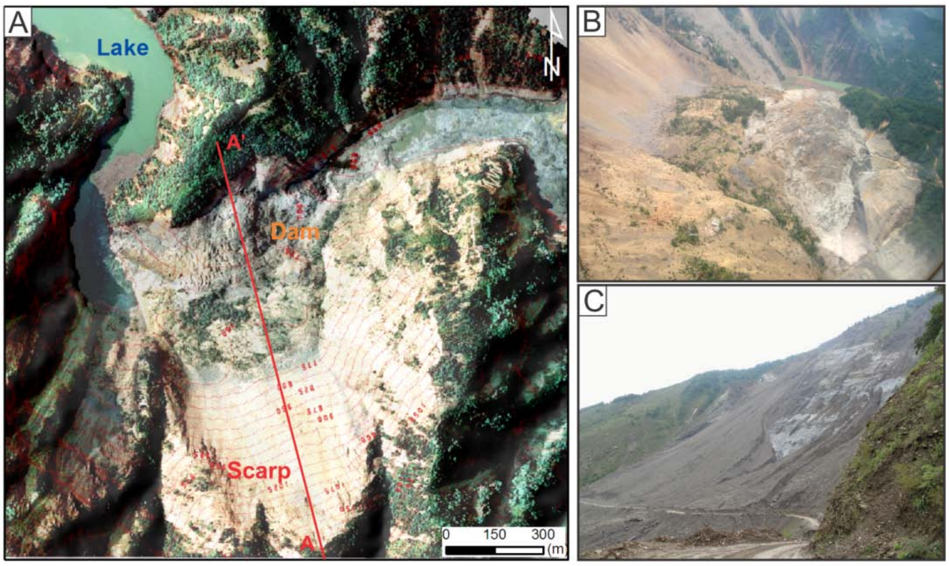

Figure 7.2 A: Aerial photo of the Tangjiashan landslide dam (source: Ministry of Land and Resources); B: Photo of the dam body; C: Photo of the landslide back scarp

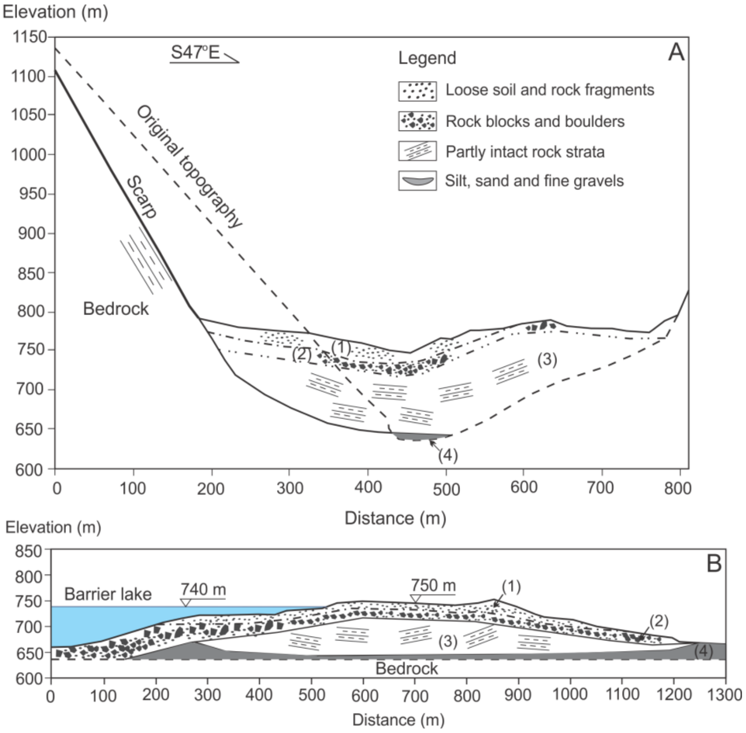

Figure 7.3 A: Geological profile (A-A' in Fig. 7.2) of the Tangjiashan landslide; B: Longitudinal cross-section of the dam body along the valley showing four-layered structure, modified based on Chengdu Hydroelectric Investigation and Design Institute (CHIDI) in China (2008) and Xu et al. (2009).

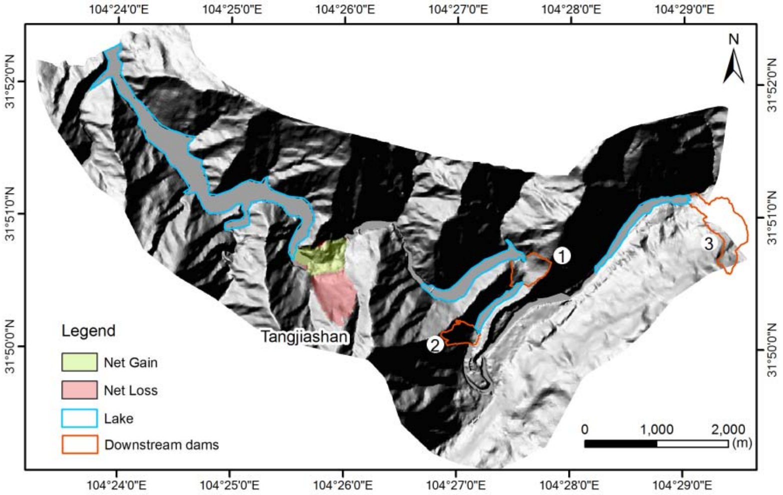

Figure 7.4 Post-earthquake 5-m DEM of the Tangjiashan dam and three of the four downstream dams (the fourth one is at the further downstream)

The detailed geological survey and boreholes were carried out by Chengdu Hydroelectric Investigation and Design Institute (CHIDI) in China (2008), revealing that the Tangjiashan landslide dam body is complex in its geological structure with four different layers from the top to the bottom (Fig. 7.3): (1) a 5-15 m thick layer of loose soil (60%) and rock fragments (40%) with grain sizes < 5 cm, which are easily erodible; (2) a 10-30 m thick layer of strongly-weathered rock blocks (6-40 cm in diameter) and boulders (1-2 m); (3) a 50-67 m thick layer consisting of partly intact rock strata retaining the original structure, which is relatively more densely packed and has lower permeability than the above two layers; and (4) a 6-15.7 m thick layer of silt, sand and fine gravels mostly from the alluvial deposits on the river bed.

7.2.2 Mitigation measures

The Tangjiashan landslide dam was formed in the monsoon season, thus the high inflow filled the lake rapidly and made the mitigation more urgent. Cui et al. (2010) mentioned that the daily increase of the lake volume was 7.2×10^6 m^3 from 23 May to 28 May 2008, corresponding to an increase of the upstream inundated area of about 6 km^2 per day. To reduce this risk, the Chinese government carried out several mitigation measures, including 24-h monitoring of the lake level and the dam stability situation, construction of a large emergency spillway and evacuation of the people in the possible flooded area. The spillway was designed as a trapezoid cross-section with a slope of 1:1.5 on both sides of the channel (Fig. 7.5A). It was 13 m wide, up to 9 m deep, 695 m long, and designed to be capable to accommodate 1,160 m^3/s. The longitudinal channel gradient of the spillway varies from 0.6% to 24% from the upper reaches to the lower reaches (Liu et al., 2009). The construction work started on 26 May and was completed on 1 June 2008, lowering the lowest point on the dam crest from 750m to 740.7 m. On 7 June when the impounded water level rose to the lowest point on the dam crest, the spillway started to drain the lake. The peak discharge of 6, 500m^3/s appeared at 12:30 h (LT) on 10 June and declined quickly to 79 m^3/s at 8:45 h (LT) on 11 June (Fig. 7.5B). During this period, 1.6×10^8 m^3 water was released and the water level of the lake dropped ~27 m (Cui et al., 2010). Due to the strong incision and erosion of the two top layers of the dam body, the spillway rapidly enlarged to a width of 100-130 m and a depth of 40-60 m eventually, and about 5×10^6 m^3 of material was eroded (Liu et al., 2009). Currently, the remaining part of the dam body is enhanced by concrete, still impounding about 8×10^7 m^3 of water (Fig. 7.5C and D).

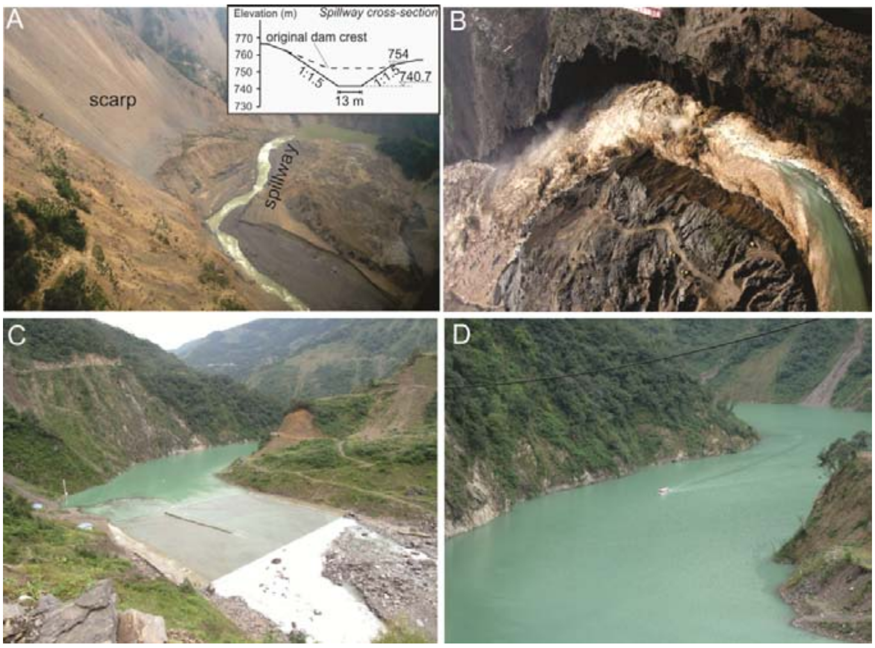

Figure 7.5 A: Helicopter view of the artificial spillway, inset shows the spillway cross-section; B: Releasing impounded water through the spillway, taken on June 10, 2008 when the discharge reached its peak (provided by Dr.Liu, N. from Ministry of Water Resources of the People's Republic of China); C: Remaining dam; D: Remaining lake, C and D were field photo taken in Sep, 2011.

7.3 Data and Methods

To simulate the dam-breach flood, we integrated the BREACH model (Fread, 1991) and the SOBEK 1D-2D model developed by Deltares (Dhondia and Stelling, 2002). The BREACH model can simulate the outflow hydrograph emanating from a dam and quantify the dam breach process. To calibrate the model, we reconstructed the 2008 event by setting up the spillway as a base scenario. The outputs of the BREACH model for different scenarios were subsequently used in the SOBEK model. The integrated simulation approach is depicted in the flowchart in Fig. 7.6.

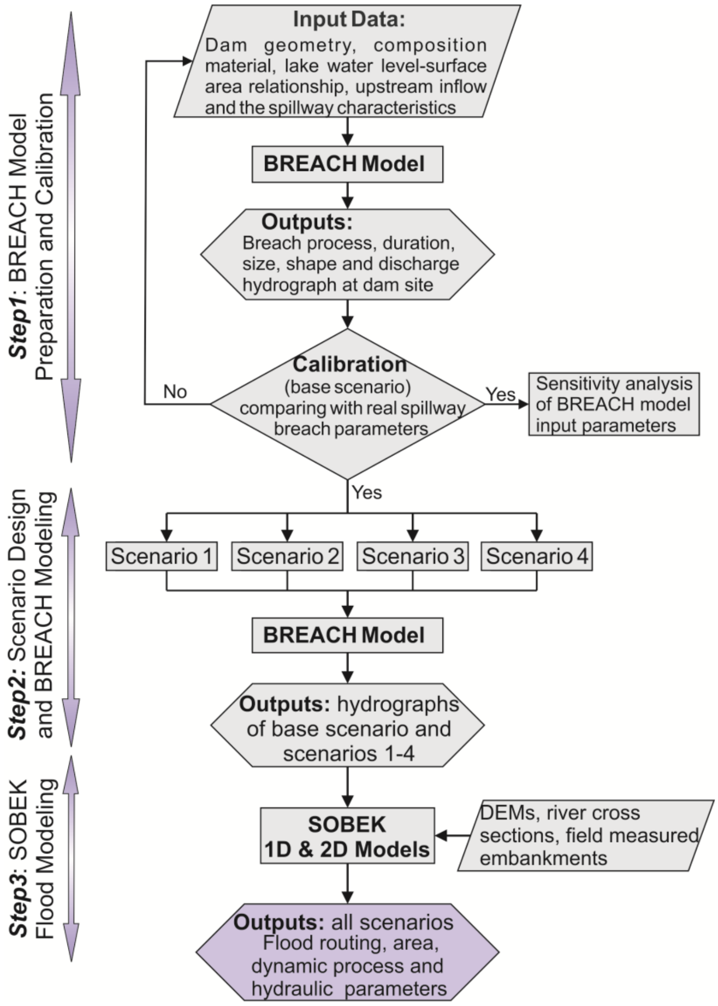

Figure 7.6 Flowchart of the integrated simulation approach

Four scenarios were considered in this study:

Scenarios 1: assuming that the dam would breach naturally without the spillway under the same hydrological condition as the base (calibrated) scenario for the purpose of evaluating the effects of the spillway.

Scenarios 2: the same as *Scenario 1*, but also considering that the breach of the Tangjiashan dam would cause the cascading breach of the four smaller downstream dams as shown in Fig. 7.1 and 7.4.

Scenarios 3: assuming that the dam would breach naturally given a 5-year return period flood discharge of 2190 m^3/s (see Table 7.1) as inflow to lake, under a heavy rainstorm situation. The 5-year return period was selected as it is likely to occur and can provide largely different outputs from other scenarios.

Scenarios 4: assuming the geotechnical parameters of dam material would be the most unfavourable (worst combination), leading to the whole breach of the dam and the completely releasing all the water in the barrier lake, which is the most catastrophic scenario compared to others.

7.3.1 BREACH model and data requirements

The BREACH model is a physically based mathematical model capable of predicting the breach characteristics and the discharge hydrograph from the breach of a man-made dam or a naturally-formed landslide dam, developed by Fread D.L. (1991) at the U.S. National Weather Service. This model is created by coupling the conservation of mass of the reservoir inflow, spillway outflow, and breach outflow with the sediment transport capacity of the unsteady uniform flow along a breach channel formed by erosion. Cencetti et al. (2006) modified the bed-load transport formula (the Meyer-Peter and Muller formula, modified by Smart, 1984) used in the BREACH model to better suit the simulation of channel erosion on landslide dams. The model can deal with breach caused by overtopping and piping, and has been applied to landslide dam breach modelling (Dai et al., 2010 and Li et al., 2011). Previous studies (Liu et al., 2009; Kuang et al., 2009; Cui et al., 2010) have a good agreement that the most probable failure mode of the Tangjiashan dam will be overtopping rather than piping and complete collapse, due to the its geological structure.

The required input parameters of the BREACH model include the relationship between the water level and the coverage area of the barrier lake, the upstream inflow rate to the barrier lake and the spillway geometry, the dam geometry and material geotechnical properties (Table 2). To obtain a range of material properties of the Tangjiashan dam, 15 samples from dam surface and boreholes were collected and tested in laboratory using various methods (e.g. the quick direct shear test, density test, permeability test and triaxial compression test etc.) by Chengdu Hydroelectric Investigation and Design Institute (CHIDI) in China (2008). Within this range, the most critical combination of the values was determined by the calibrated model (base scenario), which was also used in *Scenarios 1-3*. For *Scenario 4*, we have selected the most unfavourable geotechnical properties from the range. A detailed explanation of the physical meaning of the parameters and the model theory can be found in Fread (1991) and Cencetti et al. (2006).

Table 7.2 Input parameters for the BREACH model. A range of the dam material geotechnical properties was measured using laboratory tests shown in the brackets in the base scenario column.

Parameters	Base scenario	Scenarios 1 and 2	Scenario 3	Scenario 4
Lake parameters				
Inflow to lake (m^3/s)	90	90	2190	90
Lake water level, H (m)	740.7	750	750	750
Lake volume, V (m^3)	2.3×10^8	3.1×10^8	3.1×10^8	3.1×10^8
Average depth of lake, D (m)	30.6	33.7	33.7	33.7
Lake covered area, S_a (m^2)	7.4×10^6	9×10^6	9×10^6	9×10^6
Dam and spillway geometry				
Dam crest elevation, H_u (m)	750	750	750	750
Dam downstream face gradient, S	0.1	0.18	0.18	0.18
Initial breach bottom elevation, H_c (m)	740.7	-	-	-
Initial width of breach bottom, B_o (m)	13	-	-	-
Spillway length, L (m)	695	-	-	-
Geotechnical properties of dam material				
Unit weight, ρ (kg/m^3)	2400 (1900-2500)	2400	2400	1900
Internal friction angle φ, (°)	30 (24-36)	30	30	24
Cohesion, C (kPa)	13 (10-15)	13	13	10
D_{50} (m)	1.1 (0.4-2)	1.1	1.1	0.4
Porosity ratio, P_{or}	0.32 (0.28-0.45)	0.32	0.32	0.45

Note: D_{50} is defined as the grain diameter at which 50% of dam sediments are finer than; porosity ratio, P_{or} is the ratio of voids to the total volume of a specimen.

We used the pre-earthquake Digital Elevation Model with a spatial resolution of 25 meters to calculate the lake volume and coverage area for a given lake water level using the Open-Source GIS software ILWIS, which has a specific volume calculation function (Fig. 7.7). The result is consistent with previous estimations (Liu et al., 2009 and Cui et al., 2010), showing that the maximum capacity of the barrier lake is 3.1×10^8 m^3 with the lake water level at 750 m, and about 1.5 $\times10^8$ m^3 water was drained by the spillway as the lake water level was lowered from 740.7 m to 714.0 m. (Fig. 7.8).

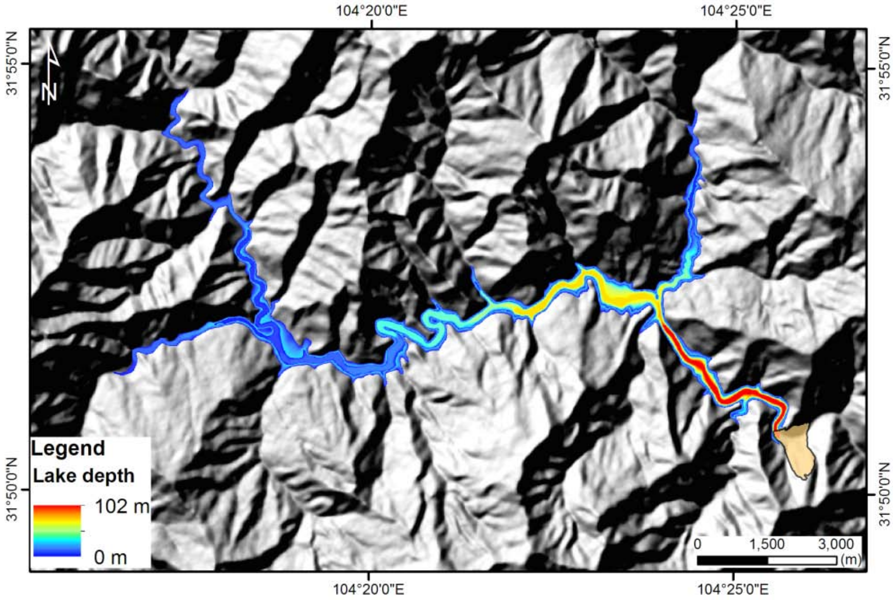

Figure 7.7 Variation of the barrier lake depth (the background is the shaded relief map of the pre-earthquake 25-m DEM)

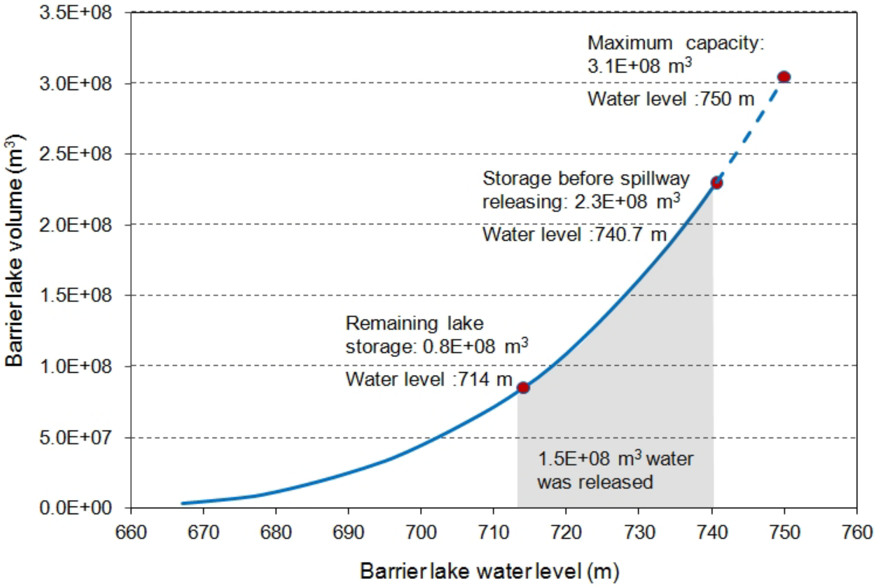

Figure 7.8 Relationship between the volume and the water level of the barrier lake

7.3.2 SOBEK 1D-2D model and data acquisition

The SOBEK 1D-2D model was used to calculate the spatial and temporal variation in flood parameters (e.g. the flood area, depth, velocity, arrival time etc.), which is a graphically orientated model. This model combines the one-dimensional river flow and two-dimensional overland flow, switching from 1D simulation of the flow in the river in the normal condition to 2D when water overflows the channel and inundates areas along the river (see Dhondia and Stelling, 2002 for the background principles and the detailed hydrodynamic equations). It has been used for reconstructing a large-magnitude outburst flood from a glacial lake by Carrivick (2006).

To set up the model for the Tangjiashan dam-break flood simulation following data were collected:

- Field surveyed cross-sections and embankments of the Tongkou river channel: 35 cross-sections and 40 embankments were measured in the field by a handheld GPS and a laser distance meter (Fig. 7.1).
- The pre-earthquake Digital Elevation Model (DEM) with 25 m spatial resolution was generated from 1:50,000 scale digital topographic maps by interpolating contour lines with intervals of 10 m and 20 m for low- and high-relief terrain, respectively (Fig. 7.1). The DEM was pre-processed before inputting into the model by filling the sinks and adding the embankments present at the time of the earthquake.
- The discharge and historical flood records of the Tongkou river were obtained from the Beichuan hydraulic stations and by reconstructing flood heights through field interviews (Table 7.1 and Fig. 7.1).
- The channel and floodplain roughness coefficients were estimated based on field observations and available land cover maps.

7.4 Results

7.4.1 BREACH model calibration and parameter sensitivity analysis

The BREACH model was calibrated through reconstructing the 2008 event, by adjusting the geotechnical material properties of the dam within the range of measured values, until the results were in correspondence with the observed hydrograph, showing a peak of ~6500 m^3/s appearing around 77 hrs after the first flow out of the spillway on 7 June 2008 (Fig. 7.9 and Table 7.3). The breach channel predicted by the model was a bit deeper and narrower than the observations (Table 7.3).

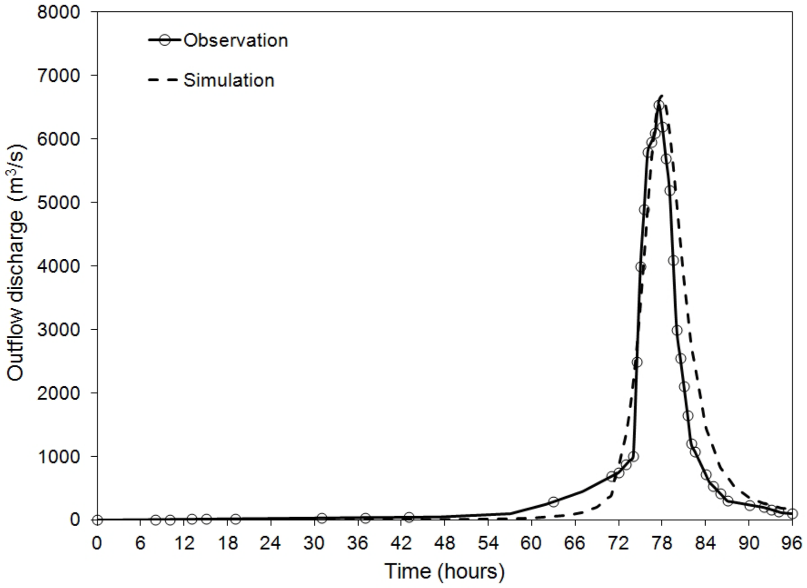

Figure 7.9 Outflow hydrographs from the BREACH model and the observational data

Table 7.3 BREACH model calibration results. The peak duration represents the lasted time for the discharge being over 1000 m^3/s; the peak appearing time is referred to the time from the first flow released through the spillway till the peak arrived; and the total released volume includes not only the lake volume but also the inflow volume during the breach.

Output parameters	Simulation	Observation
Peak discharge (m^3/s)	6678	6540
Total released-volume (m^3)	1.94×10^8	1.86×10^8
Peak duration (hrs)	12	9
Peak appearing time at the dam site (hrs)	77.9	77.5
Ultimate breach depth (m)	33.6	30.0
Ultimate breach width (m)	77.6	100
Ultimate breach bottom elevation (m)	706.4	710.0

A sensitivity analysis of dam material properties (Table 7.2) was carried out based on the *Scenario 1*. We found that the outflow hydrograph is more sensitive the grain size, the unit weight and the porosity (Fig. 7.10A-C), while less sensitive to the internal friction angle and cohesion. Larger grain size has little effect on the peak discharge, but postpones the peak arrival time obviously, as it controls the sediment transport rate (Fig. 7.10A). Lower values for the unit weight of the dam material lead to larger and faster outflow hydrograph peaks (Fig. 7.10B). The same effect is obtained by increasing the porosity (Fig.7.10 C).

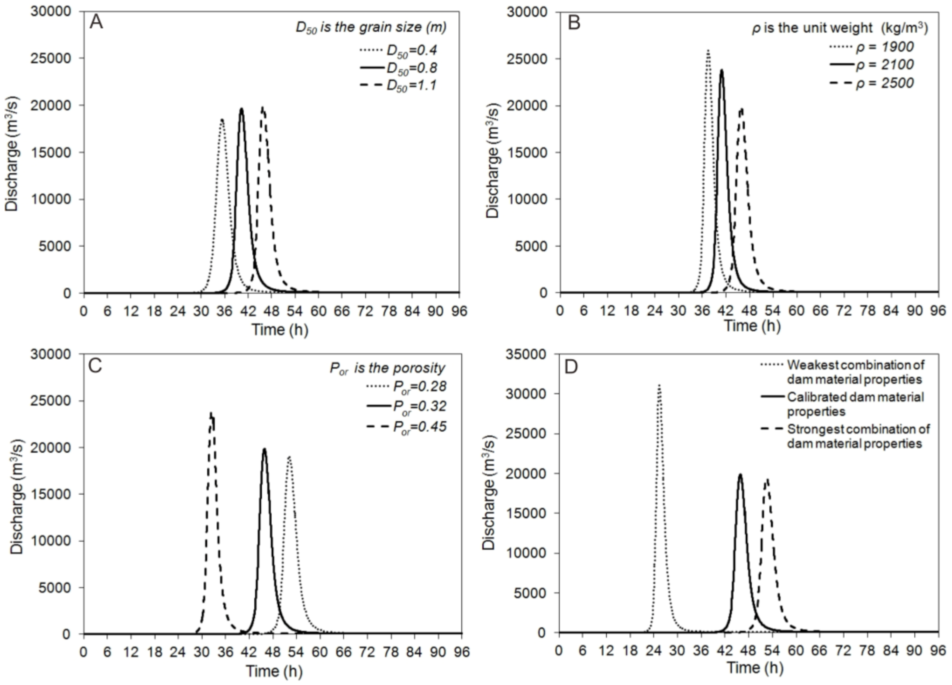

Figure 7.10 Sensitivity analysis of the BREACH model outflow hydrograph to dam material properties (A: D_{50} grain size; B: dam material unit weight; and C: porosity) and uncertainty analysis of the BREACH model outputs (D)

7.4.2 BREACH model output uncertainty and results

The uncertainties of the model outputs were analyzed by using the extreme values from the range of the dam material properties of the dam, and using the *Scenario 1.* The peak discharge and time of the flood generated from the weakest combination were ~10,000 m³/s higher and near 27 hrs earlier than those from the strongest case (Fig. 7.10D). The resulting variations of the flood 2D simulation will be discussed in Section 7.4.3.

The BREACH model results demonstrate that the most catastrophic scenario (*Scenario 4)* produces the highest flood peak discharge of ~ 75,500 m^3/s, but the shortest peak duration, the lasted time for the discharge being over 1000 m^3/s (Fig. 7.11). The peak arrival time of the flood is the shortest for *Scenario 3*, due to the higher inflow rate, the lake would be filled up faster and the dam breach process would be accelerated. Compared to *Scenario 1*, in the base (calibrated) scenario the peak discharge decreases significantly and the peak arrival time is delayed by nearly 32 hrs, which proves that the spillway played a crucial role in reducing the dam-break outburst flood hazard. The difference of the *Scenarios 1 and 2* is due to the cascading breach of the downstream dams, which can only be analyzed in the SOBEK model.

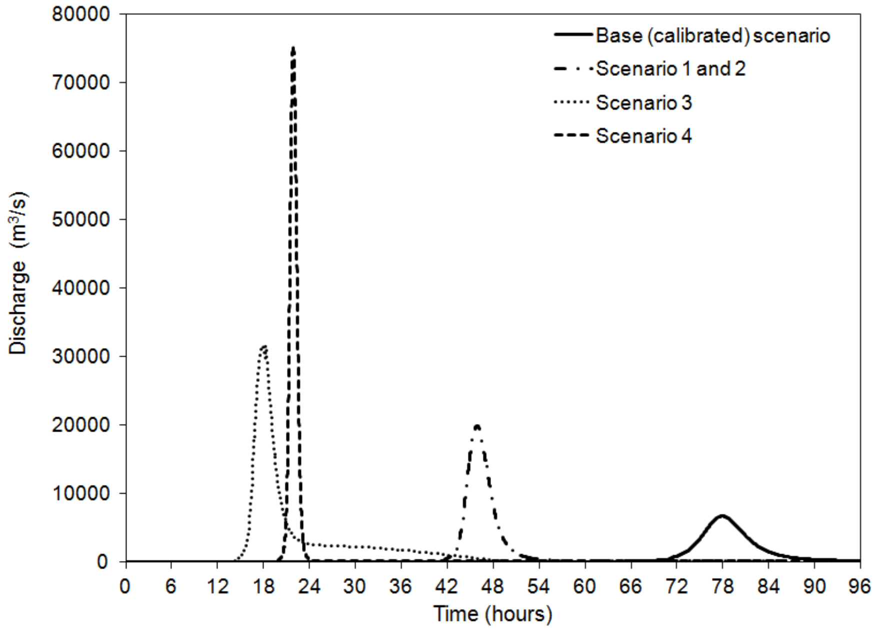

Figure 7.11 Output hydrographs of the BREACH model

7.4.3 SOBEK 1D-2D model results

The SOBEK 1D-2D modelling was done with a special focus on the following issues:

(1) Cascading breach of four dams at the downstream of the Tangjiashan dam

The *Scenario 2* (cascading breach of downstream dams) (Fig. 7.1 and 7.4) is based on the assumption that these dams would fail by overtopping, which is supported by the previous conclusion that the majority of the landslide dams worldwide were documented to fail by overtopping (Costa and Schuster, 1988). The overtopping time of the downstream dams can be estimated by their geometry, the terrain and the outflow hydrograph of the Tangjiashan dam. Table 7.4 shows that their overtopping time is all a bit earlier than the peak arrival time at the Tangjiashan dam (45.9 h, Fig. 7.11). They were estimated to be breaching during 44.2 to 45.3 hours after the Tangjiashan dam was overtopped. Fig. 7.12 demonstrates the cascading breach process of these dams.

Table 7.4 Estimated failure time (by overtopping) of the downstream dams. The dam height and lake volume were reported by Xu et al. (2009), and are consistent with the calculation results by comparing the pre- and post-earthquake DEMs.

Number	Dam height (m)	Lake volume (m^3)	Overtopping time (hrs)	Breach duration (hrs)
1	60	2.0×10^6	44.2	1.3
2	20	0.6×10^6	44.4	0.5
3	20	0.8×10^6	44.7	0.5
4	30	4.0×10^6	45.3	0.8

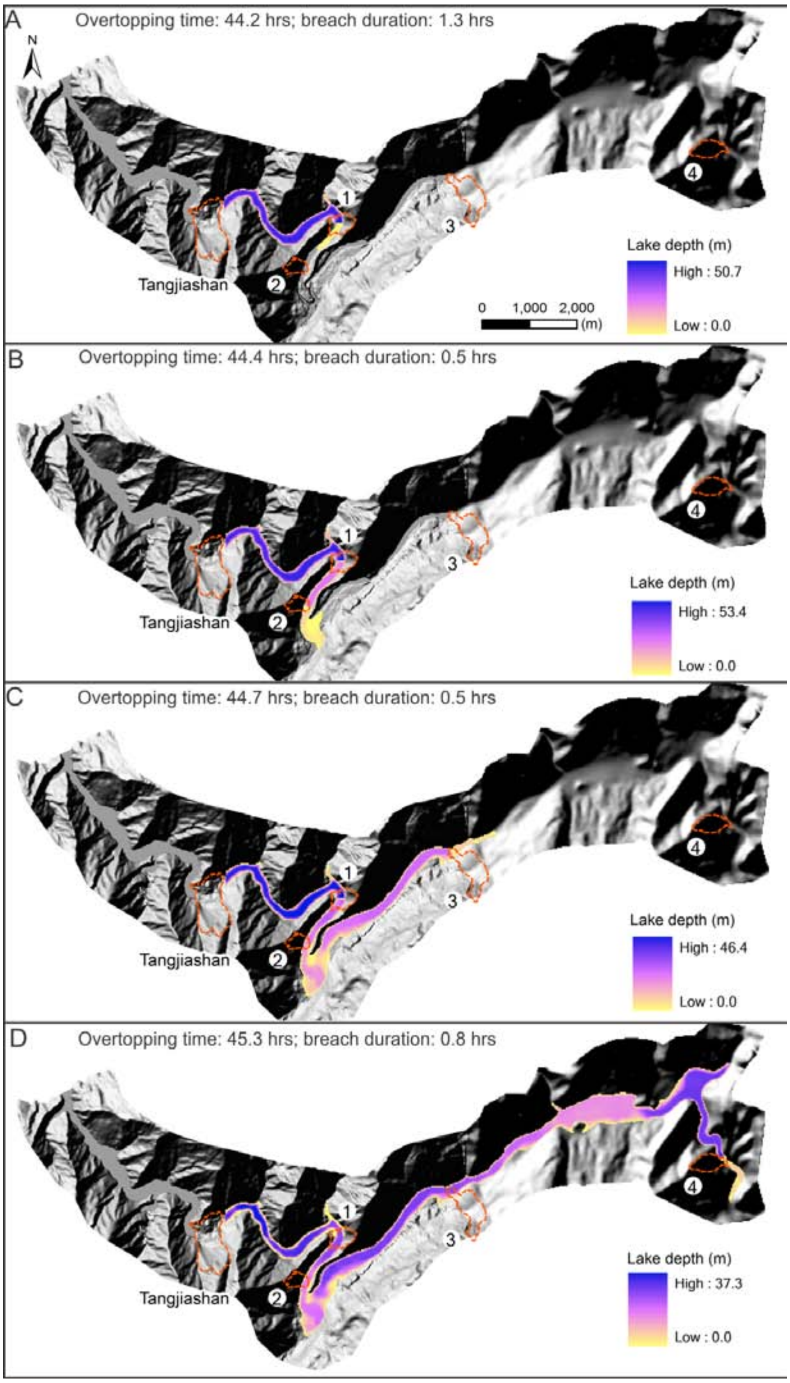

Figure 7.12 Cascading breach of dam ①-④ (A-D) at the downstream part of the Tangjiashan dam

(2) Simulation of flood hydrodynamics at the downstream towns

We selected four measurement locations in the major towns and Mianyang city located downstream of the Tangjiashan dam to check the flood hydraulic parameters (Fig. 7.1). The result of the base scenario agrees well with the observational data (Table 7.5), which further verified that the BREACH model provided robust results and the SOBEK 1D-2D model results resemble reality. Fig. 7.13 depicts the variation of the peak discharge and peak arrival time at these towns for different scenarios. In general, the peak discharge attenuates with an increase of the distance from the dam site. Flood control structures in Mianyang city were designed for a maximum discharge of 13,000 m^3/s, therefore all scenarios except the base scenario would cause flooding in the city (Fig. 7.13). Hence, the construction of the spillway did avoid serious flooding in Mianyang city. The *Scenario 4* would generate a peak discharge which is almost five times larger and an arrival time that is 1.3 hrs earlier than the base scenario. The comparison of the Scenarios 1 and 2 indicates that the cascading breach of the downstream dams did not significantly increase the peak discharge and delay of the peak arrival time. This is because these dams were estimated to impound rather small amounts of water (in total, 7.4×10^6 m^3), which is only 2% of the volume of the Tangjiashan lake (Fig. 7.13). The Tongkou town located nearest to the Tangjiashan dam downstream would be most influenced.

Table 7.5 SOBEK simulation results of base scenario compared with observational data. The peak arrival time is referred to as the time lag between the peak appearing time at the Tangjiashan dam site and the time when it reaches the downstream towns.

Towns	Distance fromdam (km)	SOBEK simulation results			Observations	
		Maximum depth (m)	Peak discharge (m^3/s)	Peak arrival time (h)	Peak discharge (m^3/s)	Peak arrival time (h)
Beichuan	5.3	6.4	6665.3	0.18	6500	0.20
Dengjia	12.3	11.7	6622.0	0.55	-	-
Tongkou	27.3	18.3	6589.1	1.18	6300	1.25
Qinglian	46.7	5.6	6481.0	2.25	-	-
Mianyang	74.9	4.1	6281.4	4.48	6100	4.33

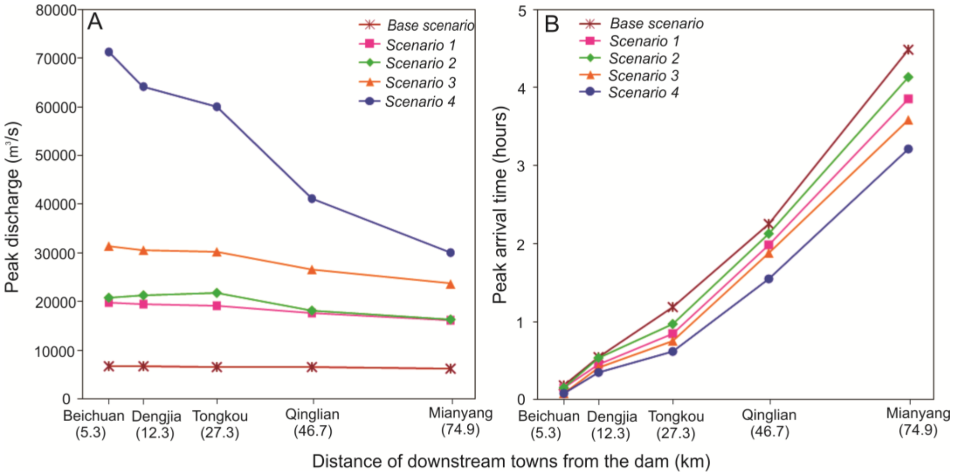

Figure 7.13 Flood peak discharge (A) and peak arrival (B) passing through the towns located downstream of the Tangjiashan dam.

Fig. 7.14 presents the flooded area, which occurs mainly on the floodplain, as the surrounding areas are substantial higher in elevation. The flooded area of *Scenarios 1 and 2* are almost identical (~62 km^2) due to the limited effect of the cascading breaches of the downstream dams. *Scenarios 3* and *4* may cause flooded areas of 70.5 and 78.7 km^2 respectively, including most parts of Mianyang city. The spatial variation in flood parameters in different scenarios is presented in Appendix 4.

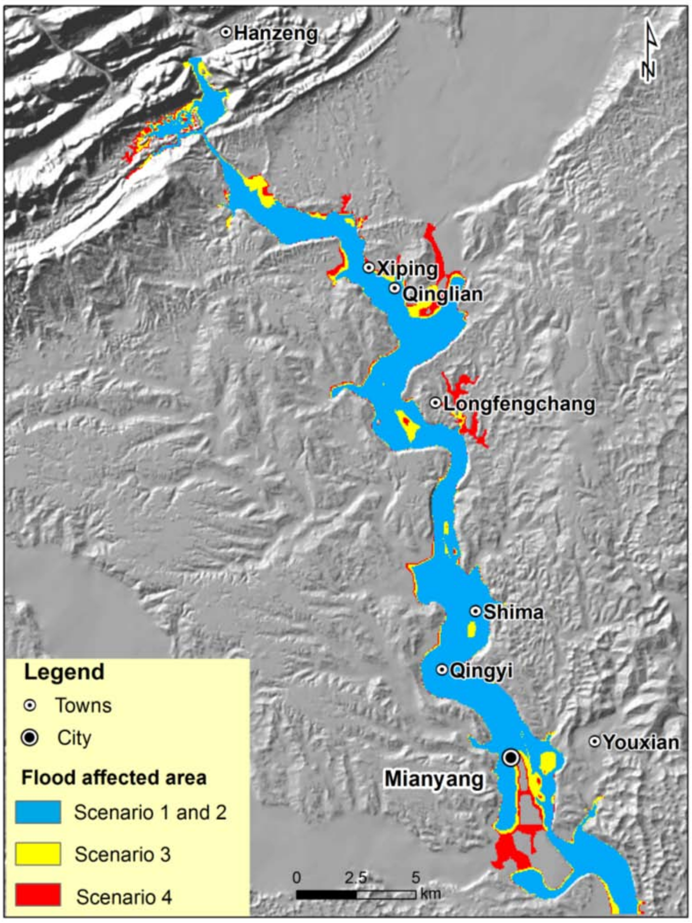

Figure 7.14 Modelled flooded area for different scenarios. The yellow and red areas represent the increase in flooded area for Scenario 3 and 4, respectively.

(3) Variations of the 2D flood simulation related to the SOBEK model input

The variations of the 2D flood simulation are highly related to the range of dam material properties. To assess these variations (uncertainties), we used as input in the SOBEK model the variations of BREACH model output hydrographs of both the weakest and strongest combinations of dam material properties shown in Fig. 7.10D. For *Scenario 1* as an example, the resulting flooded area varies between 61 km^2 (using the strongest dam properties) to 66 km^2 (using the weakest ones). The maximum flood depth generated from the strongest combination is generally smaller than that from the weakest case (Fig. 7.15A and B). The difference between them at the downstream towns is less than 1 m. In Mianyang city, the estimated variation of the flood depth is 3.09-3.65 m. Fig. 7.15C and D depict that the flood peak appearing time in the weakest case is about 27 hrs earlier than that in the strongest case, which is determined by the BREACH model output (Fig. 7.10D). The variability of the dam material properties causes a large uncertainty in the estimation of the peak arrival time, as it controls the dam breach speed and process. However, it has little influence on the flood inundation area and flood depth downstream, because which are more determined by the lake volume. The time here is referred as starting from the Tangjiashan dam was overtopped till the peak appeared at different locations. It can be converted to the relative time lag as shown in Table 7.5 and Fig. 7.13 by subtracting the peak appearing time at the Tangjiashan dam site (52.7 and 25.4 hrs for the strongest and weakest combinations, respectively; Fig. 7.10D). Thus, the time when it reaches Mianyang city after the peak appears at the dam site varies from 3.6 to 3.9 hrs.

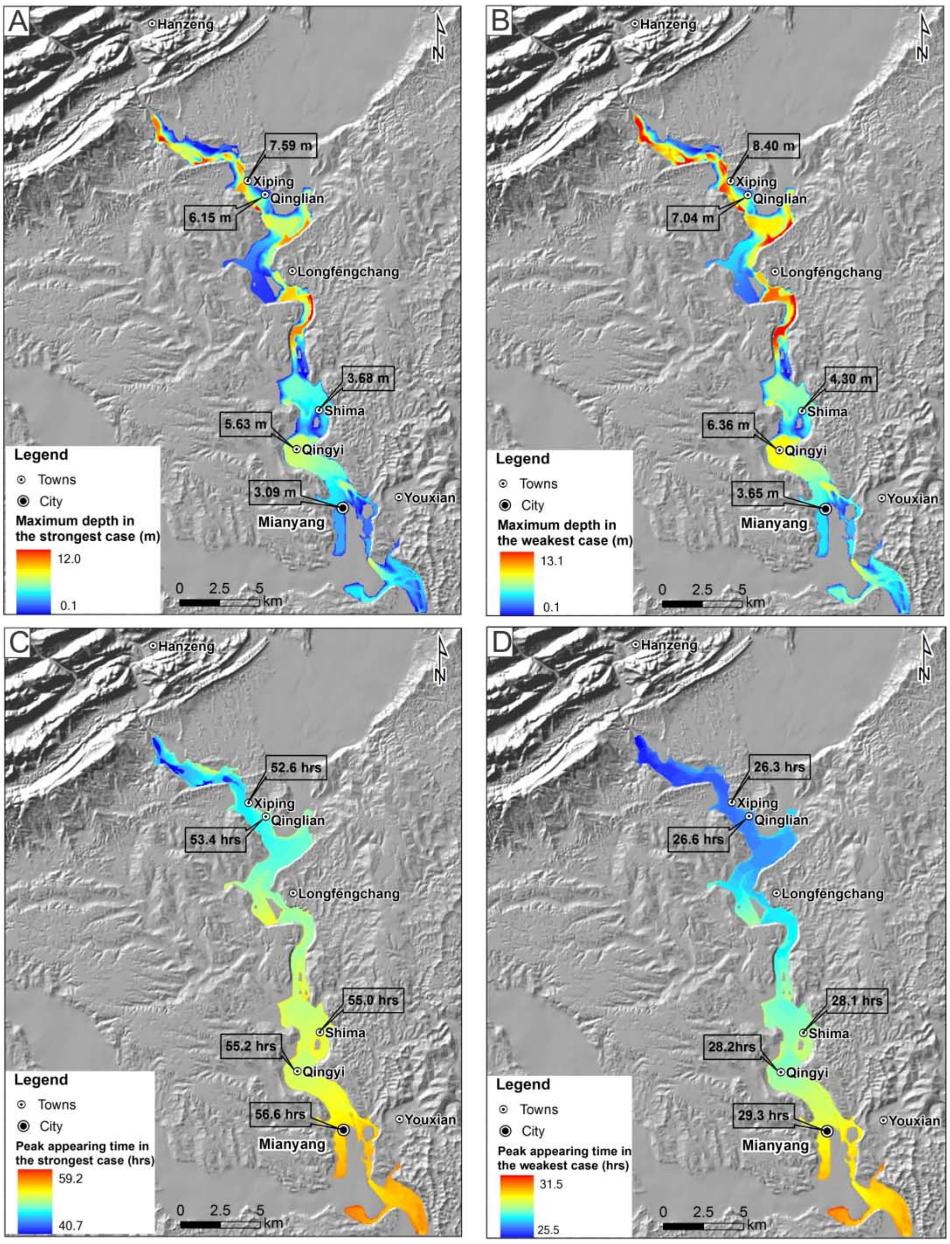

Figure 7.15 Variation related to the inputs in the SOBEK model expressed as: the maximum flood depth generated from the strongest and weakest combinations of dam material properties (A and B), and the peak appearing time in the strongest and weakest cases (C and D) based on the Scenario 1.

7.5 Discussion

After the sudden formation of a landslide dam, it is important to assess the dam stability and possible failure mode rapidly, to predict the dam-break flood magnitude, and to estimate the dam failure time and flood arrival time.

(1) Dam stability assessment

The Tangjiashan landslide dam was considered unstable and might fail by overtopping (Cui et al., 2010; Fan et al., 2012b). The BREACH model was able to reconstruct the Tangjiashan event well. However, it cannot account for the heterogeneity of the dam composition materials. The existence of a thick layer of partly intact rock strata in the middle and bottom part of the dam were the main factors that prevented the dam to breach or collapse totally, except in extreme situations (e.g., heavy rainstorm, strong aftershocks). A sensitivity analysis of these parameters can help to quantify the uncertainty and diminish the effect of this limitation. Further improvement of the model is needed especially for inhomogeneous landslide dams, but this is beyond the scope of this study.

(2) Dam-break flood magnitude estimation

The physically based and numerical models can provide more accurate results compared to the empirical method, but rely on more detailed dam and lake geometry data and geotechnical parameters of the dam materials. The predictions of peak discharge of the Tangjiashan dam from empirical equations proposed by previous studies in Table 7.6 are compared with those from the *Scenario 4* of BREACH model, as both of them consider the whole breach of the dam. These equations are based on either the lake volume (V_L) or on the potential energy (P_E), which is the product of dam height, lake volume, and specific weight of water. The predicted peak discharge (Q_p) varies from 1.28×10^4 to 7.55×10^4 m^3/s, with an average of 3.7×10^4 m^3/s. The deviations of different empirical equations might result from site-specific characteristics of the original sample lakes in different study areas. The empirical equations underestimate the peak discharge compared to the results of the BREACH model. We consider the prediction from the BREACH model to be more reliable, as the model was calibrated by observational data (Fig. 7.9). In the Tangjiashan case, the equation proposed by Clague and Evans (2000) provides the closest prediction compared to the results of the BREACH model.

Table 7.6 Comparison of predictions of the peak discharge of the Tangjiashan landslide dam from empirical equations and the BREACH model

Empirical equations	Reference	Peak discharge (m^3/s)
$Q_p=0.72V_L^{0.53}$	Evans (1986)	2.28×10^4
$Q_p=1.6V_L^{0.46}$	Walder and O'Connor (1997)	1.29×10^4
$Q_p=3.4V_L^{0.46}$	Cenderelli (2000)	2.74×10^4
$Q_p=0.0158P_E^{0.41}$	Costa and Schuster (1988)	1.28×10^4
$Q_p=0.063P_E^{0.42}$	Clague and Evans (2000)	7.08×10^4
BREACH model	Fread (1991)	7.55×10^4

Note: V_L equals to 3.1×10^8 m^3 for the Tangjiashan dam; and P_E is 2.55×10^{14} joules, given the dam height of 84 m and the specific weight of water of 9800 N/m^3.

(3) Dam failure time and flood arrival time prediction

The estimation of the dam failure time and flood arrival time is normally a race against the clock in an emergency situation. The prediction of dam overtopping (failure starting) time and peak arrival time at the downstream towns is crucial to determine the appropriate mitigation measures and available time for the engineering works or evacuation planning. The relation between the barrier lake volume and water level in Fig. 7.8 can be employed to predict the dam overtopping time for a given inflow rate. Using this method, we calculated the time needed for the lake to reach a certain level, given the measured-inflow in May 2008 (90 m^3/s) and the average discharge of the Tongkou river in the monsoon season (167 m^3/s) in Fig. 7.16. The time is referred to the number of days after the dam was formed, e.g. "0" represents 12 May 2008. The spillway was constructed when the lake level was ~720 m and designed to be overtopped when the lake level reached ~740 m, so the maximum available time for construction was 15 days with a 90 m^3/s inflow rate, and would be shortened to 8 days with the inflow increasing to 167 m^3/s. Our calculation was consistent with the reality that the spillway was overtopped on 7 June, 14 days after its construction on 26 May 2008.

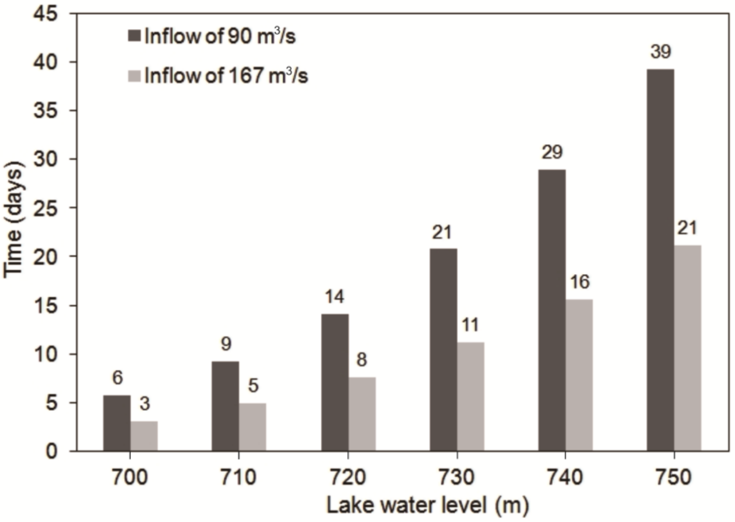

V_L (m³)	4.5E+7	7.2E+7	1.1E+8	1.6E+8	2.3E+8	3.1E+8

Figure 7.16 Time needed for the barrier lake rising to a certain level and the lake volume (V_L)

The peak arrival time at the downstream towns was predicted by the SOBEK 1D-2D hydraulic model in this study with the consideration of the terrain, channel and embankment features. Previous studies (Cui et al., 2010; Liu et al., 2010) have applied empirical equations to predict the flood peak discharge (Q_{PL} in Equation 7.1) and the peak arrival time (t in the unit of second in Equation 7.2) downstream from a landslide dam.

$$Q_{PL} = \frac{W}{\frac{W}{Q_P}+\frac{L}{VK}} \tag{7.1}$$

where L is the distance from the dam (m); W is the capacity of the lake (m³); Q_P is the peak discharge at the dam (m³/s), and VK is an empirical coefficient, equaling to 3.13 for rivers on plains, 7.15 for mountain rivers, and 4.76 for rivers flowing through the terrain with intermediate relief (Li, 1980).

$$t = k\frac{L^{1.4}}{W^{0.2}H_0^{0.5}h_m^{0.25}} \tag{7.2}$$

where k is a coefficient, ranging from 0.8 to 1.2 , H_0 is the lake water level before dam failure (m), and h_m is the water level (m) at a control section when the peak discharge reaches (Hydrological manual of Sichuan Province, 1979).

We compared our SOBEK simulation results of *Scenario 1* with the results of 50% dam failure scenario from the empirical equations (7.1) and (7.2) obtained by Cui et al. (2010) in Table 7.7, as in *Scenario 1* near half of dam material was estimated to be eroded. The empirical equations overestimated the peak discharge in the Beichuan and Dengjia towns, but underestimated it for the downstream towns and Mianyang city. The peak arrival time in the downstream towns was all overestimated, although they still can give a preliminary estimation, especially in the data scarcity and emergent situation.

Table 7.7 Peak flood discharge and arrival time obtained from SOBEK 1D-2D model and from the empirical equations (7.1) and (7.2)

Locations (towns)	Distance from dam (km)	SOBEK simulation results *Scenario 2*		Results from empirical equations	
		Peak discharge (m^3/s)	Peak arrival time (h)	Peak discharge (m^3/s)	Peak arrival time (h)
Beichuan	5.3	19752.3 ± 6512.7	0.15 ± 0.04	25028.3 ± 974.0	0.05 ± 0.02
Dengjia	12.3	19430.0 ± 6280.5	0.45 ± 0.02	22096.7 ± 1732.0	0.20 ± 0.06
Tongkou	27.3	19164.4 ± 6193.3	0.85 ± 0.05	17956.5 ± 2505.9	0.57 ± 0.16
Qinglian	46.7	17610.0 ± 5082.8	1.98 ± 0.04	14453.9 ± 2766.3	1.39 ± 0.40
Mianyang	74.9	16157.1 ± 4226.9	3.85 ± 0.03	11260.9 ± 2698.0	2.95 ± 0.85

Note: the values in the table are mean ± standard deviation. The range of the SOBEK simulation results is generated from the strongest and weakest combinations of dam material properties.

(4) Discuss the design of the spillway

The construction of the spillway played a significant role in preventing catastrophic flooding to the downstream towns and Mianyang city. However, in retrospect, there are lessons that can be learned for optimizing the design of the spillway and the excavation planning. For instance, the breach process was quite slow initially, with low discharge in the first three days after the breach (from 7 to 9 June), but suddenly accelerated on 10 June, reaching the peak of ~6500 m^3/s just within 3 hrs (Fig. 7.9). This was faster than expected and increased the risk of catastrophic failure. Through the BREACH model parameter sensitivity analysis, we found that decreasing the channel gradient and material porosity of the coating of the channel bottom would have reduced the peak flood discharge and delayed the arrival time effectively. In addition, Cui et al. (2010) recommended that a compound cross-section combining a triangular configuration with that of a small trapezoid would have increased the low initial discharge.

7.6 Conclusions

The Tangjiashan landslide dam was the most dangerous one of the approximately 800 coseismic landslide dams induced by the Wenchuan earthquake, and impounded the largest lake whose catastrophic outburst flooding threatened ~2.5 million people downstream. This research provided insights in the dam-breach process and the resulting flood propagation in possible scenarios. The integration of the BREACH model and the SOBEK model can provide predictions that agreed well with the observations. The uncertainty analysis revealed that the variability of the dam material properties will not significantly affect the flood inundation area and the maximum flood depth in the downstream area. However, it will cause large variation in the flood peak discharge and peak arrival time. We found that the cascading breach of the downstream dams did not have a major influence on the modelled flood parameters, because they had lake volumes much smaller than that of the Tangjiashan Lake. Based on the experience and lessons we learned from the simulations of the Tangjiashan event, we recommend making the mitigation measures on the basis of predictions from physically and hydraulically based models whenever possible. In data scarce situation, and in emergency situations with limited time to take decisions, the empirical method can also provide relatively good first-hand estimations.

8 Synthesis

This chapter is based on:

Xuanmei Fan, Cees J. van Westen, Victor Jetten, Qiang Xu, Tolga Görüm. 2013. Constructing an event tree for quantitative hazard assessment of earthquake-induced landslide dam break floods. (in preparation)

Runqiu Huang and **Xuanmei Fan**, 2013. The landslide story. Nature Geosciences 6, 325-326, 2013

8.1 Introduction

On May 12, 2008, a devastating earthquake of magnitude M_w 7.9 hit China's Sichuan province. The quake, originating in the Longmen Shan fault zone at the eastern margin of Tibetan Plateau, was the country's largest seismic event in more than 50 years. As well as the immediate devastation through shaking, the earthquake triggered more than 60,000 destructive landslides (Görüm et al., 2011) over an area of 35,000 km^2; the landslides caused about one-third of the total number of fatalities. More than 800 landslides during the earthquake blocked rivers, and thus produced numerous quake lakes that posed a serious threat to people downstream (Fan et al., 2012a).

The landslide damming and subsequent flood hazard are secondary effects of coseismic landslides. It is a representative domino hazard chain. This chapter aims to construct a generic event tree scheme to better understand such kind of cascading cause-effect relationships of an earthquake on the consequent geohazards. In the second part of this chapter we attempt to conclude the main results of this thesis (Chapter 3 to Chapter 7). The results from these chapters are used to estimate the probability at each node. The limitations and the scope for future research are also discussed in this chapter.

It is well known that earthquakes may trigger a series of multiple cascading geohazard phenomena. Quantifying the probability of these cascading phenomena following a triggering event has been a main research challenge. Event trees (ET) are recognized as a useful framework for discussing, from a probabilistic point of view, all the possible outcomes of adverse events (Newhall and Hoblitt, 2002). Basically, an ET is a graphical, hierarchical and tree-like representation of possible events in which branches are logical steps from a general prior event through increasingly specific subsequent events (intermediate outcomes) to final outcomes. In this way, an event tree shows the most relevant possible outcomes produced by the interactions among different hazardous events, i.e. cascading effects.

Marzocchi et al. (2004) developed the Bayesian event tree (BET) based on the event tree scheme created by Newhall and Hoblitt (2002), because the Bayesian approach can estimate the uncertainty and determine the posterior probability on the basis of a prior probability distribution. BET is regarded as a flexible tool to quantify the probabilities of any specific series of events, by combining all the relevant available information such as theoretical models, empirical and deterministic models, prior knowledge and beliefs, monitoring data and any kind of historical data. This method has been well developed and widely applied in the short- and long- term volcanic hazard assessment (i.e. Marzocchi et al., 2010; Neri et al., 2008; Selva et al., 2012). However, few studies have been done on applying the event tree approach in landslide hazard assessment (Wong et al., 1997 and 2002; Lee et al., 2000; Lacasse et al., 2008), let alone the application in seismically triggered geohazards. These applications are either descriptive or assign a single value rather than a probability distribution function to each node (defined as the point on the graph where new branches are created, Newhall and Hoblitt, 2002).

8.2 A Conceptual Event Tree Model for the Coseismic Landslide Dam Break Flood Assessment

A conceptual ET model for the earthquake-triggered hazard sequence was constructed, after many discussions with specialists in different fields (Fig. 8.1). A conditional probability, written in the form of $p(\theta_n|\theta_{n-1})$, is the probability of event n given that event ($n-1$) has occurred. As defined by Newhall and Hoblitt (2002), the probability of any outcome, $p(\theta_n)$, is the product of the probability of an initial event, $p(\theta_1)$, and all further conditional probabilities, as shown in Equation (8.1). The possible events at each node need not be mutually exclusive or exhaustive.

$$p(\theta_n)= p(\theta_1)\cdot p(\theta_2|\theta_1) \cdot p(\theta_3|\theta_2) \cdot\ldots\cdot p(\theta_n|\theta_{n-1}) \qquad (8.1)$$

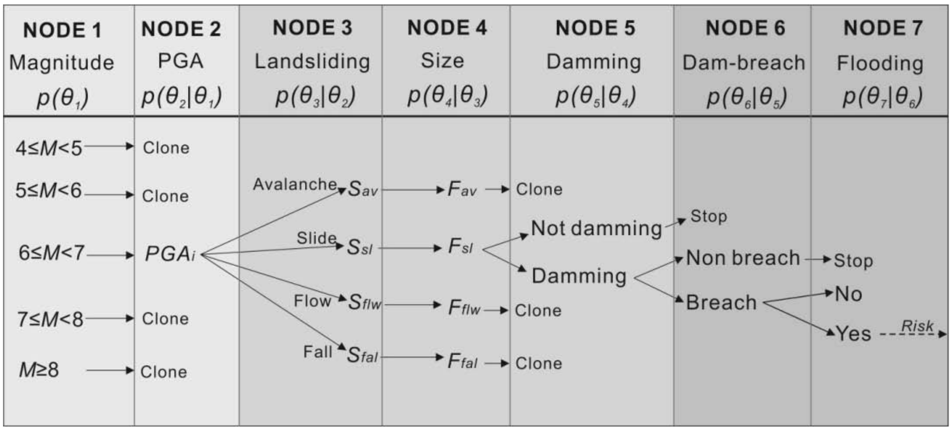

Figure 8.1 A conceptual event tree scheme for the earthquake-triggered geohazards. The seven steps of estimation progress from general to more specific events, which are explained in the text. Note that any branch that terminates with “Clone” is identical to the subsequent central branch. For example, at NODE1, the other magnitude bins are identical to the central

$6 \leq M < 7$ branch. AT NODE2, the PGA stands for the peak ground acceleration that is commonly used to represent amplitude of ground shaking. At NODE 3, the S_{av}-S_{fal} represents the spatial probability (susceptibility) of different types of landslides ($_{av}$=avalanche, $_{sl}$=slide, $_{flw}$=flow, $_{fal}$=fall types) given specified seismic source parameters (i.e. magnitude, fault type and length, PGA etc). At NODE 4, the F_{av}-F_{fal} means the size-frequency distribution of different types of landslides.

In the conceptual ET model, we define the probability for the subsequent outcomes at each node as follows:

$p(\theta_1)$ Probability that a given magnitude earthquake will be triggered by known active faults (seismogenic zones) in a region of interest;

$p(\theta_2|\theta_1)$ Probability that, given seismic source parameters (i.e. magnitude, distance to seismic source, fault type, geometry etc.) and site-specific parameters, the peak ground acceleration (PGA) in a certain area will reach a specified value;

$p(\theta_3|\theta_2)$ Probability that, given above seismic source parameters and ground motions, landslides with a specified type will happen in a certain area;

$p(\theta_4|\theta_3)$ Probability that, given the certain type of landslide occurrence, it will be of a specified size (in terms of landslide area or volume);

$p(\theta_5|\theta_4)$ Probability that, given a specified landslide size and type, the landslide will reach and block a river with a certain width, forming a landslide dam;

$p(\theta_6|\theta_5)$ Probability that, given a landslide dam formation, it will break;

$p(\theta_7|\theta_6)$ Probability that, given the dam breach, it will cause flooding to the exposures at downstream;

The ET starts from an assumed earthquake from known possible seismogenic faults, progressively develops to more specific levels, therefore it can also be called a scenario-based ET. Note that NODE 1 focuses on different known active fault zones (the seismic sources on which future earthquakes are likely to occur); NODE 2 is about ground motion variation in a region, which can be terrain or geological-unit based considering the site amplification effects; NODE 3 estimates the spatial probability (susceptibility) of coseismic landslides, which are normally grid-based; NODE 4 and 5 are specific for each potential landslide site; NODE 6 is then focusing on individual landslide dams; and NODE 7 is different for each area downstream of a potential dam site. NODE 2, 3 and 7 are spatial maps with probabilities, while the probability of the other nodes can be estimated as a single value. The ET can be extended for risk assessment by adding some nodes at the right side of NODE 7, for example, the probability that there will be exposed individuals or buildings given a specified flooding area; the probability that, given a certain type of elements at risk, the degree of damage (vulnerability) will reach a certain value; and the probability that losses will be caused by a specified flood.

8.3 Illustration of the Event Tree Model

After presenting the ET scheme, this section discusses possible approaches and methods for estimating probabilities at the successive nodes, based on the results from Chapter 3 to 7 and empirical relationships from literature. With the current level of knowledge it is still not possible to provide a quantitative example of the ET, as essential steps within it can still not be sufficiently quantified.

NODE 1 and NODE 2

These nodes estimate the probability of the seismologic source parameters, which control the coseismic landslide occurrence as discussed in Chapter 4. Earthquake activity varies spatially and temporally. Many seismologists have worked on probabilistic seismic hazard assessment of earthquakes, trying to estimate the likelihood of different levels of ground shaking intensity being experienced at a site (i.e. Cornell, 1968; Loh et al., 1991; Bommer, 2003; Cheng et al., 2007; Wang et al., 2012). Based on their results, we discuss the possible methods to estimate the probability at NODE 1 and 2.

(1) $p(\theta_1)$: what is the probability that a given magnitude earthquake will occur in a certain region within a given time interval?

At NODE 1, the different earthquake magnitude bins are determined based on the classification of NEIC (National Earthquake Information Center). The earthquakes with the magnitude lower than 4 are not considered, since these hardly triggered any catastrophic landslides according to the review on earthquake-induced landslides by Keefer (1984 and 2002). $p(\theta_1)$, the magnitude recurrence probability can be estimated by a statistical model, the Gutenberg-Richter magnitude-frequency power-law, using historic earthquake catalog of the known active fault zone:

$$log_{10}N=a - bM \tag{8.2}$$

where *N* is the cumulative number of earthquakes, *M* is the magnitude of the earthquake, a and b are constants. This relation allows, using the past earthquake records, to estimate the annul probability of an earthquake with the magnitude exceeding a certain value *Mt*:

$$p(\theta_1)=p(M>Mt)=10^{(a-bM)}/dT \tag{8.3}$$

where *dT* is the observation period. Just in order to illustrate this method better, we collected the earthquake catalog in the study area from U.S. Geological Survey. It covers the time window from 1966 to 2012, containing *N*=1177 events with magnitude $M \geq 3$. Fig. 8.2 shows that the observations with a magnitude lower than four do not follow the Gutenberg-Richter power-law, because of the incompleteness of the record of small earthquakes. Using a=7.37 and b=1.06, we calculate that a *M8* or larger event has an annual probability of about 0.16%. In other words, the Longmen Shan region can expect a *M8+* earthquake once about every 650 years, but the probability that this will be at the same fault or location as the 2008 Wenchuan earthquake is much lower (about once every 2000-4000 yr according to Shen et al., 2009; Ran et al., 2010). The annual probabilities of *M7+* and *M6+* earthquakes are 1.9% (about every 50 years) and 22.2% (about every 5 years), respectively.

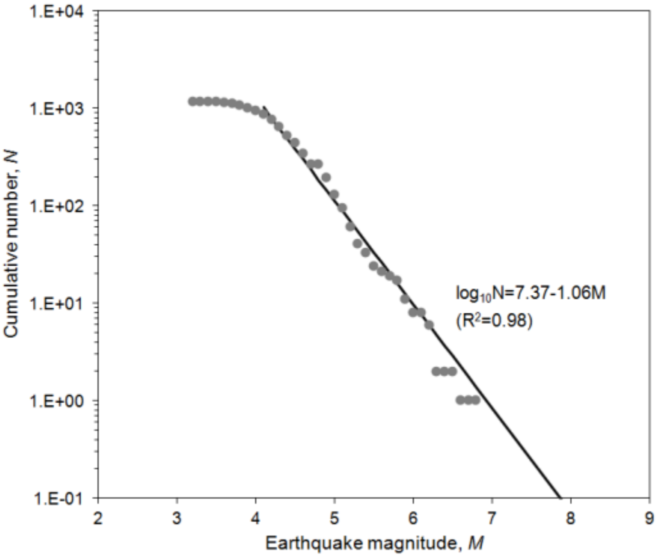

Figure 8.2 Frequency-magnitude distribution of events recorded in the study area in the period 1966-2012

This kind of estimation largely depends on the completeness of the dataset. Stein et al. (2012) stated that earthquake occurrence is typically more complicated than the models on which hazard maps are based, and that the available history of seismicity is almost always too short to reliably establish the spatiotemporal pattern of large earthquake occurrence. Another unsolved problem is that large earthquakes may not appear to occur at uniform time intervals, or to rupture exactly the same fault from one earthquake to next. The probability of this node can be more reliably estimated by fault movement measurement data, for example high precision GPS measurement and Interferometric Synthetic Aperture Radar (InSAR) (Kreemer et al., 2000; Bird et al., 2010).

(2) $p(\theta_2|\theta_1)$: how to estimate the probability of reaching a certain PGA level given specified seismic source parameters and site-specific parameters of a certain area?

Ground shaking generated by earthquakes plays a key role in triggering secondary hazards such as landslides, liquefaction, ground deformation etc. Amplitude of ground shaking is represented by acceleration (peak ground acceleration, PGA), velocity (peak horizontal velocity, PHV) and displacement. The acceleration differs for different frequencies of earthquake waves, and therefore in practice it is better to use spectral acceleration, instead of Peak Ground Acceleration, but this is more complicated to obtain over large areas, as it requires a network of strong motions seismographs. For coseismic landslide studies, PGA is commonly considered (Newmark, 1965 and Jibson et al., 2000). The intensity and duration of earthquake induced ground shaking at a site is a function of three main factors: earthquake source, medium of propagation as well as physical and geotechnical characteristics of the site denoted as site effects (Kramer, 1996; van der Meijde and Shafique, 2010; Shafique, 2011). The commonly used method for estimating ground motion is a simplified empirical attenuation models based on strong motion data. In this model, the effects of earthquake source are simplified as earthquake magnitude; the effects of wave propagation are specified by a distance to epicentre or fault; and the effects of the site are specified by a site category. The simplified equation of the empirical ground motion model is presented as:

$$ln(\mathrm{PGA})=f(M, D) \tag{8.4}$$

where f denotes the prediction function; M and D are the magnitude and source-to-site distance, respectively. The reader is referred to Cornell (1968); Bommer and Abrahamson (2006) and Wang et al. (2012) for a detailed description of the attenuation functions used for different tectonic setting.

This model (Equation (8.4)) has a large degree of uncertainty because it oversimplifies some key factors compared to the complex reality (Somerville, 2000; Bommer and Abrahamson, 2006). Several factors that are known to have a significant influence on PGA are not taken into account, such as depth of hypocenter, location of epicenter, source mechanism (thrusting, strike-slip or normal), fault geometry and location of the site on or off the hanging wall of fault (Somerville, 2000; Oglesby and Martin Mai, 2012). In addition, site amplification effects also play a critical role, which are often evaluated by exploring the impact of site-specific geology and topography (Havenith et al., 2003; Shafique, 2011). Seismologists have studied this effect by numerical simulations, experimental tests and seismic site response monitoring mostly at a local scale (Olsen, 2000; Stewart and Liu, 2000; Govindaraju and Bhattacharya, 2012; Lin and Wang, 2006; Wang et al., 2012). However, it remains a big challenge for seismologists and geologists due to the lack of detailed data on geological structure, topography and geomorphology. The PGA map used in this thesis is the USGS ShakeMap, which is quite rough and neglects the site amplification effects. Further improvement of the PGA map is needed for a better understanding of coseismic landslide occurrence.

NODE 3 to NODE 5

These nodes are about assessing the susceptibility of coseismic landslides and their consequent damming probability.

(3) $p(\theta_3|\theta_2)$: what is the spatial probability of a certain type of landslide given a specified seismic information scenario?

This is actually the susceptibility assessment of coseismic landslides of a certain type, which can be defined as a function of relevant spatial factors (i.e. seismic, geological, topographic and hydrological factors as discussed in Chapter 4):

$$S = f(L|X_1,\ldots\ldots X_n) \tag{8.5}$$

Equation (8.5) expresses the joint conditional probability that a given region will be affected by future landslides of a certain type given the n variables $X_1, X_2 \ldots X_n$ in the same region. There are a variety of methods available for landslide susceptibility assessment, including heuristic, deterministic and statistical approaches as reviewed in Chapter 4. The landslide susceptibility can be obtained based on pixels, terrain units, mapping units or catchment units etc. However, these methods are mainly based on the analysis of the relation between coseismic landslide occurrences and causal factors after the earthquakes have occurred, which is much more difficult to do this before an earthquake has occurred. Xu et al. (2012) have applied several susceptibility models in a catchment in the Wenchuan earthquake-hit region. Several studies have focused on susceptibility assessment of landslides triggered by other earthquakes, i.e. Loma Prieta earthquake (Miles and Keefer, 2007); Northridge earthquake (Parise and Jibson, 2000); Chi-Chi earthquake (Lee et al., 2008) and Kashmir earthquake (Kamp et al, 2008). In addition, most of these studies only considered the most commonly used factors, overlooking the geological structure and site amplification effects, due to the difficulty in obtaining and measuring these factors. Based on the field data and numerical modeling, Havenith et al. (2003) observed that amplification effects could be related to the local geological conditions and particularly to the surface morphology as well as to the presence of deeply weathered layers in rock strata. In the Wenchuan area, most of the landslides were observed in the upper part of the slopes and mostly convex slopes (especially where there was a major change in slope angle, so called “bumping” part of the slopes), indicating that the topographic amplification might play an important role.

As discussed by Gorüm (2013 in preparation, PhD thesis), research of earthquake-triggered landslides has less progressed than other natural triggers, owing not only to a limited number of available substantially complete event-inventories but also a less clearly defined understanding of the contribution of earthquake dynamics to coseismic landsliding. His research focuses on improving current state of coseismic landslide knowledge in a global context with exploring the role of earthquake rupture dynamics, faulting styles, topography and rock-type on the size, abundance and the distribution pattern of the coseismic landslides in different seismo-tectonic and geomorphic environments. He found that the abundance and the spatial distribution of coseismic landslides strongly vary with faulting styles. The observation from global data shows that thrust/reverse faults induce more coseismic landslides than normal and strike-slip faults, even if occurring on segments along a single main fault. However, these factors were largely neglected in previous studies. Therefore, more attention should be paid to them in order to improve the coseismic landslide susceptibility assessment in the future.

(4) $p(\theta_4|\theta_3)$: what is the size probability of a certain type of coseismic landslides?

The exact size of landslides is not possible to be predicted beforehand, due to the intrinsic complexity of landslide failure mechanisms, site-specific geomorphology, geological and tectonic setting, as stressed in Chapter 5. In case that there are available landslide inventories or an event-based inventory, the landslide size probability can be assessed by a magnitude (size)-frequency analysis. For the study of individual landslides at a large scale, detailed geological, geophysical survey and landslide deformation monitoring may help to estimate landslide size. The landslide size (area or volume) is an essential component for landslide dam hazard assessment, as it controls landslide runout and damming probability. The landslide size can be fitted to various statistic distributions as reviewed by van den Eeckhaut et al. (2007). We have applied the inverse gamma probability density function (Equation 6.1) from Malamud et al. (2004) to describe the area distribution of landslides, dams and barrier lakes in Section 6.1.

Various factors affect the magnitude-frequency distribution of landslides, such as topography (ten Brink et al., 2009), material strength (Stark and Guzzetti, 2009) and magnitude of triggering events (i.e. precipitation, rainfall intensity, earthquake magnitude and ground acceleration as discussed by Korup et al., 2012). Fig. 8.3A shows that earthquakes with different magnitude and seismic features produce landslides with different size-frequency distribution (Gorüm et al., 2012). Based on the detailed inventory and volume calculation (Equation 5.1) of landslides in the Mianyuan catchment as discussed in Chapter 5, we analyzed landslide volume distribution that varies largely with landslide type, following the inverse gamma distribution, as shown in Fig.8.3B. Debris/rock avalanches are generally larger than other types, followed by debris flows, debris/rock slides and rock falls.

A single probability density function (PDF) of landslide size is normally obtained for an entire region in previous studies (i.e, Guzzetti et al., 2002; Guthrie and Evans, 2004), regardless of the landslide type. However, toward to a more detailed hazard assessment in future, a PDF is required at each slope unit or other units classified according to certain criteria. To achieve this, a landslide inventory should be first divided into subgroups based on terrain, geological or other units, and then the size-frequency distribution analysis for each subgroup needs to be carried out to obtain the size distribution curves (i.e. Fig.8.3), but it might be difficult to make a reliable size-frequency distribution, if there are not enough landslide samples for such subunits.

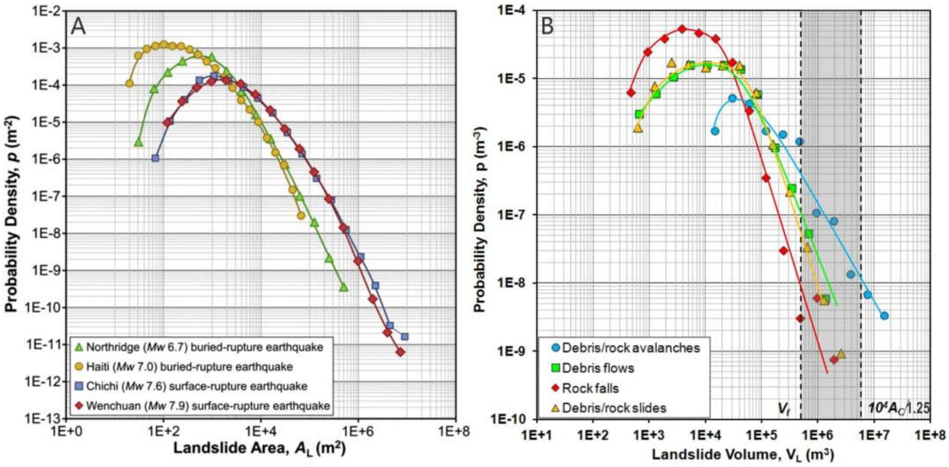

Figure 8.3 (A) Size distributions of landslide areas vary with different triggering events; (B) Size distributions of log-binned landslide volumes vary with landslide types

(5) $p(\theta_5|\theta_4)$: how to estimate the probability that a landslide of a certain type and size from a specific area can dam a river with a certain width?

This can be solved by the empirical model presented in Chapter 5, together with the landslide susceptibility assessment at NODE 3 and size-frequency distribution at NODE 4. The dam-formation threshold volume for a certain type of landslides was determined based on the empirical runout model as well as the correlation between river width and required damming volume, which allows a landslide to reach and block a river with a certain width (i.e. Fig.5.9, Chapter 5). Therefore, the damming probability is the likelihood of a landslide having a volume larger than the threshold volume, which can be expressed as the exceedance probability of Equation (6.1), the landslide size PDF:

$$p(\theta_5|\theta_4) = P(V_L > V_f) = \int_{V_f}^{\infty} p(V_L; \rho, a, s)dV_L$$

$$= \int_{V_f}^{\infty} \frac{1}{a\Gamma(\rho)} \left[\frac{a}{V_L - s}\right]^{\rho+1} exp\left[-\frac{a}{V_L - s}\right] dV_L \qquad (8.6)$$

where V_L is the potential landslide initiation volume, V_f is the dam-formation volume threshold, ρ, a and s are the coefficients, see Equation (6.1) for explanation. $p(\theta_5|\theta_4)$ equals to the area under the curve at the right side of the V_f in Fig. 8.3B, indicating that rock avalanches have the highest probability to dam a river in contrast to the other types, especially, rock falls.

NODE 6 and NODE 7

These two nodes are associated with the dam-break hazard evaluation.

(7) $p(\theta_6|\theta_5)$: how to estimate the dam-breach probability?

This node relates to the stability of landslide dams, which is a function of their geometry, internal structure, material properties, lake volume, inflow rate, and seepage processes (Costa and Schuster, 1988; Korup and Tweed, 2007). We tried to link the landslides and the consequent dam typology to the dam stability in Chapter 2. It is believed that the dams composed by large boulders or almost intact rock strata are more stable than those composed by unconsolidated fine debris. At large or detailed scale, the reliable stability assessment of landslide dams requires a geotechnical approach considering a variety of dynamic loading scenarios (Schneider et al., 2004). Geophysical methods such as seismic refraction and electrical resistivity can provide an insight into the internal structure of natural dams (Korup and Tweed, 2007). Wang et al. (2013) analyzed the internal structure of a rockslide dam induced by the Wenchuan earthquake by measuring the shear-wave velocity profile of the dam site. The monitoring of inflow and outflow (seepage) rate is also an essential component.

However, most of these factors are difficult to investigate, especially the internal structure and particle size distribution, which become evident only after dam failure. Therefore reliably predicting landslide-dam stability remains a key challenge, as discussed in Chapter 6. At the regional scale, the preliminary dam stability assessment in an emergency situation is in most cases carried out using a geomorphologic approach, such as the blockage index, $I_b = log(V_D/A_C)$ proposed by Casagli and Ermini (2003), which is shown in Equation (6.5). According to the observed data of landslide dams induced by the Wenchuan earthquake, we assume that dams with $I_b < 4$ will breach (Chapter 6), which is consistent with the threshold I_b obtained by previous studies in the Apennines (Casagli and Ermini, 1999) and in New Zealand (Korup, 2004). Therefore, the dam breach probability can be expressed as:

$$p(\theta_6|\theta_5) = \mathrm{P}(\log(V_D/A_C) < 4) = P(V_D < 10^4 A_C) = P(1.25 V_L < 10^4 A_C)$$

$$= \int_{V_f}^{10^4 A_C/1.25} \frac{1}{a\Gamma(\rho)} \left[\frac{a}{V_D - s}\right]^{\rho+1} exp\left[-\frac{a}{V_D - S}\right] dV_D \qquad (8.7)$$

where ρ, a and s are the coefficients, see Equation (6.1) for explanation, A_C is the catchment area upstream of the dam [km^2], V_D is the volume of the landslide dam [m^3], which is assumed to equal to 1.25 V_L (the landslide initiation volume in Equation (8.6)), considering a value of 25% volume expansion as suggested by Hungr and Evans (2004) for rock fragmentation. V_D also follows the inverse gamma distribution, so that $p(\theta_6|\theta_5)$ is equal to the area under the size-frequency curve between the vertical threshold line V_f and $10^4A_C/1.25$ depicted by the gray shaded area in Fig. 8.3B. Eventually, the dam formation and breach probability can be quantified. Note that there are some other indices or equations available for the dam stability assessment using the dam volume as one of the parameters (i.e. Ermini and Casagli, 2002; Peng and Zhang, 2012).

(8) $p(\theta_7|\theta_6)$: how to estimate the dam-break flood probability?

This node requires dynamic hydraulic modelling to estimate the spatial variation of flood parameters. The dam-break flood probability is controlled by the discharge capacity of the river that flows into the dammed lake and the probable flood parameters (flood peak discharge, depth, velocity and duration) that are determined by the lake volume, dam-breach process and downstream terrain. The flood parameters can be estimated by physically–based numerical models and GIS-based hydraulic models as discussed in Chapter 7. In Chapter 7, we have modelled a scenario-based dam-break flood of the largest landside-dammed lake, the Tangjiashan lake, by integrating the physically–based BREACH model and GIS-based SOBEK model. This integrated approach provided good predictions that agreed well with the observations, and is recommended to provide scientific support for the decision makers to determine the mitigation measures.

At the regional scale or in an emergency situation, the NODE 6 and 7 can be combined and simplified in order to rapidly assess the potential hazard of landslide dams. As discussed in our previous study (Xu et al., 2009), after the Wenchuan earthquake, the experts used three criteria (dam height, maximum capacity of barrier lake and composing materials of dam) to empirically rank the dam hazard into four levels (very high, high, moderate and low). The mitigation plan was made on the basis of this classification. Based on the experience and the lessons learned from the emergency mitigation of landslide dams induced by the Wenchuan earthquake, we propose a general work procedure for landslide dam mitigation after a lake is identified (Fig. 8.4). This procedure can be generally divided into two phases: rapid assessment of damming hazard and emergency mitigation based on preliminary investigation of landslide dams (which normally should be done within two weeks); and detailed investigation and monitoring of the relatively large dams that may be temporarily stabilized by emergency mitigation measures but still have a considerable failure probability.

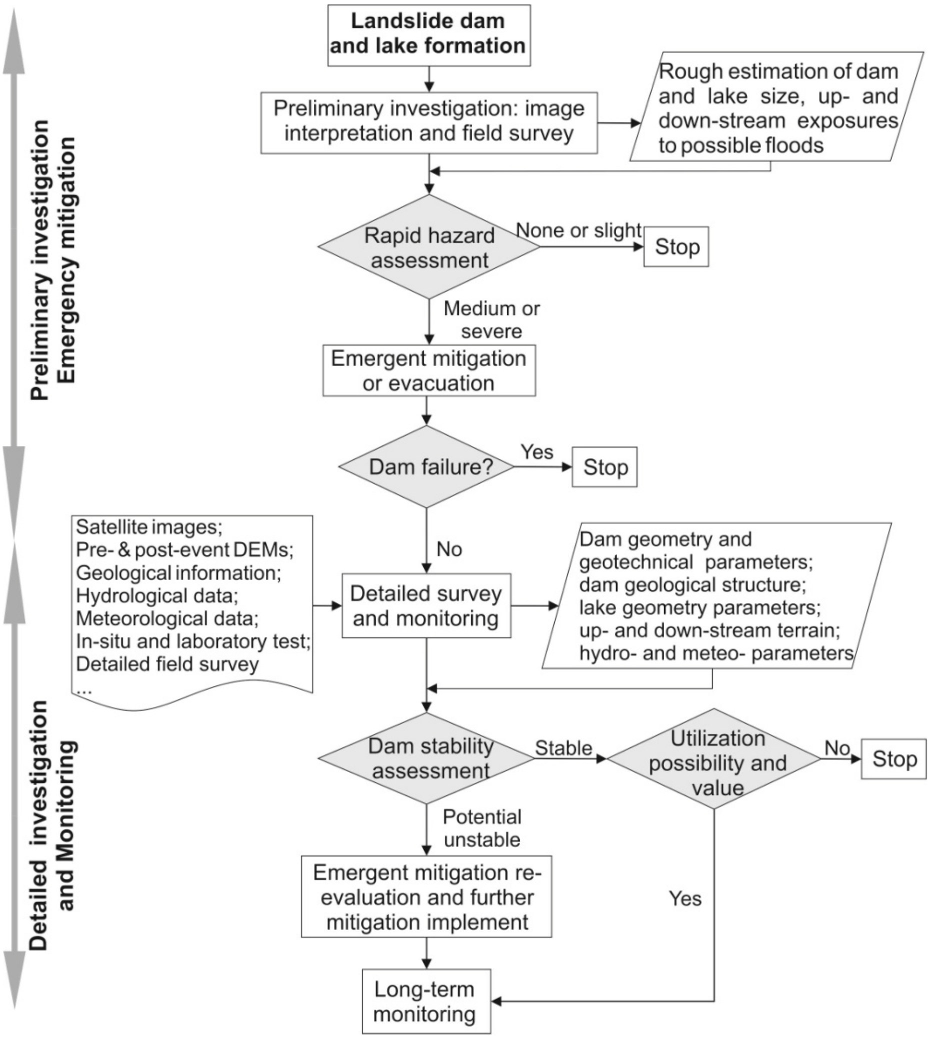

Figure 8.4 A generalized work procedure after a landslide dam is formed

To conclude, the coseismic landslide damming hazard could theoretically be quantified or estimated by the event tree model using a step-by-step approach (Fig. 8.1). The methods and issues discussed in previous chapters are closely linked to the probability estimation at different nodes of the event tree. The event tree model is a new and challenging approach with virtually no application in earthquake and landslide studies. This thesis constructs only a conceptual event tree model and discusses the possible methods for estimating the probability at each node, but unfortunately it does not provide an example of calculating the probability of landslide dam break floods in the study area. The main reason is that NODE 2 (PGA estimation) and NODE 3 (coseismic landslide susceptibility assessment) are beyond the scope of this study, therefore the probabilities of these two nodes are unknown. It obviously requires a large amount of available data and further theoretical research that makes the ET more suitable and applicable for assessing the cascading hazard of earthquakes and their consequent geohazards at the present stage. It is worth mentioning that the ET model is not necessarily started from the first node, i.e. the first node can be removed for a known (or already happened) earthquake. According to different situations, it can be started from every node.

8.4 Highlights of the Research

This research is the first systematic study on the landslide dams induced by the Wenchuan earthquake with an aim for a better understanding of the causes and effects of landslide dams. The main highlights of the research are:

- The research created one of the most comprehensive event-based inventories with an unprecedented number of landslide dams, enriching the worldwide landslide dam database. This is the first and foremost step for studying the characteristics, spatial distribution pattern and its controlling factors, formation and prediction of landslide dams.
- The research analyzed the immediate post-earthquake dynamics of landslide dams, their geomorphometric features and the spatial distribution pattern at the regional scale.
- The research developed an empirical-statistical method to predict coseismic landslide dam formation at a regional scale using landscape parameters that can be obtained from digital elevation models, considering river features and the corresponding landslide runout and volume required to block a river. The method needs empirical region specific parameters, but is generic enough to be tested in other regions.
- The research quantitatively analyzed the residence time of landslide dams and lakes, and discussed the implications of their gradual geomorphic decay, which is essential for assessing and mitigating potentially adverse consequences of coseismic river blockage, and its control on post-earthquake sediment flux in the Longmen Shan mountain.

- The research proposed an integrated approach using the physically-based BREACH model and the 1D-2D SOBEK hydrodynamic model to simulate the dam-breach floods for a number of possible scenarios of the Tangjiashan landslide dam that impounded the largest lake in the area. The effect of emergency mitigation measures was re-evaluated using the simulation results. The experience and lessons we learned from the Tangjiashan case will contribute to improving the hazard mitigation and risk management planning of similar events in future.
- We constructed a conceptual Event Tree model to evaluate the cascading cause-effect of geohazards associated with large earthquakes. The possible methods for estimating the probability at each node were discussed and linked with previous chapters. This model presents an overview picture of this research, which initiates from an assumed earthquake, to coseismic landslides and landslide dams, and ends with dam-break flooding hazard. It will contribute to a better understanding of the causes and effects of landslide dams as well as the multi-hazard assessment in the future.

8.5 Limitations and Future Scope of Research

This research has some inherent limitations owing mainly to the lack of source data, which also exist in most of the previous studies on the Wenchuan earthquake-triggered landslides and landslide dams. Future work is advised to obtain the following types of data:

- The best way to estimate landslide volume is by elevation change analysis using pre- and post- earthquake DEMs (i.e. Kerle, 2002; Martha et al., 2010). However, due to the scarcity of post-earthquake DEMs, the landslide volume used in this research was estimated by the volume-area scaling relationship (Equation 5.1). Even the inherent error can be quantified by the Monte-Carlo simulation (Chapter 6), but it cannot be reduced. Thus constructing multi-temporal DEMs using stereo-images, such as ASTER, Cartosat, ALOS etc. in the future, will improve this research and also contribute to detect the changes of post-earthquake landslide activities.
- So far, few previous studies on the landslides triggered by the Wenchuan earthquake have taken the geological structure into account, except in a number of case studies on the large-scale landslides (i.e. Dai et al., 2011; Huang et al., 2012). The difficulty lies in the measurement of geological structure over such a large area and also in regionalizing (i.e. interpolating) the point observations of 3D orientations of

structural discontinuities in rocks. This is one of the most important factors for landslide and landslide dam susceptibility assessment, and should be studied more in detail in the future research. Günther and Thiel (2009) suggested that deriving discrete directional information on individual rock discontinuity sets for suitable mapping units using vector statistical considerations may be useful in situations of data scarcity in large areas. Ghosh et al. (2010) followed the method from Günther (2003) created and compared digital structure models in two regions at different spatial scales: one small region with dense and well-distributed measurements and the other relatively large region with sparse and poorly-distributed data.

- There is very limited data on the hydrological and meteorological measurements, in-situ monitoring and geotechnical features of dam materials (i.e. sedimentological features, particle size distribution, friction, cohesion, permeability, porosity ratio etc.). This precludes the accurate evaluation of the role of different factors and also the stability of landslide dams. River width and other river features as introduced in Chapter 2 were mainly estimated using empirical scaling relationships, because spatially continuous measurement in a large region requires high-resolution imagery and time-consuming ground survey. This research mainly applied a geomorphologic approach to assess the dam stability, which can be definitely improved by considering above geotechnical and hydraulic features.
- This research analyzed the relative importance of triggering and geo-environmental factors for landslide occurrence using the bi-variate weight of evidence method (Chapter4). The weak point of this analysis is that it neglects the combining effect of factors, i.e., PGA with terrain (or geological) factors, terrain factors with distance-to-fault factor, etc. This can be improved by multi-variate analysis in the future.
- The contribution of coseismic landslides to sediment flux is evaluated by analyzing the landslide dam and lake volume decay after the earthquake in Chapter 6. Yet quantifying the post-earthquake sediment flux is still problematic, mainly because of the lack of pre- and post-earthquake sediment discharge data in many of the Longmen Shan's valleys. It is now realised that increases in sedimentation as a result of the shaking will pose a significant problem for rivers and their downstream reaches. Some riverbeds have already been raised by more than ten meters. This change raises the probability of floods in the future, and could severely affect the generation of hydropower. Therefore, specific efforts should be invested into quantifying and mitigating such kind of long-term post-earthquake hazards.
- This research presents a basic framework, the "Event Tree Model", to assess the multi-hazard associated with a high-magnitude earthquake.

This approach has been successfully applied in volcanic hazard assessment, but the application in earthquake-induced landslide research still needs to be tested in more regions. Future research is directed towards the improvement of the shortcomings of this method (that lacks a spatial capability), and better illustrating the model by giving a calculation example. Such a model needs to be integrated with GISs to cope with data with dynamical position and attributes. In addition, further effort is needed to assign conditional probabilities, with their confidence boundaries, to each of the primary and secondary branches (nodes).

Bibliography

Adams, J., 1981, Earthquake-dammed lakes in New Zealand: Geology, v. 9, no. 5, p. 215-219.

Alexander, D., 1988, Valtellina landslide and flood emergency, northern Italy: Disasters, v. 12, no. 3, p. 212-222.

Alford, D. K., and Schuster, R. L., 2000, Usoi Landslide Dam and Lake Sarez: An assessment of hazard and risk in the Pamir Mountains, Tajikistan, UN New York, NY, USA and Geneva, Switerland.

Asanza, M., Plaza-Nieto, G., Yepes, H., Shuster, R., and Ribadeneira, S., Landslide blockage of the Pisque River, northern Ecuador, *in* Proceedings Landslides. Glissements de terrain. Proceedings of the sixth international symposium1992, p. 10-14.

Ashford, S. A., Sitar, N., Lysmer, J., and Deng, N., 1997, Topographic effects on the seismic response of steep slopes: Bulletin of the Seismological Society of America, v. 87, no. 3, p. 701-709.

Awal, R., 2008, Study on landslide dam failure due to sliding and overtopping.

Ayalew, L., and Yamagishi, H., 2005a, The application of GIS-based logistic regression for landslide susceptibility mapping in the Kakuda-Yahiko Mountains, Central Japan: Geomorphology, v. 65, no. 1–2, p. 15-31.

Berman, M., 1977. Distance distributions associated with Poisson processes of geometric figures: Journal of Applied Probability, v. 14, p. 195–199.

Berman, M., 1986. Testing for spatial associations between a point process and another stochastic process: Applied Statistics, v. 35, p. 62–64

Bird, P., C. Kreemer, W.E., 2010. Holt. A long-term forecast of shallow seismicity based on the global strain rate map: Seismological Research Letters, v.81, p. 184-194.

Blahut, J., van Westen, C. J., and Sterlacchini, S., 2010, Analysis of landslide inventories for accurate prediction of debris-flow source areas: Geomorphology, v. 119, no. 1, p. 36-51.

Blake, M., Graymer, R. W., and Stamski, R., 2002, Geologic map and map database of western Sonoma, northernmost Marin, and southernmost Mendocino Counties, California, US Geological Survey.

Bommer, J. J., 2003, Uncertainty about the uncertainty in seismic hazard analysis: Engineering Geology, v. 70, no. 1, p. 165-168.

Bonham-Carter, G., Agterberg, F., and Wright, D., 1989, Weights of evidence modelling: a new approach to mapping mineral potential: Statistical Applications in Earth Sciences, v. 89, no. 9, p. 171-183.

Bonham-Carter, G. F., 1994, Geographic information systems for geoscientists: modelling with GIS, Access Online via Elsevier.

Bouchon, M., and Barker, J. S., 1996, Seismic response of a hill: the example of Tarzana, California: Bulletin of the Seismological Society of America, v. 86, no. 1A, p. 66-72.

Brown, C. A., and Graham, W. J., 1988, ASSESSING THE THREAT TO LIFE FROM DAM FAILURE1: JAWRA Journal of the American Water Resources Association, v. 24, no. 6, p. 1303-1309.

Brune, J. N., 2001, Shattered rock and precarious rock evidence for strong asymmetry in ground motions during thrust faulting: Bulletin of the Seismological Society of America, v. 91, no. 3, p. 441-447.

Brunetti MT, G. F., Rossi M., 2009, Probability distributions of landslide volumes: Nonlinear Processes in Geophysics, v. 16, p. 179–188.

Burchfiel, B. C., Zhiliang, C., Yupinc, L., and Royden, L. H., 1995, Tectonics of the Longmen Shan and Adjacent Regions, Central China: International Geology Review, v. 37, no. 8, p. 661-735.

Bureau, S. S., 1983, Diexi earthquake in 1933: Sichuan Science and Technology Press, Chengdu (in Chinese).

Canuti, P., Casagli, N., and Catani, F., Successes and failures in fighting landslides: some experiences from Italy and elsewhere, *in* Proceedings Sub-Forum on Science and Technology in support of Natural Disaster Reduction1999, p. 89.

Carrara, A., Crosta, G., and Frattini, P., 2003, Geomorphological and historical data in assessing landslide hazard: Earth Surface Processes and Landforms, v. 28, no. 10, p. 1125-1142.

Carrivick, J. L., 2006, Application of 2D hydrodynamic modeling to high-magnitude outburst floods: An example from Kverkfjöll, Iceland: J. Hydrol., v. 321, p. 187–199.

Casagli, N., and Ermini, L., 1999, Geomorphic analysis of landslide dams in the Northern Apennine: Transactions of the Japanese Geomorphological Union, v. 20, p. 219–249.

Casagli, N., Ermini, L., and Rosati, G., 2003, Determining grain size distribution of the material composing landslide dams in the Northern Apennines: sampling and processing methods: Engineering Geology, v. 69, no. 1–2, p. 83-97.

Castellanos Abella, E. A., and Van Westen, C. J., 2008, Qualitative landslide susceptibility assessment by multicriteria analysis: a case study from San Antonio del Sur, Guantánamo, Cuba: Geomorphology, v. 94, no. 3, p. 453-466.

Cencetti, C., Fredduzzi, A., Marchesini, I., Naccini, M., Tacconi, P., 2006, Some considerations about the simulation of breach channel erosion on landslide dams: Computat. Geosci., v. 10, p. 201–219.

Cenderelli, D. A., 2000, Floods from natural and artificial dam failures, In: Wohl, E.E. (Ed.), Inland Flood Hazards: Cambridge University Press, New York, p. 73–103.

Chai, H., Liu, H., and Zhang, Z., 1995, Landslide dams induced by Diexi Earthquake in 1933 and its environmental effect: Journal of Geological Hazards and Environment Preservation, v. 6, no. 1, p. 7-17.

Chai, H., Liu, H., Zhang, Z., 1995, The catalog of Chinese landslide dam events: Journal of Geological Hazards and Environment Preservation, v. 6, no. 4, p. 1–9(In Chinese).

Chai, H., Liu, H., Zhang, Z., Xu, Z., 2000, The distribution, causes and effects of damming landslides in China: Journal of the Chengdu Institute of Technology, v. 27, p. 302–307(In Chinese).

Chang, D. S., Zhang, L.M., 2010, Simulation of the erosion process of landslide dams due to overtopping considering variations in soil erodibility along depth: Nat. Hazards Earth Syst. Sci., v. 10, no. 4, p. 933-946.

Chen, H., Lin, G.-W., Lu, M.-H., Shih, T.-Y., Horng, M.-J., Wu, S.-J., and Chuang, B., 2011, Effects of topography, lithology, rainfall and earthquake on landslide and sediment discharge in mountain catchments of southeastern Taiwan: Geomorphology, v. 133, no. 3, p. 132-142.

Chen, R.-F., Chang, K.-J., Angelier, J., Chan, Y.-C., Deffontaines, B., Lee, C.-T., and Lin, M.-L., 2006, Topographical changes revealed by high-resolution airborne LiDAR data: The 1999 Tsaoling landslide induced by the Chi–Chi earthquake: Engineering Geology, v. 88, no. 3–4, p. 160-172.

Cheng, C.-T., Chiou, S.-J., Lee, C.-T., and Tsai, Y.-B., 2007, Study on probabilistic seismic hazard maps of Taiwan after Chi–Chi earthquake: J GeoEng, v. 2, no. 1, p. 19-28.

Chigira, M., Wu, X., Inokuchi, T., and Wang, G., 2010, Landslides induced by the 2008 Wenchuan earthquake, Sichuan, China: Geomorphology, v. 118, no. 3–4, p. 225-238.

China, C. H. I. a. D. I. C. i., 2008, Report on the stability assessment of the Tangjiashan landslide dam and up- and downstream slopes.

Chuang, S.-C., Chen, H., Lin, G.-W., Lin, C.-W., and Chang, C.-P., 2009, Increase in basin sediment yield from landslides in storms following major seismic disturbance: Engineering Geology, v. 103, no. 1, p. 59-65.

Clague, J. J., Evans, S.G., 1994, Formation and failure of natural dams in the Canadian Cordillera: Geological Survey of Canada Bulletin, v. 464, no. 35.

Clague, J. J., Evans, S.G., 2000, A review of catastrophic drainage of moraine-dammed lakes in British Columbia: Quaternary Sci. Rev., v. 19, p. 1763–1783.

Cornell, C. A., 1968, Engineering seismic risk analysis: Bulletin of the Seismological Society of America, v. 58, no. 5, p. 1583-1606.

Corominas, J., 1996, The angle of reach as a mobility index for small and large landslides: Canadian Geotechnical Journal v. 33, p. 260–271.

Corominas, J., and Moya, J., 2008, A review of assessing landslide frequency for hazard zoning purposes: Engineering Geology, v. 102, no. 3–4, p. 193-213.

Costa, J. E., Schuster, R.L, 1988, The formation and failure of natural dams: Geol. Soc. Am. Bull., v. 100, p. 1054-1068.

Costa, J. E., Schuster, R.L., 1991, Documented historical landslide dams from around the world: U.S. Geological Survey Open-File Report, v. 486, p. 91-239.

Cotecchia, V., and Melidoro, G., 1974, Some principal geological aspects of the landslides of Southern Italy: Bulletin of the International Association of Engineering Geology - Bulletin de l'Association Internationale de Géologie de l'Ingénieur, v. 9, no. 1, p. 23-32.

Crosta, G., Dal Negro, P., and Frattini, P., 2003, Soil slips and debris flows on terraced slopes: Natural Hazards and Earth System Sciences, v. 3, no. 1-2, p. 31-42.

Cruden, D. M., Miller, B.G.N., 2002, The Eureka River landslide and dam, Peace River Lowlands: Alberta. Can. Geotch. J., v. 39, p. 863–878.

Cruden, D. M., Varnes, D.J., 1996, Landslide types and processes. In: Turner, A.K., Schuster, R.L. (Eds.), Landslides, Investigation and Mitigation: Special Report, Transportation Research Board, National Research Council, v. 247, p. 36-75.

Cui, P., Dang, C., Zhuang, J., You, Y., Chen, X., Scott, K.M., 2010, Landslide-dammed lake at Tangjiashan, Sichuan Province, China (triggered by the Wenchuan earthquake, May 12, 2008): risk assessment, mitigation strategy, and lessons learned: Environ. Earth Sci., doi:10.1007/s12665-010-0749-2.

Cui, P., Zhu, Y.-y., Han, Y.-s., Chen, X.-q., and Zhuang, J.-q., 2009, The 12 May Wenchuan earthquake-induced landslide lakes: distribution and preliminary risk evaluation: Landslides, v. 6, no. 3, p. 209-223.

Dadson, S. J., Hovius, N., Chen, H., Dade, W. B., Lin, J.-C., Hsu, M.-L., Lin, C.-W., Horng, M.-J., Chen, T.-C., Milliman, J., and Stark, C. P., 2004, Earthquake-triggered increase in sediment delivery from an active mountain belt: Geology, v. 32, no. 8, p. 733-736.

Dai, F. C., Lee, C. F., Deng, J. H., and Tham, L. G., 2005, The 1786 earthquake-triggered landslide dam and subsequent dam-break flood on the Dadu River, southwestern China: Geomorphology, v. 65, no. 3–4, p. 205-221.

Dai, F. C., Xu, C., Yao, X., Xu, L., Tu, X. B., and Gong, Q. M., 2011, Spatial distribution of landslides triggered by the 2008 Ms 8.0 Wenchuan earthquake, China: Journal of Asian Earth Sciences, v. 40, no. 4, p. 883-895.

Davies, T., and McSaveney, M., 2002, Dynamic simulation of the motion of fragmenting rock avalanches: Canadian Geotechnical Journal, v. 39, no. 4, p. 789-798.

DeKay, M. L., and McClelland, G. H., 1993, Predicting loss of life in cases of dam failure and flash flood: Risk Analysis, v. 13, no. 2, p. 193-205.

Dhondia, J., and Stelling, G., Application of one-dimensional-two-dimensional integrated hydraulic model for flood simulation and damage assessment, *in* Proceedings Proc 5th International Conference in Hydroinformatics2002, Volume 1, p. 265-276.

Dhondia, J. F., Stelling, G.S, 2002, Application of the one dimensional-two dimensional integrated hydraulic model for flood simulation and damage assessment Hydroinformatics 2002: Proceedings of the Fifth International Conference on Hydroinformatics, Cardiff, UK.

Dikau, R., Brunsden, D., Schrott, L., Ibsen, M.L., 1996, Landslide recognition: identification, movement and Courses, Wiley & Sons, ISBN: 0-471-96477-8.

Dong, J.-J., Tung, Y.-H., Chen, C.-C., Liao, J.-J., and Pan, Y.-W., 2009, Discriminant analysis of the geomorphic characteristics and stability of landslide dams: Geomorphology, v. 110, no. 3–4, p. 162-171.

Duman, T. Y., 2009, The largest landslide dam in Turkey: Tortum landslide: Engineering Geology, v. 104, no. 1–2, p. 66-79.

Dunning, S. A., and Armitage, P., 2011, The grain-size distribution of rock-avalanche deposits: implications for natural dam stability, Natural and Artificial Rockslide Dams, Springer, p. 479-498.

Dunning, S. A., Petley, D.N., Rosser, N.J., 2005, The morphology and sendimentology of valley confined rock-avalanche deposits and their effect on potential dam hazard: Landslide risk management, Hungr, O., Fell, R., Couture, R. & Eberhardt, E. (eds), Taylor & Francis Group, London, ISBN 04 1538 043X.

Dunning, S. A., Rosser, N. J., Petley, D. N., and Massey, C. R., 2006, Formation and failure of the Tsatichhu landslide dam, Bhutan: Landslides, v. 3, no. 2, p. 107-113.

Efron, B., 1979, Bootstrap methods: Another look at jackknife: Annals of Statistics, v. 1, p. 1–26.

Ermini, L., and Casagli, N., 2003, Prediction of the behaviour of landslide dams using a geomorphological dimensionless index: Earth Surface Processes and Landforms, v. 28, no. 1, p. 31-47.

Evans, S., Delaney, K., Hermanns, R., Strom, A., and Scarascia-Mugnozza, G., 2011, The Formation and Behaviour of Natural and Artificial Rockslide Dams; Implications for Engineering Performance and Hazard Management, *in* Evans, S. G., Hermanns, R. L., Strom, A., and Scarascia-Mugnozza, G., eds., Natural and Artificial Rockslide Dams, Volume 133, Springer Berlin Heidelberg, p. 1-75.

Evans, S. G., 1986, The maximum discharge of outburst floods caused by the breaching of man-made and natural dams: Can. Geotch. J., v. 23, p. 385–387.

Evgeniou, T., Pontil, M., and Elisseeff, A., 2004, Leave One Out Error, Stability, and Generalization of Voting Combinations of Classifiers: Machine Learning, v. 55, no. 1, p. 71-97.

Fan, X., van Westen, C. J., Xu, Q., Görüm, T., and Dai, F., 2012a, Analysis of landslide dams induced by the 2008 Wenchuan earthquake: Journal of Asian Earth Sciences, v. 57, p. 25-37.

Fan, X., Tang, C.X., van Westen, C.J., Alkema D., 2012b, Simulating dam-breach scenarios of the Tangjiashan landslide dam induced by the Wenchuan earthquake: Natural Hazards and Earth System Sciences, v. 12, p. 3031–3044.

Fan, X., van Westen, C. J., Korup, O., Görüm, T., Xu, Q., Dai, F., Huang, R., and Wang, G., 2012c, Transient water and sediment storage of the decaying landslide dams induced by the 2008 Wenchuan earthquake, China: Geomorphology, v. 171–172,, p. 58-68.

Fan, X., Xu, Qiang, 2010, Xiejiadianzi landslide, Pengzhou. In: Xu, Q., Pei, X., Huang, R. (eds), Large-scale landslides induced by the Wenchuan earthquake. : Beijing: Science Press, p. 407-422 (book chapter in Chinese)

Fleiss, J.L., 1991. Statistical Methods for Rates and Proportions. John Wiley and Sons, Chichester.

Finnegan, N. J., Roe, G., Montgomery, D. R., and Hallet, B., 2005, Controls on the channel width of rivers: Implications for modeling fluvial incision of bedrock: Geology, v. 33, no. 3, p. 229-232.

Flint, J. J., 1974, stream gradient as a function of order, magnitude and discharge: WATER RESOURCES RESEARCH, v. 10, no. 5, p. 969-973.

Fread, D. L., 1991, BREACH: an erosion model for earth dam failures: Hydrologic Research Laboratory, US National Weather Service.

Gómez, H., and Kavzoglu, T., 2005, Assessment of shallow landslide susceptibility using artificial neural networks in Jabonosa River Basin, Venezuela: Engineering Geology, v. 78, no. 1–2, p. 11-27.

Günther, A., and Thiel, C., 2009, Combined rock slope stability and shallow landslide susceptibility assessment of the Jasmund cliff area (R¨ugen Island, Germany): Nat. Hazards Earth Syst. Sci., v. 9, p. 687–698.

García-Rodríguez, M. J., Malpica, J., Benito, B., and Díaz, M., 2008, Susceptibility assessment of earthquake-triggered landslides in El Salvador using logistic regression: Geomorphology, v. 95, no. 3, p. 172-191.

Gasiev, E., 1984, Study of the Usoy landslide in Pamir, in Proc: 4th Int'l . Symp. on Landslides, Toronto, v. 1, p. 511–515.

Gelebi, M., 1988, Topographic and geological amplifications determined from strong-motion and aftershock records of 3 March 1985 earthquake: Bull. Seis. Soc. Arm, v. 77, no. 4, p. 1147-1167.

Ghosh, S., Carranza, E. J. M., van Westen, C. J., Jetten, V. G., and Bhattacharya, D. N., 2011, Selecting and weighting spatial predictors for empirical modeling of landslide susceptibility in the Darjeeling Himalayas (India): Geomorphology, v. 131, no. 1, p. 35-56.

Görüm, T., Fan, X., van Westen, C. J., Huang, R. Q., Xu, Q., Tang, C., and Wang, G., 2011, Distribution pattern of earthquake-induced landslides triggered by the 12 May 2008 Wenchuan earthquake: Geomorphology, v. 133, no. 3–4, p. 152-167.

Görüm, T., van Westen, C.J., Korup, O., van der Meijde, M., Fan, X., van der Meer, D., 2012, Complex rupture mechanism and topography control symmetry of mass-wasting pattern, 2010 Haiti earthquake: Geomorphology, v.184, p.127-138 .

Govindaraju, L., and Bhattacharya, S., 2012, Site-specific earthquake response study for hazard assessment in Kolkata city, India: Natural hazards, v. 61, no. 3, p. 943-965.

Gupta, V., and Sah, M. P., 2008, Impact of the Trans-Himalayan Landslide Lake Outburst Flood (LLOF) in the Satluj catchment, Himachal Pradesh, India: Natural Hazards, v. 45, no. 3, p. 379-390.

Guthrie, R., and Evans, S., 2004, Magnitude and frequency of landslides triggered by a storm event, Loughborough Inlet, British Columbia: Natural Hazards and Earth System Science, v. 4, no. 3, p. 475-483.

Guzzetti, F., Ardizzone, F., Cardinali, M., Rossi, M., and Valigi, D., 2009, Landslide volumes and landslide mobilization rates in Umbria, central Italy: Earth and Planetary Science Letters, v. 279, no. 3–4, p. 222-229.

Guzzetti, F., Malamud, B. D., Turcotte, D. L., and Reichenbach, P., 2002, Power-law correlations of landslide areas in central Italy: Earth and Planetary Science Letters, v. 195, no. 3–4, p. 169-183.

Guzzetti, F., Mondini, A. C., Cardinali, M., Fiorucci, F., Santangelo, M., and Chang, K.-T., 2012, Landslide inventory maps: New tools for an old problem: Earth-Science Reviews, v. 112, no. 1–2, p. 42-66.

Guzzetti, F., Reichenbach, P., Cardinali, M., Galli, M., and Ardizzone, F., 2005, Probabilistic landslide hazard assessment at the basin scale: Geomorphology, v. 72, no. 1–4, p. 272-299.

Kreemer, C. , Holt, W.E., Goes, S., Govers,R., 2000, Active deformation in eastern Indonesia and the Philippines from GPS and seismicity data: Journal of Geophysical Research, v.105, p.663-680.

Hancox, G. T., McSaveney, M. J., Manville, V. R., and Davies, T. R., 2005, The October 1999 Mt Adams rock avalanche and subsequent landslide dam-break flood and effects in Poerua river, Westland, New Zealand: New Zealand Journal of Geology and Geophysics, v. 48, no. 4, p. 683-705.

Hancox, G. T., Perrin, N.D., Dellow, G.D., 1997, Earthquake-induced landsliding in New Zealand and implications for MM intensity and seismic hazard assessment: Lower Hutt: Institute of Geological and Nuclear Sciences Client Report 43601B prepared for Earthquake Commission Research Foundation, p. .

Haneberg, W. C., 2004, A Rational Probabilistic Method for Spatially Distributed Landslide Hazard Assessment: Environmental & Engineering Geoscience, v. 10, no. 1, p. 27-43.

Hao, K. X., Si, H., Fujiwara, H., and Ozawa, T., 2009, Coseismic surface-ruptures and crustal deformations of the 2008 Wenchuan earthquake Mw7.9, China: Geophysical Research Letters, v. 36, no. 11, p. L11303.

Harp, E. L., Crone, A.J., 2006, Landslides Triggered by the October 8, 2005, Pakistan Earthquake and Associated Landslide-Dammed Reservoirs: U.S. Geological Survey Open-file Report, v. 2006–1052, no. 13.

Havenith, H.-B., Vanini, M., Jongmans, D., and Faccioli, E., 2003, Initiation of earthquake-induced slope failure: influence of topographical and other site specific amplification effects: Journal of seismology, v. 7, no. 3, p. 397-412.

Heim, A., 1932, Bergsturz und Menschenleben. Zürich, Fretz und Wasmuth; 218: (English translation by Skermer NA. 1989. Landslide and human lives. BiTech Publishers, Vancouver, B.C.; 195).

Hermanns, R., Folguera, A., Penna, I., Fauqué, L., and Niedermann, S., 2011, Landslide Dams in the Central Andes of Argentina (Northern Patagonia and the Argentine Northwest), *in* Evans, S. G., Hermanns, R. L., Strom, A., and Scarascia-Mugnozza, G., eds., Natural and Artificial Rockslide Dams, Volume 133, Springer Berlin Heidelberg, p. 147-176.

Hermanns, R., Naumann, R., Folguera, A., and Pagenkopf, A., 2004, Sedimentologic analyses of deposits of a historic landslide dam failure in Barrancas valley causing the catastrophic 1914 Rio Colorado flood, northern Patagonia, Argentina: Landslides: evaluation and stabilization, Balkema, v. 2, p. 1439-1445.

Hermanns, R. L., Hewitt, K., Strom, A.L., Evans, E.G., Dunning, S.A., Scarascia-Mugnozza, G., 2011, The classification of rock slide dams: In: Natural and artificial rockslide dams. Lecture Series in Earth Sciences. Evans SG, Hermanns RL, Strom A, Scarascia Mugnozza, G (eds). Springer: Berlin, p. 581–593.

Hewitt, K., 1998, Catastrophic landslides and their effects on the Upper Indus streams, Karakoram Himalaya, northern Pakistan: Geomorphology, v. 26, no. 1–3, p. 47-80.

Hewitt, K., 2006, Disturbance regime landscapes: mountain drainage systems interrupted by large rockslides: Progress in Physical Geography, v. 30, no. 3, p. 365-393.

Hewitt, K., Gosse, J., and Clague, J. J., 2011, Rock avalanches and the pace of late Quaternary development of river valleys in the Karakoram Himalaya: Geological Society of America Bulletin, v. 123, no. 9-10, p. 1836-1850.

Horton, P., Jaboyedoff, M., and Bardou, E., Debris flow susceptibility mapping at a regional scale, *in* Proceedings 4th Canadian Conference on Geohazards2008, p. 399-406.

Hovius, N., Meunier, P., Lin, C.-W., Chen, H., Chen, Y.-G., Dadson, S., Horng, M.-J., and Lines, M., 2011, Prolonged seismically induced erosion and the mass balance of a large earthquake: Earth and Planetary Science Letters, v. 304, no. 3–4, p. 347-355.

Hovius, N., Stark, C.P., Chu, H.T., Lin, J.C., 2000, Supply and removal of sediment in a landslide-dominated mountain belt: Central Rang, Taiwan: The Journal of Geology, v. 100, p. 73-89.

HSÜ, K. J., 1975, Catastrophic Debris Streams (Sturzstroms) Generated by Rockfalls: Geological Society of America Bulletin, v. 86, no. 1, p. 129-140.

Huang, R., and Fan, X., 2013, The landslide story: Nature Geoscience, v. 6, no. 5, p. 325-326.

Huang, R., Pei, X., Fan, X., Zhang, W., Li, S., and Li, B., 2012, The characteristics and failure mechanism of the largest landslide triggered by the Wenchuan earthquake, May 12, 2008, China: Landslides, v. 9, no. 1, p. 131-142.

Huang, R. Q., and Li, W. L., 2009, Analysis of the geo-hazards triggered by the 12 May 2008 Wenchuan Earthquake, China: Bulletin of Engineering Geology and the Environment, v. 68, no. 3, p. 363-371.

Hungr, O., 1995, A model for the runout analysis of rapid flow slides, debris flows, and avalanches: Canadian Geotechnical Journal, v. 32, no. 4, p. 610-623.

Hungr, O., and Evans, S., 2004, Entrainment of debris in rock avalanches: An analysis of a long run-out mechanism: Geological Society of America Bulletin, v. 116, no. 9-10, p. 1240-1252.

Hutchinson, J., 1986, A sliding-consolidation model for flow slides: Canadian Geotechnical Journal, v. 23, no. 2, p. 115-126.

Hutchinson, J. N., Kojan, E., 1975, The Mayunmarca landslide of 25th April, 1974, Peru: UNESCO Report Serial No. 3124 Paris, UNESCO.

Iverson, R. M., 1997, The physics of debris flows: Reviews of geophysics, v. 35, no. 3, p. 245-296.

Iverson, R.M., Denlinger, R.P. 2001, Flow of variably fluidized granular masses across three-dimensional terrain: 1. Coulomb mixture theory: Journal of Geophysical Research, v106 (B1), p.537-552.

Iverson, R.M., Reid, M.E., Logan, M., LaHusen, R.G., Godt, J.W., and Griswold, J.P., 2011, Positive feedback and momentum growth during debris-flow entrainment of wet bed sediment: Nature Geoscience, v. 4, no. 2, p. 116–121.

Jaboyedoff, M., and Labiouse, V., Preliminary assessment of rockfall hazard based on GIS data, *in* Proceedings 10th International Congress on Rock Mechanics ISRM2003, p. 575-578.

Jibson, R. W., Harp, E. L., and Michael, J. A., 2000, A method for producing digital probabilistic seismic landslide hazard maps: Engineering Geology, v. 58, no. 3–4, p. 271-289.

Jonkman, S., Bočkarjova, M., Kok, M., and Bernardini, P., 2008, Integrated hydrodynamic and economic modelling of flood damage in the Netherlands: Ecological Economics, v. 66, no. 1, p. 77-90.

Jonkman, S. N., and Kelman, I., 2005, An analysis of the causes and circumstances of flood disaster deaths: Disasters, v. 29, no. 1, p. 75-97.

Kamp, U., Growley, B. J., Khattak, G. A., and Owen, L. A., 2008, GIS-based landslide susceptibility mapping for the 2005 Kashmir earthquake region: Geomorphology, v. 101, no. 4, p. 631-642.

Kawabata, D., and Bandibas, J., 2009, Landslide susceptibility mapping using geological data, a DEM from ASTER images and an Artificial Neural Network (ANN): Geomorphology, v. 113, no. 1–2, p. 97-109.

Kayen, R., Mitchell, J., Seed, R., and Nishio, S., 1998, Soil liquefaction in the east bay during the earthquake: US Geological Survey professional paper, no. 1551B.

Keefer, D. K., 1984, Landslides caused by earthquakes: Geological Society of America Bulletin, v. 95, no. 4, p. 406-421.

Keefer, D. K., 2000, Statistical analysis of an earthquake-induced landslide distribution—the 1989 Loma Prieta, California event: Engineering Geology, v. 58, no. 3, p. 231-249.

Keefer, D. K., 2002, Investigating Landslides Caused by Earthquakes – A Historical Review: Surveys in Geophysics, v. 23, no. 6, p. 473-510.

Kerle, N., 2002, Volume estimation of the 1998 flank collapse at Casita volcano, Nicaragua: a comparison of photogrammetric and conventional techniques: Earth surface processes and landforms, v. 27, no. 7, p. 759-772.

Khazai, B., and Sitar, N., 2004, Evaluation of factors controlling earthquake-induced landslides caused by Chi-Chi earthquake and comparison with the Northridge and Loma Prieta events: Engineering Geology, v. 71, no. 1–2, p. 79-95.

Kirby, E., and Ouimet, W., 2011, Tectonic geomorphology along the eastern margin of Tibet: Insights into the pattern and processes of active deformation adjacent to the Sichuan Basin: Geological Society, London, Special Publications, v. 353, no. 1, p. 165-188.

Kirby, E., Whipple, K. X., Burchfiel, B. C., Tang, W., Berger, G., Sun, Z., and Chen, Z., 2000, Neotectonics of the Min Shan, China: Implications for mechanisms driving Quaternary deformation along the eastern margin of the Tibetan Plateau: Geological Society of America Bulletin, v. 112, no. 3, p. 375-393.

Kirby, E., Whipple, K. X., Tang, W., and Chen, Z., 2003, Distribution of active rock uplift along the eastern margin of the Tibetan Plateau: Inferences from bedrock channel longitudinal profiles: Journal of Geophysical Research: Solid Earth, v. 108, no. B4, p. 2217.

Koi, T., Hotta, N., Ishigaki, I., Matuzaki, N., Uchiyama, Y., and Suzuki, M., 2008, Prolonged impact of earthquake-induced landslides on sediment yield in a mountain watershed: the Tanzawa region, Japan: Geomorphology, v. 101, no. 4, p. 692-702.

Kong, W. K., 2002, Risk assessment of slopes: Quarterly Journal of Engineering Geology and Hydrogeology, v. 35, no. 3, p. 213-222.

Korup, O., 2002, Recent research on landslide dams-a literature review with special attention to New Zealand: Prog. Phys. Geog., v. 26, p. 206-235.

Korup, O., 2004, Geomorphometric characteristics of New Zealand landslide dams: Engineering Geology, v. 73, no. 1–2, p. 13-35.

Korup, O., 2005, Geomorphic hazard assessment of landslide dams in South Westland, New Zealand: fundamental problems and approaches: Geomorphology, v. 66, no. 1–4, p. 167-188.

Korup, O., and Tweed, F., 2007, Ice, moraine, and landslide dams in mountainous terrain: Quaternary Science Reviews, v. 26, no. 25, p. 3406-3422.

Korup, O., Densmore, A. L., and Schlunegger, F., 2010, The role of landslides in mountain range evolution: Geomorphology, v. 120, no. 1, p. 77-90.

Korup, O., 2012, Earth's portfolio of extreme sediment transport events: Earth-Science Reviews, v. 112, no. 3, p. 115-125.

Korup, O., Görüm, T., and Hayakawa, Y., 2012, Without power? Landslide inventories in the face of climate change: Earth Surface Processes and Landforms, v. 37, no. 1, p. 92-99.

Kramer, S. L., 1996, Geotechnical earthquake engineering, Pearson Education India.

Kuang, S. F., Wang, X.G., Huang, J.C., Wei, Y.Q., 2009, Affect analysis of dam break risk for Tangjiashan Quake Lake in Sichuan: 33rd IAHR Congress: Water Engineering for a Sustainable Environment, ISBN: 978-94-90365-01-1.

Lacasse, S., Eidsvig, U., Nadim, F., Høeg, K., and Blikra, L. H., Event tree analysis of Åknes rock slide hazard, *in* Proceedings 4th Canadian conference on geohazards, Université Laval2008, p. 20-24.

Larsen, I. J., Montgomery, D. R., and Korup, O., 2010, Landslide erosion controlled by hillslope material: Nature Geosci, v. 3, no. 4, p. 247-251.

Lee, C.-T., Huang, C.-C., Lee, J.-F., Pan, K.-L., Lin, M.-L., and Dong, J.-J., 2008, Statistical approach to earthquake-induced landslide susceptibility: Engineering Geology, v. 100, no. 1–2, p. 43-58.

Lee, E. M., Brunsden, D., Sellwood, M., 2000, Quantitative risk assessment of coastal landslide problems, Lyme Regis, UK: Bromhead, E., Dixon, N., Ibsen, M.-L. (Eds.), Landslides, in research theory and practice. VIII International Symposium on Landslides, v. 2, p. 899-904.

Lee, S., 2004, Application of Likelihood Ratio and Logistic Regression Models to Landslide Susceptibility Mapping Using GIS: Environmental Management, v. 34, no. 2, p. 223-232.

Legros, F., 2002, The mobility of long-runout landslides: Engineering Geology, v. 63, no. 3, p. 301-331.

Li, M.-H., Sung, R.-T., Dong, J.-J., Lee, C.-T., and Chen, C.-C., 2011, The formation and breaching of a short-lived landslide dam at Hsiaolin Village, Taiwan — Part II: Simulation of debris flow with landslide dam breach: Engineering Geology, v. 123, no. 1–2, p. 60-71.

Li, W., 1980, Handbook of hydraulic calculations: Water Publication, Beijing(in Chinese).

Li, X., Zhou, Z., Yu, H., Wen, R., Lu, D., Huang, M., Zhou, Y., and Cu, J., 2008, Strong motion observations and recordings from the great Wenchuan Earthquake: Earthquake Engineering and Engineering Vibration, v. 7, no. 3, p. 235-246.

Lin, A., Ren, Z., Jia, D., and Wu, X., 2009, Co-seismic thrusting rupture and slip distribution produced by the 2008 Mw 7.9 Wenchuan earthquake, China: Tectonophysics, v. 471, no. 3–4, p. 203-215.

Lin, G.-W., Chen, H., Shih, T.-Y., and Lin, S., 2012, Various links between landslide debris and sediment flux during earthquake and rainstorm events: Journal of Asian Earth Sciences, v. 54, p. 41-48.

Lin, J., Lin, J., and Lee, J., Hazard Assessment of Potential Debris Flows in the Watershed of Chen-Yu-Lan River, *in* Proceedings Proceedings of the Third International Conference on Debris-Flow Hazards Mitigation, Davos, Switzerland. Millpress, Rotterdam. ISBN2003, Volume 90, p. 78.

Lin, M.-L., and Wang, K.-L., 2006, Seismic slope behavior in a large-scale shaking table model test: Engineering Geology, v. 86, no. 2, p. 118-133.

Liou, Y.-A., Kar, S. K., and Chang, L., 2010, Use of high-resolution FORMOSAT-2 satellite images for post-earthquake disaster assessment: a study following the

12 May 2008 Wenchuan Earthquake: International Journal of Remote Sensing, v. 31, no. 13, p. 3355-3368.

Liu-Zeng, J., Zhang, Z., Wen, L., Tapponnier, P., Sun, J., Xing, X., Hu, G., Xu, Q., Zeng, L., Ding, L., Ji, C., Hudnut, K. W., and van der Woerd, J., 2009, Co-seismic ruptures of the 12 May 2008, Ms 8.0 Wenchuan earthquake, Sichuan: East–west crustal shortening on oblique, parallel thrusts along the eastern edge of Tibet: Earth and Planetary Science Letters, v. 286, no. 3-4, p. 355-370.

Liu, N., Zhang, J., Lin, W., Cheng, W., and Chen, Z., 2009, Draining Tangjiashan Barrier Lake after Wenchuan Earthquake and the flood propagation after the dam break: Science in China Series E: Technological Sciences, v. 52, no. 4, p. 801-809.

Loh, C.-H., 1991, Spatial variability of seismic waves and its engineering application: Structural safety, v. 10, no. 1, p. 95-111.

Luna, B. Q., Blahut, J., Van Westen, C., Sterlacchini, C., van Asch, T. W., and Akbas, S., 2011, The application of numerical debris flow of modelling for the generation physical vulnerability curves: Natural Hazards and Earth System Sciences, v. 11, p. 2047-2060.

Malamud, B. D., Turcotte, D. L., Guzzetti, F., and Reichenbach, P., 2004, Landslides, earthquakes, and erosion: Earth and Planetary Science Letters, v. 229, no. 1–2, p. 45-59.

Manville, V., 2001, Techniques for evaluating the size of potential dam-break floods from natural dams, Institute of Geological & Nuclear Sciences.

Martha, T. R., Kerle, N., Jetten, V., van Westen, C. J., and Kumar, K. V., 2010, Landslide volumetric analysis using Cartosat-1-derived DEMs: Geoscience and Remote Sensing Letters, IEEE, v. 7, no. 3, p. 582-586.

Marzocchi, W., Sandri, L., Gasparini, P., Newhall, C., and Boschi, E., 2004, Quantifying probabilities of volcanic events: The example of volcanic hazard at Mount Vesuvius: Journal of Geophysical Research: Solid Earth, v. 109, no. B11, p. B11201.

Marzocchi, W., Sandri, L., Selva, J., 2010, BET_VH: a probabilistic tool for long-time volcanic hazard assessment: Bull Volcanol, v. 72, p. 705-716.

Mason, K., 1929, Indus floods and Shyok glaciers: Himalayan Journal, v. 1, p. 10–29.

McDougall, S., and Hungr, O., 2004, A model for the analysis of rapid landslide motion across three-dimensional terrain: Canadian Geotechnical Journal, v. 41, no. 6, p. 1084-1097.

Meunier, P., Hovius, N., and Haines, J. A., 2008, Topographic site effects and the location of earthquake induced landslides: Earth and Planetary Science Letters, v. 275, no. 3–4, p. 221-232.

Miles, S. B., and Keefer, D. K., 2007, Comprehensive areal model of earthquake-induced landslides: technical specification and user guide, US Geological Survey.

Nakamura, T., Tsuboi, S., Kaneda, Y., and Yamanaka, Y., 2010, Rupture process of the 2008 Wenchuan, China earthquake inferred from teleseismic waveform inversion and forward modeling of broadband seismic waves: Tectonophysics, v. 491, no. 1-4, p. 72-84.

Nash, T., Bell, D., Davies, T., and Nathan, S., 2008, Analysis of the formation and failure of Ram Creek landslide dam, South Island, New Zealand: New Zealand Journal of Geology and Geophysics, v. 51, no. 3, p. 187-193.

Neri, A., Aspinall, W. P., Cioni, R., Bertagnini, A., Baxter, P. J., Zuccaro, G., Andronico, D., Barsotti, S., Cole, P. D., Ongaro, T. E., Hincks, T. K., Macedonio, G., Papale, P., Rosi, M., Santacroce, R., and Woo, G., 2008, Developing an Event Tree for probabilistic hazard and risk assessment at Vesuvius: Journal of Volcanology and Geothermal Research, v. 178, no. 3, p. 397-415.

Neuhäuser, B., and Terhorst, B., 2007, Landslide susceptibility assessment using “weights-of-evidence” applied to a study area at the Jurassic escarpment (SW-Germany): Geomorphology, v. 86, no. 1, p. 12-24.

Newhall, C., and Hoblitt, R., 2002, Constructing event trees for volcanic crises: Bulletin of Volcanology, v. 64, no. 1, p. 3-20.

Newmark, N. M., STATE OF THE ART IN DYNAMIC ANALYSIS AND TECHNIQUES FOR THE DESIGN OF UNDERGROUND PROTECTIVE CONSTRUCTION, *in* Proceedings Protective Structures for Civilian Populations: Proceedings of the Symposium Held at Washington, DC, April 19-23, 19651965, National Academy of Sciences-National Research Council, p. 166.

O’Connor, J. E., Costa, J.E., 2004, The world’s largest floods, past and present—Their causes and magnitudes: U.S. Geological Survey Circular, v. 1254, no. 13.

Oglesby, D. D., and Mai, P. M., 2012, Fault geometry, rupture dynamics and ground motion from potential earthquakes on the North Anatolian Fault under the Sea of Marmara: Geophysical Journal International, v. 188, no. 3, p. 1071-1087.

Olsen, K., 2000, Site amplification in the Los Angeles basin from three-dimensional modeling of ground motion: Bulletin of the Seismological Society of America, v. 90, no. 6B, p. S77-S94.

Ouimet, W., Whipple, K., Royden, L., and Granger, D., Long transient response times of rivers in eastern Tibet to regional plateau uplift: The effect of mega-landslides, *in* Proceedings Geophys. Res. Abstr2007, Volume 7, p. 05743.

Ouimet, W. B., 2010, Landslides associated with the May 12, 2008 Wenchuan earthquake: Implications for the erosion and tectonic evolution of the Longmen Shan: Tectonophysics, v. 491, no. 1–4, p. 244-252.

Owen, L. A., Kamp, U., Khattak, G. A., Harp, E. L., Keefer, D. K., and Bauer, M. A., 2008, Landslides triggered by the 8 October 2005 Kashmir earthquake: Geomorphology, v. 94, no. 1–2, p. 1-9.

Parise, M., and Jibson, R. W., 2000, A seismic landslide susceptibility rating of geologic units based on analysis of characteristics of landslides triggered by the 17 January, 1994 Northridge, California earthquake: Engineering Geology, v. 58, no. 3, p. 251-270.

Parker, R. N., Densmore, A. L., Rosser, N. J., de Michele, M., Li, Y., Huang, R., Whadcoat, S., and Petley, D. N., 2011, Mass wasting triggered by the 2008 Wenchuan earthquake is greater than orogenic growth: Nature Geosci, v. 4, no. 7, p. 449-452.

Pearce, A. J., and Watson, A. J., 1986, Effects of earthquake-induced landslides on sediment budget and transport over a 50-yr period: Geology, v. 14, no. 1, p. 52-55.

Peng, M., and Zhang, L. M., 2012, Breaching parameters of landslide dams: Landslides, v. 9, no. 1, p. 13-31.

Province, H. o. o. S., 1979, Hydrological manual of Sichuan Province: Sichuan Science and Technique House, Chengdu(in Chinese).

Qi, S., Xu, Q., Lan, H., Zhang, B., and Liu, J., 2010, Spatial distribution analysis of landslides triggered by 2008.5. 12 Wenchuan Earthquake, China: Engineering Geology, v. 116, no. 1, p. 95-108.

Regmi, N. R., Giardino, J. R., and Vitek, J. D., 2010, Modeling susceptibility to landslides using the weight of evidence approach: Western Colorado, USA: Geomorphology, v. 115, no. 1, p. 172-187.

Ren, Z., and Lin, A., 2010, Co-seismic landslides induced by the 2008 Wenchuan magnitude 8.0 Earthquake, as revealed by ALOS PRISM and AVNIR2 imagery data: International Journal of Remote Sensing, v. 31, no. 13, p. 3479-3493.

Reneau, S. L., and Dethier, D. P., 1996, Late Pleistocene landslide-dammed lakes along the Rio Grande, White Rock Canyon, New Mexico: Geological Society of America Bulletin, v. 108, no. 11, p. 1492-1507.

Rickenmann, D., 1999, Empirical relationships for debris flows: Natural Hazards, v. 19, no. 1, p. 47-77.

Risley, J. C., Walder, J. S., and Denlinger, R. P., 2006, Usoi Dam wave overtopping and flood routing in the Bartang and Panj Rivers, Tajikistan: Natural Hazards, v. 38, no. 3, p. 375-390.

Sassa, K., 2005, Landslide disasters triggered by the 2004 Mid-Niigata Prefecture earthquake in Japan: Landslides, v. 2, no. 2, p. 135-142.

Sassa, K., Kaibori, M., and Kitera, N., Liquefaction and undrained shear of torrent deposits as the cause of debris flows, *in* Proceedings Proceedings International Symposium on Erosion, Debris Flows and Disaster Prevention1985, p. 231-236.

Sato, H. P., and Harp, E. L., 2009, Interpretation of earthquake-induced landslides triggered by the 12 May 2008, M7.9 Wenchuan earthquake in the Beichuan area, Sichuan Province, China using satellite imagery and Google Earth: Landslides, v. 6, no. 2, p. 153-159.

Sato, H. P., Hasegawa, H., Fujiwara, S., Tobita, M., Koarai, M., Une, H., and Iwahashi, J., 2007, Interpretation of landslide distribution triggered by the 2005 Northern Pakistan earthquake using SPOT 5 imagery: Landslides, v. 4, no. 2, p. 113-122.

Savage, S., and Hutter, K., 1989, The motion of a finite mass of granular material down a rough incline: Journal of Fluid Mechanics, v. 199, no. 1, p. 177-215.

Scheidegger, A. E., 1973, On the prediction of the reach and velocity of catastrophic landslides: Rock mechanics, v. 5, no. 4, p. 231-236.

Schneider, J. F., 2009, Seismically reactivated Hattian slide in Kashmir, Northern Pakistan: Journal of seismology, v. 13, no. 3, p. 387-398.

Selva, J., Orsi, G., Di Vito, M., Marzocchi, W., and Sandri, L., 2012, Probability hazard map for future vent opening at the Campi Flegrei caldera, Italy: Bulletin of Volcanology, v. 74, no. 2, p. 497-510.

Shafique, M., van der Meijde, M., Kerle, N., and van der Meer, F., 2011, Impact of DEM source and resolution on topographic seismic amplification: International Journal of Applied Earth Observation and Geoinformation, v. 13, no. 3, p. 420-427.

Shang, Y., Yang, Z., Li, L., Liu, D. a., Liao, Q., and Wang, Y., 2003, A super-large landslide in Tibet in 2000: background, occurrence, disaster, and origin: Geomorphology, v. 54, no. 3–4, p. 225-243.

Shen, Z.-K., Sun, J., Zhang, P., Wan, Y., Wang, M., Burgmann, R., Zeng, Y., Gan, W., Liao, H., and Wang, Q., 2009, Slip maxima at fault junctions and rupturing of barriers during the 2008 Wenchuan earthquake: Nature Geosci, v. 2, no. 10, p. 718-724.

Shroder Jr, J. F., 1998, Slope failure and denudation in the western Himalaya: Geomorphology, v. 26, no. 1–3, p. 81-105.

Singh, V. P., 1996, Hydrology of disasters, Kluwer Academic Publishers.

Smart, G., 1984, Sediment Transport Formula for Steep Channels: Journal of Hydraulic Engineering, v. 110, no. 3, p. 267-276.

Somerville, P. G., K. Irikura, R. Graves, S. Sawada, D. Wald, N. Abrahamson, Y. Iwasaki, T. Kagawa, N. Smith and A. Kowada, 1999, Characterizing earthquake slip models for the prediction of strong ground motion.: Seismological Research Letters, v. 70, p. 59-80.

Song, Y., Gong, J., Gao, S., Wang, D., Cui, T., Li, Y., and Wei, B., 2012, Susceptibility assessment of earthquake-induced landslides using Bayesian network: A case study in Beichuan, China: Computers & Geosciences, v. 42, p. 189-199.

Stark, C., and Guzzetti, F., 2009, Landslide rupture and the probability distribution of mobilized debris volumes: Journal of Geophysical Research: Earth Surface (2003–2012), v. 114, no. F2.

Stark, C. P., and Hovius, N., 2001, The characterization of landslide size distributions: Geophysical Research Letters, v. 28, no. 6, p. 1091-1094.

Stein, S., Geller, R. J., and Liu, M., 2012, Why earthquake hazard maps often fail and what to do about it: Tectonophysics.

Stewart, J. P., and Liu, A. H., Ground motion amplification as a function of surface geology, *in* Proceedings Proc. SMIP2000 Seminar on Utilization of Strong Motion Data, California Strong Motion Instrumentation Program, Sacramento, California2000, p. 1-22.

Stone, M., 1974, Cross-validatory choice and assessment of statistical predictions: Journal of the Royal Statistical Society. Series B (Methodological), p. 111-147.

Sun, P., Zhang, Y., Shi, J., and Chen, L., 2011, Analysis on the dynamical process of Donghekou rockslide-debris flow triggered by 5.12 Wenchuan earthquake: Journal of Mountain Science, v. 8, no. 2, p. 140-148.

Survey, U. S. G., 2008, Magnitude 7.9 - Eastern Sichuan, China, 2008 May 12 06:28:01UTC: http://earthquake.usgs.gov/earthquakes/eqinthenews/2008/us2008ryan/.

Swanson, F. J., Oyagi, N., and Tominaga, M., Landslide dams in Japan, *in* Proceedings Landslide Dams@ sProcesses, Risk, and Mitigation1986, ASCE, p. 131-145.

Tabata, S., Mizuyama, T., and Inoue, K., 2002, Natural Landslide Dams Hazards. Kokonshoin, Tokyo.

Tang, C., Van Asch, T., Chang, M., Chen, G., Zhao, X., and Huang, X., 2012a, Catastrophic debris flows on 13 August 2010 in the Qingping area, southwestern China: The combined effects of a strong earthquake and subsequent rainstorms: Geomorphology, v. 139, p. 559-576.

Tang, C., Zhu, J., Chang, M., Ding, J., and Qi, X., 2012b, An empirical–statistical model for predicting debris-flow runout zones in the Wenchuan earthquake area: Quaternary International, v. 250, p. 63-73.

Tang, C., Zhu, J., Li, W. L., and Liang, J. T., 2009, Rainfall-triggered debris flows following the Wenchuan earthquake: Bulletin of Engineering Geology and the Environment, v. 68, no. 2, p. 187-194.

Tang, C., Zhu, J., Qi, X., and Ding, J., 2011, Landslides induced by the Wenchuan earthquake and the subsequent strong rainfall event: A case study in the Beichuan area of China: Engineering Geology, v. 122, no. 1-2, p. 22-33.

Ten Brink, U., Barkan, R., Andrews, B. D., and Chaytor, J., 2009, Size distributions and failure initiation of submarine and subaerial landslides: Earth and Planetary Science Letters, v. 287, no. 1, p. 31-42.

Tsutsui, K., Rokugawa, S., Nakagawa, H., Miyazaki, S., Cheng, C.-T., Shiraishi, T., and Yang, S.-D., 2007, Detection and volume estimation of large-scale landslides based on elevation-change analysis using DEMs extracted from high-resolution satellite stereo imagery: Geoscience and Remote Sensing, IEEE Transactions on, v. 45, no. 6, p. 1681-1696.

Van Asch, T. W., Malet, J., Remaıtre, A., and Maquaire, O., Numerical modelling of the run-out of a muddy debris flow. The effect of rheology on velocity and deposit thickness along the run-out track, *in* Proceedings Proceedings of the 9th international symposium on landslides, Rio de Janeiro, Balkema, Leiden2004, Volume 2, p. 1433-1439.

Van Den Eeckhaut, M., Poesen, J., Govers, G., Verstraeten, G., and Demoulin, A., 2007, Characteristics of the size distribution of recent and historical landslides in a populated hilly region: Earth and Planetary Science Letters, v. 256, no. 3–4, p. 588-603.

Van Westen, C. J., Terlien, M.T.J., 1996, Deterministic landslide hazard analysis in GIS: A case study from Manizales (Columbia): Earth Surface Processes Landforms, v. 21, p. 853-868.

Van Westen, C., Rengers, N., and Soeters, R., 2003, Use of geomorphological information in indirect landslide susceptibility assessment: Natural Hazards, v. 30, no. 3, p. 399-419.

Van Westen, C., Van Asch, T. W., and Soeters, R., 2006, Landslide hazard and risk zonation—why is it still so difficult?: Bulletin of Engineering geology and the Environment, v. 65, no. 2, p. 167-184.

Van Westen, C. J., Castellanos, E., and Kuriakose, S. L., 2008, Spatial data for landslide susceptibility, hazard, and vulnerability assessment: An overview: Engineering Geology, v. 102, no. 3–4, p. 112-131.

Walder, J. S., and O'Connor, J. E., 1997, Methods for predicting peak discharge of floods caused by failure of natural and constructed earthen dams: Water Resources Research, v. 33, no. 10, p. 2337-2348.

Wang, G., Liu, F., Fu, X., and Li, T., 2008, Simulation of dam breach development for emergency treatment of the Tangjiashan Quake Lake in China: Science in China Series E: Technological Sciences, v. 51, no. 2, p. 82-94.

Wang, G., Huang, R., Chigira, M., Wu, X., Lourenco, S.D.N., 2013. Landslide amplification by liquefaction of runout-path material after the 2008 Wenchuan

(M 8.0) earthquake, China: Earth Surface Processes and Landforms, v. 38, p. 265-274.

Wanson, F. J., Oyagi, N., Tominaga, M., 1986, Landslide dams: process, risk, and mitigation: New York: American Society of Civil Engineers Special Publication, v. 3, p. 273–378.

Weidinger, J. T., 2011, Stability and Life Span of Landslide Dams in the Himalayas (India, Nepal) and the Qin Ling Mountains (China), *in* Evans, S. G., Hermanns, R. L., Strom, A., and Scarascia-Mugnozza, G., eds., Natural and Artificial Rockslide Dams, Volume 133, Springer Berlin Heidelberg, p. 243-277.

Weidinger, J. T., Wang, J., and Ma, N., 2002, The earthquake-triggered rock avalanche of Cui Hua, Qin Ling Mountains, PR of China—the benefits of a lake-damming prehistoric natural disaster: Quaternary international, v. 93, p. 207-214.

Wenske, D., Jen, C.-H., Böse, M., and Lin, J.-C., 2012, Assessment of sediment delivery from successive erosion on stream-coupled hillslopes via a time series of topographic surveys in the central high mountain range of Taiwan: Quaternary International, v. 263, p. 14-25.

Whipple, K. X., 2004, Bedrock rivers and the geomorphology of active orogens: Annual Reviews in Earth and Planetary Sciences, v. 32, p. 151-185.

Whittaker, A. C., Cowie, P. A., Attal, M., Tucker, G. E., and Roberts, G. P., 2007, Bedrock channel adjustment to tectonic forcing: Implications for predicting river incision rates: Geology, v. 35, no. 2, p. 103-106.

Wilson, J. P., and Gallant, J. C., 2000, Terrain analysis: principles and applications, John Wiley & Sons.

Wishart, J. S., 2007, Overtopping breaching of rock-avalanche dams.

Wong, H. N., Ho,K.K.S., Chan,Y.C., 1997, Assessment of consequence of landslides: Cruden, D., Fell, R. (Eds.), Landslide risk assessment. A.A. Balkema, Rotterdam, p. 111-149.

Wu, W., and Sidle, R. C., 1995, A distributed slope stability model for steep forested basins: Water Resources Research, v. 31, no. 8, p. 2097-2110.

Xu, M., Cao, C., Zhang, H., Guo, J., Nakane, K., He, Q., Guo, J., Chang, C., Bao, Y., and Gao, M., 2010, Change detection of an earthquake-induced barrier lake based on remote sensing image classification: International Journal of Remote Sensing, v. 31, no. 13, p. 3521-3534.

Xu, Q., Fan, X.-M., Huang, R.-Q., and Westen, C., 2009, Landslide dams triggered by the Wenchuan Earthquake, Sichuan Province, south west China: Bulletin of Engineering Geology and the Environment, v. 68, no. 3, p. 373-386.

Xu, Q., Shang, Y., van Asch, T., Wang, S., Zhang, Z., and Dong, X., 2012, Observations from the large, rapid Yigong rock slide – debris avalanche, southeast Tibet: Canadian Geotechnical Journal, v. 49, no. 5, p. 589-606.

Xu, X., Wen, X., Yu, G., Chen, G., Klinger, Y., Hubbard, J., and Shaw, J., 2009, Coseismic reverse- and oblique-slip surface faulting generated by the 2008 Mw 7.9 Wenchuan earthquake, China: Geology, v. 37, no. 6, p. 515-518.

Yarai, H., Nishimura, T., Tobita, M., Amagai, T., Suzuki, A., Suito, H., Ozawa, S., Imakiire, T., Masaharu, H., 2008, A fault model of the 2008 Wenchuan earthquake estimated from SAR measurements: 7th ASC meeting, X2-040.

Yin, J., Chen, J., Xu, X., Wang, X., and Zheng, Y., 2010, The characteristics of the landslides triggered by the Wenchuan Ms 8.0 earthquake from Anxian to Beichuan: Journal of Asian Earth Sciences, v. 37, no. 5–6, p. 452-459.

Yin, Y., Wang, F., and Sun, P., 2009, Landslide hazards triggered by the 2008 Wenchuan earthquake, Sichuan, China: Landslides, v. 6, no. 2, p. 139-152.

Yule, G.U., 1912. On the methods of measuring association between two attributes: Journal of the Royal Statistical Society, v. 75, p. 579–642

Zhang, X. J., 2010, Preliminary study on hydrological emergency monitoring scheme for dammed lakes: Automation in Water Recourses and Hydrology, v. 1, p. 1-5 (in Chinese).

Appendices

Appendix 1: Satellite images data index table

Pre-Earthquake

Id	Date	Sensor	Resolution (m)	Spectral Information	Source	Production ID
1	02/19/03	ASTER	15	MS(VNIR)	Terra-ASTER	L1A0030219200303572803142003165639
2	02/19/03	ASTER	15	MS(VNIR)	Terra-ASTER	L1A0030219200303574603142003165712
3	02/19/03	ASTER	15	MS(VNIR)	Terra-ASTER	L1A0030219200303573703142003165656
4	08/30/00	ASTER	15	MS(VNIR)	Terra-ASTER	L1A0030830200004053101012003173757
5	03/31/06	ASTER	15	MS(VNIR)	Terra-ASTER	L1A0030331200603554504022006161342
6	09/05/02	ASTER	15	MS(VNIR)	Terra-ASTER	L1A0030905200203514109202002201647
7	06/14/01	ASTER	15	MS(VNIR)	Terra-ASTER	L1A0030614200103590706192001193607
8	06/14/01	ASTER	15	MS(VNIR)	Terra-ASTER	L1A0030614200103585806192001193546
9	06/30/01	ASTER	15	MS(VNIR)	Terra-ASTER	L1A0030630200103581907062001152354
10	04/18/01	ASTER	15	MS(VNIR)	Terra-ASTER	L1A0030418200104065501202004225713
11	08/27/02	ASTER	15	MS(VNIR)	Terra-ASTER	L1A0030827200203581210052002170010
12	02/19/03	ASTER	15	MS(VNIR)	Terra-ASTER	L1A0030219200303571903142003165623
13	08/30/00	ASTER	15	MS(VNIR)	Terra-ASTER	L1A0030830200004052201012003173741
14	08/30/00	ASTER	15	MS(VNIR)	Terra-ASTER	L1A0030830200004051301012003173724
15	03/31/07	ALOS	10	MS (AVNIR-2)	JAXA	ALAV2A062882960
16	03/31/07	ALOS	10	MS (AVNIR-2)	JAXA	ALAV2A062882970
17	04/17/07	ALOS	10	MS (AVNIR-2)	JAXA	ALAV2A065362960
18	01/02/07	ALOS	10	MS (AVNIR-2)	JAXA	ALAV2A054422950
19	11/28/07	ALOS	10	MS (AVNIR-2)	JAXA	ALAV2A098182940
20	11/28/07	ALOS	10	MS (AVNIR-2)	JAXA	ALAV2A098182950
21	05/06/08	ALOS	2.5	PAN (PRISM)	JAXA	ALPSMN121522965
22	05/06/08	ALOS	2.5	PAN (PRISM)	JAXA	ALPSMN121522970
23	08/30/06	ALOS	2.5	PAN (PRISM)	JAXA	ALPSMN031812960
24	04/19/07	CARTOSAT-1	2.5	PAN	ISRO	097027500102
25	04/19/07	CARTOSAT-1	2.5	PAN	ISRO	097027500202
26	04/19/07	CARTOSAT-1	2.5	PAN	ISRO	097027500302

Post-Earthquake

1	07/10/08	ASTER	15	MS(VNIR)	Terra-ASTER	L1A0030710200803570207152008112907
2	05/30/08	ASTER	15	MS(VNIR)	Terra-ASTER	L1A0030530200804024606022008170420
3	07/10/08	ASTER	15	MS(VNIR)	Terra-	L1A0030710200803565307152 0

					ASTER	08112859
4	05/23/08	ASTER	15	MS(VNIR)	Terra-ASTER	L1A0030523200803570905282008121510
5	05/23/08	ASTER	15	MS(VNIR)	Terra-ASTER	L1A0030523200803565105282008121456
6	05/23/08	ASTER	15	MS(VNIR)	Terra-ASTER	L1A0030523200803570005282008121503
7	05/16/08	ASTER	15	MS(VNIR)	Terra-ASTER	L1A0030516200803504705192008111553
8	06/08/08	ASTER	15	MS(VNIR)	Terra-ASTER	L1A0030608200803571206112008121132
9	12/10/08	ASTER	15	MS(VNIR)	Terra-ASTER	L1A0031210200803504612132008113610
10	07/26/08	ASTER	15	MS(VNIR)	Terra-ASTER	L1A0030726200803564009262008160248
11	12/10/08	ASTER	15	MS(VNIR)	Terra-ASTER	L1A0031210200803505512132008113619
12	05/16/08	ASTER	15	MS(VNIR)	Terra-ASTER	L1A0030516200803502905192008111529
13	***05/18/08***	***ALOS***	***2.5***	***PAN (PRISM)***	***JAXA***	***ALPSMW123272955***
14	05/23/08	ALOS	10	MS (AVNIR-2)	JAXA	ALAV2A124002930
15	***06/04/08***	***ALOS***	***10***	***MS (AVNIR-2)***	***JAXA***	***ALAV2A125752950***
16	***06/04/08***	***ALOS***	***10***	***MS (AVNIR-2)***	***JAXA***	***ALAV2A125752960***
17	06/04/08	ALOS	10	MS (AVNIR-2)	JAXA	ALAV2A125752970
18	***10/13/08***	***SPOT-5***	***2.5***	***PAN***	***Spot Image S.A***	***5261286/108/10/13***
19	07/01/08	IKONOS	2.5+4	PAN+MS	Geo-Eye	325523
20	05/23/08	IKONOS	2.5+4	PAN+MS	Geo-Eye	325578
21	06/28/08	IKONOS	2.5+4	PAN+MS	Geo-Eye	325583
22	05/23/08	IKONOS	2.5+4	PAN+MS	Geo-Eye	325579
23	06/28/08	IKONOS	2.5+4	PAN+MS	Geo-Eye	325584
24	***01/24/09***	***CARTOSAT-1***	***2.5***	***PAN***	***ISRO***	***097027500402***
25	***01/24/09***	***CARTOSAT-1***	***2.5***	***PAN***	***ISRO***	***097027500502***
26	***01/24/09***	***CARTOSAT-1***	***2.5***	***PAN***	***ISRO***	***097027500602***
27	***07/19/10***	***ASTER***	***15***	***MS(VNIR)***	***Terra-ASTER***	***L1B00301212010035628201007190900057***
28	***07/19/10***	***ASTER***	***15***	***MS(VNIR)***	***Terra-ASTER***	***L1B00301212010035637201007190900057***
29	***07/19/10***	***ASTER***	***15***	***MS(VNIR)***	***Terra-ASTER***	***L1B00302222010035619201007190900037***
30	***07/19/10***	***ASTER***	***15***	***MS(VNIR)***	***Terra-ASTER***	***L1B00302222010035628201007190900037***
31	***07/19/10***	***ASTER***	***15***	***MS(VNIR)***	***Terra-ASTER***	***L1B00302222010035637201007190900037***
32	***07/19/10***	***ASTER***	***15***	***MS(VNIR)***	***Terra-ASTER***	***L1B00302222010035646201007190900037***
33	***07/19/10***	***ASTER***	***15***	***MS(VNIR)***	***Terra-ASTER***	***L1B00302242010034406201007190900047***
34	***07/19/10***	***ASTER***	***15***	***MS(VNIR)***	***Terra-ASTER***	***L1B00302242010034415201007190900047***
35	***07/19/10***	***ASTER***	***15***	***MS(VNIR)***	***Terra-ASTER***	***L1B00305032009035119201007190900057***
36	***07/19/10***	***ASTER***	***15***	***MS(VNIR)***	***Terra-ASTER***	***L1B00308302009035636201007190900057***
37	***07/08/08***	***EO-1***	***10***	***PAN***	***USGS***	***EO1A1300382008189110K0***

**The images used for landslide dam failure rate analysis were marked in bold and italic.*

Appendix 2:

Weights of the factor classes for non-damming and damming landslides

Factor	Class	Non-damming landslides			Damming landslides		
		W^+	W^-	C	W^+	W^-	C
Seismic factors							
PGA (g)	0 to 0.20	-2.28	0.14	-2.42	-8.76	0.16	-8.92
	0.20 to 0.28	-2.02	0.19	-2.20	-3.75	0.21	-3.96
	0.28 to 0.36	-1.24	0.09	-1.34	-4.54	0.12	-4.67
	0.36 to 0.52	-0.33	0.05	-0.39	-2.21	0.16	-2.37
	0.52 to 0.60	0.06	0.00	**0.06**	-0.66	0.03	-0.70
	0.60 to 0.68	0.42	-0.04	**0.46**	0.40	-0.04	**0.44**
	0.68 to 0.76	0.49	-0.05	**0.54**	0.68	-0.09	**0.77**
	0.76 to 0.80	1.01	-0.13	**1.14**	1.40	-0.24	**1.64**
	>0.8	1.21	-0.28	**1.49**	1.46	-0.44	**1.90**
Fault type	Thrusting	0.37	-0.72	**1.10**	0.38	-0.75	**1.13**
	Strike-slip	-0.72	0.37	-1.10	-0.75	0.38	-1.13
Hanging/footwall effect	Hanging wall	0.08	-0.45	**0.53**	0.14	-1.09	**1.23**
	Footwall	-0.45	0.08	-0.53	-1.09	0.14	-1.23
Geological factor							
Unconsolidated deposits (Q)		-1.73	0.01	-1.74	0.49	-0.01	**0.50**
Quartzy sandstone,schist,slate, metamorphoic (J)		-1.69	0.10	-1.79	-3.04	0.11	-3.15
Metamorphic sandstone and phyllite with limestone (T)		-1.75	0.12	-1.86	-7.64	0.14	-7.77
Phyllite with limestone and siltstone (T)		-0.58	0.00	-0.58	-5.96	0.01	-5.97
Sandstone, siltstone with shale and coal seam (T)		-0.26	0.01	-0.27	-0.01	0.00	-0.01
Shale, mudstone and siltstone (T)		0.37	-0.01	**0.37**	0.79	-0.02	**0.80**
Limestone and shale (P)		0.99	-0.01	**1.00**	1.99	-0.05	**2.04**
Limestone, phyllite and basalt (C-P)		-0.78	0.01	-0.79	-6.80	0.02	-6.82
Limestone, phyllite, slate and sandstone (C)		-0.75	0.00	-0.75	-3.00	0.00	-3.01
Phyllite and limestone (D)		0.53	-0.01	**0.54**	-1.63	0.01	-1.63
Phyllite and sandstone (D)		-0.90	0.02	-0.92	-7.18	0.03	-7.21
Phyllite, sandstone and limestone (D)		-1.75	0.04	-1.79	-7.68	0.05	-7.73
Sandstone, mudstone and shale (D)		-1.52	0.00	-1.52	-4.72	0.00	-4.72
Limestone, shale and sandstone (D)		0.15	0.00	**0.16**	-2.04	0.02	-2.06
Limestone (T-D)		0.76	-0.05	**0.81**	0.74	-0.05	**0.78**
Limestone, muddy limestone intercalated with slate (O)		0.36	0.00	**0.36**	-4.98	0.00	-4.98
Sandstone and siltstone intercalated with slate (Cam)		1.36	-0.10	**1.46**	1.75	-0.17	**1.93**
Phyllite,schist,slate with sandstone and limestone (Z)		-0.59	0.17	-0.76	-1.88	0.30	-2.18

Keratophyre, spilite and tuff (Pz)		-1.49	0.00	-1.49	-4.66	0.00	-4.66
Schist and andesite (Pz)		1.97	-0.04	**2.01**	2.33	-0.06	**2.39**
Granitic rocks		1.12	-0.27	**1.39**	1.35	-0.41	**1.76**
Topographic and hydrological factors							
Curvature (m^{-1})	-32.8 to -1.29	-0.71	0.03	-0.74	0.18	-0.01	**0.19**
	-1.29 to -0.83	-0.46	0.03	-0.49	-0.02	0.00	-0.02
	-0.83 to -0.6	-0.32	0.03	-0.35	-0.05	0.01	-0.06
	-0.6 to -0.37	-0.25	0.02	-0.27	-0.04	0.00	-0.04
	-0.37 to -0.14	-0.18	0.03	-0.21	-0.03	0.00	-0.03
	-0.14 to 0.09	-0.14	0.01	-0.15	-0.08	0.01	-0.09
	0.09 to 0.55	0.07	-0.02	**0.09**	0.04	-0.01	**0.05**
	0.55 to 0.78	0.22	-0.01	**0.23**	0.03	0.00	**0.03**
	0.78 to 1.24	0.36	-0.05	**0.41**	0.04	0.00	**0.04**
	1.24 to 26.08	0.59	-0.07	**0.66**	-0.09	0.01	-0.10
Drainage density (m^{-1})	0 to 06-1.13E-04	-0.06	0.01	-0.07	-2.02	0.11	-2.13
	1.13E-04 to 2.24E-04	-0.16	0.15	-0.31	-0.34	0.27	-0.62
	2.24E-04 to 3.35E-04	0.24	-0.11	**0.36**	0.53	-0.32	**0.85**
	3.35E-04 to 4.46E-04	-0.01	0.00	-0.01	-0.12	0.01	-0.13
	4.46E-04 to 5.57E-04	0.47	-0.01	**0.48**	1.41	-0.05	**1.46**
	5.57E-04 to 7.79E-04	-0.38	0.00	-0.38	0.65	-0.01	**0.66**
	7.79E-04 to 2.83E-02	0.38	0.00	**0.38**	1.18	-0.01	**1.18**

Note: *C* is the weigh contrast, W^{+}-W^{-}; values in bold represent the classes with positive weight contrast.

Weight contrast of most effective lithology in different distance-to-fault zones

Distance to fault (km)	Non-damming landslides			Damming landslides		
	Schist and andesite (Pz)	Granitic rocks	Sandstone and siltstone intercalated with slate (Cam)	Schist and andesite (Pz)	Limestone and shale (P)	Granitic rocks
5	1.92	1.64	1.75	2.96	2.53	2.40
10	2.40	1.64	1.40	2.59	2.76	2.24
15	1.77	1.02	1.14	-4.13	0.21	0.41
20	-0.28	1.45	0.98	-3.03	-2.69	0.98
25	2.21	1.54	0.00	2.63	-3.86	1.13
30	2.11	1.02	-0.23	2.26	-3.92	1.34
35	1.72	1.03	0.30	-1.38	-2.03	-0.50
40	-	0.46	0.91	-	1.16	-5.58
45	-	0.01	-	-1.52	-	-4.55
50	-	-1.28	-	-	-0.74	-4.89

Appendix 3:

The landslide volume regression models

Table S1. Best-fit regression models for volume of different types of damming and non-damming landslides

* Regression models for damming landslides				
Slide type	Intercept	Coefficient of ln(H)	Coefficient of ln(H/L)	Adjusted R^2
Debris/rock avalanche	-1.002 ± 2.386	2.142 ± 0.360	-2.378 ± 0.594	0.462
Debris flow	-2.404 ± 2.991	2.240 ± 0.454	-1.764 ± 0.489	0.627
Rock fall	-2.236 ± 4.900	2.402 ± 0.778	0.498 ± 1.302	0.312
Debris/rock slide	-1.655 ± 1.679	2.346 ± 0.276	-1.585 ± 0.409	0.547
All	-2.079 ± 1.050	1.725 ± 0.169	-0.909 ± 0.194	0.434
Regression models for non-damming landslides				
Slide type	Intercept	Coefficient of ln(H)	Coefficient of ln(H/L)	Adjusted R^2
Debris/rock avalanche	-2.548 ± 2.704	2.313 ± 0.411	-1.495 ± 0.450	0.492
Debris flow	-2.034 ± 1.641	1.958 ± 0.249	-2.336 ± 0.395	0.515
Rock fall	3.024 ± 2.683	1.517 ± 0.435	0.009 ± 0.828	0.444
Debris/rock slide	1.238 ± 1.408	1.719 ± 0.228	0.229 ± 0.413	0.466
All	1.512 ± 0.960	1.612 ± 0.152	-0.742 ± 0.256	0.359

Values in the table are mean ± standard error

Table S1 shows that *H*, *H/L* ratio and landslide type are the most significant variables controlling landslide volume. The volume regression models generally have quite low adjusted R^2 (< 0.5), as the complex triggering mechanisms, geological and geomorphologic settings exemplify the difficulties of this task. The success of the best-fit models for different types of damming and non-damming landslides is quite variable, from 31.2% to 62.7 % of samples successfully predicted. This might be because landslide volume is also dominated by other site-specific factors, such as local geological structures, the depth of sliding plane, and geotechnical parameters (e.g. friction angle, cohesion).

Appendix 4:

SOBEK 2D model outputs: spatial variation of flood parameters (maximum flood depth, peak flood arrival time, maximum flood velocity) in Scenarios 1 and 2 (A-C), Scenarios 3 (D-F) and Scenario 4 (G-I).

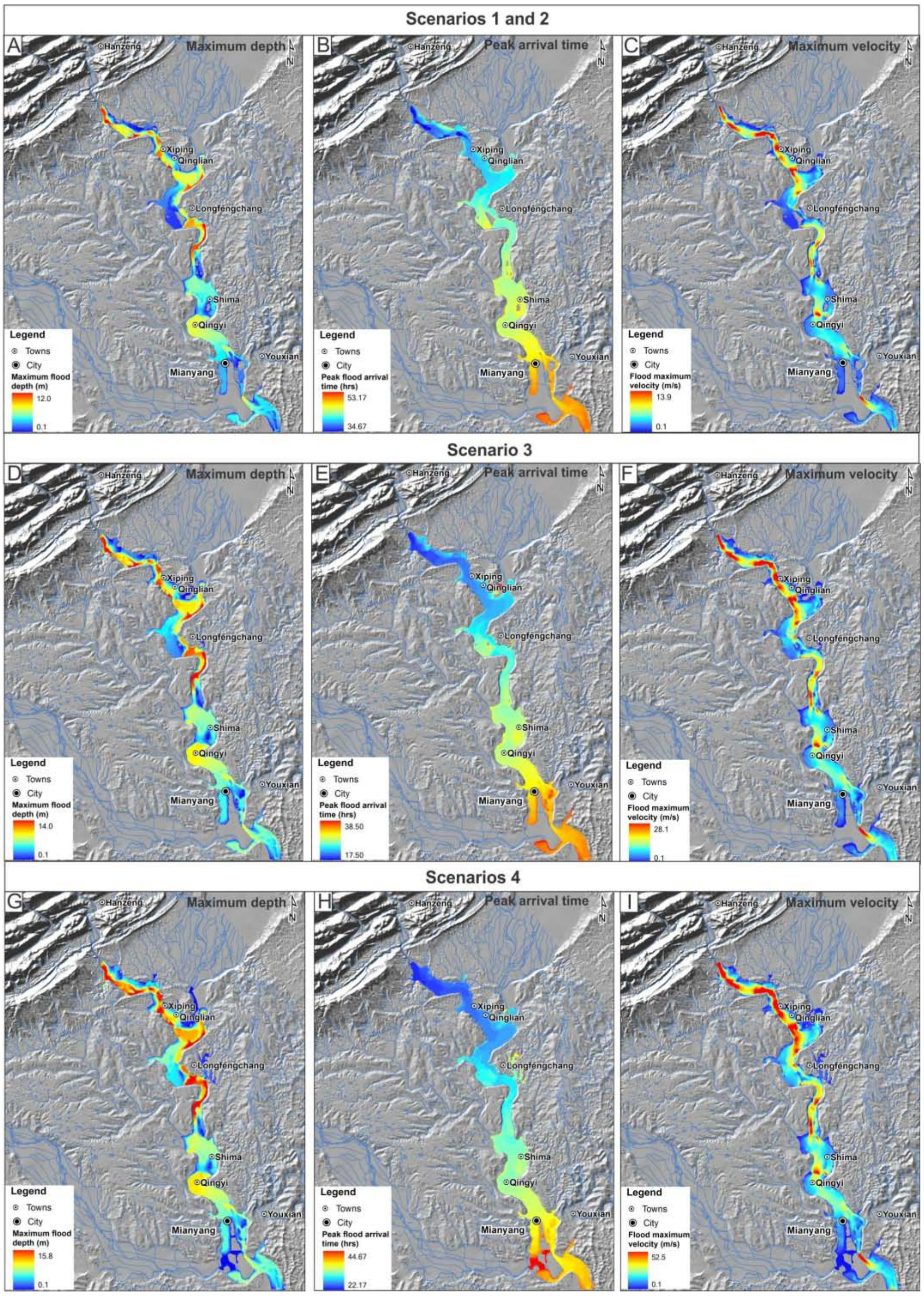

Summary

Landslide dams are potentially dangerous obstructions caused by river-blocking slope failures that occur frequently in tectonically active mountains with narrow and steep valleys. The catastrophic release of water masses from landslide-impounded lakes is capable to produce outburst floods and debris flows, causing loss of lives, housing and infrastructure. Strong earthquakes are among the prime triggering factors of landslide dams. On 12 May 2008, a devastating earthquake of magnitude M_w7.9 hit China's Sichuan province. The quake, originating in the Longmen Shan fault zone at the eastern margin of Tibetan Plateau, was the country's largest seismic event in more than 50 years. As well as the immediate devastation through shaking, the earthquake triggered more than 60,000 destructive landslides and more than 800 landslide dams over an area of 35,000 km^2. It provides an unprecedented opportunity for systematically studying the earthquake-induced landslide dams.

Despite a large body of literature on case studies of catastrophic landslide dams, evaluating the geomorphic impacts and stability of landslide dams, relatively limited work has been carried out on a number of issues, such as: (1) so far few studies have focused specifically on landslide dams that have been triggered by the same earthquake due to the scarcity of direct observational data; (2) no study has systematically analyzed the controlling factors of event-based coseismic landslide dam inventories, and their comparison with general landslide inventories; (3) there is little research carried out on the threshold values of the factors involved that cause a temporal and spatial landslide blockage of a river course; (4) little work has been done to investigate the longevity and geomorphic decay of coseismic landslide dams, as well as their impacts on modulating the immediate post-earthquake flux of water and sediment at the regional scale; and (5) the estimation of the multi-hazard that involves several cascading phenomena is poorly documented in the literature.

This research aims to a better understanding of the causes and effects of landslide dams with the focus on above research gaps. To achieve this goal, an event-based inventory is first created by visual interpretation of remote sensing images, assisted by field checks in accessible areas. Based on this inventory, the spatial distribution patterns of coseismic landslides and landslide dams are analyzed, showing that they are most abundant in the Pengguan massif, along the thrusting part of the main fault, the Yingxiu-Beichuan fault. The weight of predisposing factors that control the coseismic landslide occurrence is quantified by the weight of evidence (WOE) method. The results demonstrate that distance to fault surface

rupture, PGA (Peak Ground Acceleration) and lithology are the most critical factors. The fault type and hanging/foot wall effect were ignored in previous studies, but are found important for coseismic landslides.

To predict the coseismic landslide dam formation at the regional scale, an empirical-statistical method is developed to estimate the volume threshold for coseismic landslide dam formation using landscape parameters obtained from DEMs. This method includes two steps: determining a first volume threshold for a landslide to reach a river by obtaining empirical runout models using stepwise multivariate regression; and then determining a second volume threshold above which a landslide is predicted to block a river by considering the correlation between river width and landslide volume of the known damming landslides. This method is applied to several landslide types over a fine geographic grid of assumed initiation points in a selected catchment in the study area. The overall prediction accuracy is 97.2% and 86.0% for non-damming and damming landslides, respectively.

To quantify the geomorphic decay of landslide dams after the Wenchuan earthquake and their impacts on post-earthquake sediment flux, the residence time of the landslide dams is estimated based on multi-temporal remote sensing images. The transient water and sediment storage of landslide dams are also evaluated. It is found that about 25% of the dams failed one week after the earthquake; these figures had risen to 60% and >90% within one month and one year, respectively. In essence, about only a third of the sediment volumes contained in landslide dams has been flushed downstream. However, the remaining landslide-dam debris together with that of the bulk volume (>85%) of smaller landslides awaits flushing during major sediment pulses in years and decades to come.

Dam-break flood hazard is the major effect of landslide dams. This research takes the Tangjiashan landslide dam (the most dangerous one induced by the Wenchuan earthquake) as an example to simulate the dam-breach process and the resulting flood propagation in possible scenarios. An integrated approach using the physically-based BREACH model and the 1D-2D SOBEK hydrodynamic model is developed. Firstly, the physically-based BREACH model is applied to predict the flood hydrographs at the dam location, which were calibrated with observational data of the flood resulting from the artificial breaching. The output hydrographs from this model are inputted into the 1D-2D SOBEK hydrodynamic model to simulate the spatial variations in flood parameters. The simulated flood hydrograph, peak discharge and peak arrival time at the downstream towns fit the observations. Thus this approach is capable of providing reliable predictions for the decision makers to determine the mitigation plans.

To conclude, the results from this research can be used to construct a conceptual Event Tree model for the quantitative assessment of earthquake-induced landslide dam break floods. This model initiates from an assumed earthquake, to coseismic landslides and landslide dams, and ends with dam-break flooding hazard. It contributes to a better understanding of the cascading cause-effect of geohazards associated with large earthquakes.

Samenvatting

Aardverschuivingen veroorzaken vaak potentieel gevaarlijke rivierafdamming in smalle steile dalen in aardbevingsgevoelige gebieden. Het bezwijken van dergelijke door aardverschuivingen gevormde dammen kan catastrofale vloedgolven en modderstromen veroorzaken die leiden tot verlies van mensenlevens, woningen en infrastructuur. Zware aardbevingen behoren tot de belangrijkste natuurlijke processen die dergelijke aardverschuivingen veroorzaken. Op 12 mei 2008 werd de Chinese provincie Sichuan getroffen door de verwoestende Wenchuan aardbeving met magnitude $M_w = 7{,}9$. Deze aardbeving die plaatsvond in de Longmen Shan breukzone aan de oostrand van het Tibetaans plateau, was China's zwaarste aardbeving in meer dan 50 jaar. Behalve de onmiddellijke schade door aardschokken veroorzaakte de aardbeving in een gebied van 35.000 km^2 ook meer dan 60.000 verwoestende aardverschuivingen waarvan meer dan 800 rivierafdamming veroorzaakten. Deze natuurramp heeft een ongekende mogelijkheid verschaft voor een systematisch onderzoek aan aardverschuivingen die door aardbevingen zijn veroorzaakt en rivieren afdammen.

Ondanks omvangrijke literatuur met case-histories over catastrofale aardverschuivings-dammen, met daarin evaluaties van de geomorfologische impact en de stabiliteit van dergelijke dammen en simulaties van de vloedgolf die optreedt na het bezwijken van de dam, is toch betrekkelijk weinig onderzoek gedaan naar de volgende belangrijke aspecten: (1) tot dusverre zijn weinig vergelijkende studies gedaan aan dammen veroorzaakt door een en dezelfde aardbeving door de schaarste van dergelijke waarnemingen (2) er is nooit systematisch onderzoek gedaan naar de vergelijking van de kritische factoren van aardverschuivings-dammen die door een aardbeving zijn veroorzaakt tegenover aardverschuivings-dammen die zijn ontstaan als gevolg van andere processen (3) er is weinig onderzoek gedaan naar de drempelwaarden van de factoren die bepalen hoe lang en waar afdamming van een rivier plaatsvindt (4) weinig onderzoek is uitgevoerd naar de levensduur van door aardbevingen veroorzaakte dammen, en naar de invloed daarvan op de water- en sedimentafvoer op een regionale schaal onmiddellijk na de aardbeving (5) de inschatting van een meervoudige gevarensituatie die kan ontstaan door opeenstapeling van een aantal natuuramp-processen is maar beperkt beschreven in de vakliteratuur.

Dit onderzoek is gericht op een beter begrip van de oorzaken en gevolgen van aardverschuivings-dammen met nadruk op de 5 bovengenoemde lacunes in eerder onderzoek. Hiertoe werd eerst een inventarisatie gemaakt van dammen veroorzaakt door de 2008 Sichuan aardbeving met behulp van visuele interpretatie van remote sensing beelden, aangevuld door veldonderzoek in de daarvoor toegankelijke gebieden. Met behulp van deze inventarisatie is een analyse gemaakt van het ruimtelijke distributie patroon van alle door de Wenchuan aardbeving veroorzaakte aardverschuivingen en het distributie patroon van de rivier afdammingen. Beide verschijnselen komen het meest voor in het Pengguan massief, langs de hoofdbreuk van de Yingxiu-Beichuan breukzone. Het relatieve gewicht van de factoren die het voorkomen van deze aardverschuivingen bepalen is bepaald met behulp van de “weight of evidence” (WOE) methode. De resultaten daarvan tonen aan dat de afstand tot de aardbevings-breuk, de maximale versnelling van de grond (peak ground acceleration, PGA) en de lithologie de belangrijkste bepalende factoren zijn. Het type van de breuk en het effect van de opgeschoven dan wel afgeschoven zijde van de breuk werden in eerdere studies buiten beschouwing gelaten, maar zij blijken wel van invloed te zijn op het ontstaan van aardverschuivingen door aardbevingen.

Om voorspellingen te kunnen doen op een regionale schaal over de vorming van rivier afdammingen door aardverschuivingen als gevolg van aardbevingen is een empirisch-statistische methode ontwikkeld waarmee de drempelwaarde kan worden geschat voor het volume van de aardverschuiving dat nodig is om een rivierafdamming te veroorzaken, waarbij gebruik gemaakt wordt van landschaps-parameters die worden verkregen uit digitale terreinhoogte modellen (DEM’s). De methode bestaat uit twee stappen: een eerste stap is de bepaling van het minimum volume van de aardverschuiving dat nodig is om de rivier te kunnen bereiken, waarvoor stapsgewijze multivariante regressie wordt gebruikt. Vervolgens wordt een tweede minimum volume bepaald, dat overschreden moet worden om de rivier af te dammen, gebaseerd op correlatie van de rivier breedte met het volume van de aardverschuivings-dammen. Deze methode werd toegepast op verschillende typen aardverschuivingen die zouden kunnen ontstaan op een groot aantal punten in een fijnmazig netwerk in een daarvoor geselecteerd stroomgebied in het onderzoekgebied. De gemiddelde voorspellings-betrouwbaarheid is 97.2% en 86.0% voor respectievelijk niet afdammende en afdammende aardverschuivingen.

Om de geomorfologische levensduur van aardverschuivings-dammen die het gevolg waren van de Wenchuan aardbeving en het effect van hun bezwijken op het sediment transport na de aardbeving te kunnen kwantificeren, is de lengte van de periode tot bezwijken geschat door gebruik te maken van multi-temporele remote sensing beelden. Het volume van de tijdelijke opslag (tot het moment van bezwijken van de dam) van water en sediment is ook op deze wijze bepaald. Het kon worden vastgesteld dat 25% van de afdammingen binnen een week na de aardbeving bezweken, 60% en 90% binnen respectievelijk een maand en een jaar tijd. Slechts ongeveer een derde van het totale volume van de aardverschuivingen werd door het bezwijken weggespoeld. Het resterende gedeelte van het volume van de afdammingen, samen met het grootste deel (meer dan 85%) van de kleinere aardverschuivingen die de rivier bereikten zal nog in de komende tientallen jaren stroomafwaarts getransporteerd worden tijdens extreme rivier afvoer waarden.

Vloedgolven die optreden na het bezwijken zijn het meest gevaarlijke gevolg van afdammende aardverschuivingen. Bij dit onderzoek is de Tangjiashan dam (de gevaarlijkste afdamming als gevolg van de Wenchuan aardbeving) gebruikt als voorbeeld om scenarios voor de dambreuk en de daardoor ontstane vloedgolf te simuleren. Daartoe is een geintegreerde aanpak ontwikkeld die gebaseerd is op de fysieke BREACH modellering en de 1 en 2 dimensionale SOBEK hydrodynamische modellering. Allereerst werd het BREACH model toegepast om de vloedgolf parameters te bepalen op de plaats van de dam, die gecalibreerd werden met veldwaarnemingen van de vloedgolf na het kunstmatig veroorzaakte bezwijken. Deze vloedgolf parameters werden gebruikt als invoergegevens in het 1D-2D SOBEK model voor de simulatie van de ruimtelijke variatie van de vloedgolf parameters. De gevonden simulatie waarden komen overeen met de waargenomen maximale afvoer en de aankomsttijd van de vloedgolf bij de stroomafwaarts gelegen grote steden. Met deze aanpak kunnen dus betrouwbare voorspellingen worden gedaan waarop de beleidsmakers hun mitigatie plannen kunnen baseren.

De conclusie kan worden getrokken dat de resultaten van het onderzoek gebruikt kunnen worden voor het opstellen van een conceptueel decision support systeem voor de kwantitatieve inschatting van vloedgolven die het resultaat zijn van bezwijken van door aardbevingen veroorzaakte rivier afdammingen. Dit model gaat uit van een bepaalde aardbeving, die leidt tot aardverschuivingen en rivierafdammingen en resulteert in de bepaling van de gevaren verbonden aan een damdoorbraak. Bovendien dragen de resultaten van het onderzoek bij aan een beter begrip van het stapelingsproces van oorzaak en gevolgen van verschillende processen van natuurgevaren die veroorzaakt kunnen worden door zware aardbevingen.

总 结

滑坡堵江事件是地质构造活跃带高山峡谷地区的一种常见地质灾害。滑坡坝溃决产生的洪水和泥石流可能造成严重的人员伤亡、损毁房屋和其它基础设施。地震是诱发滑坡坝的主要因素之一，例如 2008 年“5.12 汶川大地震”。该地震发生于青藏高原东部的四川龙门山地区，是中国近 50 年来最大的地震灾害。汶川地震诱发了数以万计的次生地质灾害，其中包括滑坡 6 万余处、滑坡坝 800 余处，在全世界范围内都极为罕见和独特，为强震触发滑坡和滑坡坝的系统研究提供了难得的机会。

目前国内外研究现状表明，大部分研究集中于对大型滑坡坝的事例分析，包括滑坡坝对地貌的影响和滑坡坝稳定性等，而对下述问题的认识十分不足：（1）由于缺少直接观测数据，仅针对地震诱发滑坡坝的研究极少；（2）很少有研究对地震诱发滑坡坝的控制因素进行系统分析，并将其与滑坡的控制因素进行比较；（3）对滑坡堵江临界条件判定方面的研究基本为空白；（4）关于滑坡坝寿命及其对地貌演化，特别是对震后河流泥沙含量影响的区域性研究十分不足；（5）对多类型地质灾害的灾害链效应的研究也十分有限。

本论文旨在提高对地震诱发滑坡坝的成因及灾害链效应的认识，从而弥补上述研究空缺。为此，本研究首先根据对遥感图像的解译和野外调查，建立了汶川地震诱发滑坡坝数据库，并以此为基础对同震诱发滑坡和滑坡坝的空间分布规律进行了分析对比。研究结果表明，大部分滑坡和滑坡坝集中分布于位于中央主断裂带（映秀 - 北川断裂带）的逆冲断层段的彭灌断层块上。本研究还利用证据权重法（Weight of Evidence）对影响滑坡和滑坡坝发生的因子进行了定量分析。结果表明，距地表破裂带的距离、地面峰值加速度和岩性起着主控作用。此外，在以往研究中被忽视的断层类型和上 / 下盘效应对同震滑坡的发生也起着关键作用。

为了预测区域性地震诱发滑坡坝的形成，本研究利用可从 DEM 上简单提取的地形参数，建立了一套经验统计预测方法。该方法主要包括两个

步骤：一是通过多元统计回归方法获取滑坡滑动距离预测模型，从而确定使得滑坡能够到达河流的第一临界方量；二是通过河流宽度和滑坡坝方量之间的关系，确定使得滑坡能够完全堵塞河流的第二临界方量。该方法被应用于预测研究区域内不同类型滑坡的堵江概率。结果显示，非堵江滑坡和堵江滑坡的预测准确率分别为 97.2%和 86%。

为了定量评价汶川地震对河流泥沙含量的影响，本研究通过对多期遥感影响的解译，估测了滑坡坝的存活时间，同时估算了滑坡坝短期储存的松散物质（泥沙量）及堰塞湖容量。研究结果显示 25%的滑坡坝在地震发生 1 周内即会溃决，60%和高于 90%的滑坡坝会在震后 1 个月和 1 年内溃决。滑坡坝溃决导致约 1/3 的坝体物质被携带冲刷到下游，但仍然有大量的滑坡物质堆积在河流周围，等待未来几年或几十年的河流冲刷。

溃坝洪水是滑坡坝造成的主要危害之一。本研究以唐家山滑坡坝（汶川地震诱发的最危险的滑坡坝）为例，对多种工况下其溃坝过程和洪水进行了模拟。研究针对溃坝洪水模拟，建立了一种将 BREACH 模型（基于力学）和 SOBEK 模型（基于水动力学）相结合的新方法。该方法首先利用 BREACH 模型模拟实际工况（通过溢洪道泄洪）下，坝址处的水文曲线，并将其与实际观测的水文曲线进行对比，用以矫正模型。通过 BREACH 模型获取的水文曲线被作为主要参数输入到 SOBEK 一维和二维水动力学模型，模拟洪水的空间分布及相关参数。模拟所得的水文曲线、洪水峰值流量及到达下游城镇的时间均与实际观测值吻合的较好，从而说明该方法可以为决策者和滑坡坝治理，提供可靠的、准确的预测信息。

本论文的研究结果可以用于建立一个事件树概念模型，用于地震诱发灾害链效应进行定量评价。该模型可对“地震→地震诱发滑坡→滑坡堵江→滑坡坝溃决→溃坝洪水”这一灾害链的多个事件的成因、后果及发生可能性进行评价。因此，有助于提高对地震诱发及震后地质灾害链效应的认识和预测。

Author's Biography

Xuanmei Fan was born on 9th of July in China. From 2000 to 2004, she studied in Chengdu University of Technology, China, and obtained Bachelor degree on Geotechnical Engineering. Prior to her graduation, she was awarded a scholarship to continue a master study on Engineering Geology in the same university. In 2007, she received her M.Sc. degree with distinction in natural hazard and earth science. Her M.Sc. thesis title "Study on the genetic mechanism of translation landslides" won the best thesis award of the Sichuan Province, China. On 12th May 2008, the catastrophic Wenchuan earthquake hit Sichuan province, triggering an unprecedented number of geohazards. It motivated her research on coseismic landslides and landslide dams. In Sep 2009, she started her PhD research with a joint PhD scholarship provided by the Chinese Scholarship Council (CSC) in a sandwich Phd program between Faculty of Geo-information Science and Earth Observation (ITC), University of Twente, the Netherlands and State Key Laboratory of Geohazard Prevention and Geoenvironment Protection, Chengdu University of Technology, China. During her PhD, she published 12 peer reviewed ISI papers, one book chapter and presented her research in 5 international conferences.

From 2004 onwards, she has participated in many research projects in China on landslide mechanism, prediction, early warning and mitigation. Now she is also the coordinator of a research project on "The cascading effect of the post-seismic debris flows in the Wenchuan earthquake region" (No.41302241) funded by the National Natural Science Foundation of China(NSFC). Her main research interests include landslide hazard assessment, earthquake-induced landslides, landslide dam research, tectonic geomorphology, sediment flux in active mountain belts.

Publication list:

ISI journal articles:

[1] **Fan, X.**, van Westen, C.J., Korup, O., Gorum, T., Xu, Q., Dai, F.C., Huang, R., Wang, G., Transient Water and Sediment Storage Following the 2008 Wenchuan Earthquake, China, *Geomorphology*, 171-172, 58-68, 2012.

[2] **Fan, X.**, van Westen, C.J., Xu, Q., Gorum, T., Dai, F., Analysis of landslide dams induced by the 2008 Wenchuan earthquake, *Journal of Asian Earth Sciences*, 57, 25-37, 2012.

[3] **Fan, X.**, Tang, CX, van Westen, C.J., Alkema D., Simulating dam-breach scenarios of the Tangjiashan landslide dam induced by the Wenchuan earthquake, *Natural Hazards and Earth System Sciences*, 12, 3031-3044, 2012.

[4] **Fan, X.**, Rossiter, D.G., van Westen, C.J., Xu, Q., Gorum, T., Empirical prediction of coseismic landslide dam formation at regional scale, *Earth Surface Processes and Landforms* (moderate revision under review). 2013.

[5] **Fan, X.**, Xu, Q., Zhang, Z., Dong, S., Tang, R., The genetic mechanism of a translation landslide, *Bulletin of Engineering Geology and Environment*, 68, 231-244, 2009.

[6] Huang, R. and **Fan, X*.** 2013. The landslide story. *Nature Geosciences* 6, 325-326, 2013. (*corresponding author)

[7] Huang, R., Pei, X., **Fan, X.***, Zhang, W., Li, S., Li, B., The characteristics and failure mechanism of the largest landslide triggered by the Wenchuan earthquake, May 12, 2008, China, *Landslides*, 9, 1, 131-142, 2011. (*corresponding author)

[8] Gorum, T., **Fan, X.**, van Westen, C.J., Huang, R.Q., Xu, Q., Tang, C., Wang, G.H., Distribution pattern of earthquake-induced landslides triggered by the 12 May 2008 Wenchuan earthquake, *Geomorphology*, 133, 152-167, 2011.

[9] Xu, Q., **Fan, X.**, Huang, R.Q., van Westen, C.J., Landslide dams triggered by the Wenchuan earthquake, Sichuan Province, south west China, *Bulletin of Engineering Geology and Environment*, 68, 373-386, 2009.

[10] Xu, Q., **Fan, X.**, Dong, X., Characteristics and formation mechanism of a catastrophic rainfall-induced rock avalanche-mud flow in Sichuan, China, 2010, *Landslides*, 9, 143-154, 2011.

[11] Xu, Q., **Fan, X.**, Huang, R., Yin, Y., Hou, S., Dong, X., Tang, M., A catastrophic rockslide-debris flow in Wulong, Chongqing, China in 2009: background, characterization, and causes, *Landslides*, 7, 75-87, 2010.

[12] Gorum, T., van Westen, C.J., Korup, O., van der Meijde, M., **Fan, X.**, van der Meer, D., Complex rupture mechanism and topography control symmetry of mass-wasting pattern, 2010 Haiti earthquake, *Geomorphology*,184,127-138 , 2012.

ISI journal articles in preparation:

[13] Fan, X., van Westen, C.J., Xu, Q., Jetten, V., Huang, R., Tang, C., Gorum ,T. 2012. Five years on: what have we learned from the landslides associated with the Wenchuan earthquake. *Engineering Geology.* (invited paper for a special issue, in preparation).

[14] Fan, X., van Westen, C.J., Jetten, V., Xu, Q., Gorum ,T., Huang, R. 2013. Controls on the distribution of landslides and landslide dams induced by the 2008 Wenchuan earthquake. *Natural Hazards and Earth System Sciences.* (in preparation)

[15] Fan, X., van Westen, C.J., Xu, Q., Jetten, V., Gorum ,T. Constructing an event tree for quantitative hazard assessment of earthquake-induced landslide dam break floods. *Geomorphology*. (in preparation)

Book Chapter:

[16] Fan, X.,, Xu, Q., 2010. Xiejiadianzi landslide, Pengzhou. In: Xu, Q., Pei, X., Huang, R. (eds), Large-scale landslides induced by the Wenchuan earthquake. Beijing: Science Press, pp. 407-422. (in Chinese)

Peer-reviewed conference papers:

[17] Fan, X., van Westen, C.J., Xu, Q., Gorum, T., Wang, G., Huang, R. 2011. Spatial distribution of landslide dams triggered by the 2008 Wenchuan earthquake. In: Proceedings of the Second World Landslide Forum, Roma, Italy.

[18] Fan, X., van Westen, C.J., Havenith, H.B., Tang C.X. 2013. Analysis of the distribution of landslide and landslide dams induced by the Wenchuan earthquake. In: Proceedings of the 4th international INQUA Meeting on Paleoseismology, Active Tectonics and Archeoseismology (PATA), 9-14 October, 2013 (in process)

International conference presentations and abstracts:

[19] Fan, X., Gorum, T., van Westen, C.J., Xu, Q., Huang, R. Distribution of large landslides and landslide dams triggered by the Wenchuan earthquake, Sichuan, China. Geophysical Research Abstract, Vol. 11, EGU2009-2863, 2009

[20] Fan, X., van Westen, C.J., Gorum, T., Xu, Q., Spatial distribution and causal factors of landslide dams triggered by the 2008 Wenchuan earthquake, Geophysical Research Abstract, Vol. 13, EGU2011-722, 2011.

[21] Fan, X., van Westen, C.J., Korup, O., Xu, Q., Gorum, T., Huang, R, Dai, F., Analysis of landslide dams induced by the 2008 Wenchuan earthquake. In: the International Symposium in Commemoration of the 3rd Anniversary of the 2008 Wenchuan Earthquake, Chengdu, China, 2011

[22] Fan, X., Rossiter, D., van Westen, C.J., Xu, Q. Empirical prediction of coesismic landslide dams. In: the International Symposium in Commemoration of the 5th Anniversary of the 2008 Wenchuan Earthquake, Chengdu, China, 2013.

ITC Dissertation List

http://www.itc.nl/Pub/research/Graduate-programme/Graduate-programme-PhD_Graduates.html

The thesis cover is a copy of a famous Chinese landscape painting from Mr. Guangcan Li (painter) (http://hanfengyuanlin.blog.163.com/blog/static/481108332013593361767/)

The Chinese calligraphy, the poetry, on the back cover is from Yueqi Jin, who is an over sea calligrapher in Germany.

The general meaning of this poetry is:

> *"In the face of pitiless natural disasters, our empathy is unbounded.*
> *Where there is suffering, relief comes from the four corners of the Earth.*
> *China unites in one common heart full of pure compassion."*

------translated by David Rossiter

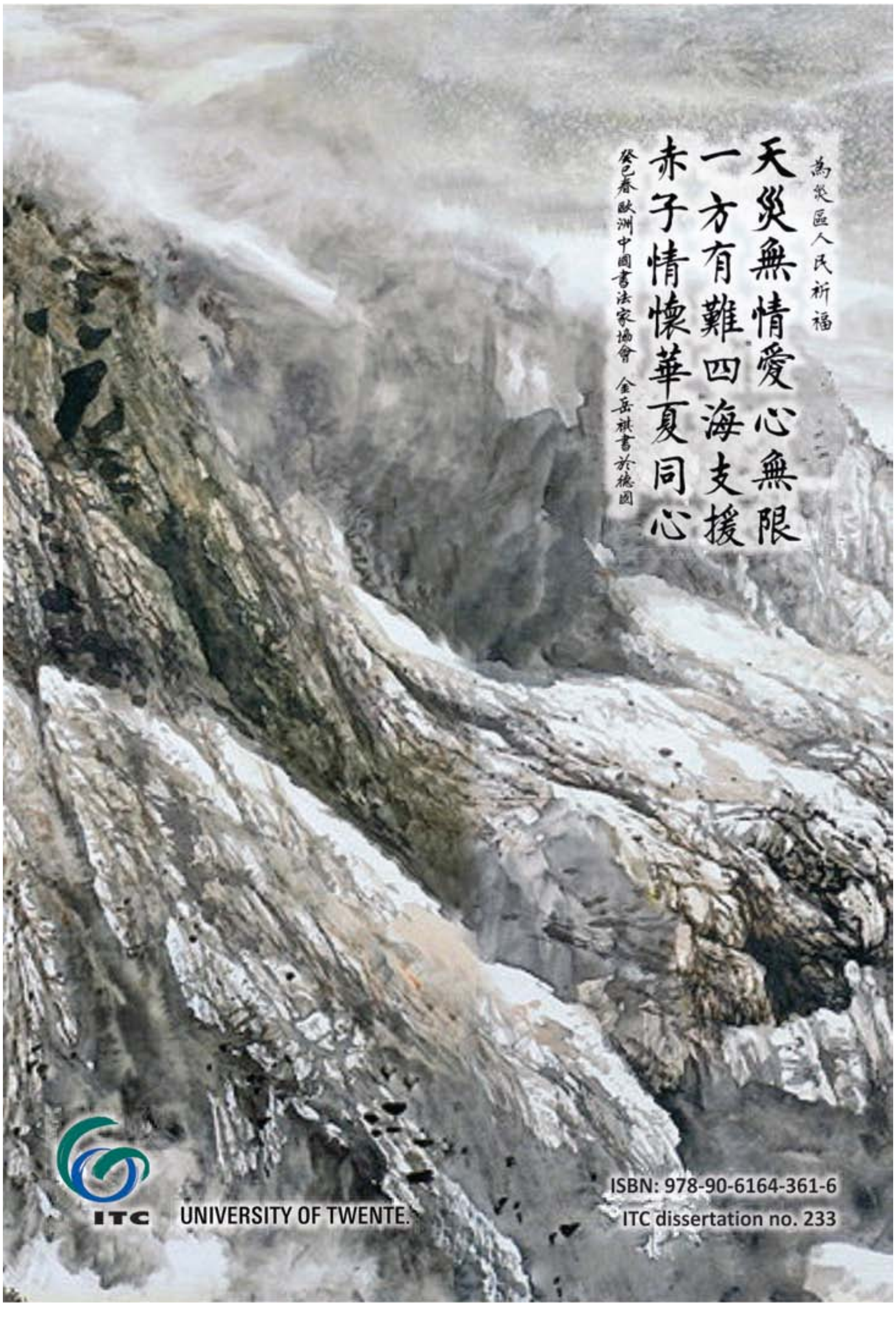

為災區人民祈福
天災無情愛心無限
一方有難四海支援
赤子情懷華夏同心
癸巳春 歐洲中國書法家協會 金岳祺書於德國

UNIVERSITY OF TWENTE.

ISBN: 978-90-6164-361-6
ITC dissertation no. 233